CRYSTAL PLASTICITY MODELING OF TI-6AL-4V AND ITS APPLICATION IN CYCLIC AND FRETTING FATIGUE ANALYSIS

A Thesis
Presented to
The Academic Faculty

by

Ming Zhang

In Partial Fulfillment
of the Requirements for the Degree
Doctor of Philosophy in the
School of Mechanical Engineering

Georgia Institute of Technology
April 2008

CRYSTAL PLASTICITY MODELING OF TI-6AL-4V AND ITS APPLICATION IN CYCLIC AND FRETTING FATIGUE ANALYSIS

Approved by:

Dr. David. L. McDowell, Advisor
School of Mechanical Engineering
Georgia Institute of Technology

Dr. Naresh N. Thadhani
School of Material Science and Engineering
Georgia Institute of Technology

Dr. Richard W. Neu
School of Mechanical Engineering
Georgia Institute of Technology

Dr. Rami M. Haj-Ali
School of Civil and Environmental Engineering
Georgia Institute of Technology

Dr. Min Zhou
School of Mechanical Engineering
Georgia Institute of Technology

Date Approved: 11/19/ 2007

To my wife, Xiangjun, and my daughter, Yiran.

ACKNOWLEDGEMENTS

First, I would like to express my gratitude to my advisor, Dr. David McDowell, for his guidance, support and encouragement throughout my stay at Georgia Tech. I would also like to thank Dr. Richard Neu for his help and guidance in the course of this work. They have taught me innumerable lessons and insights on the workings of academic research in general. I am thankful for the invaluable feedback and suggestions from the distinguished members of my committee: Dr. Min Zhou, Dr. Naresh Thadani and Dr. Rami Haj-Ali.

I would like to express my sincere gratitude to members of the research groups of Dr. McDowell and Dr. Neu. Special thanks are given to Dr. Aijun Wang, Dr. Jixi Zhang, and Dr. Florent Bridier for their assistance to my research. I am grateful to my friends: Dr. Rajesh Kumar, Dr. Doug Spearot, Dr. Mahesh Shenoy, Jason Mayeur, Dr. Jim Shepherd, Dr. Mark Tschopp, Rajesh Prasanna, Nima Salajegheh and Yustianto Tjiptowidjojo for their help and support during my graduate studies.

None of this work could have been done without the support provided by Air Force Office of Scientific Research (AFOSR), Defense Advanced Research Projects Agency (DARPA), and the Carter N. Paden, Jr. Distinguished Chair in Metals Processing.

Finally, I want to thank my dear family; my wife, Xiangjun, my daughter, Yiran, who have accompanied me with love during my studies, as well as my parents, my brother and his family, who have backed me throughout the course of my PhD.

TABLE OF CONTENTS

LIST OF TABLES

LIST OF FIGURES

SUMMARY

Ti-6Al-4V, known for high strength-to-weight ratio and good resistance to corrosion, has been widely used in aerospace, biomedical, and high-performance sports applications. A wide range of physical and mechanical properties of Ti-6Al-4V can be achieved by varying the microstructures via deformation and recrystallization processes. The aim of this thesis is to establish a microstructure-sensitive fatigue analysis approach that can be applied in engineering applications such as fretting fatigue to permit explicit assessment of the influence of microstructure. In this thesis, crystal plasticity constitutive relations are developed to model the cyclic deformation behavior of Ti-6Al-4V. The development of the slip bands within α-TiAl has been widely reported and has been found to play an important role in deformation and fatigue behaviors of Ti-6Al-4V. The shear enhanced model is used to simulate the formation and evolution of slip bands triggered by planar slip under static or quasi-static loading at room temperature. Fatigue Indicator Parameters (FIPs) are introduced to reflect driving force for the different crack formation mechanisms in Ti-6Al-4V. The cyclic stress-strain behavior and fretting fatigue sensitivity to microstructure and loading parameters in dual phase Ti-6Al-4V are investigated.

CHAPTER 1

INTRODUCTION

1.1 Microstructure and Deformation Behavior of Ti-6Al-4V

Titanium alloys, known for high strength-to-weight ratio and good resistance to corrosion, have been widely used in aerospace, biomedical, and high-performance sporting good applications. A wide range of physical and mechanical properties can be achieved by alloying Ti. Depending on the predominant phase or phases in their microstructure, titanium alloys are categorized as α, α/β, or β alloys, or γ-titanium aluminides (Kar, 2005).

The α phase of pure titanium has a hexagonal close packed (HCP) structure and remains stable at low temperature. At a temperature of approximately 980°C (transus temperature), the α phase transforms to the β phase which has body centered cubic structure and remains stable up to the melting point of about 1650°C. The transus temperature of Ti can be raised by adding certain α stabilizing elements such as aluminum, gallium and germanium. The α strengthening elements, notably tin and zirconium, have a high solubility in the α phase and can strengthen the α phase with little effect on the transus temperature (Kar, 2005). Single-phase and near-single-phase α Ti alloys have good strength, toughness, creep resistance and weldability. Furthermore, the generally high aluminum content of this group of alloys ensures good strength characteristic and oxidation resistance at elevated temperatures (in the range of 150 to 315°C) (Kar, 2005).

Elements such as chromium, columbium, copper, iron, manganese, molybdenum, tantalum, and vanadium stabilize the β phase by lowering the temperature of transformation from α to β. Titanium alloys with high percentage of β–stabilizing

elements remain stable as β phase at room temperature; β alloys have good formability and can be strengthened considerably by heat treatment.

The γ based titanium aluminides, having an aluminum level of 45-52%, are actually a mixture with γ phase of L10 structure and α_2 phases (Ti_3Al). The γ-TiAl based alloys display some attractive properties such as low density, high specific yield strength, high specific stiffness, good oxidation resistance, good resistance against long-term heat, and good creep properties at elevated temperatures, and therefore are considered for high-temperature applications in aerospace and automotive industries (Kruzic et al., 1998).

The α/β titanium alloys contain a mixture of α and β phases and, roughly speaking, combine the properties of strength of the α phase and ductility of β phase. A wide range of microstructure and properties of α/β titanium alloys can be achieved by appropriate heat treatment and thermomechanical processing. It is therefore important to tailor the alloy and its microstructure for a particular application.

Among Ti alloys, Ti-6Al-4V commands the biggest share of the present aerospace market for its combination of reasonable strength and ductility due to modest quantities of α stabilizer (Al) and β stabilizer (V) (Picu and Majorell, 2002). The typical chemical composition of Ti-6Al-4V is shown in Table 1 (Majorell et al., 2002).

Table 1.1 Chemical composition of a typical Ti-6Al-4V, wt.%

Al	V	O	Fe	Mo	C	Si	Mn
6.31	4.06	0.18	1.16	0.02	0.016	0.01	0.01
Cu	B	Zr	Y	N	Sn	Cr	Ti
0.02	0.001	0.02	0.001	0.008	0.02	0.01	Bal

At temperatures above 980°C, Ti-6Al-4V is composed of equiaxed β grains. Cooling the material slowly from the β phase field into the two-phase field, a coarse lamellar arrangement of the α phase is generated. Subsequent deformation and recrystallization processes can produce a wide range of microstructures ranging from bimodal to fully lamellar, as shown in Fig. 1.1 (Kar, 2005). The fully lamellar structure is used in applications that require fatigue crack propagation resistance, high fracture toughness, and creep resistance (Lütjering and Gysler, 1992). Bimodal or duplex structures, containing both globular and Widmanstatten features, provide good yield strength, tensile ductility, and fatigue strength (resistance to crack initiation in HCF) and are the focus of this study.

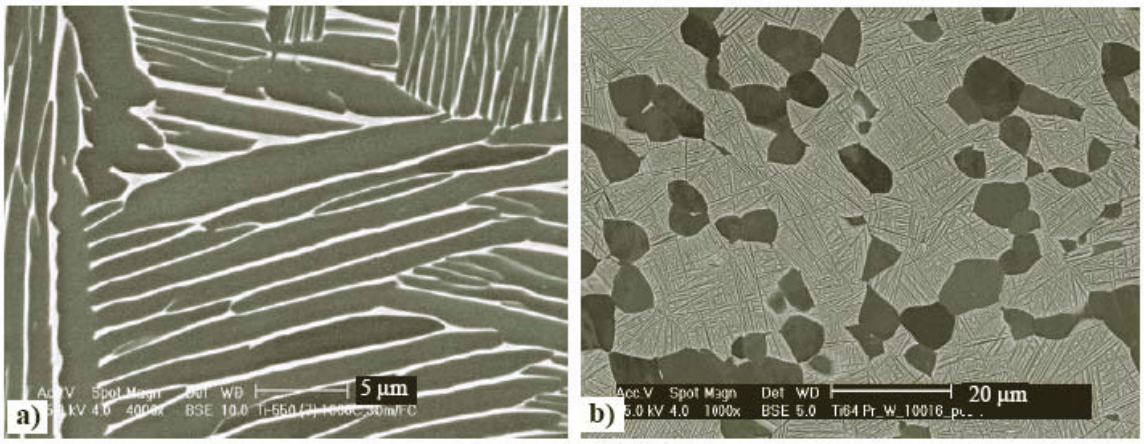

Figure 1.1 a) lamellar microstructure (Optical micrograph: bright phase is α phase); b) bimodal or duplex microstructure (SEM micrograph: dark phase is α phase) (Kar, 2005).

The mechanical behavior of Ti-6Al-4V is significantly affected by its texture and microstructure morphology. The colony size, width of the lamellae and the character of the inter-lamellar interface were found to be important for lamellar structured Ti-6Al-4V (Lütjering et al., 1992, 1995, 1998). For the bimodal structure, Lütjering (1998) suggested that grain size and volume fraction of primary α phase were the dominant

microstructural features with respect to mechanical behavior. The grain size determines the effective slip distance within the globular α phase, and in turn affects the yield strength. Experiments conducted by Lütjering (1998) showed an increase of material strength with decreasing volume fraction of primary α phase. In summary, the key microstructural features of Ti-6Al-4V include: average grain size of globular (primary) α phase, lamellar colony size, volume fraction of primary α phase, and mean thicknesses of the secondary α and β phases in the lamellar structure.

Due to highly anisotropic nature of crystallographic slip and low symmetry of HCP crystals, the orientation distribution of grains strongly affects the mechanical behavior of the bulk material (Fager and Spurr, 1968). For certain applications, as much as 30% increase of Young's modulus or 40% enhancement of yield strength can be achieved from textured Ti-Al alloys (Lee et al., 1966). Fager and Spurr (1968) reported a pronounced influence of texture on stress-corrosion resistance. Textures produced via thermomechanical processing of Ti-6Al-4V are generally grouped into three distinct categories: basal, transverse, and basal/transverse textures (Schoenfeld and Kad, 2002). Thermomechanical processing (e.g., rolling) of the α–dominated microstructure at around 815°C produces a basal texture. As temperature increases to 980 °C, rolling of the β–dominated microstructure generates a transverse texture. A mixed basal/transverse texture is created via thermomechanical processing at intermediate working temperatures ranging from 815°C to 980°C. A random texture, in which grain orientations are randomly distributed, is also found in commercial Ti-6Al-4V alloys. Examples of basal plane pole figures of these textures are shown in Fig. 1.2, with ND the direction normal to the rolled sheet (through thickness).

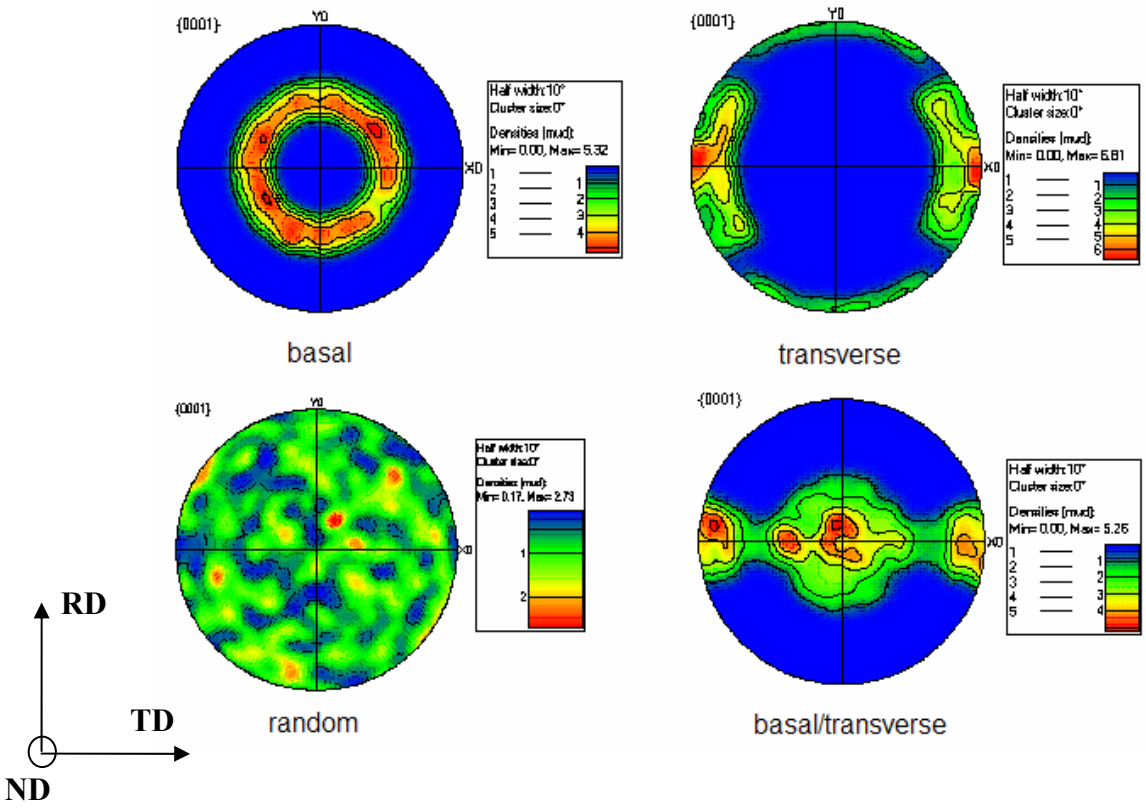

Figure 1.2 Basal pole figures of representative textures (Mayeur, 2004).

Table 1.2 Relative CRSS of slip systems reported in the literature for α-titanium and α/β Ti-Al alloys, normalized to the CRSS for prismatic slip at room temperature (Mayeur, 2004).

$\tau_{CRSS}^{basal} / \tau_{CRSS}^{prism}$	$\tau_{CRSS}^{pyr\langle a\rangle} / \tau_{CRSS}^{prism}$	$\tau_{CRSS}^{pyr\langle c+a\rangle} / \tau_{CRSS}^{prism}$	Reference
0.93 - 1.3	1	1.1 - 1.6	Medina et al., 1995
1.25	-	2.625	Paton et al., 1973
5	5	8.0 - 15.0	Fundenberger et al., 1997
1.5	1	3	Dunst and Mecking, 1996
1	-	8	Lebensohn and Canova, 1997
1.43	-	4.23	Bieler and Semiatin, 2001

Extensive studies have been conducted on the deformation behavior of α Ti-Al alloys subjected to a wide range of strain rates at different temperatures. Nanoindentation tests were also conducted by Viswanathan et al. (2005) on Ti-6Al-4V alloys containing high volume fraction of globular α phase. It was shown that mechanisms of plastic deformation in α Ti-based alloys include glide, twinning, and/or stress induced phase transformations, depending on Al content. As for other HCP crystalline materials, there are four different families of slip systems for the α phase: basal, prismatic, first order pyramidal and second order pyramidal slip systems (Naka and Lasalmonie, 1982), as shown in Fig. 1.3. The critical resolved shear stress (CRSS) of slip systems reported in literature for α-titanium and α/β Ti-Al alloys at room temperature are summarized by Mayeur (2004), and are shown in Table 1.2. It is clear that the slip resistance of the basal system is higher than that of the prismatic system. The pyramidal systems have the largest CRSS of all slip systems.

At temperatures below 980°C, a slight enrichment of Al in α phase leads to formation of α_2 precipitates (Ti_3Al) in the form of very fine particles. A large number of α_2 particles can homogeneously precipitate inside the α phase after an overaging process. Picu and Majorell (2002) found that the influence of α_2 precipitation on the CRSS for prismatic slip was negligible. However, a high content of α_2 phase was found to decrease the strength and ductility but increase the possibility of adiabatic shear band formation under dynamic loading (Lee et al., 1966).

Previous studies (Williams et al., 2002; Picu and Majorell, 2002) have shown that both Al concentration and deformation temperature have a pronounced effect on both the resolved stress for slip and the deformation character of α Ti-Al. It was shown that prismatic slip dominates polycrystal deformation of α Ti-Al alloys with low fraction of Al (e.g., < 2.9 wt.%) at room temperature. With increasing Al concentration, basal slip becomes increasing important. Prismatic and basal slip should be about equally important

in deformation of Ti-Al alloys when the Al concentration reaches 5 wt.% to 6 wt.%. At the same time, the transition from wavy to planar slip was observed as the Al content increases from 1.4 wt.% to 6.6 wt.% (Williams et al., 2002). The CRSS of every slip system decreases with increasing temperature. The drop of CRSS with increasing temperature for pyramidal slip systems is much steeper than for the prismatic/basal planes. This results in the critical resolved shear stress values in all active slip planes converging at temperatures above 325°C (Paton et al., 1973). The equalization of CRSS in all slip systems was reported (Williams et al., 2002) to result in a shift of slip in α phase Ti-Al from planar to wavy. However, Paton and Backofen (1970) showed that <c+a> pyramidal slip was always more difficult to activate than either prism or basal slip at all temperatures below 730°C.

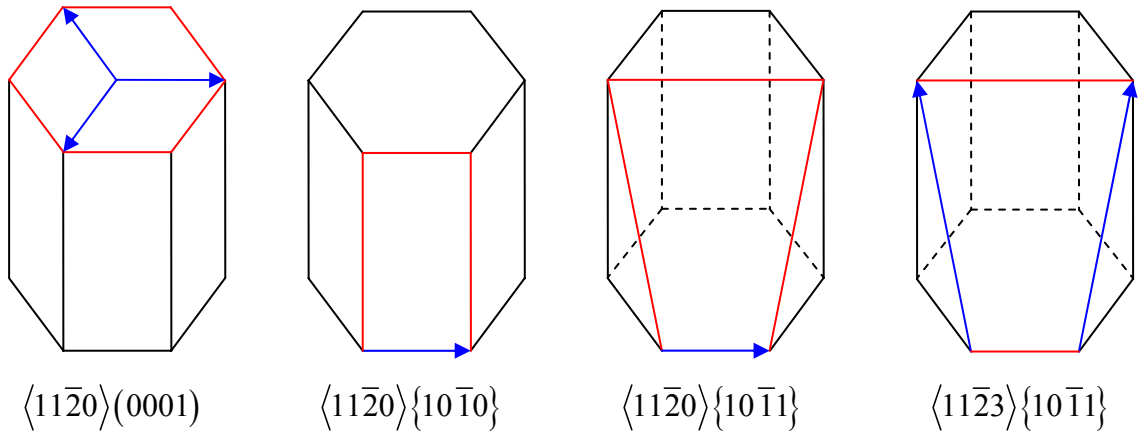

(a) Basal. (b) Prismatic. (c) 1st order pyramidal. (d) 2nd order pyramidal.

Figure 1.3 Slip systems for the primary α-phase, with slip direction shown in blue.

The highly planar nature of slip at low temperature is an important slip feature of α-TiAl. Picu and Majorell (2002) suggested that the presence of α_2 (Ti_3Al) precipitate as a material imperfection in the alpha matrix triggered the planar slip. Another generally accepted explanation for the planar slip is the breakdown of short-range order (SRO)

between titanium, aluminum and oxygen atoms (Williams et al., 2002; Neeraj et al., 2001; Xiao and Umakoshi, 2002, 2003). It was suggested that the leading dislocation moving through the lattice breaks down the SRO; subsequent dislocations cannot restore the order. As a result, a favorable dislocation path is introduced due to the lower friction stress exerted on trailing dislocations. Therefore, further slip concentrates in this slip plane, leading to planar deformation. The strong planar slip character inhibits cross-slip of screw segments; even though there is interaction between slip systems, it is observed that the slip bands are able to pass through one another with only minor difficulty (Xiao and Umakoshi, 2002, 2003).

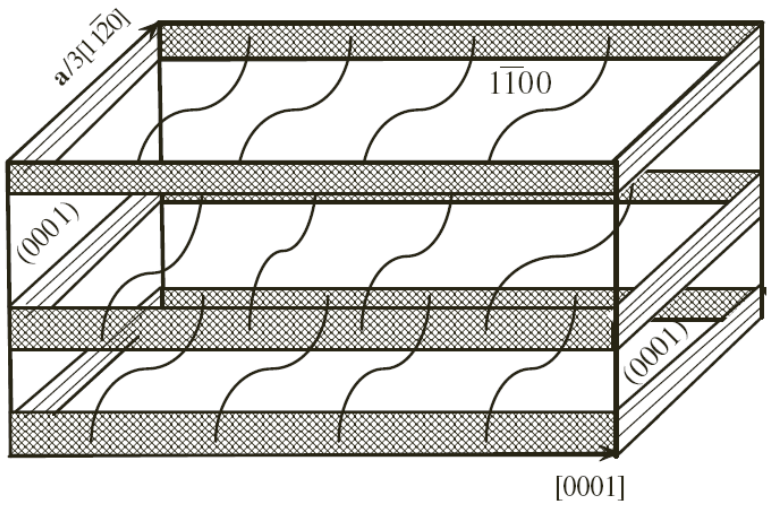

Figure 1.4. Three-dimensional crystallographic sketch of slip bands in Ti-5Al single crystal oriented for single prismatic slip (Xiao and Umakoshi, 2003).

Dislocation configurations in form of the band structures have been widely reported for the higher-Al-content α Ti-Al alloys deformed under monotonic (Blackburn and Williams, 1969), cyclic (Xiao and Umakoshi, 2003), creep (Neeraj et al., 2001), and dynamic loading (Xue et al., 2002) at room temperature. The reason for slip band formation has been postulated as the highly planar nature of slip. The formation of slip

bands results in very little work hardening in slip systems. In the case of monotonic deformation, unusually low strain hardening exponent values are found when a strain rate-sensitive Hollomon flow law is used to fit the stress-strain curve (Neeraj et al., 2000). An obvious cyclic softening stage was observed by Umakoshi and Xiao (2003) in the cyclic stress-strain curves of the α Ti-5Al single crystal oriented for single and double prismatic slips. The low work-hardening manifests significant low temperature creep behavior of α TiAl alloys compared to many other metals and alloys (Neeraj et al., 2000). Xiao and Umakoshi (2003) investigated the dislocation structure in single crystals oriented for single prismatic slip under cyclic loading. The dislocations were found to be arranged in a banded structure, as shown in Fig. 1.4. Slip bands were found parallel to the active slip plane and were uniformly distributed over the specimen surface; they widened as the cyclic deformation continued. The TEM observations showed that the width of slip bands increased while spacing between bands decreased with increasing cyclic plastic strain amplitude (CPSA) in the α Ti5Al single crystal oriented for single prismatic slip (Xiao and Umakoshi, 2002). In the case of the single crystal oriented for double prismatic slip, both the width and spacing of slip bands decreased as the CPSA increased, indicating that new slip bands were formed (Xiao and Umakoshi, 2003).

Twinning is potentially an important deformation mechanism in hcp materials. Pure α Ti subjected to low strain rates experiences deformation twinning at temperatures below 500ºC. At higher temperatures, Ti twins only under dynamic loading. Increasing Al concentration inhibits twinning. Ti-6%Al does not twin even at very low temperatures, e.g., -170ºC (Paton et al., 1976). Twinning is only observed in Ti-6Al-4V loaded at high strain rates (5000 s^{-1}) at room temperature. Thus, twinning is not a major deformation mechanism in Ti-6Al-4V at rates and temperatures of practical interest to aerospace structures such as blades and disks in the compressor section of an aircraft gas turbine engine (Picu and Majorell, 2002).

In duplex Ti-6Al-4V, the lamellar colonies contain secondary α and β phases arranged in a lamellar structure. TEM observations show that the Burgers orientation relation (BOR), shown in Fig. 1.5, holds between these two phases. The BOR is given as $(0001)_\alpha \| \{110\}_\beta$, $\langle 11\bar{2}0 \rangle_\alpha \| \langle 111 \rangle_\beta$ (Ankem and Margolin, 1980). The deformation behavior of a α/β lamellar colony is not very well-understood due to the difficulties of in-situ testing and characterization of the very fine structure. Picu and Majorell (2002) found that the mechanical behavior of Ti-6Al-4V changed markedly only when the wt% of β was larger than 50% at 970ºC. They believed that the soft V-enriched β phase plays a marginal role in deformation of the lamellar colonies at low homologous temperature due to the very low volume fraction. Therefore, it was suggested that the deformation of the lamellar colony was mainly controlled by the secondary α phase, and the deformation mechanism of secondary α phase was similar to that of primary α phase (Picu and Majorell, 2002). The interface between secondary α and β phases was considered to have little resistance to dislocation transmission by Lin et al. (1984). However, Suri et al. (1999) reported pronounced anisotropy in the primary creep response of two prismatic slip systems which could be attributed to the near-Burgers orientation relationship observed in α/β titanium alloys. Savage et al. (2001) observed that the slip resistance of an interface for one basal slip system in colonies of Ti6242 is much lower that that of other two basal slip systems. Ambard et al. (2001) reported that slip occurred primarily on prismatic slip planes in equiaxed α regions of Ti-6Al-4V, while basal slip dominated in the α/β colonies. Savage et al. (2004) investigated the anistropic deformation of α/β colonies of Ti6242 and showed that the CRSS for a1, a2 and a3 basal slips ordered as a2>a3>>a1. Dislocation annihilation in the a1 system is possible due to slip transmission through the β laths, resulting in lower strength and work hardening, while the a2 and a3 systems show significant dislocation pile-ups at the α/β interfaces. Those observations revealed the significant effects of α/β interfaces on the slip behavior.

Mayeur (2004) proposed a model for the α/β colonies by homogenizing the lamellar structure with 24 possible slip systems: 3 basal $\langle 11\bar{2}0\rangle(0001)$, 3 prismatic $\langle 11\bar{2}0\rangle\{10\bar{1}0\}$, 6 <a> first-order pyramidal $\langle 11\bar{2}0\rangle\{10\bar{1}1\}$, and 12 $\langle 111\rangle\{110\}$ bcc systems, as illustrated in Fig. 1.6. Prior to assigning grain orientation, the bcc slip systems are transformed into the hexagonal coordinate system according to the Burgers orientation relation (BOR). The slip systems that either glide parallel to the α/β interface or have parallel slip planes in both the α and β phases are considered as the soft deformation modes. The set of soft deformation modes consists of 3 basal, 1 prismatic, and 2 $\langle 111\rangle\{110\}$ bcc slip systems. Within the set of soft deformation modes assumed in this model, dislocations on the prismatic system glide parallel to the α/β interface, whereas the basal and close packed bcc planes are parallel and dislocations gliding in these planes are effectively able to transmit and traverse the length of the lamellar colony, as shown in Fig. 1.5. The hard modes of deformation correspond to the slip systems for which dislocations cannot transmit through the interface, therefore leading to high CRSS for these systems due to net residual dislocation density at the α/β interfaces.

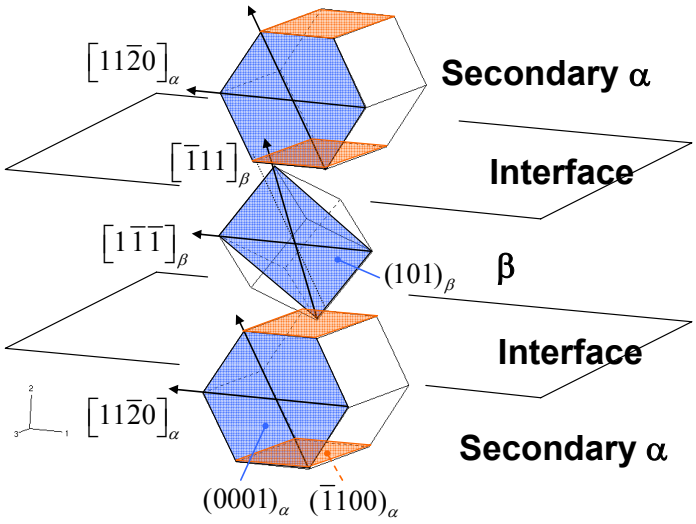

Figure 1.5 Lamellar Burgers orientation relationships (BOR).

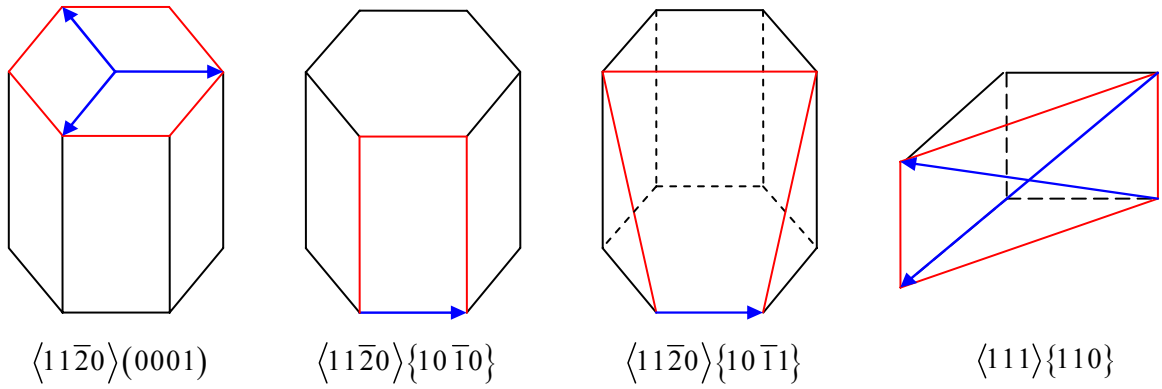

Figure 1.6 Slip geometry for equivalent representation of α/β colonies, with slip direction shown in blue (Mayeur, 2005).

Considerable effort has been devoted to modeling the mechanical behavior of Ti-6Al-4V for a wide range of loading histories. Classical rate-independent isotropic plasticity theory (J_2 plasticity) with nonlinear isotropic and kinematic hardening rules was used by Goh (2002) to simulate the fretting behavior of Ti-6Al-4V. Neeraj et al. (2000) used a relatively simple Hollomon flow equation to describe the constant strain rate behavior of Ti-6Al-4V. It was shown that the creep response of these alloys at room temperature can be correlated by first fitting their constant strain rate response. Barboza et al. (2004) developed a power-law model to describe the normal creep behavior of Ti-6Al-4V at 500ºC and 600ºC. It was shown that dislocation climb dominated the primary and steady-state creep regimes. Guo et al. (2005) applied both a phenomenological Johnson-Cook equation of state plasticity model and a dislocation-mechanics-based BCJ (Bammann-Chiesa-Johnson) model to describe the response of Ti-6Al-4V under dynamic loading. The BCJ model incorporates strain rate and temperature dependence, as well as damage, and was found to be the more accurate approach to predict the effect of loading history, once calibrated to experimental data for other histories.

While conventional plasticity was found useful to model the macroscopic stress-strain response of Ti-6Al-4V, the homogenized approach is incapable of explicitly

describing the effects of microstructure on mechanical behavior. Goh et al. (2001) and Morrissey et al. (2003) developed a microstructure-scale two-dimensional crystal plasticity model of duplex Ti-6Al-4V that employed a planar triple slip idealization; fretting fatigue simulations were conducted using a two-dimensional finite element model. The two-dimensional crystal plasticity model was extended to a full three-dimensional version by Mayeur (2004). The slip geometry of a lamellar colony was modeled by homogenizing the fine structure with 24 slip systems. As just discussed, the hard and soft deformation modes were introduced based on the BOR. The CRSS of each slip system of the two phases depends on the corresponding length scale. Finite element (FE) models used to simulate fretting fatigue (Mayeur, 2004; Zhang et al., 2006) reveal a significant influence of the microstructural features of Ti-6Al-4V on the plastic deformation behavior in the region of contact.

Similar effects of microstructural features on creep, fretting and high strain rate deformation behavior of Ti-6Al-4V were shown in the studies by Hasijia et al.(2003), Dick and Cailletaud (2006) and Schoenfeld and Kad (2002), respectively. Picu and Majorell (2002) developed a dislocation density dependent approach in which the stress is assumed to be composed of thermally activated and athermal components. The thermally activated stress is described by a Kocks-Mecking model while the athermal component is the function of the generic dislocation density and the grain size. In Picu and Majorell (2002), the primary α phase and lamellar colony are assumed to have the same deformation behavior at room temperature, which is counter to experimental observations. Marin and Dawson (1998) proposed an elasto-viscoplastic constitutive model for polycrystalline materials which was applied to both face centered cubic and hexagonal close-packed crystals subjected to both monotonic and non-monotonic loading histories. Based on this model, a series of simulations of hot rolling of α/β Ti-6Al-4V alloys were carried out to examine the misorientation structure within grains for different textured materials loaded at various directions (Barton and Dawson, 2001). To

investigate the anisotropic strength of heat-treated Ti-6Al-4V, the iso-strain hypothesis (Taylor model) was employed to corporate the evolving orientation distribution (Dawson, et. al, 2005). It should be noted that the iso-strain hypothesis is not good for HCP polycrystal due to their highly anisotropic nature of crystallographic slip and low symmetry. Dick and Cailletaud (2006) developed crystal plastic constitutive relations for Ti-6Al-4V in which only the primary α phase is considered. Fretting fatigue simulations were conducted on Ti-6Al-4V with more realistic modeling of grain shapes using Voronoi polyhedra. All these studies showed that the crystal plasticity model is able to capture the significant microstructure and texture effects on the mechanical deformation behavior of Ti-6Al-4V, which is important for a microstructure sensitivity study and microstructure-scale fatigue analysis.

1.2 Slip Localization and Slip Bands

Slip bands are regions with localized slip in crystals. The dislocation density in a slip band can be up to two orders higher than that in the matrix. In crystalline material, slip bands initiate and thicken as dislocations accumulate within the bands; the orientation of slip bands in a single crystal depends on the crystallographic orientation relative to applied strain. Under quasi-static loading at room temperature, slip bands in α Ti-Al alloys can develop as previously discussed. Experiments on single crystal metals subjected to tensile and compressive loading at large strain are summarized by Dao and Asaro (1996). Experimental observations regarding the structure of slip bands and corresponding internal stresses within FCC metals can be found in Antonopoulos and Winter (1976) and Kassner et al. (1997, 2000, 2001). The nucleation, propagation and evolution of slip bands lead to cyclic strain softening of the crystalline materials. Slip bands play an important role in the high cycle fatigue (HCF) response of crystalline

materials. Dao and Asaro (1996) showed that microvoids formed near the banded region due to the intensive shear and contributed to the material failure. In cyclically deformed α Ti-Al alloys, slip bands impinge on the grain boundary, leading to high stress concentrations that promote grain boundary decohesion.

Slip band phenomena are known to play a role in the initiation of fatigue cracks of crystalline materials. It is generally believed that slip bands are triggered by material instabilities, including material defects, microvoid nucleation (Steninger and Melander, 1982), hard or soft inclusions (Sukumar et al., 2001), texture (Nealea et al., 2003), strain softening (Argon, 1973), reorientation of smaller grain in nano-crystalline materials (Fu et al., 2004), and strain rate softening (Wang and Yao, 1997). Asaro and Rice (1977) argued that localization can also arise from constitutive instability such as non-Schmid effects. Boundary constraints can also trigger the non-uniform deformation, as shown by Lemonds et al. (1985).

For materials described by idealized rate independent constitutive laws, Hill (1962) has developed a general theory of bifurcation of a homogeneous elastic-plastic flow field into bands of localized deformation. By considering the non-Schmid effect due to contribution from components of stress other than the resolved shear stress, Asaro and Rice (1977) showed that the orientation of slip bands and critical plastic-hardening modulus could be predicted in the crystal plasticity framework, based on Hill's bifurcation rule. With this theory, strain localization in single and bi-crystals was then investigated by Dao and Asaro (1993, 1996), Paidar et al. (1984) and Lemonds et al. (1985). Shear localization phenomena in bi-crystals were shown to be very similar to those in single crystals after finite deformation. These simulations suggested that the misorientation between grains can trigger the slip localization and significantly affect the deformation patterns. It should be noted that these approaches are typically more closely associated with the large strain regime.

Many works have been done to explicitly model the slip bands using macroscopic plasticity or crystal plasticity models combined with conventional finite element method. Winter (1974) employed a two-phase model in which the volume fraction of PSBs (persistent slip bands) was linear with respect to plastic strain amplitude. Sluys and Estrin (2000) used a dislocation based gradient crystal plasticity model to investigate the slip localization in a single crystal subjected to monotonic tensile loading. The strain localization under cyclic loading in nickel-based superalloys was studied by Flouriot et al. (2003) by using a crystal plasticity algorithm. Zaiser et al., (1998) modeled the strain localization in persistent slip band (PSB) structure by using a strain gradient approach. Mughrabi (2004) indicated that although a promising match of size effects between experimental observation and prediction of strain gradient plasticity model was obtained by Aifantis (1984) and Fleck et al. (1994), lack of detailed microscopic consideration and unique internal length scale for a given material deformed to a certain plastic strain lead to the difficulties in explaining the physical meaning of the material length scale relating to measurable microstructural dimensions. In the "composite model" developed by Mughrabi (2001), the material was divided into hard and soft regions representing dislocation cell wall and cell interiors, respectively. The strain gradient was considered to be developed between these two regions and layers of GND of opposite sign formed on the either side of the dislocation walls. Thus, the strain gradient term could be linked to the length scale of the slip band.

It should be noted that in the previous works on explicitly modeling the slip bands in crystalline materials, prescribed perturbations were necessary to trigger the localized deformation. The prescribed perturbations include: material imperfection, thickness inhomogeneities of FE model, material points with different properties, boundary constraints, and so on. The assumption of such prescribed conditions is consistent with the concept that slip localization results from the material instability. It should be noted that the parameters of prescribed perturbations can significantly influence the geometry

and structure of the simulated slip band. Zhou et al. (2005) indicated that the deformation behavior of slip band and matrix should be different based on uniaxial cyclic loading experiments on nickel single crystal oriented for single slip. To account for this, distinct constitutive models are used for the slip band and matrix "phases". A stress-based criterion was employed to determine the propagation of slip bands. Thus, the prescribed perturbations were not required to trigger the shear localization, since the local stress perturbations were used. It was found that the resulting average boundary stresses at the onset of PSBs were quite consistent with those reported in the literature (Zhou et al., 2005).

The slip band spacing is an intrinsic length scale reflecting dislocation substructures and internal stresses. A theory of slip band spacing in fatigued materials has been developed by Venkataraman et al. (1991) based on a criterion of minimum strain energy. Crack nucleation is considered to occur in the slip band when the strain energy in a local region exceeds the surface energy necessary to open up the crack (Venkataraman et al., 1991). Olmstead et al. (1993) developed a theoretical characterization of a slip band as a surface of discontinuity for a one-dimensional problem. The slip band was idealized as an infinitesimally thin domain. Evolutions of stress and temperature within a slip band were obtained. The principle of minimum energy was used by many other researchers to calculate the wavelength and thickness of PSB. Hecker (1998) assumed that the strain is constant in PSB and predicted extremely small PSB wall width and unrealistically high internal stresses. Kratochvil et al. (1998, 2001) assumed that the strain in PSB varies during deformation. The calculated PSB width was shown to be very close to the experimental data of single crystal Ni cycled at room temperature by Kratochvil et al. (1998, 2001). A set of partial nonlinear differential equations (reaction-diffusion) was suggested by Differt and Essmann (1993, 1996) to describe the walls in PSBs. The shape of the walls can be obtained by solving the

equations. It should be noted that FCC metals such as pure Cu and Ni were considered in these studies.

Ortiz et al. (1999, 2000) developed a nonlocal micromechanical theory to characterize analytically dislocation structures in fatigue FCC single crystals (e.g. Ni and Cu), including PSB. It is shown that the development of dislocation structure is caused by the lack of convexity of the incremental energy functional. In this theory, the development of complex dislocation structures and the corresponding softening effect are accounted by a sequence of simple lamellate process. So far, this theory was only applied to FCC single crystals. Implementation of this theory in finite element simulation to explicitly simulate the slip band in HCP crystals is unavailable.

The phase field theory has been widely used in material science to model the grain growth (Granasy et al., 2006), phase transformation (Charach et al., 2004), and dislocation interaction (Wang et al. 2001). Fried and Gurtin (1993) extended the Ginsburg-Landau theory (Landau and Khalatnikov, 1965) of phase transition by introducing a micro-force balance law between phases. Bammann et al. (1999) used this theory to develop a gradient model of dislocation evolution. Slip band and matrix display different deformation behaviors. Therefore, Onuki (2003) suggested that a phase field approach would be useful to model the slip localization. The basis of the phase field theory is the functional of the local free energy density depending on the order parameter of the system and its spatial derivatives. Different phases such as matrix and slip band have different ordered status. The motion of individual phases can be derived by minimizing the free energy functional (Steinbach et al., 1995). In order to modeling the interaction between the slip band and matrix, the local free energy of the two "phases", is required.

One aim of this study is to explicitly simulate the development of slip band in α TiAl alloys. In this study, a composite modeling approach is employed, in which we intentionally introduce soft regions in a matrix. Similar to other composite modeling

approaches (Winter, 1974; Zhou et al., 2005), different material constants are assigned to the slip band (soft region) and matrix. We limit localization by using reduced integration elements on the order of the intended width of the slip band. The width and spacing of slip bands are obtained from the experimental observations. It is possible that the nonlocal approach such as certain forms of strain gradient crystal plasticity can be used to model slip bands. However, compared to the strain gradient crystal plasticity models, the approach used in this study is simpler, more robust for fatigue simulation, and less computationally expensive. Furthermore, the strain gradient approach faces the similar issues as the nonlocal approach. For example, the wavelength of slip band effectively needs to be determined a priori by assignment of a suitable gradient coefficient. Similar to the approach used in this study, these coefficients are constants and independent of deformation (Ortiz et al., 2000).

1.3 Crystal Plasticity

Microstructure has significant influence on the macroscopic properties. Traditional macroscopic models of plasticity are unable to capture the local details of the deformation mechanisms at the microstructural level. Crystal plasticity theory was developed to describe slip at the single crystal level.

The anisotropic elastic response of the crystal is modeled using independent components of the elastic stiffness tensor with symmetries that correspond to each crystal class. Plastic deformation reflects the accumulation of slips on each active slip systems. The crystal plasticity algorithm follows that described in Bennett (1999) and McGinty and McDowell (1999). The total deformation gradient is decomposed multiplicatively, i.e.,

$$\mathbf{F} = \mathbf{F}^{e}\mathbf{F}^{p} \tag{1.1}$$

where $\mathbf{F}^{e}$ denotes the elastic deformation gradient which incorporates reversible elastic stretch and rigid body rotation of the lattice. The plastic deformation gradient $\mathbf{F}^{p}$ describes the change in the shape of the grain due to dislocation glide while the lattice is unchanged. The velocity gradient **L** in the current configuration is given by

$$\mathbf{L} = \dot{\mathbf{F}}\mathbf{F}^{-1} \tag{1.2}$$

and can be decomposed as

$$\mathbf{L} = \mathbf{L}^{e} + \mathbf{L}^{p} \tag{1.3}$$

where

$$\mathbf{L}^{e} = \dot{\mathbf{F}}^{e}\mathbf{F}^{e-1} \text{ and } \mathbf{L}^{p} = \mathbf{F}^{e}\dot{\mathbf{F}}^{p}\mathbf{F}^{p-1}\mathbf{F}^{e-1} \tag{1.4}$$

The kinematics of elastic-plastic deformation of crystals are shown in Fig. 1.7. The grids represent the crystal lattice; $\mathbf{s}_0^{\alpha}$ and $\mathbf{n}_0^{\alpha}$ denote unit vectors in the slip direction and the slip plane normal direction, respectively, for the α^{th} slip system in the undeformed configuration. Note that $\mathbf{s}^{\alpha}$ and are $\mathbf{n}^{\alpha}$ not generally unit vectors, but remain orthogonal during deformation. As the material plastically deforms, the lattice undergoes elastic deformation and rigid rotations. Correspondingly, the unit vectors in the current configuration, deform with the lattice, i.e.,

$$\mathbf{s}^{\alpha} = \mathbf{F}^{e}\mathbf{s}_0^{\alpha} \text{ and } \mathbf{n}^{\alpha} = \mathbf{n}_0^{\alpha}\mathbf{F}^{e-1} \tag{1.5}$$

The plastic velocity gradient in the intermediate configuration is based on the sum of shearing rates on active slip systems, i.e.,

$$\hat{\boldsymbol{L}}^{p} = \sum_{\alpha=1}^{N_{sys}} \dot{\gamma}^{\alpha} \left(\boldsymbol{s}_0^{\alpha} \otimes \boldsymbol{m}_0^{\alpha} \right) \tag{1.6}$$

where $\dot{\gamma}^{\alpha}$ is the shearing rate on the α^{th} slip system.

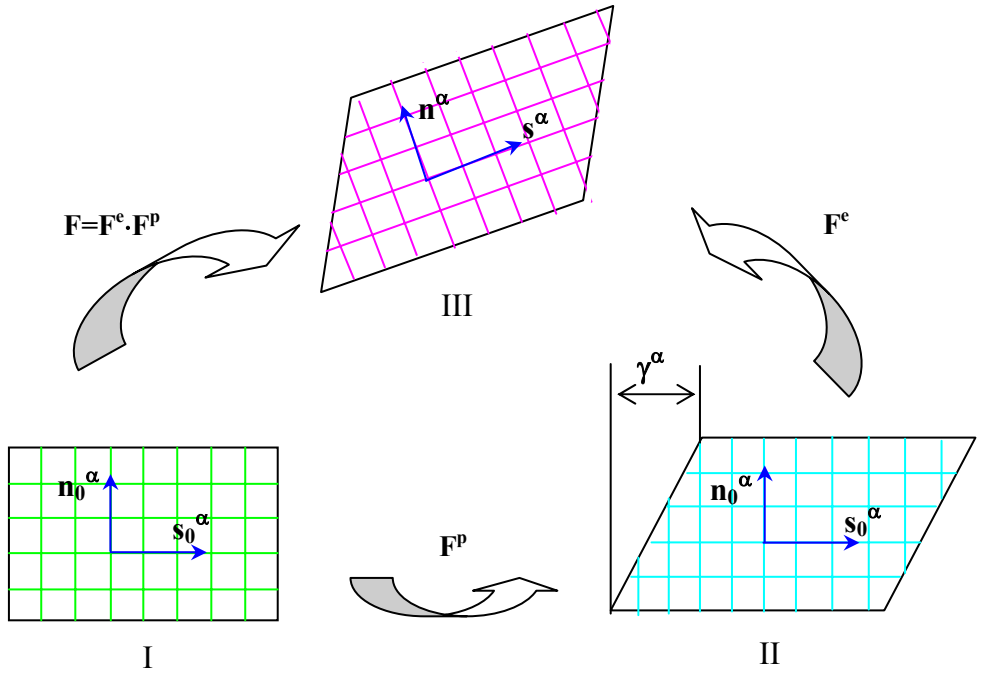

Figure 1.7 Kinematics of elastic-plastic deformation of crystalline solid deforming by crystallographic slip
(I: Undeformed, II: Intermediate, III: Deformed (or Current) Configuration).

The elastic Green strain tensor is defined as

$$\boldsymbol{E}^{e} = \frac{1}{2}(\boldsymbol{C}^{e} - \boldsymbol{I}) \tag{1.7}$$

with the right Cauchy-Green deformation tensor defined as

$$\boldsymbol{C}^e = \boldsymbol{F}^{eT}\boldsymbol{F}^e \tag{1.8}$$

The Cauchy stress $\boldsymbol{\sigma}$ is defined in the deformed configuration as force/(unit deformed area). In the intermediate configuration, the symmetric 2nd Piola-Kirchhoff stress tensor $\boldsymbol{\sigma}^{\mathrm{pk2}}$ is defined by

$$\boldsymbol{\sigma}^{\mathrm{pk2}} = \det\left(\mathbf{F}^e\right)\mathbf{F}^{e-1}\boldsymbol{\sigma}\mathbf{F}^{e-T} \tag{1.9}$$

Therefore, the elasic stress-strain relation with respect to the intermediate configuration can be written as

$$\boldsymbol{\sigma}^{\mathrm{pk2}} = \mathbf{C}\cdot\mathbf{E}^e \tag{1.10}$$

where **C** is a fourth rank anisotropic elasticity tensor.

The rate of viscoplastic shear strain ($\dot{\gamma}^\alpha$), for the α^{th} slip system, is given in this work by

$$\dot{\gamma}^\alpha = \dot{\gamma}_0 \left\langle \frac{\left|\tau^\alpha - \chi^\alpha\right| - \kappa^\alpha}{D^\alpha} \right\rangle^m \operatorname{sgn}\left(\tau^\alpha - \chi^\alpha\right) \tag{1.11}$$

where m is the inverse strain-rate sensitivity exponent, χ^α represents the kinematic hardening or back stress variable on the α^{th} slip system, κ^α is the scalar threshold stress, D^α is the drag stress, and $\dot{\gamma}_\mathbf{o}$ is the reference shearing rate. The Macauley bracket in Eq.

(1.11) is defined by <x> = xH(x), where H(x) is the Heaviside step function. In Eqn. (1.11), τ^{α} is the resolved shear stress applied on αth slip system and is given by

$$\tau^{\alpha} = \boldsymbol{\sigma}^{\mathrm{pk2}} \cdot \left(\boldsymbol{s}_0^{\alpha} \otimes \boldsymbol{n}_0^{\alpha} \right) \tag{1.12}$$

It is important to use several internal state variables to model deformation behavior of metallic cyrstals because the sources of internal stress are fundamentally different in nature. The drag stress accounts for the component of slip resistance that can be overcome by thermal fluctuation, e.g., climb-assisted glide. The threshold stress can be viewed as resistance arising from athermal statistical strengthening mechanisms associated with an increase in the dislocation density. Variation of the threshold stress leads to variation of size of the viscoplastic flow potential. The back stress reflects a directional dependence of current plastic flow on previous strain. Origins of back stress were discussed in McDowell (1994), including differential yielding among grains, pile-ups of dislocations against hard obstacles, differential resistance to slip in forward or reverse directions, and statistical aspects of dislocations bypassing barriers. Variation of back stress results in a shift of the viscoplastic potential surface. Both back stress and threshold stress depend on loading history and temperature.

Evolution laws of back stress, threshold stress and drag stress prescribe the deformation behavior of material. Numerous equations have been proposed. A form of evolution equation for the drag stress is (Asaro and Needelman, 1985)

$$\dot{D}^{\alpha} = \sum_{\beta} h_{\alpha\beta} \left| \dot{\gamma}^{\beta} \right| \tag{1.13}$$

where $h_{\alpha\beta}$ are slip-plane hardening moduli; diagonal terms $h_{\alpha\alpha}$ represent "self-hardening" on a slip system and the off-diagonal terms reflect "latent hardening".

The Armstrong-Frederick (Armstrong and Frederick, 1966) type nonlinear kinematic hardening rule is generally used for evolution of the back stress on each slip system (McGinty, 2001), i.e.,

$$\dot{\chi}^{\alpha} = C\dot{\gamma}^{\alpha} - D\chi^{\alpha}\left|\dot{\gamma}^{\alpha}\right| \tag{1.14}$$

where C and D are direct hardening and dynamic recovery coefficients, respectively.

A form of evolution equation for threshold stress is written as (McGinty, 2001)

$$\dot{\kappa}^{\alpha} = \left(A_{\kappa} - B_{\kappa}\kappa^{\alpha}\right)\sum_{\beta}\left|\dot{\gamma}^{\beta}\right| \tag{1.15}$$

where A_{κ} and B_{κ} are direct hardening and dynamic recovery coefficients, respectively. Later in present work, only Eq. (1.14) will be used for Ti-6Al-4V.

The Hall-Petch relation states that flow stress increases with decreasing grain size, and has been widely observed for polycrystalline metals. Several mechanisms have been proposed (dislocation pile-ups), but all tend to relate to the mean free path for dislocation motion. A Hall-Petch type relation for threshold stress of α TiAl crystals was proposed by Picu and Majorell (2002). Mayeur and McDowell (2007) employed a Hall-Petch type relation for a component of the threshold stress to manifest the length scale effect of Ti-6Al-4V, i.e.,

$$\kappa_1^{\alpha} = k_y\left(d^{\alpha}\right)^{-0.5} \tag{1.16}$$

where k_y is the Hall-Petch coefficient and d^{α} is the microstructure scale relating to the free slip length of the αth slip system. Several length scales, including grain size, colony size and thickness of lamellar laths, serve as controlling length scales to capture the scale effects for this dual phase alloy (Mayeur, McDowell, 2007).

1.4 Fatigue Indicator Parameters

Microstructure plays an important role in fatigue crack formation and early growth (McDowell, 1996). Fatigue is a complex, load history dependent process at the microstructure level. A substantial amount of research has been devoted to understanding the mechanisms associated with fatigue crack formation and propagation. Conventional fatigue studies often involve a large number of experiments with uniaxial stress states. To understand the effect of microstructure on fatigue behavior, fatigue tests must be conducted on various microstructures for ostensibly the same material. These tests are generally expensive to conduct and time-consuming.

A computational-based microstructure sensitive approach to fatigue has been advanced by McDowell (1996b) using the measured microstructural features to quantify the statistical distribution of fatigue responses. In addition to microstructure parameters, sensitivity of fatigue to loading parameters such as the amplitude of the applied strain, the load ratio, and multiaxiality can also be explored using computational methods. This approach involves the following steps (McDowell, 2005):

I. Identify controlling microstructure features for crack formation and early growth.

II. Conduct numerical analyses (e.g. finite element) of various microstructures for representative loading cases.

III. Calculate the fatigue indicator parameters as a function of applied strain amplitude, mean stress or strain, and variable amplitude loading, as appropriate.

IV. Apply microstructure-scale crack formation/incubation relations based on simple Coffin-Manson forms to model crack formation life.

V. Calibrate constants of Coffin-Manson and small crack propagation relations to results for experimentally characterized microstructure(s) and then use these constants to predict results for other microstructures.

This approach can provide microstructure-sensitive parameters in fatigue models for structural application. Various fatigue damage mechanisms are considered to support fatigue life prediction. This computational approach can also greatly reduce the number of required experiments to assess scatter in fatigue, providing predictive assessment of sensitivity of fatigue life to microstructure.

The total fatigue life can be decomposed into several stages (McDowell, 2007), i.e.,

$$N_T = N_{inc} + N_{MSC} + N_{LC} \tag{1.17}$$

Here, N_{inc} is the number of cycles for small crack incubation/formation with initial length on the order of microstructure feature, and N_{MSC} is the number of cycles to propagate in microstructurally small regime. At this stage, the crack length or plastic zone size is on the order of microstructure features and crack growth cannot be calculated based on the conventional linear elastic fracture mechanics (LEFM). The crack driving force is the cyclic crack tip displacement range, ΔCTD, which can be related to the fatigue crack propagation rate by

$$\left(\frac{da}{dN}\right)_{MSC} = C\left(\Delta CTD - \Delta CTD_{th}\right) \tag{1.18}$$

where ΔCTD_{th} is the threshold for crack propagation and C is the slip irreversibility factor. Cycles N_{LC} denote the crack propagation life in long crack regime, for which LEFM is applicable. During HCF, the formation of a fatigue crack can comprise a large fraction of the fatigue life of a material (Lankford and Kusenberger, 1973). Consequently, for HCF it is important to quantify the relevant driving force for fatigue crack nucleation from various microstructural inhomogeneities.

Various models have been proposed to predict the crack incubation life (fatigue crack formation) of materials under multiaxial fatigue loading. Two types of models are generally used for HCF loading conditions: equivalent stress model and critical plane model. The equivalent stress models are essentially extensions of static yield criteria, such as the von Mises criterion.

The critical plane models were developed based on observations that Stage I fatigue cracks often form on critical planes. The term "Fatigue Indicator Parameters" (FIPs) is used in this study when such parameters are applied at the microstructure level. Both strain-based and stress-based critical plane approaches have appeared in the literature for various alloys. Strain-based approaches, such as the Smith-Watson-Topper (SWT) (Smith et al., 1970) and the Fatemi-Socie (FS) (1988) parameters, allow identification of the critical planes that undergo maximum normal strain or maximum cyclic plastic shear strain. On the other hand, stress-based parameters such as that of Findley (1957) adopt the maximum shear stress plane as the critical plane. In Gallagher et al. (2005), the critical plane is not defined by the value of an individual stress or strain component; the critical plane is the plane experiencing the maximum value of the critical plane parameter.

Critical plane parameters are found to provide good correlation with multiaxial crack initiation test data when applied at the macroscale. At the level of microstructure,

fatigue crack formation is mainly driven by the localized cyclic plastic deformation. Consequently, the FIPs used in this study are strain-based critical-plane models.

Three strain-based critical plane parameters at the macroscale (denoted as *DP*) are generally used in literature: Smith-Watson-Topper (SWT) (Smith et al., 1970), Fatimi-Socie (FS) (1988) maximum cyclic plastic shear strain. The SWT parameter is a tensile-dominated parameter, i.e.,

$$DP_{SWT} = \frac{\Delta\varepsilon^{p}_{\max}}{2}\sigma_{\max} \tag{1.19}$$

where $\frac{\Delta\varepsilon^{p}_{\max}}{2}$ is the amplitude of the maximum normal plastic strain and $\sigma_{\max}$ is the maximum normal stress on this plane during a loading cycle. The FS parameter is a shear-dominated parameter, i.e.,

$$DP_{FS} = \frac{\Delta\gamma^{p}_{\max}}{2}\left(1 + K\frac{\sigma_n^{\max}}{\sigma_y}\right) \tag{1.20}$$

Here, $\Delta\gamma^{p}_{\max}$ is the maximum plastic shear strain range, $\sigma_n^{\max}$ is the maximum normal stress on the corresponding critical plane, and K is a material parameter. Another widely used multiaxial parameter is the maximum plastic shear strain range, $\Delta\gamma^{p}_{\max}$, with respect to all possible plastic shear strain range planes, i.e.,

$$DP_{\gamma} = \frac{\Delta\gamma^{p}_{\max}}{2} \tag{1.21}$$

All three parameters are used in Gallagher et al. (2005) to study the fatigue behavior of Ti-6Al-4V. It was shown that SWT parameter produced very poor correlation

of the biaxial damage, while the shear-based models were reasonably accurate; it can be concluded that the initiation of fatigue cracks in Ti-6Al-4V is driven primarily by cyclic plastic shear strain. Among the shear dominated parameters, the Fatemi-Socie parameter includes the maximum normal stress to the critical plane and therefore is considered to be more suitable than $\Delta\gamma^{p}_{\max}$ for the prediction of fatigue life of Ti-6Al-4V (Mayeur et. al, 2006). Moreover, as shown by Berard and McDowell (1992), it more closely mimics the mixed mode ΔCTD for small cracks.

At the microstructure level, FIPs (denoted as P) such as Fatemi-Socie (FS) (1988) and maximum cyclic plastic shear strain parameters are applied as nonlocal indicators of driving force for fatigue crack formation and early growth. The maximum plastic shear strain range is linked to the fatigue life of crack formation when the crack formation life is mainly controlled by to and fro irreversible motion of the dislocations i.e.,

$$P_{FS} = \frac{\Delta\gamma^{p*}_{\max}}{2}\left(1 + K\frac{\sigma_n^{\max*}}{\sigma_y}\right) \tag{1.22}$$

$$P_{\gamma} = \frac{\Delta\gamma^{p*}_{\max}}{2} \tag{1.23}$$

where $\Delta\gamma^{p*}_{\max}/2$ is the average value of maximum $\Delta\gamma^{p}_{\max}/2$ over a finite domain which we will designate with an asterisk, and $\sigma_n^{\max*}$ denotes the maximum normal stress on the corresponding critical plane over the same averaging domain. It is noted that the process of fatigue crack formation at the microstructure level operates over a finite domain. Therefore, an averaged $\Delta\gamma^{p*}_{\max}/2$ is more appropriate for the purpose of quantifying the driving force for fatigue crack nucleation. The length scale of averaging domain should represent a characteristic length of crack formation at the microstructure level. A typical

size of averaging domain is the grain size, for example, or sometime a few micros for crack embryos.

The defined FIPs P_{FS} and P_{γ} can be related to the crack formation life at the scale of a grain according to the nonlocal Coffin-Manson laws given in (Goh, 2002), i.e.,

$$P_{FS} = \gamma_f^{'}(2N_f)^{c'} \tag{1.24}$$

$$P_{\gamma} = \gamma_f^{'}(2N_f)^{c'} \tag{1.25}$$

The material constants used in Eqs. (1.22)-(1.25) can be the same as that described in previous works (Goh, 2002; Mayeur, 2006); they are: $c' = -0.684$, $\gamma_f^{'} = 0.687$ and $K = 1$.

Shear-dominated FIPs account for the classical to-and-fro slip mechanism for crack formation. This mechanism is not responsible for all crack formation at the microstructure scale. Progressive pileup of dislocations in slip bands (Zener mechanism) (Hollomon and Zener, 1946) that impinge on grain or phase boundaries can lead to formation and propagation of small cracks in the microstructure. Thus, two crack formation mechanisms of HCF α-TiAl must be considered: decohesion of the slip band interface due to intense shear along the slip band and slip band impingement on the grain boundary. In this study, additional FIPs are proposed to account for various mechanisms for crack formation in Chapter 7.

An important application of the fatigue model is fretting fatigue. Fretting fatigue occurs as a result of mixed stick-slip conditions at the interface of two contacting bodies under repetitive reversed slip. Fretting fatigue is drawing increasing attention as one of the leading causes of premature failure for gas turbine engines. For example, the vibratory load applied on the blade and disk causes a fretting motion (micron scale relative motion) at their interface (Cortez et al., 1999). Fretting fatigue is a near-surface

phenomenon that occurs over a very small region. Damage and plastic deformation accumulate within a depth of several grains in the material. The tangential relative surface displacement between two bodies is also extremely small (several μm). Since the material microstructure is of comparable dimensions, it can significantly influence the mechanical behavior. Experimental observations show that fretting fatigue cracks may form at the edge of contact region, at the boundary between the slip and non-slip regions, or at the center of contact of the specimens (Antoniou and Radtke, 1997).

1.5 Scope of Thesis

The aim of this study is to develop a computational approach that can capture the sensitivity of cyclic deformation and fatigue behavior to microstructure of Ti-6Al-4V. This approach consists of microstructure-scale constitutive relations for Ti-6Al-4V, a finite element mesh that can adequately represent the microstructure of material, with FIPs used to indicate the driving force for fatigue crack formation at the microstructure level.

In this study, three-dimensional microstructure-scale crystal plasticity constitutive relations of Ti-6Al-4V are fit to the measured stress-strain responses of a heat-treated Ti-6Al-4V subject to a complex loading history. The finite element model is constructed to adequately represent the microstructure of actual materials. The mesh developed which consist of a series of simulated annealing processes performed on the periodic Voronoi tessellation. The calibrated crystal plasticity model can then be used for the microstructure sensitivity study of Ti-6Al-4V. Tensile, cyclic and fretting simulations are performed on microstructures with various orientation and misorientation distributions, average grain sizes and grain size distributions, represented by finite element meshes.

Both macroscopic stress-strain response and local stress-strain distribution can be obtained and compared. The deformation behavior is simulated as the function of microstructure attributes. The most influential microstructure attributes of Ti-6Al-4V include average grain size, volume fraction of primary α phase, thickness of laths of lamellar colony, texture, and grain size distribution.

Slip banding plays an important role in deformation and fatigue behavior of Ti-6Al-4V. Therefore, it is important to simulate the development of slip bands in primary α grains. A shear-enhanced crystal plasticity model is proposed. Cyclic simulations are carried out on single crystal α Ti5Al oriented for single and double prismatic slip. Simulation results are compared with the experimental data in terms of stress-strain responses and slip distribution.

This new approach is examined in term of its capability to capture the localized slip behavior of Ti-6Al-4V, including dominance of single slip in the HCF regime.

1.6 Thesis Layout

Chapters are assembled to address the thesis scope as follows:

1. In Chapter 2, three-dimensional cyclic simulations are performed on various microstructures of Ti-6Al-4V by using the crystal plasticity model developed by Mayeur and McDowell (2006). The sensitivity of cyclic plastic strain behavior and FIPs to microstructure attributes of Ti-6Al-4V, such as grain size, texture, and grain size distribution are investigated.
2. Chapter 3 focuses on variation of fretting fatigue behavior of Ti-6Al-4V with respect to variation of microstructure attributes. Three-dimensional fretting fatigue simulations are conducted on various microstructures.

Effects of microstructure on cyclic plastic strain, plastic strain behavior and fatigue indicator parameter are examined.

3. A three-dimensional crystal plasticity model for Ti-6Al-4V is proposed in Chapter 4 which includes enhanced evolution laws for threshold stress and back stress. The model includes length scale effects associated with dislocation interactions with different microstructure features, and is calibrated using finite element method to fit the measured macroscopic responses (overall stress-strain behavior) of a duplex heat treated Ti-6Al-4V alloy subjected to a complex cyclic loading history. The finite element models are established to adequately represent the microstructures of the tested material. Equivalent orientations with similar probability density distributions of the crystallographic orientations are assigned to the finite element mesh. A simulated annealing method is used to fit the misorientation distributions of the sample. The microstructure sensitivity of the model is examined by comparing the experimental data with simulation results in terms of yield strength.

4. In Chapter 5, variation of tensile behavior of Ti-6Al-4V with respect to variation of grain size distribution is systematically studied. A series of microstructures are created in such a way that only the grain size distribution varies. Microstructures with various grain size distributions are realized in FE meshes, using a sequence of simulated annealing performed on random Voronoi tessellations to fit microstructure attributes such as grain size distribution and orientation and minimum misorientation distributions.

5. In Chapter 6, formation of slip bands in single crystal α Ti5Al subject to various loading histories is simulated. The shear enhanced crystal plasticity model is used to model the planar slip behavior of α Ti5Al.

Material perturbations are used to trigger the formation of slip bands. Simulation results are compared with the experimental data in term of both macroscopic stress-strain response and slip behavior.

6. In Chapter 7, the slip behavior of polycrystalline Ti-6Al-4V is studied using a new computational approach. This approach consists of the shear enhanced crystal plasticity model with a slip system softening strategy. A two-dimensional microstructure is created via EBSD measurements on the microstructure of Ti-6Al-4V. The slip behavior of a Ti-6Al-4V subjected to tensile load is investigated. It is shown that the proposed approach can qualitatively capture the slip behavior shown in experiments.
7. In Chapter 8, new FIPs are proposed that can account for the driving forces for crack formation at the microstructure level. The so-called "rogue" grain combination is introduced and compared with the microstructure used in Chapter 7 in terms of its influence on cyclic fatigue behavior. A significant enhancement of driving force for crack formation due to slip band impingement is obtained for "rogue" grain combinations. This result agrees with other studies and experimental observations.
8. The summary and conclusions of this study are given in Chapter 9. Recommendations for future work are also provided in this chapter.

CHAPTER 2

MICROSTRUCTURE-SENSITIVE CRYSTAL PLASTICITY MODELING

2.1 Introduction

The fatigue process consists of crack formation and growth. It depends on morphology of second phases and grains, as well as the presence of inclusions. Fatigue crack formation life can be a significant portion of total fatigue life for metallic materials. Fatigue crack formation is controlled by three primary factors: microstructure, temperature/environments, and loading history. It is well known that for engineering materials such as aluminum alloys and titanium alloys, various microstructures can be achieved by adjusting components of alloys and heat treatment and thermomechanical processes. Thus, it is desired to understand scatter in fatigue as a function of microstructure in order to tailor microstructure to improve fatigue resistance. An engineering approach to fatigue life estimation for components typically requires a large number of fatigue tests for various microstructures. Here, we pursue a computational means of augmenting experiments to accelerate alloy modification and/or design.

A computational microstructure-sensitive approach developed by McDowell (1996b) uses the measured microstructure attributes to quantify the statistical variation of fatigue responses. In addition to microstructure sensitivity, the sensitivity of probability of fatigue crack formation to the amplitude of the applied strain, the load ratio, and multiaxiality can also be explored using computational methods. Such an approach seems much more satisfying for purposes of microstructure selection or design aimed at improving mean fatigue resistance as well as quantifying variability (McDowell, 2005).

Various macro- and micro- scale constitutive relations of Ti-6Al-4V have been proposed to model the mechanical behavior as summarized in Chapter 1. The aim of present study is to quantify the influence of the microstructure of Ti-6Al-4V on the cyclic fatigue. A three-dimensional crystal plasticity model proposed by Mayeur and McDowell (2007) is used to describe the deformation behaviors of primary α phase and lamellar colony. Microstructure attributes considered in this study includes: texture, average grain size, and grain size distribution. Complex grain size distributions are introduced via Voronoi tessellation and modeled using 3D crystal plasticity to compare with uniform grain size results.

In this Chapter, the descriptions of material and constitutive model are given in Sections 2.2 and 2.3, respectively. The Voronoi tessellations for construction of 3D polycrystalline material are described in Section 2.4. The predicted tensile responses of Ti-6Al-4V of different microstructures are shown in Section 2.5. The cyclic and fatigue behaviors of Ti-6Al-4V are reported in Section 2.6 and 2.7, respectively. Summary and conclusions are given in the last Section.

2.2 Material

The microstructure and deformation behavior of Ti-6Al-4V have been described in Chapter 1. In this Chapter, a duplex microstructure is considered which contains a mixture of primary hcp α phase, and secondary α plus bcc β phase arranged in a lamellar structure, as shown in Fig. 2.1. It is well known that the texture and microstructure morphology have profound influence on performance of Ti-6Al-4V. For example, the grain size determines the effective slip distance within the globular α phase, and in turn has an effect on the yield strength (Lütjering, 1998). The key first order microstructure attributes of Ti-6Al-4V include average globular (primary) α size, lamellar colony size,

volume fraction of the primary α phase, and mean thicknesses of the secondary α and β phases in the lamellar structure, as previously discussed.

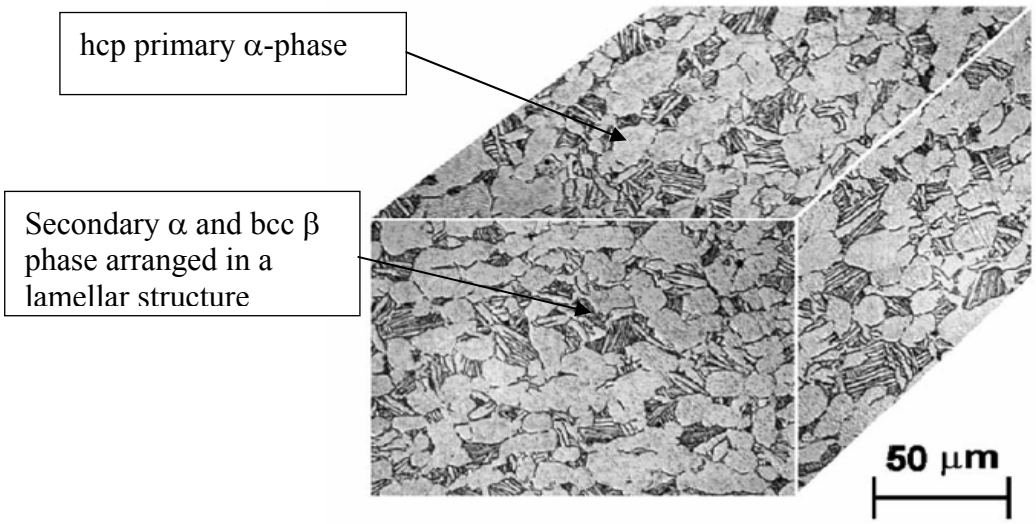

Figure 2.1. Microstructure of duplex Ti-6Al-4V.

Due to the highly anisotropic nature of crystallographic slip in hcp crystals, along with the low symmetry of the hcp structure, the orientation distributions of grains strongly affect the mechanical behavior of the bulk material (Fager and Spurr,1968), as previously discussed. Textures created via thermomechanical processing of Ti-6Al-4V are generally grouped into three distinct categories: basal, transverse, and basal/transverse textures (Schoenfeld and Kad, 2002). Some commercial Ti-6Al-4V alloys have random texture, i.e., grain orientations are randomly distributed. The measured basal plane pole figures for these simulated textures are shown in Fig. 2.2 (Mayeur, 2004).

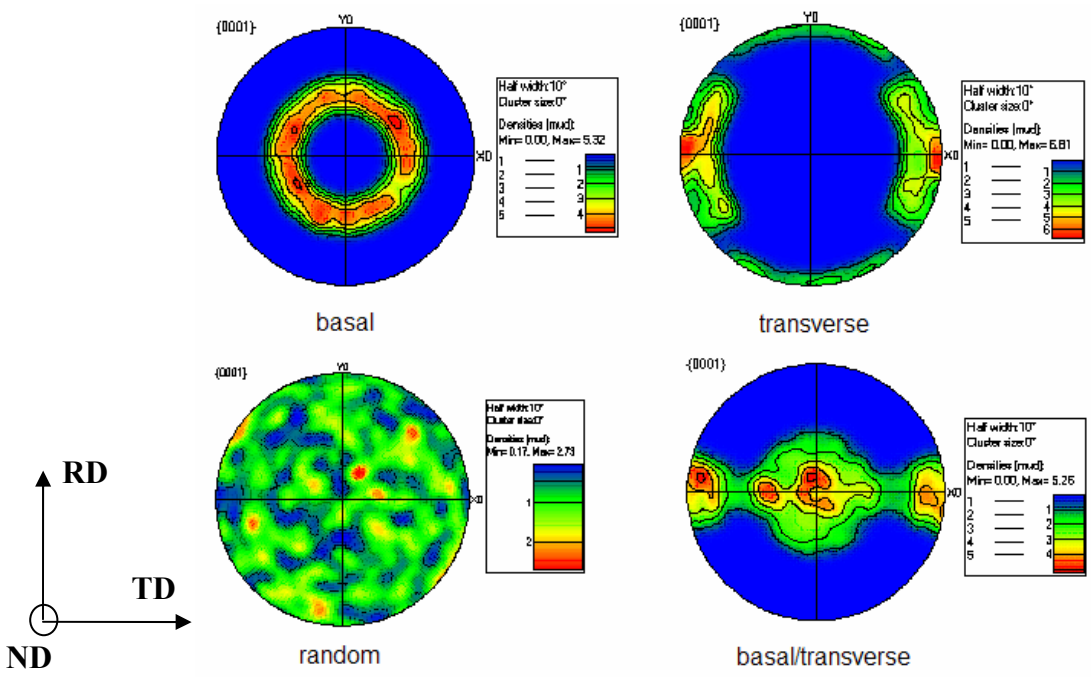

Figure 2.2. Basal plane pole figures of representative textures (Mayeur, 2004).

2.3 Crystal plasticity model

For the primary α phase, four families of slip systems are included in the model: three $<11\bar{2}0>(0001)$ basal, three $<11\bar{2}0>\{10\bar{1}0\}$ prismatic, six $<11\bar{2}0>\{10\bar{1}1\}$ first order pyramidal, and twelve $<11\bar{2}3>\{10\bar{1}1\}$ second order pyramidal slip systems, as illustrated in Fig. 1.3. The dominant slip systems of the primary α phase are the basal and prismatic due to their relatively low critical resolved shear stress (CRSS). The slip resistance of the first order pyramidal slip system is about twice those of the basal and prismatic slip systems. Among all slip systems, the second order pyramidal system has the highest CRSS, more than four times higher than the CRSS of basal and prismatic slip systems (Bieler and Semiatin, 2001). A Hall-Petch assumption is invoked that the CRSS of each of the slip systems depends inversely on the square root of the mean free path for

dislocation motion. For the primary α phase, this is the mean grain size, d. It has been shown that this predicts measured scale effects relatively well for this alloy (Zhang et al., 2007).

The α/β colony contains secondary α and β phases arranged in lamellar structure. The thicknesses of the secondary α and β phase range from hundreds of nanometers to several microns. It is extremely difficult to explicitly model such small structures using a finite element mesh that must include a large number of grains. Thus, the α/β lamellar colony is homogenized by considering the crystallographic relationships between the secondary α and β laths given by $(0001)_\alpha // \{110\}_\beta$ and $<11\bar{2}0>_\alpha // <111>_\beta$ (Lütjering and Williams, 2003), as illustrated in Fig. 1.5. Following the approach described by Mayeur and McDowell (2007), there are 24 possible slip systems in the lamellar colony: three $<11\bar{2}0>\{0001\}$ basal, three $<11\bar{2}0>\{10\bar{1}0\}$ prismatic, six $<11\bar{2}0>\{10\bar{1}1\}$ first-order pyramidal and twelve <111>{110} bcc slip systems, which are transformed into the hexagonal coordinate system according to the Burgers orientation relationship, as illustrated in Fig. 1.6. Pyramidal <c+a> systems are not included in the model of the lamellar grains because this hard mode of deformation is unlikely to be active in the secondary α laths. Additionally, the accommodation of plastic deformation along the c-axis in these lamellar regions can be accounted for by the softer bcc systems.

Three different microstructure length scales, corresponding to secondary α lath thickness, β lath thickness, and lamellar colony size, respectively, are considered in terms of their effect on strengthening. The slip systems with a slip direction that intersects the secondary α/β interface are considered to be "hard" due to the relatively small effective slip distance. The slip resistances of the hard systems that belong to the hcp slip systems and bcc slip systems are governed by the lath thicknesses of the secondary α and β phases, respectively. The soft deformation modes correspond to slip systems that either glide parallel to the α/β interface or have parallel slip planes in both the α and β phases.

The set of soft deformation mode consists of 3 basal, 1 prismatic and 2 <111>{110} bcc slip systems. Within the set of soft deformation modes assumed in this study, the prismatic system glides parallel to the α/β interface, whereas the basal and close packed bcc planes are parallel and dislocations gliding in these planes are effectively able to traverse the entire length of the lamellar colonies. Figure 2.3 illustrates the relevant microstructural length parameters as well the soft lamellar deformation modes. Table 2.1 summarizes the soft and hard slip systems of the lamellar colonies and corresponding microstructure length scales l^{α}.

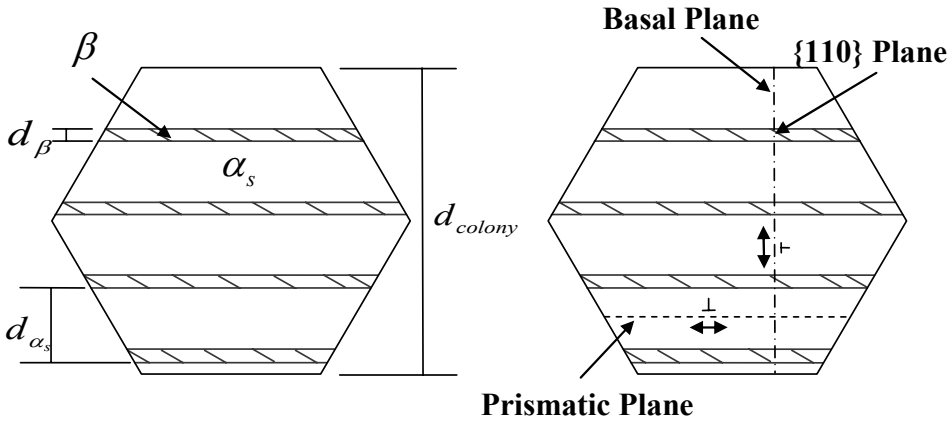

Figure 2.3 Lamellar colony length scales (left) and section view along aligned hcp basal and {110} bcc slip planes that promote soft deformation modes (right).

Table 2.1 Soft and hard slip systems of the lamellar colony.

Soft slip systems		Hard slip systems	
Slip systems	l^{α}	Slip systems	l^{α}
3 $\langle 1\bar{2}10\rangle(0001)$ basal	d_{colony}	$\langle \bar{1}2\bar{1}0\rangle(10\bar{1}0)$ prismatic	d_{α_s}
$\langle 2\bar{1}\bar{1}0\rangle(0\bar{1}10)$ prismatic	d_{colony}	$\langle \bar{1}\bar{1}20\rangle(\bar{1}100)$ prismatic	d_{α_s}
$\langle \bar{1}\bar{1}1\rangle(101)$ bcc	d_{colony}	Other $\langle 111\rangle(101)$ bcc	d_β
$\langle \bar{1}11\rangle(101)$ bcc	d_{colony}		

Kinetic equations provide the relationship between slip system shearing rates and the driving forces (resolved shear stresses). In a rate dependent formulation, all slip systems are considered to be active for stresses above the threshold, and a flow rule relates the shearing rates $\dot{\gamma}^{\alpha}$ for the α^{th} slip system to the resolved shear stress and the current state of the microstructure, i.e.,

$$\dot{\gamma}^{\alpha} = \dot{\gamma}_o \left\langle \frac{\left|\tau^{\alpha} - \chi^{\alpha}\right| - \kappa^{\alpha}}{D^{\alpha}} \right\rangle^{m} \operatorname{sgn}\left(\tau^{\alpha} - \chi^{\alpha}\right) \tag{2.1}$$

for $\alpha = 1 \ldots h$, where h is the number of slip systems. Here, τ^{α} is the resolved shear stress, D^{α} is the drag stress, m is the inverse strain-rate sensitivity exponent, χ^{α} represents the kinematic hardening variable or back stress on the α^{th} slip system, κ^{α} is the scalar threshold stress, and $\dot{\gamma}_o$ is the reference shearing rate. Superscript "α" denotes to the α^{th} slip system in all cases.

The drag stress on each system of the primary α phase is assumed constant at room temperature. For the hcp slip systems of the secondary α–β lamellar colonies, the drag stresses are taken to be the same as their counterparts in the primary α phase (i.e., $D_{\alpha}^{prism} = D_{\alpha+\beta}^{prism}$, $D_{\alpha}^{basal} = D_{\alpha+\beta}^{basal}$, etc.), whereas the drag stress for the bcc systems is taken to be slightly lower than the drag stress for prismatic systems ($D_{\alpha+\beta}^{\langle 111\rangle\{110\}} = 0.9 D_{\alpha}^{prism}$) to represent the mechanically softer nature of β-Ti alloys.

The back stress on each slip system evolves according to a nonlinear kinematic hardening rule of Armstrong-Frederick type, i.e.,

$$\dot{\chi} = C\dot{\gamma}^{\alpha} - D\chi^{\alpha}\left|\dot{\gamma}^{\alpha}\right| \tag{2.2}$$

where C and D are direct hardening and dynamic recovery coefficients, respectively.

The threshold stress does not evolve, i.e., $\dot{\kappa}^{\alpha} = 0$, for slip systems other than the prismatic systems of the primary α phase. However, a component of the threshold stress depends on certain microstructure length scales, including grain size, colony size, and lath size and spacing. The threshold stress scales according to the Hall-Petch relationship

$$\kappa_1^{\alpha} = k_y \left(l^{\alpha} \right)^{-0.5} \tag{2.3}$$

where k_y is the Hall-Petch coefficient and l^{α} is the microstructure scale relating to the mean free path for dislocation glide on the α^{th} slip system. For the primary α phase, l^{α} corresponds to the grain size, as mentioned before. For lamellar colonies, three different length scales are invoked for different slip systems, corresponding to lamellar colony size and α and β lath thicknesses. In addition, the threshold stress for prismatic slip systems of the primary α phase includes a component with non-Schmid effects associated with dislocation core spreading, i.e.,

$$\kappa^{\alpha}{}_{prism} = \kappa_1^{\alpha} + A(\tau_{Pyr1} - \tau_{Pyr2}) \tag{2.4}$$

where κ_1^{α} is defined in Eq. (2.3). The second term in Eq. (2.4) corresponds to the non-Schmid effect and will either increase or decrease the threshold stress, depending on the sense of the applied load with respect to the crystal orientation. Shear stresses τ_{pyr1} and τ_{pyr2} are non-Schmid resolved shear stresses on pyramidal planes that share the $<11\bar{2}0>$ burgers vector with each prismatic plane and promote recombination of the dissociated core (Mayeur and McDowell, 2007). This non-Schmid term is included only for

prismatic systems of the primary α phase and leads to tension/compression yield asymmetry for these systems.

Table 2.2 Constitutive Equations for Ti-6Al-4V.

Flow Rule:

$$\dot{\gamma}^{\alpha} = \dot{\gamma}_o \left\langle \frac{\left|\tau^{\alpha} - \chi^{\alpha}\right| - \kappa^{\alpha}}{D^{\alpha}} \right\rangle^{m} \operatorname{sgn}\left(\tau^{\alpha} - \chi^{\alpha}\right) \qquad \text{for all slip systems}$$

Evolution Equations for Hardening Variables:

Back stress (primary α phase and lamellar colony)

$$\dot{\chi}^{\alpha} = B\dot{\gamma}^{\alpha} - C\chi^{\alpha}\left|\dot{\gamma}^{\alpha}\right|$$

Threshold stress

Primary α phase

$$\kappa^{\alpha}{}_{prism} = \kappa_1^{\alpha}\Big|_{prism} + A(\tau_{Pyr1} - \tau_{Pyr2}) \qquad \kappa^{\alpha}{}_{basal} = \kappa_1^{\alpha}\Big|_{basal} \qquad \kappa^{\alpha}{}_{pry} = \kappa_1^{\alpha}\Big|_{pry}$$

Lamellar colony

$$\kappa^{\alpha}{}_{soft} = \kappa_1^{\alpha}\Big|_{soft} \qquad \kappa^{\alpha}{}_{hard} = \kappa_1^{\alpha}\Big|_{hard} \qquad \kappa_1^{\alpha} = k_y\left(l^{\alpha}\right)^{-0.5}$$

Soft and hard slip systems of the lamellar colony and corresponding microstructure length scales l^{α} l are summarized in Table 2.1

Drag stress

$$\dot{D}^{\alpha} = 0$$

$$D_{\alpha}^{prism} = D_{\alpha+\beta}^{prism} \qquad D_{\alpha}^{basal} = D_{\alpha+\beta}^{basal} \qquad D_{\alpha+\beta}^{\langle 111\rangle\{110\}} = 0.9D_{\alpha}^{prism}$$

The constitutive equations are summarized in Table 2.2. The crystal plasticity is implemented as a User MATerial (UMAT) subroutine in ABAQUS (2005) using a Newton-Raphson (N-R) scheme (McGinty, 2001). The complete set of material parameters are given in Mayeur and McDowell (2007).

2.4 Finite Element Model

Three microstructure attributes are considered in the microstructure sensitivity study: texture, average grain size *d*, and grain size distribution. Table 2.3 summarizes the microstructure attributes of three Groups of Ti-6Al-4V considered in the simulations corresponding to three studied microstructure attributes. For each Group, other important microstructure attributes are assumed unchanged. These include maintaining the volume fraction of primary α phase at 60% and the lath thicknesses of secondary α and β phases at 1.5 μm and 0.5 μm, respectively. Microstructure IV is used as reference microstructure which appears in every group. It should be noted that, owing to lack of detailed stereological information regarding lamellar colony size, the average primary α size and lamellar colony size are assumed to be identical.

Chapter 4 (Zhang et al., 2007) shows that finite element models containing at least 125 grains are needed to sufficiently represent the texture of Ti-6Al-4V. Although improved fitting of texture can be achieved with a larger number of grains, the computational cost significantly increases with addition of more grains. Thus, in this Chapter, the finite element model contains 125 grains (5×5×5 grain statistical volume). Each grain is meshed using $3\times3\times3$ elements as shown in Fig. 2.4. To simulate the behavior of bulk material, random periodic boundary conditions are applied to all three directions: RD, TD, and the normal direction. This boundary condition imposes constraints on the sides such that the opposite edges deform in the same manner (cf.

(Smit, et al., 1998; Van der Sluis et al., 2000; Ostoja-Starzewski et al., 1994; Kumar, et al., 2006). Displacements are enforced (specified) in the normal direction, as shown in Fig. 2.4. It is noted that when the displacement is specified on an upper boundary, as in uniaxial loading, the sides of the mesh (other two directions) experience approximately zero net traction, in accordance with the axial loading condition.

Table 2.3 Microstructure attributes considered in this study.

	Group I	Group II	Group III	Microstructure IV
Studied attribute	Texture	Grain size	Grain size distribution	
Average grain size, d (micron)	30	10, 15, 20, 30, 35	30	30
Grain size distribution (d_c/d)	1	1	0.3, 0.5, 0.8, 1	1
Vol. Fraction of primary α phase, V_f (%)	60	60	60	60
Texture	Basal Transverse Basal/Trans. Random	Random	Random	Random
Mean thickness of α lath (micron)	1.5	1.5	1.5	1.5
Mean thickness of β lath (micron)	0.5	0.5	0.5	0.5

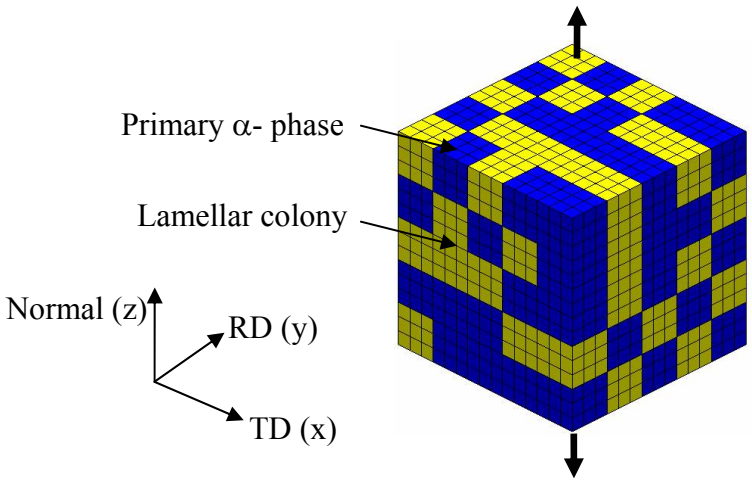

Figure 2.4 Finite element model of periodic polycrystal.

The finite element model shown in Fig. 2.4 idealizes the polycrystalline material as an aggregate of cubic crystals of identical size. Such an idealization represents a highly idealized, uniform grain size distribution. A uniform distribution of heterogeneities in microstructure can be sometimes sufficient to predict the macroscopic mechanical response. It is known that the local stress-strain field is closely related to the morphology of the neighboring grains and higher order spatial statistics. Thus, reasonably realistic representation of the microstructure is often preferred for fatigue analysis, although the level of reality necessary to achieve useful results is still an open research question. Several tessellation models, such as homogeneous Johnson-Mehl model (HJM), nonhomogeneous Johnson-Mehl (NHJM) model and Voronoi tessellation for approximating three-dimensional realistic microstructures have been proposed (Horalek, 1990). Among them, Voronoi tessellation has been extensively used in materials science to model polycrystals (Nygards, 2003), intergranular cracks (Cizelj and Riesch-Oppermann, 2002) and composites (Winterfeld et al., 1981). It is therefore chosen in this study to compare with the idealized uniform grain size distribution. Although tessellation has shortcomings in terms of detail of grain boundary angles at triple junctions, when

used along with information on grain size distribution, orientation and disorientation distribution as constraints to be satisfied in the reconstruction process based on simulated annealing, it may offer reasonable results (Zhang et al., 2007). Certainly it is useful as a basis for conducting parametric studies to discern systematic effects of microstructure attributes, which is our present purpose.

The Voronoi tessellation algorithm employed here involves constructing a cell structure from a Poisson point process by introducing planar cell walls perpendicular to lines connecting neighboring points (Horalek, 1990). Before assigning the nuclei, a characteristic size of the polycrystalline grains is needed. The average grain size d measured from two-dimensional micrographs is (Horalek, 1990)

$$d \approx 0.7\sqrt[3]{V} \tag{2.5}$$

where V is the average volume of grains. Based on Eq. (2.5), the size of the polycrystalline finite element model can be determined from a given average grain size and number of grains. For the cubic model, the edge size follows the relation

$$L = \sqrt[3]{n}d / 0.7 \tag{2.6}$$

where n is the number of grains. In case of a cuboidal grain model, the product of width *w*, length *l*, and height *h* of the rectangular box is related to the average grain size and number of grains by

$$wlh = nd^3 / 0.7^3 \tag{2.7}$$

In Voronoi tessellation, *n* nuclei are randomly distributed in space. The nuclei grow simultaneously at a constant rate until mutual contact prevents further expansion. The random distribution of nuclei results in a log-normal distribution of grain size (Kumar and Kurtz, 1994). The distance between two neighboring grains should be larger than a critical value, d_c. This critical distance can significantly influence the initial grain size distribution. Three different grain size distributions are obtained by assigning the ratio of the critical distance to the average grain size d_c/d = 0.3, 0.5 and 0.8. The larger the critical distance, the lower the variance of the grain size distribution about its mean value, as shown in Fig. 2.5. The previous idealized structure with the cubic grains of identical size is a special case with d_c/d = 1. Figure 2.5 shows that the grain size ranges from 0.3d to 3d when d_c/d = 0.3, where d is the average grain size. In case of d_c/d = 1, all grains have the same size, d. Clearly, the range of grain size distribution decreases from 2.7d (81 μm) to 0 μm as d_c/d increases from 0.3 to 1.0, respectively.

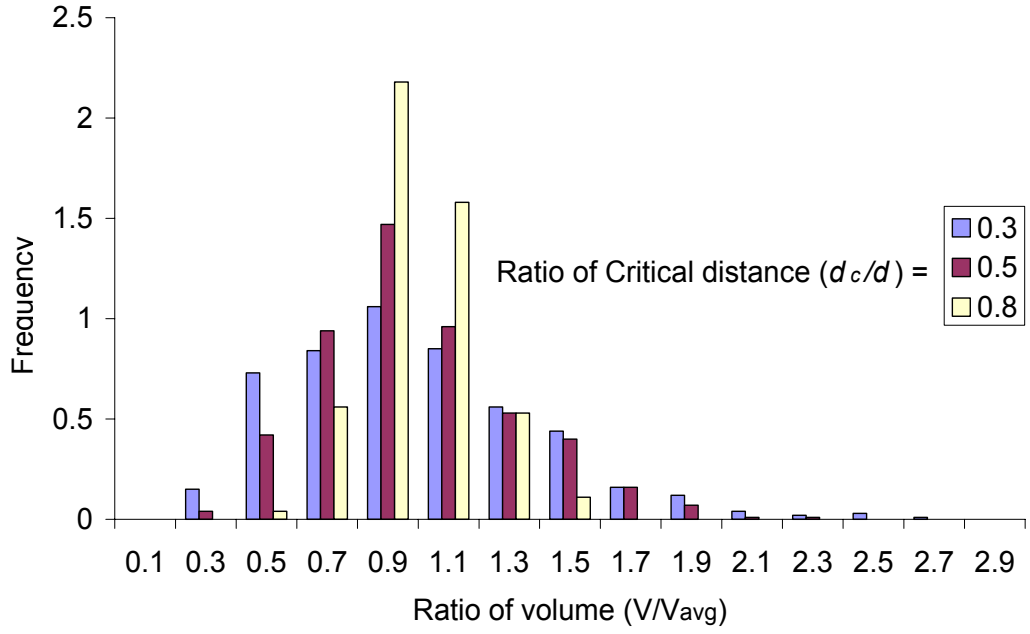

Fig. 2.5. Grain size distributions for several values of d_c/d.

To assign the phase (primary α or lamellar colony) of material when $d_c/d = 1$, the number of grains of each phase is defined by the volume fraction of that phase, since all grains in the finite element model considered here are assumed to have same size. In case of $d_c/d \neq 1$, all grains are divided into 15 groups (bins) according to their grain size. The number of grains m_i of primary α phase in each group *i* is determined by

$$m_i = V_f n_i \qquad i = 1,2,....,15 \tag{2.8}$$

where V_f is the volume fraction of the primary α phase and n_i is the number of grains in the group *i*. It is assumed that each of the two phases of Ti-6Al-4V is randomly distributed and follows the same grain size distribution. To achieve this, the phase of each grain in a group is initially randomly assigned and then adjusted to avoid substantial clustering of each phase. A typical microstructure generated by Voronoi tessellation is shown in Fig. 2.6(a).

To simulate the orientation distribution of grains, the Rodriguez space is evenly divided into M sub-spaces. The target probability of observing an orientation g_j in the sub-space *j* is determined by

$$f(g_j) = \frac{V_j}{V} \tag{2.9}$$

where V_j and V are the volume of crystals with the orientation in sub-space *j* and the total volume of all grains, respectively. For a finite element model with *K* grains, the orientation probability factor (P_j) for each orientation sub-space *j* is obtained as

$$P_j = K f(g_j) \tag{2.10}$$

When $d_c/d = 1$, the number of grains within each orientation sub-space j equals P_j, , which sums over all sub-spaces to give

$$K = \sum_{j=1}^{M} P_j \tag{2.11}$$

Accordingly, K sets of orientation angles are then selected from the orientation population P and are assigned to the different grains.

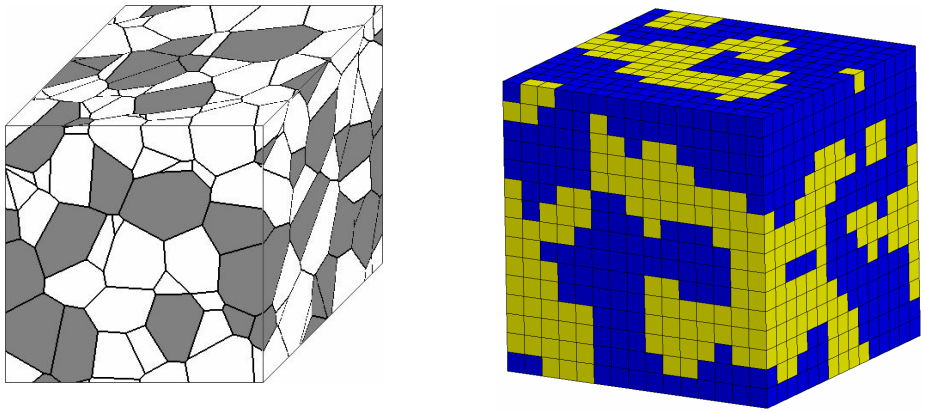

(a) (b)

Fig. 2.6. (a) Polycrystalline microstructure of Ti-6Al-4V generated by Voronoi tessellation with light grains representing primary α and dark grains representing lamellar colonies and (b) corresponding finite element representation.

In case of $d_c/d \neq 1$, the simulated annealing method is used to fit the orientation distribution (Miodownik, 1999). The error of the orientation distribution is given by

$$\pi = \sum_{j=1}^{M} [f^s(g_j) - f^t(g_j)]^2 \tag{2.12}$$

where $f^s(\Delta g_j)$ and $f^t(\Delta g_j)$ are the simulated and target frequencies of orientation distributed in the sub-domain j. The variation of error, $\Delta\pi$, is calculated after randomly change the orientation of a grain. Then, $\Delta\pi$ is used to determine whether this operation is acceptable based on a probability criterion $p(\Delta\pi)$ which, following the Metropolis algorithm, is given by

$$p(\Delta\pi) = \begin{cases} 1 & (\Delta\lambda < 0) \\ \exp(-\Delta\pi / T) & (\Delta\lambda > 0) \end{cases} \tag{2.13}$$

Here, T is a control parameter (analogous to temperature) used to define an annealing schedule. The operation is accepted if $\Delta\pi < 0$ or $\Delta\pi > 0$ but $p(\Delta\pi) \geq \rho$, where ρ is a random number; otherwise, the operation is rejected. The operations continue until the error is less than a preset critical value (for example $\pi = 10^{-5}$).

Due to the lack of experimental data, the minimum misorientation distribution is not fitted in this study. After constructing the microstructure model, its compatibility can be verified with information known from 2D observations: volume fraction, average grain size, texture, etc.

The tessellated Ti-6Al-4V polycrystal is meshed in as voxels using small regular cubic 8-node solid linear elements with reduced integration (C3D8R). Each reduced integration element has one integration point, therefore significantly reduce computational cost. For first-order reduced integration elements (e.g., C3D8R), the uniform strain (one integration point) is assumed which equals to the average strain over the element volume (ABAQUS, 2005). The number of nodes on each edge of the polycrystalline region is controlled by the mesh density. Based on the distance between the integration point of an element and the centroid of each grain, elements are assigned to grains. Figure 2.6(b) shows the finite element mesh corresponding to the microstructure in Fig. 2.6(a).

It is noted that each microstructure may have multiple realizations. For example, two realizations may have the same grain size distribution but different grain structures. Multiple realizations result in the scatter of the mechanical properties such as the yield strength. For simplicity, in this study each microstructure has only one realization.

2.5 Monotonic Tension Simulations

All monotonic tension simulations are carried out at room temperature under strain-control with the loading direction shown in Fig. 2.4. This direction is also parallel to the normal direction of material shown in Fig. 2.2. As discussed before, the sides of the mesh experience approximately zero net traction, in accordance with the axial loading condition. A strain rate of 1×10^{-3} s^{-1} is used. The variation of two material properties, elastic modulus and yield strength, with respect to the variation of microstructure is examined. As shown in Table 2.3, three groups of Ti-6Al-4V simulations are used to investigate the effects of texture, grain size, and grain size distribution d_c/d on the deformation behavior.

The simulated stress-strain responses for four microstructures of Group I with different textures are shown in Fig. 2.7. The elastic moduli of these microstructures are slightly different due to the anistropic elastic behaviors of the globular α phase and lamellar colonies. Transverse texture has the lowest elastic modulus of all samples loaded along the normal direction, as shown in Table 2.4. Following Mayeur (2004), the stress at a plastic strain of 0.001 has been defined as yield strength, σ_y. The corresponding total strain is defined as yield strain, ε_y. Both this yield strength and 0.2% offset-defined yield strength $\sigma_{0.2}$ (common in industry) are listed in Table 2.4. It is shown that the texture has strong influence on the yield strength. Among four considered textures, basal texture has the lowest yield strength. The yield strength of basal/transverse textured material is about

25% higher than that of the basal textured material when the loading direction is parallel to the normal direction of material.

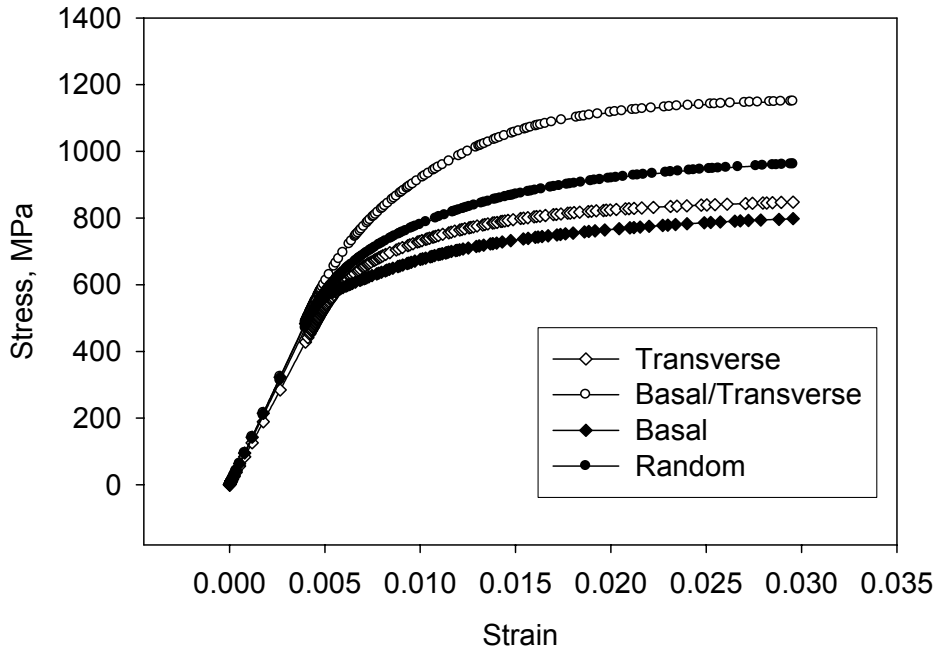

Figure 2.7. Simulated stress-strain responses for microstructures with various textures with d = 30 μm and d_c/d = 1 (Group I).

Table 2.4. Material properties for microstructures of Group I.

Texture	E (MPa)	$\sigma_{0.2}$ (MPa)	σ_y (MPa)	ε_y
Random	116,900	730	682	0.00687
Basal	120,000	619	591	0.00590
Basal/Transverse	122,400	888	805	0.00760
Transverse	107,500	700	657	0.00710

Figure 2.8 shows the simulated stress-strain responses for five microstructures of Group II with average grain sizes ranging from 10 μm to 40 μm. The elastic moduli for the five microstructures are identical. The Hall-Petch type relation between grain size and

yield strength is shown in Fig. 2.9. This can be attributed to the dependence of the threshold stress of slip systems of primary α phase and lamellar colony on the microstructural dimensions as given in Eq. (2.5). As previously discussed, each microstructure has only one realization. A small scatter of yield strength of each microstructure will be obtained if multiple realizations are used.

Figure 2.10 shows the simulated stress-strain responses for four microstructures of Group III with grain size distribution parameter d_c/d ranging from 0.3 to 1.0. The influence of d_c/d on the elastic properties of Ti-6Al-4V is negligible. Small variation of the yield strength can be observed when d_c/d increases from 0.3 to 1.0. However, there is no clear tendency.

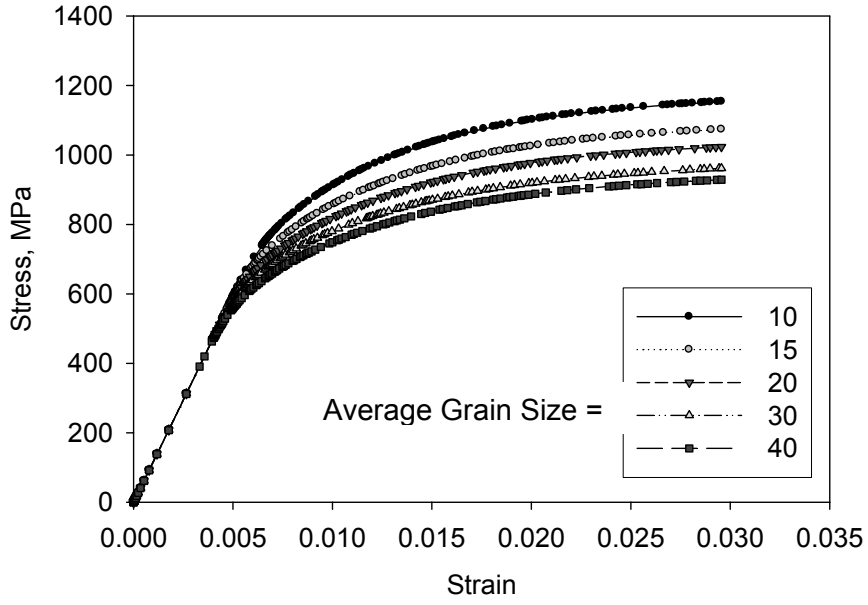

Figure 2.8. Simulated stress-strain responses for Ti-6Al-4V with random texture with various average grain size and $d_c/d = 1$ (Group II).

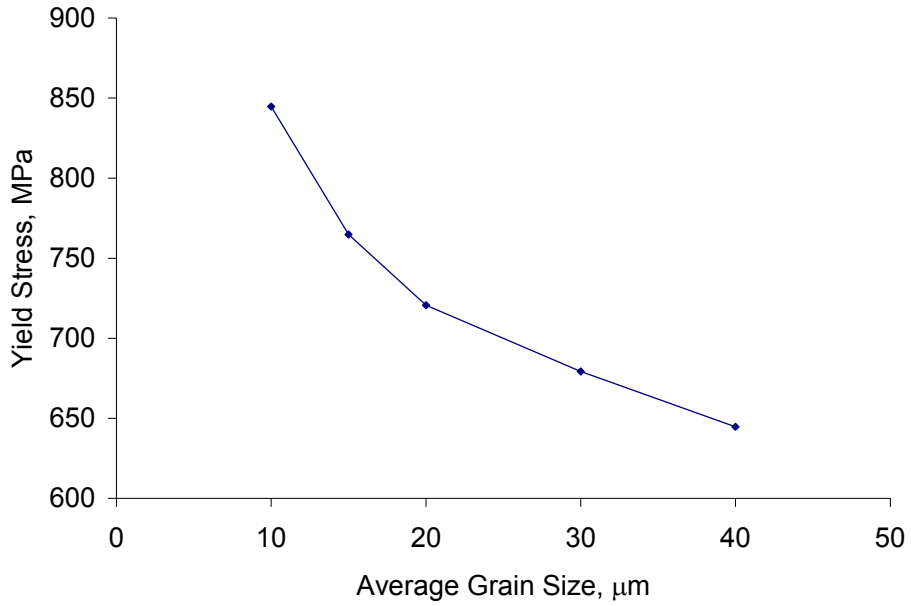

Figure 2.9 Dependence of simulated yield strength on the average grain size (Group II).

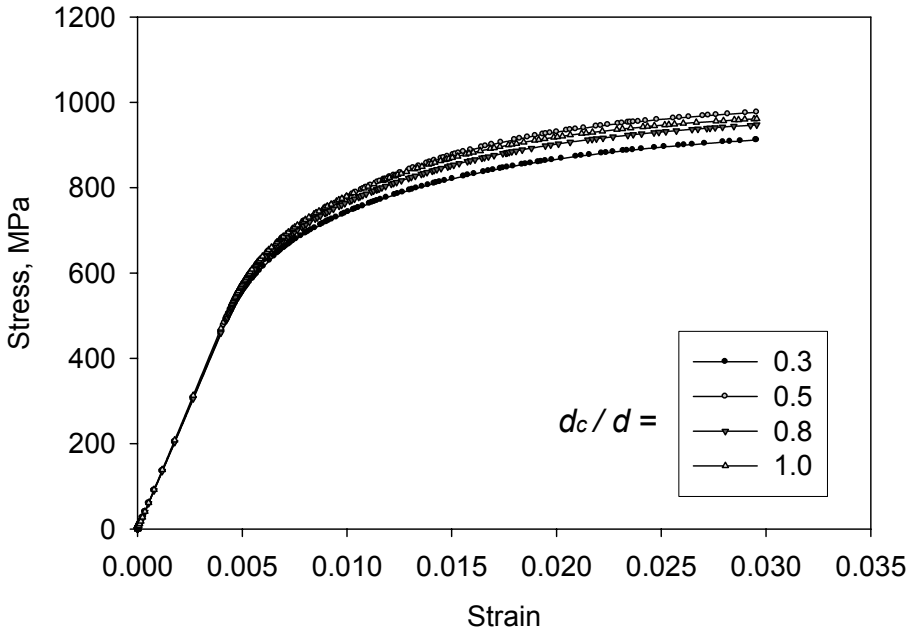

Figure 2.10 Simulated stress-strain responses for Ti-6Al-4V with random texture with d = 30 μm and various d_c/d (Group III).

2.6 Cyclic Loading Simulations

Cyclic loading simulations are performed on the finite element model shown in Fig. 2.4. For all simulations, a completely reversed (R_ε = -1) strain-controlled loading history is employed at room temperature at a strain rate of 1×10^{-3} s^{-1}. As in the monotonic tension simulations, the loading direction is parallel to the normal direction of rolled material, as shown in Fig. 2.2. The strain amplitude, $\Delta\varepsilon/2$ = 0.61%, is $0.9\varepsilon_y$ for Microstructure IV, which has a random texture with average grain size of 30 μm and d_c/d = 1, as shown in Table 2.3. Five cycles are applied in each simulation to obtain the stable cyclic behavior.

Figures 2.11-2.13 show the contours of cumulative effective plastic strain, defined by $\bar{\boldsymbol{\varepsilon}}^p = \sqrt{(2/3)\varepsilon_{ij}^p \varepsilon_{ij}^p}$, where $\boldsymbol{\varepsilon}^p = \sum_\alpha \gamma^\alpha \left(\mathbf{s}_0^\alpha \otimes \mathbf{m}_0^\alpha\right)_{sym}$, after the 5th loading cycles, for various microstructures. The contour shows localization of the cumulative plastic strain. Some grains significantly yield while the neighboring grains still undergo elastic deformation. Such phenomena can be attributed to the highly anisotropic behavior and low symmetry of HCP Ti-6Al-4V.

The contours of $\bar{\boldsymbol{\varepsilon}}^p$ for four microstructures of Group I with various textures with d = 30 μm and d_c/d = 1 are shown in Fig. 2.11. The maximum pointwise $\bar{\boldsymbol{\varepsilon}}^p$ over the model, $\bar{\varepsilon}^p_{\max}$, are also given in Fig. 2.11. It is shown that the basal texture has the highest $\bar{\varepsilon}^p_{\max}$. The basal texture is therefore softer than other three textures, which agrees with the results of monotonic tension simulations. Among four textures, basal/transverse texture has the lowest $\bar{\varepsilon}^p_{\max}$. The basal texture considered in this study is characterized by a "ring" in the pole figure, as shown in Fig. 2.2. The angles between the c-axis of grains and normal direction range from 15 to 30 degrees. Consequently, several basal and prismatic slip systems have relatively high Schmid factors under the considered loading

condition (loading direction parallel to the normal direction), resulting in the lowest yield strength among all textures considered in this study.

Figure 2.12 shows the distribution of $\bar{\boldsymbol{\varepsilon}}^p$ for microstructures of Group II with random texture with $d_c/d = 1$ and average grain sizes ranging from 10 μm to 40 μm. It is shown that the overall distributions of $\bar{\boldsymbol{\varepsilon}}^p$ for various grain sizes are similar. This can be attributed to the identical microstructural parameters assumed for Group II other than grain size; all textures are random. An increasing yield strength with decreasing grain size is observed from monotonic tension simulations in Section 2.5. In cyclic simulations, the value of $\bar{\boldsymbol{\varepsilon}}^p$ after the 5th cycles increases with increasing grain size since the threshold stress decreases according to Eq. (2.3). Therefore, fatigue resistance increases with decreasing grain size.

Figure 2.13 shows Group III microstructures with random texture with $d = 30$ μm and d_c/d ranging from 0.3 to 0.8, which can be compared to the microstructure with $d_c/d = 1$ shown in Fig. 2.11(d). Significant influence of grain size distribution on the contours of $\bar{\boldsymbol{\varepsilon}}^p$ of Group III microstructures is observed in Fig. 2.13. Such phenomena can be attributed to the variation of the size and shape of grains with respect to variation of d_c/d. No clear trend can be observed between $\bar{\varepsilon}^p_{\max}$ and d_c/d. Figure 2.5 shows that the ranges of grain size distribution decrease from 2.7d (81 μm) to 0 μm when d_c/d increases from 0.3 to 1.0. For such a large variation of grain sizes, the variation of maximum effective plastic strain is relatively low. Therefore, it is believed that the effect of grain size distribution on the deformation behavior of Ti-6Al-4V under loading conditions considered in this study is relatively weak. Since Voronoi tessellation also results in non-uniform grain shape (to within constraints of the present voxellation/meshing scheme), it may also be inferred that the effect of grain shape on $\bar{\varepsilon}^p_{\max}$ is relatively weak.

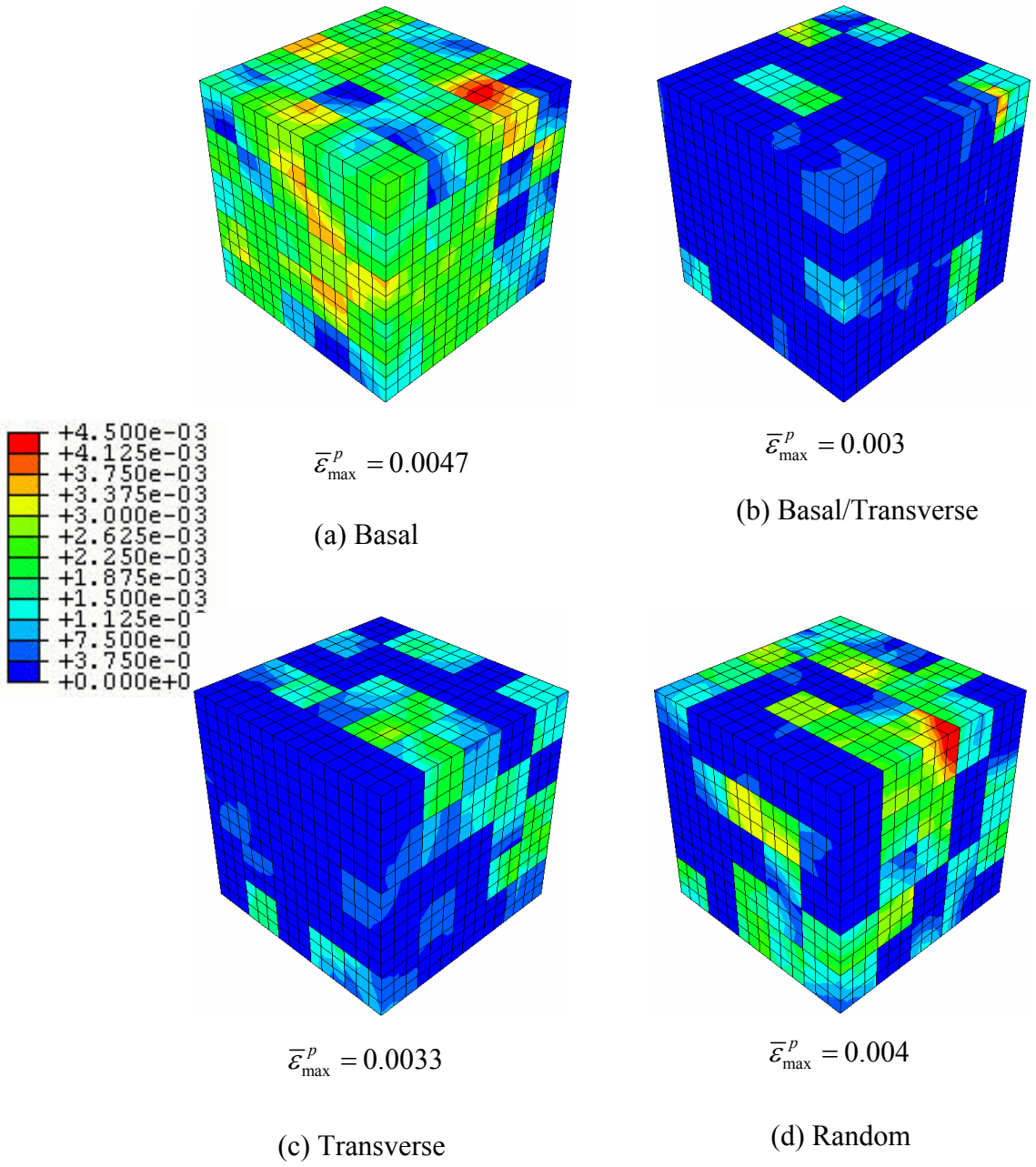

Figure 2.11. Distribution of effective plastic strain after five cycles for Ti-6Al-4V with various textures, d = 30 μm, and d_c/d = 1 (Group I), (R_ε = -1 and $\Delta\varepsilon/2$ = 0.61%).

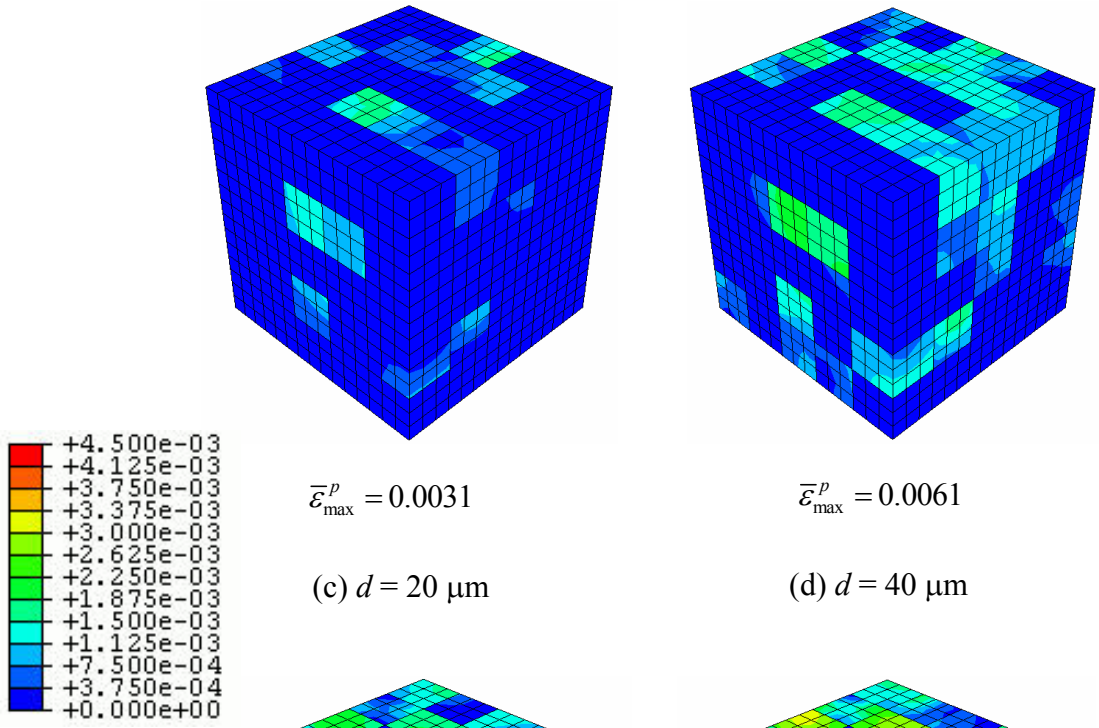

$\bar{\varepsilon}^p_{\max} = 0.0031$

(c) $d = 20$ μm

$\bar{\varepsilon}^p_{\max} = 0.0061$

(d) $d = 40$ μm

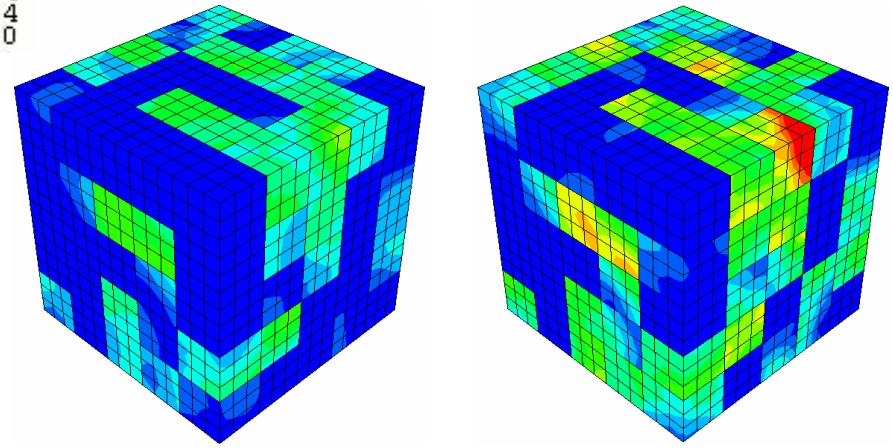

$\bar{\varepsilon}^p_{\max} = 0.0031$

(c) $d = 20$ μm

$\bar{\varepsilon}^p_{\max} = 0.0061$

(d) $d = 40$ μm

Figure 2.12. Distribution of effective plastic strain after five cycles for Ti-6Al-4V with random texture, $d_c/d = 1$, and various average grain size (Group II) , ($R_\varepsilon = -1$ and $\Delta\varepsilon/2 = 0.61\%$).

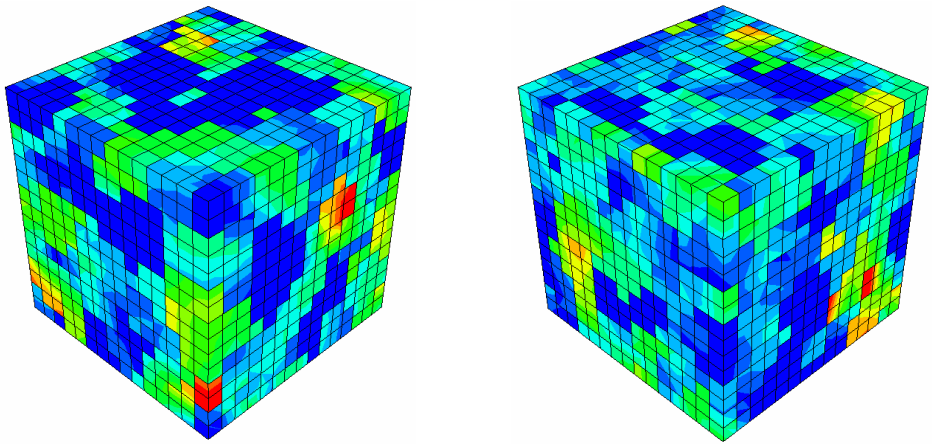

$\bar{\varepsilon}^{p}_{\max} = 0.0041$

(b) $d_c/d = 0.3$

$\bar{\varepsilon}^{p}_{\max} = 0.0042$

(b) $d_c/d = 0.5$

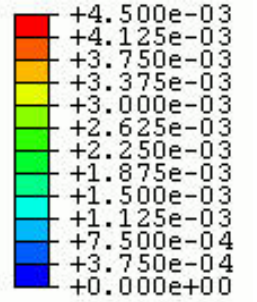

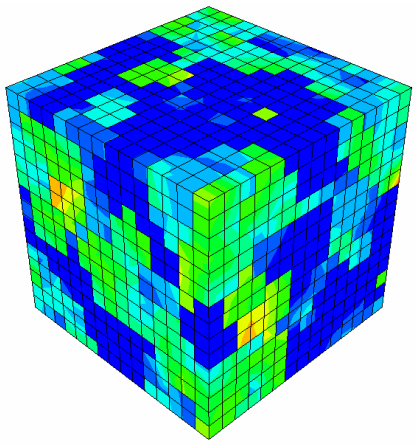

$\bar{\varepsilon}^{p}_{\max} = 0.0038$

(b) $d_c/d = 0.8$

Figure 2.13. Distribution of effective plastic strain after three cycles for Ti-6Al-4V with random texture, d = 30 μm, and (a) d_c/d = 0.3, (b) d_c/d = 0.5 and (c) d_c/d = 0.8 (Group III), (R_ε = -1 and $\Delta\varepsilon/2$ = 0.61%).

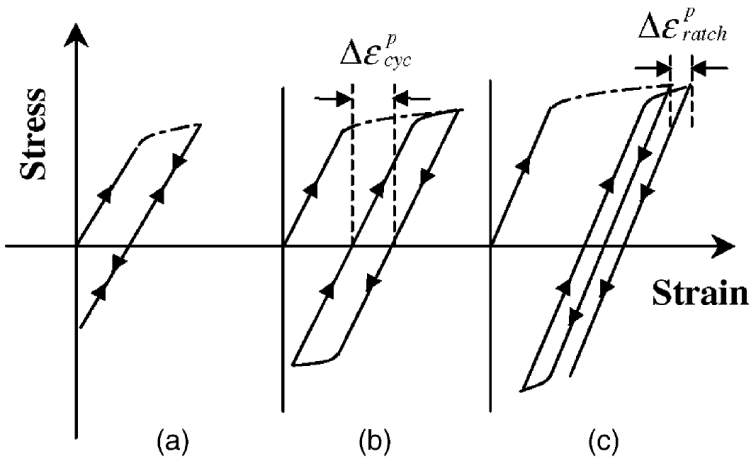

Figure 2.14. Steady-state response of plastic strain behavior during the cycle: (a) elastic shakedown; (b) reversed cyclic plasticity; and (c) plastic ratcheting (Morrissey et al., 2003).

Plots of cumulative plastic strain shown in Fig. 2.11 to 2.13 are based on the effective plastic strain. It is useful to more accurately characterize the nature of the cyclic plastic strain behavior at each point. According to Ambrico and Begley (2000), cyclic plastic strain behavior can be decomposed into three regimes: elastic shakedown, reversed cyclic plasticity, and plastic ratcheting, as shown in Fig. 2.14 (Morrissey, et. al, 2003). Elastic shakedown is defined as the condition for which the material is no longer plastically deforms under cyclic loading after initial yielding; fully elastic deformation after prior yielding is due to the build-up of internal stresses. Reversed cyclic plasticity is the condition in which the material undergoes reversed plastic straining during cycling with no net directional accumulation of plastic strain. Plastic ratcheting is said to occur when the material accumulates net (directional) plastic strain over a given cycle. The parameters of the plastic strain behavior described above are based on the 5th loading cycle. The ratchet plastic strain increment per cycle is defined as (Mayeur, 2004, Goh, 2002)

$$\left(\Delta\varepsilon_{ij}^{p}\right)_{ratch} = \varepsilon_{ij}^{p}\Big|_{\text{end of the cycle}} - \varepsilon_{ij}^{p}\Big|_{\text{start of the cycle}} \tag{2.14}$$

The reversed cyclic plastic strain range is given by,

$$\left(\Delta\varepsilon_{ij}^{p}\right)_{cyc} = \left(\Delta\varepsilon_{ij}^{p}\right)_{\max}\Big|_{\text{over the cycle}} - \left(\Delta\varepsilon_{ij}^{p}\right)_{ratch} \tag{2.15}$$

where $\left(\Delta\varepsilon_{ij}^{p}\right)_{\max}\Big|_{\text{over the cycle}}$ is the maximum range of plastic strain over the cycle, which is given by

$$\left(\Delta\varepsilon_{ij}^{p}\right)_{\max}\Big|_{\text{over the cycle}} = \varepsilon_{ij\,\max}^{p}\Big|_{\text{over the cycle}} - \varepsilon_{ij\,\min}^{p}\Big|_{\text{over the cycle}} \tag{2.16}$$

The effective cyclic plastic strain range and ratchet plastic strain increment are defined as follows:

$$\Delta\varepsilon_{\text{cyc,eff}}^{p} = \sqrt{2/3\left(\Delta\varepsilon_{ij}^{p}\right)_{cyc}\left(\Delta\varepsilon_{ij}^{p}\right)_{cyc}} \tag{2.17}$$

$$\Delta\varepsilon_{\text{ratch,eff}}^{p} = \sqrt{2/3\left(\Delta\varepsilon_{ij}^{p}\right)_{ratch}\left(\Delta\varepsilon_{ij}^{p}\right)_{ratch}} \tag{2.18}$$

Elastic shakedown is defined according to

$$\varepsilon_{ij}^{p} \neq 0 \text{ and } (\Delta\varepsilon_{\text{cyc, eff}}^{p} \text{ and } \Delta\varepsilon_{\text{ratch, eff}}^{p}) \leq C_{cut-off}\varepsilon_{y} \tag{2.19}$$

where $C_{cut-off}$ is the cut-off value that determines the transition between plastic strain behavior and elastic shakedown. The value of $C_{cut-off}$ affects the plastic strain domain size; increase of $C_{cut-off}$ decreases the amount of predicted cyclic and ratcheting plasticity zones and increases the size of the elastic shakedown region. In this study, the same value of $C_{cut-off}$ = 0.0025 as used in the previous work (Mayeur, 2004) has been chosen, which represents 0.25% of the yield strain.

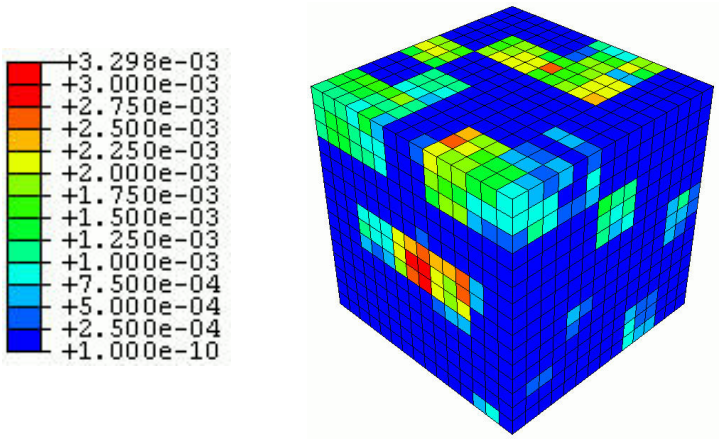

(a) $\Delta\varepsilon^{p}_{\text{cyc, eff}}$

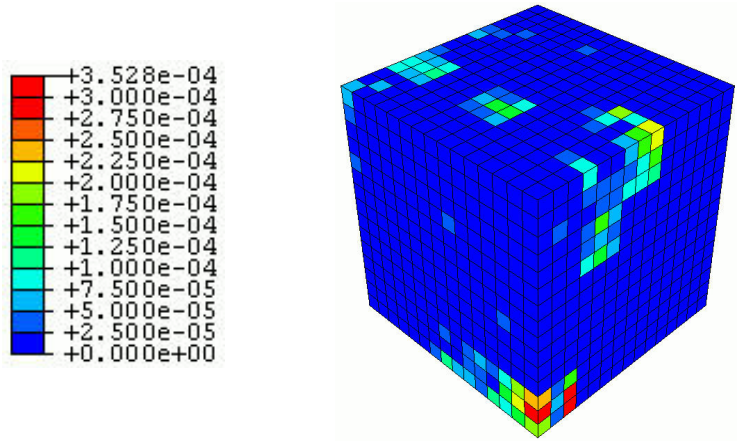

(b) $\Delta\varepsilon^{p}_{\text{ratch, eff}}$

Figure 2.15. Contour of the plastic strain parameters of Microstructure IV over the 5th cycle (R_ε = -1 and $\Delta\varepsilon/2$ = 0.61%).

Figures 2.15 (a) and (b) show the contour plots of the effective cyclic plastic strain range and the effective ratchet plastic strain increment, respectively, which are computed over the 5th cycle for Microstructure IV. Different legends are used for $\Delta\varepsilon^{p}_{\text{cyc, eff}}$ and $\Delta\varepsilon^{p}_{\text{ratch, eff}}$ due to the relatively small value of plastic ratchet strain for completely reversed loading. A large number of elements undergo plastic deformation even though the applied strain amplitude (0.61%) is lower than the yield strain. Most plastically deformed elements have higher $\Delta\varepsilon^{p}_{\text{cyc, eff}}$ than $\Delta\varepsilon^{p}_{\text{ratch, eff}}$. Therefore, cyclic plasticity is the dominant plastic strain behavior for those elements.

Following the heuristic of Ambrico and Begley (2000), also Goh et al. (2003), the deformation behaviors of every element over the 5th cycle are separated into five regimes: elastic (unyielded, $\varepsilon^{p}_{ij} = 0$), elastic shakedown, reversed cyclic plasticity, plastic ratcheting and combined cyclic plasticity and ratcheting. The plastic ratcheting regime is defined as

$$\Delta\varepsilon^{p}_{\text{ratch, eff}} \Big/ \Delta\varepsilon^{p}_{\text{cyc, eff}} > 10 \text{ and } \Delta\varepsilon^{p}_{\text{ratch, eff}} > C_{cut-off}\varepsilon_{y} \tag{2.20}$$

Likewise a region is said to undergoing cyclic plasticity if

$$\Delta\varepsilon^{p}_{\text{ratch, eff}} \Big/ \Delta\varepsilon^{p}_{\text{cyc, eff}} < 0.1 \text{ and } \Delta\varepsilon^{p}_{\text{cyc, eff}} > C_{cut-off}\varepsilon_{y} \tag{2.21}$$

Combined cyclic plasticity and ratcheting is defined as

$$0.1 \le \Delta\varepsilon^{p}_{\text{ratch, eff}} \Big/ \Delta\varepsilon^{p}_{\text{cyc, eff}} \le 10 \text{ and } \Delta\varepsilon^{p}_{\text{cyc, eff}}, \Delta\varepsilon^{p}_{\text{ratch, eff}} > C_{cut-off}\varepsilon_{y} \tag{2.22}$$

Accordingly, elastic shakedown is defined by Eq. (2.19).

With this rigorous scheme of defining the regimes of plastic strain behavior, the deformation behavior of each element is determined over the 5th loading cycle. Figure 2.16 shows the distribution of plastic strain behaviors at the single element level of Microstructure IV. Various colors are used to represent the different plastic strain behaviors. It is shown that cyclic plasticity is the dominant deformation behavior for plastically deformed elements which agrees with the observation from Fig. 2.16. Only a few elements undergo plastic ratcheting and combined cyclic plasticity and ratcheting.

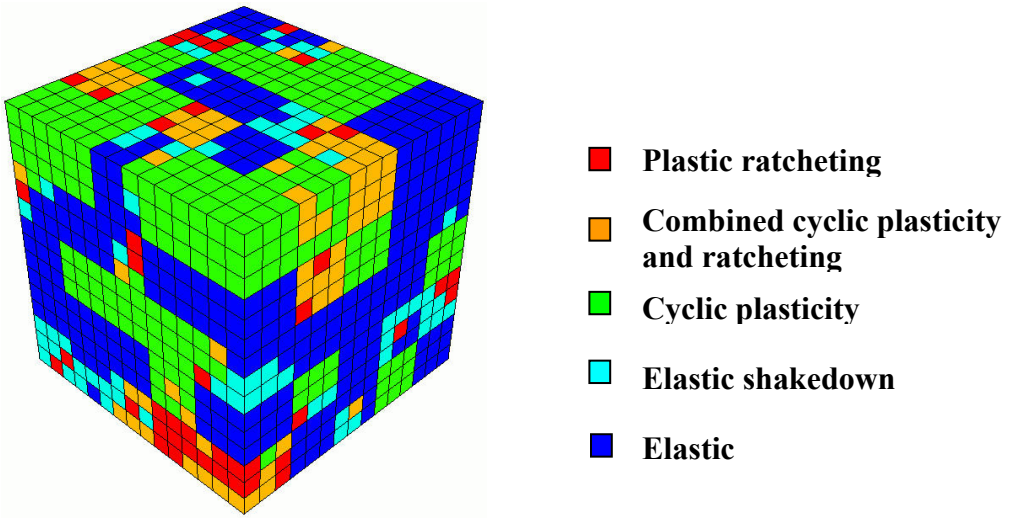

Figure 2.16. Distribution of plastic strain behaviors of Microstructure IV at the 5th cycle.

Table 2.5 summarizes the plastic strain behavior of Ti-6Al-4V for three groups of microstructures considered in this study (Table 2.3). In Table 2.5, N_p denotes the number of elements that plastically deform over the 5th cycle. A close relation between yield strength and N_p is observed for microstructures of Groups I and II. Basal texture is the softest texture and has the highest number of plastically deformed elements. Basal/Transverse texture has the highest yield strength and smallest N_p. Yield strength of random and transverse textures are similar and the N_p of these two textures are close. N_p increases and yield strength decreases with increasing average grain size. The effect of

grain size distribution d_c/d on N_p is small. For the loading history considered in this study, texture has significant influence on plastic strain behavior of Ti-6Al-4V. For basal texture, over 90% of plastically deformed elements are in the cyclic plasticity regime. Random and basal/transverse textures have 60% and 40% of plastic deformation elements undergoing cyclic plasticity, respectively. For transverse texture, the four plastic strain regimes are almost equally present. The percentage of elements that undergo cyclic plasticity slightly increases with increasing grain size. Again, there is no clear trend between grain size distribution and the distribution of plastic deformation regimes.

Table 2.5. Plastic strain behavior for different microstructures.

Microstructure attributes		N_p (% of elements)	Elastic shakedown (% of N_p)	Reversed cyclic plasticity (% of N_p)	Combined cyclic and ratcheting (% of N_p)	Ratcheting (% of N_p)
Texture (Group I)	Random	2420 (71.7%)	15.5	61.2	11.7	11.7
	Basal/ Transverse	1600 (47.4%)	26.56	40.38	21.5	11.56
	Transverse	2534 (75.1%)	21.74	17.76	31.61	28.89
	Basal	3253 (96.3%)	0.96	97.92	1.11	0
Average Grain size, *d* (Group II)	10 μm	1453 (43%)	32.07	55.88	3.99	8.05
	15 μm	2172 (64.3%)	23.34	61.33	5.39	9.94
	20 μm	2377 (70.4%)	14.05	64.07	9.45	12.43
	30 μm	2420 (71.7%)	15.5	61.2	11.7	11.7
	40 μm	2722 (80.7%)	5.5	78.9	9.3	6.3
Grain size distribution d_c/d (Group III)	0.3	2771 (82.1%)	8.7	68.2	11.4	11.7
	0.5	2701 (80.0%)	8.5	66.8	12.8	11.9
	0.8	2728 (80.8%)	3.4	87.9	8.7	0
	1.0	2420 (71.7%)	15.5	61.2	11.7	11.7

2.7 Fatigue Behavior

The magnitude and distribution of plasticity among grains are important factors in fatigue crack formation and early growth. A direct measure of cyclic microplasticity is the maximum range of cyclic plastic shear strain $\Delta\gamma^p_{\max}/2$ over all possible shear strain planes for a given loading condition in individual grains (Bennett and McDowell, 1996), i.e.,

$$\Delta\gamma^p_{\max}/2 = \left\{\left(\Delta\varepsilon^p_{ij}\right)_{cyc}\cdot\left(u_i \otimes v_j\right)\right\}/2 \tag{2.23}$$

Here, $\left(\Delta\varepsilon^p_{ij}\right)_{cyc}$ is defined by Eq. (2.15), v_j is the unit normal vector to the critical plane and u_i is the unit vector in the plane of the maximum range of cyclic plastic shear strain.

Two different methods are used to quantify $\Delta\gamma^p_{\max}/2$: the point-wise maximum (for individual elements) value $\Delta\gamma^p_{\max}/2$, and an average value of maximum $\Delta\gamma^p_{\max}/2$ over a finite domain designated with an asterisk, $\Delta\gamma^{p*}_{\max}/2$. For each element, both $\Delta\gamma^p_{\max}/2$ and $\Delta\gamma^{p*}_{\max}/2$ are calculated. The size of the averaging volume is the average grain size. The maximum $\Delta\gamma^p_{\max}/2$ and $\Delta\gamma^{p*}_{\max}/2$ over a single grain is used to indicate the driving force for crack formation of this grain. The distributions of $\Delta\gamma^p_{\max}/2$ and $\Delta\gamma^{p*}_{\max}/2$ for each grain over the 5th loading cycle for Microstructure IV are shown in Fig. 2.17. The value of the maximum $\Delta\gamma^p_{\max}/2$ is much larger than that of the average maximum $\Delta\gamma^{p*}_{\max}/2$. The peak value of $\Delta\gamma^p_{\max}/2$ is about three times higher than that of $\Delta\gamma^{p*}_{\max}/2$. Fatigue life prediction based on $\Delta\gamma^p_{\max}/2$ would be more conservative. It is noted that the process of fatigue crack formation operates over a finite volume/process

zone. Therefore, an averaged measure of $\Delta\gamma^{p*}_{\max}/2$ is more appropriate for the purpose of quantifying the driving force for fatigue crack formation. Furthermore, the volume averaging process is required to eliminate the mesh sensitivity of $\Delta\gamma^{p}_{\max}/2$ (McDowell, 2005) as a useful, objective FIP.

The maximum value of the volume averaged $\Delta\gamma^{p*}_{\max}/2$ depends on the size of the averaging volume. In a previous study, Mayeur et al. (2006) showed that the predicted fatigue life increased with increasing volume size. It is noted that the development of slip bands in primary α grains is an important mechanism of crack formation and usually extends across entire grains. Therefore, average grain size is considered as a proper size of the averaging volume to evaluate the magnitude and distribution of $\Delta\gamma^{p*}_{\max}/2$ for Ti-6Al-4V.

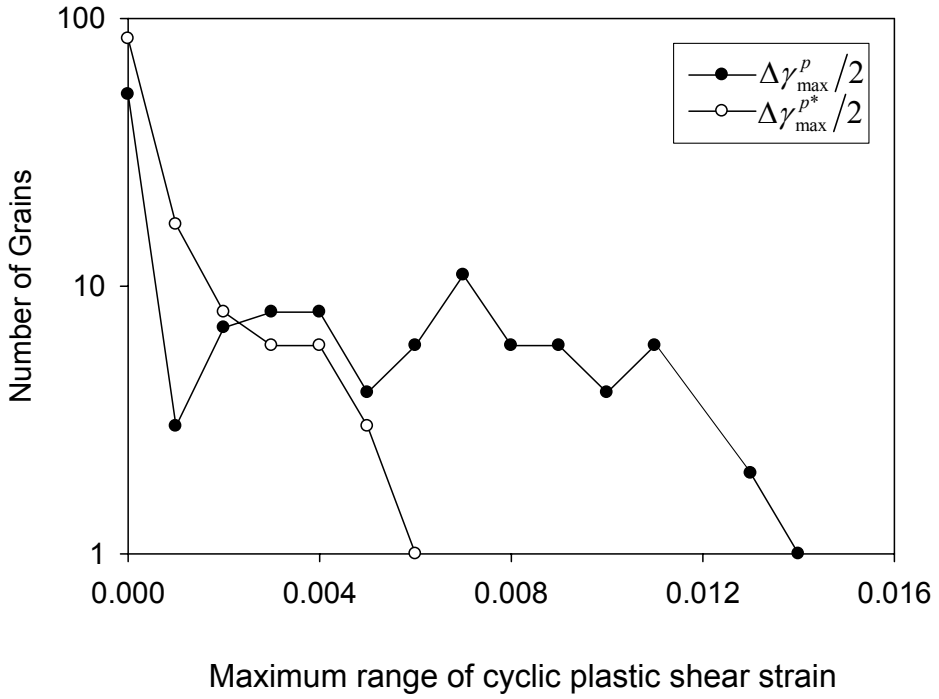

Figure 2.17. Distribution of the $\Delta\gamma^{p}_{\max}/2$ and $\Delta\gamma^{p*}_{\max}/2$ for Microstructure IV.

The distributions of $\Delta\gamma_{\max}^{p*}/2$ computed over the 5th loading cycle for microstructures of Group I simulations (texture), Group II simulations (average grain size) and Group III simulations (grain size distribution) are shown in Fig. 2.18 (a), (b) and (c), respectively. Previous results showed that the basal texture is the softest and basal/transverse texture is the hardest in terms of yield strength for loading in the normal direction. Similar results can be observed from Fig. 2.18(a). The basal texture has the largest number of grains with high $\Delta\gamma_{\max}^{p*}/2$. The maximum $\Delta\gamma_{\max}^{p*}/2$ of basal texture is also the highest among four textures. On the other hand, basal/transverse texture has lowest maximum $\Delta\gamma_{\max}^{p*}/2$ and lowest number of grains with high $\Delta\gamma_{\max}^{p*}/2$. The distributions of $\Delta\gamma_{\max}^{p*}/2$ for random and transverse textures are close. Thus, texture has significant influence on material strength and fatigue resistance of Ti-6Al-4V. In Fig. 2.18(b), it is noted that both maximum $\Delta\gamma_{\max}^{p*}/2$ and number of grains with high $\Delta\gamma_{\max}^{p*}/2$ increase with increasing grain size. Therefore, both yield strength and fatigue resistance of Ti-6Al-4V decrease with increasing grain size. No clear tendency is evident in Fig. 2.19(c) for microstructures of group III, similar distributions and maximum $\Delta\gamma_{\max}^{p*}/2$ are observed for various grain size distributions. Therefore, compared to texture and average grain size, the grain size distribution has weaker influence on the distribution of cyclic plastic deformation behavior of Ti-6Al-4V.

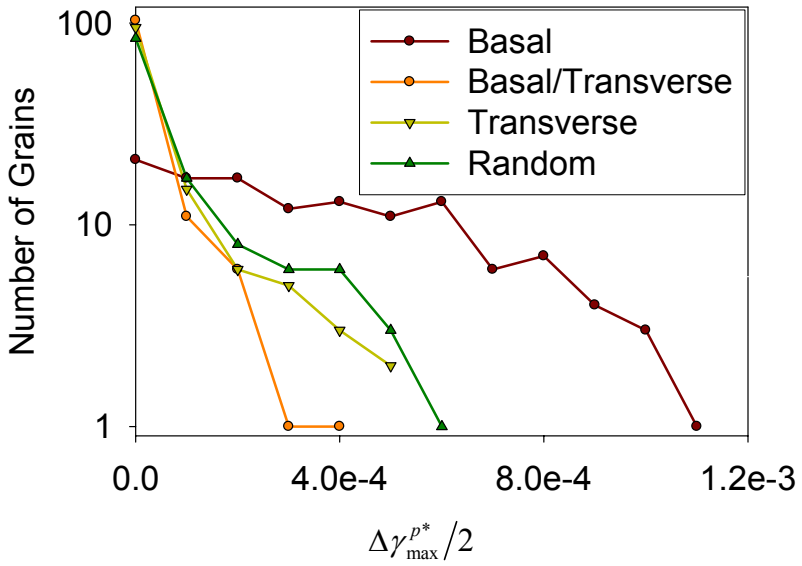

(a) Texture (Group I)

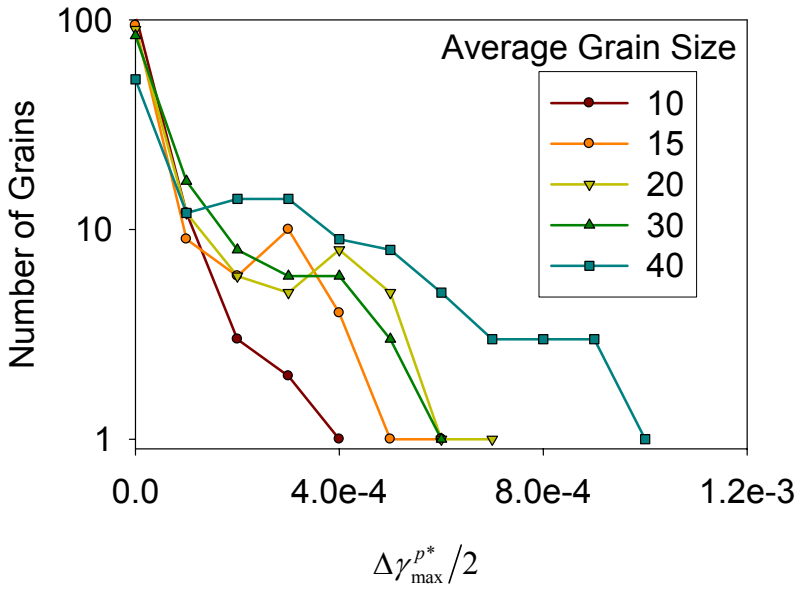

(b) Grain size (Group II)

Figure 2.18. Influence of microstructure attributes on the distribution of $\Delta\gamma^{p*}_{\max}/2$ showing the relative effect of (a) texture, (b) grain size, and (c) grain size distribution.

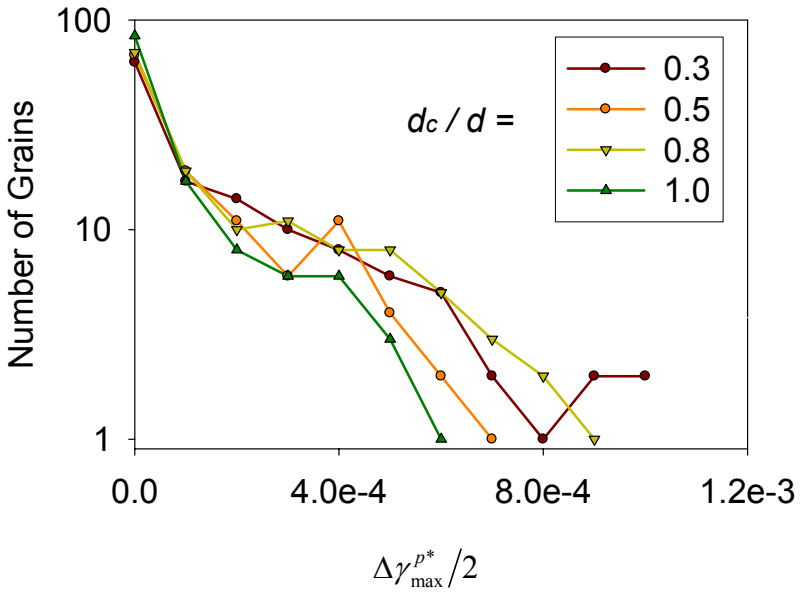

(c) Grain size distribution (Group III)

Figure 2.18. Influence of microstructure attributes on the distribution of average $\Delta\gamma^{p*}_{max}/2$ showing the relative effect of (a) texture, (b) grain size, and (c) grain size distribution (cont.).

As described in Chapter 1, various models have been proposed to predict the fatigue crack formation life of crystalline materials under multiaxial loading. Fatigue crack formation of Ti-6Al-4V is driven primarily by cyclic plastic shear strain. Therefore, plastic strain-based critical plane approaches are more appropriate for the purpose of predicting fatigue behavior of Ti-6Al-4V at the level of microstructure, i.e., FIPs. Among all critical plane approaches, the Fatemi-Socie parameter P_{FS} is shear-dominated FIP and includes maximum normal stress to the critical plane. Therefore, P_{FS} is considered to be suitable for quantifying the driving force for crack formation.

The Fatemi-Socie FIP is given by

$$P_{FS} = \frac{\Delta\gamma_{\max}^{p*}}{2}\left(1 + K\frac{\sigma_n^{\max*}}{\sigma_y}\right) \tag{2.24}$$

where K is a material constant, $\Delta\gamma_{\max}^{p*}$ has been previously defined, and $\sigma_n^{\max*}$ denotes the maximum normal stress on the corresponding critical plane over the same averaging domain. Following that of previous work (Mayeur et al., 2006), $K = 1$ is employed. As in the previous case, the averaging volume is the average grain size for both $\Delta\gamma_{\max}^{p*}/2$ and $\sigma_n^{\max*}$. For each element, P_{FS} is calculated over the averaging domain. The maximum P_{FS} over a grain is used to indicate the driving force for crack formation of this grain.

Distributions of the nonlocal Fatemi-Socie FIP in Eq. (2.24) of microstructures of Group I, Group II and Group III are shown in Fig. 2.19 (a), (b) and (c), respectively. The maximum P_{FS} over the entire model are given in Table 2.6. Distributions of P_{FS} and $\Delta\gamma_{\max}^{p*}/2$ are similar for all microstructures. In Fig. 2.19(a), it is shown that basal texture has the largest number of grains with high P_{FS}. The maximum P_{FS} for the basal texture is also the largest among all textures. It is concluded that the basal texture has the lowest fatigue resistance, in agreement with previous results. The basal/transverse texture has the lowest maximum P_{FS} and thus has the highest fatigue resistance. The same tendency is observed in Table 2.6. Distributions of P_{FS} and maximum P_{FS} for random and transverse textures are similar. The fatigue resistances of these two microstructures are between those of basal and basal/transverse textures.

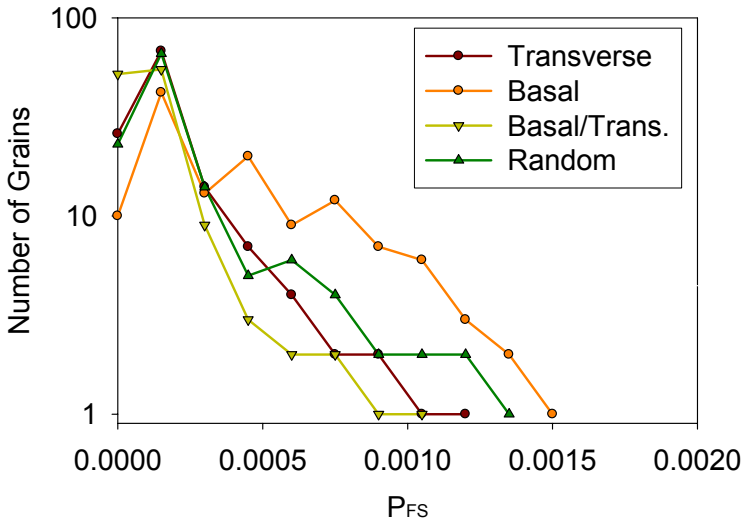

(a) Texture (Group I)

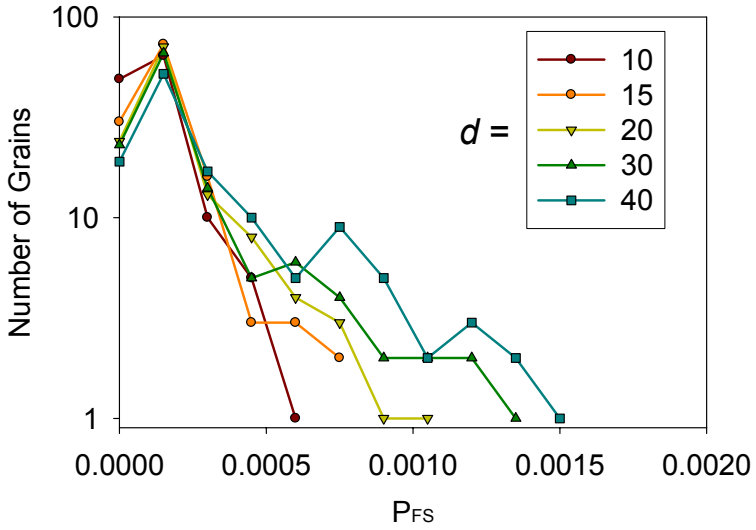

(b) Grain Size (Group II)

Figure 2.19. Variation of distribution of P_{FS} with respect to variation of microstructure attributes showing the relative effect of (a) texture, (b) average grain size, and (c) grain size distribution.

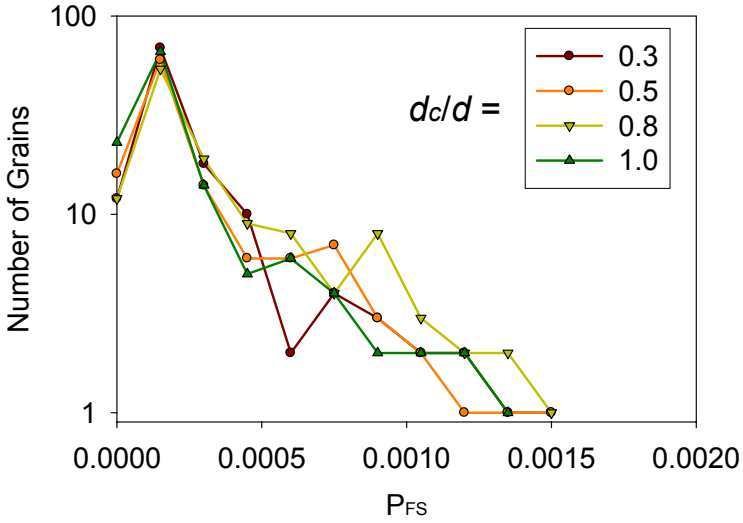

(c) Grain size distribution (Group III)

Figure 2.19. Variation of distribution of P_{FS} with respect to variation of microstructure attributes showing the relative effect of (a) texture, (b) grain size, and (c) grain size distribution (cont.).

In Fig. 2.19(b), the number of grains with high P_{FS} increases with increasing grain size. The same trend is observed in Table 2.6. The approximate linear relation between maximum P_{FS} and the square root of the grain size is shown in Fig. 2.20. Increasing grain size results in reduction of slip resistance. As the result, plastic shear among the crystals increases, which leads to increased driving force for crack formation.

Figure 2.19(c) and Table 2.6 show no clear correlation between grain size distribution parameter d_c/d and distribution and maximum P_{FS}. Therefore, it is concluded that comparing with the effects of texture and average grain size, the effect of grain size distribution on the cyclic deformation behavior of Ti-6Al-4V is relatively weak for the loading history considered.

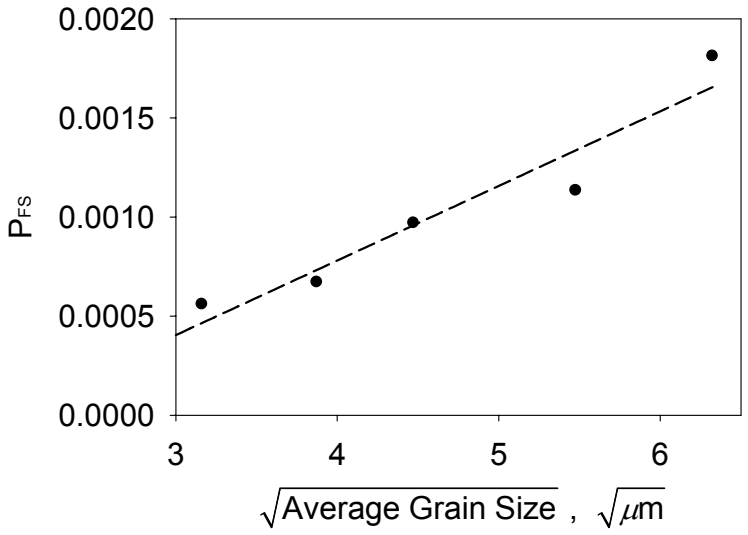

Figure 2.20. Variation of maximum P_{FS} and predicted crack formation life with respect to variation of average grain size (Group II).

Table 2.6. Maximum $\bar{\varepsilon}^p$ and P_{FS} for different microstructures.

Microstructure attributes		Max. P_{FS} averaged over grain size	Predicted crack formation life, $2N_f$
Texture (Group I)	Random	1.33×10^{-3}	7316
	Basal/ Transverse	1.03×10^{-3}	9849
	Transverse	1.16×10^{-3}	8577
	Basal	1.49×10^{-3}	6411
Average Grain size, d (Group II)	10 μm	0.56×10^{-3}	20004
	15 μm	0.67×10^{-3}	16239
	20 μm	0.97×10^{-3}	10561
	30 μm	1.33×10^{-3}	7316
	40 μm	1.81×10^{-3}	5113
Grain size distribution d_c/d (Group III)	0.3	1.4×10^{-3}	6892
	0.5	1.75×10^{-3}	5317
	0.8	1.78×10^{-3}	5213
	1.0	1.13×10^{-3}	8843

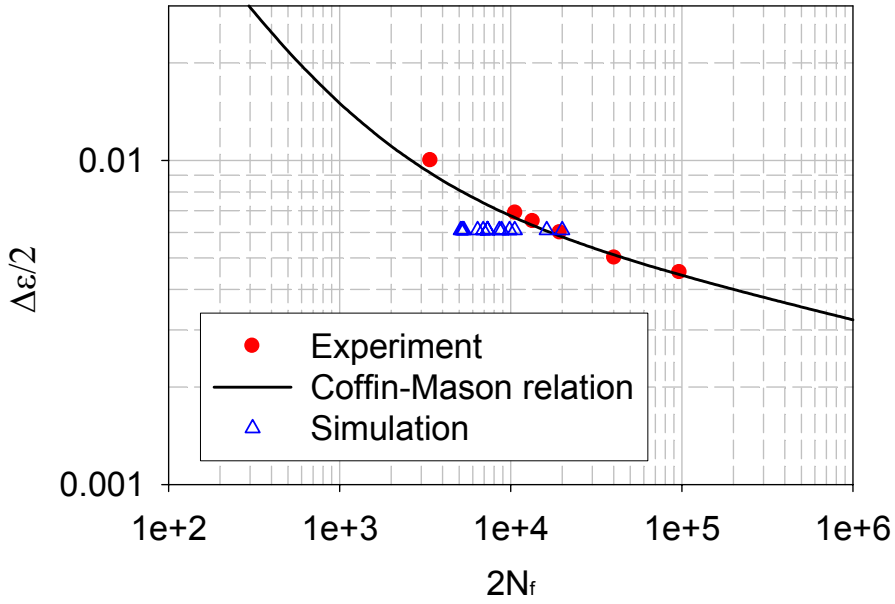

Figure 2.21. Crack formation lives.

The FS FIP can be related to the crack formation life according to a Coffin-Manson relation

$$P_{FS} = \gamma_f^{'}(2N_f)^{c'} \tag{2.25}$$

where $\gamma_f^{'}$ and c' are constants for a given critical fatigue crack length. A Coffin-Manson relation correlating plastic strain range $\Delta\varepsilon^p/2$ and fatigue crack formation life is given by

$$\frac{\Delta\varepsilon^p}{2} = \tilde{\varepsilon}_f^{'}(2N_f)^{\tilde{c}'} \tag{2.26}$$

The constants $\tilde{\varepsilon}_f^{'} = 2.8$ and $\tilde{c}'$ = -0.86 reported by Szolwinski et al. (1999) gave good fit to the uniaxial LCF data reported in (Gallagher et al., 2001), as shown in Fig. 2.21. A

completely reversed (R_ε = -1) strain-controlled history at 0.333 Hz was employed in these LCF tests at room temperature. The mechanical properties of the duplex Ti-6Al-4V are summarized in Table 2.7 (Lovrich, 2004). Fridrici et al. (2005) showed that the constants reported in (Szolwinski et al., 1999) corresponded to the critical fatigue crack length of 30 μm, which equaled to the length scale of averaging volume used in this study.

Table 2.7 Mechanical properties of Ti-6Al-4V (Lovrich, 2004)

Elastic modulus, GPa	118
Poisson's ratio	0.361
Yield strength, MPa	930

For simplicity, we assume that $\gamma_f^{'} = \tilde{\varepsilon}_f^{'}$ and $c' = \tilde{c}'$ for the critical crack length of 30 μm. For each microstructure, the maximum P_{FS} is used to calculate fatigue crack formation life according to Eq. (2.25). The predicted lives corresponding to the applied strain amplitude, $\Delta\varepsilon/2$ = 0.61%, range from 5100 to 20000 reversal which is close to the experimental data, as shown in Table 2.6 and Fig. 2.21. It is shown that the microstructure has significant effect on the scatter of fatigue crack formation life of Ti-6Al-4V.

2.8 Summary

In this Chapter, three-dimensional finite element simulations are conducted to study the effects of microstructure attributes on the cyclic deformation behavior of the duplex Ti-6Al-4V alloys. The deformation behaviors of primary α and α/β lamellar phases of Ti-6Al-4V at room temperature are described by a fully three-dimensional crystal plasticity constitutive relation developed by Mayeur and McDowell (2006).

Microstructure attributes considered in this sensitivity study include crystallographic texture, grain size, and grain size distribution. Voronoi tessellation is used to construct the three-dimensional finite element models with various grain size distributions.

In monotonic tension simulations at room temperature, a slight influence of texture on elasticity of polycrystalline Ti-6Al-4V is observed. Grain size and grain size distribution show no influence on the elastic stiffness. Strong dependence of material strength on grain size and texture is shown. Influence of grain size distribution on yield strength is minimal.

A completely reversed, strain-controlled loading history is applied in cyclic loading simulations at room temperature. The plastic strain behaviors and the distribution of the average maximum plastic shear strain among grains are analyzed and contrasted. The relative susceptibility for crack formation, including effects of various microstructure features, is assessed using the nonlocal Fatemi-Socie FIP. The results suggest that both average grain size and especially crystallographic texture have more influence on the plastic deformation and indicated fatigue behavior than the grain size distribution.

The fatigue crack formation lives of considered microstructures are calculated according to a Coffin-Manson relation. It is shown that the predicted fatigue crack formation lives is close to the experimental data. The microstructure has significant effect on the scatter of fatigue crack formation life of Ti-6Al-4V.

CHAPTER 3
MICROSTRUCTURE-SENSITIVE FRETTING FATIGUE SIMULATIONS

3.1 Introduction

In Chapter 2, a methodology for using crystal plasticity to explore the sensitivity of material strength and cyclic deformation behavior to microstructure was presented and demonstrated for duplex Ti-6Al-4V at room temperature. The crystal plasticity material model captures the crystallographic orientation dependence of the deformation behavior for both primary α phase and the lamellar colonies. A Voronoi tessellation procedure is used to render polycrystalline grain size distributions. Simulation results show a strong dependence of material strength and microstructure-level FIPs on crystallographic texture and grain size of duplex Ti-6Al-4V. In this chapter, the same methodology is used to investigate the effects of microstructure and loading parameters on the fretting fatigue of Ti-6Al-4V.

Fretting fatigue occurs as a result of mixed stick-slip conditions near the edge of contact at the interface of two contacting bodies. Fretting fatigue is drawing increasing attention as one of the leading causes of premature failure for gas turbine engines. For example, the vibratory load applied on the blade and disk causes a fretting motion (micron scale relative motion) at their interface (Cortez et al., 1999).

Fretting fatigue is a near-surface phenomenon that occurs over a very small area. Plastic deformation, damage, and microstructure transformation occur within a depth of several grains from the surface. The relative tangential surface displacement between two bodies is also extremely small (several μm). Since the material microstructure is of

comparable dimensions, it can significantly influence the mechanical behavior. Experimental observations show that fretting fatigue cracks may form at the edge of contact region, at the boundary between the slip and non-slip regions, or at the center of contact of the specimens (Antoniou and Radtke, 1997).

Fretting fatigue simulations using a two-dimensional crystal plasticity model showed the impact of microstructure on the fretting deformation behavior (Goh et al., 2001, 2003). These early works showed that differential yielding among grains due primarily to crystallographic orientation in regions of steep cyclic gradients leads to intense concentrations of shear. Plastic strain accumulation was primarily due to ratcheting. Fretting simulations using fully three-dimensional crystal plasticity models exhibited similar behaviors but allowed the study of realistic microstructures, including the distributions of grain orientations and realistic textures (Mayeur et al., 2007; Zhang et al., 2005, 2006). Dick and Cailletaud (2006) have also conducted fretting fatigue simulations on Ti-6Al-4V with more realistic modeling of grain shapes using Voronoi polyhedra, although they considered only the primary α phase. Similar effects of microstructure attributes on creep and high strain rate behaviors of Ti-6Al-4V have been studied using crystal plasticity by Hasijia et al. (2003) and Schoenfeld and Kad (2002), respectively.

In this Chapter, three-dimensional fretting simulations are conducted on duplex Ti-6Al-4V to investigate the sensitivity of three microstructure attributes on fretting behavior: the average grain size, the grain size distribution, and the texture. Various combinations of normal and tangential forces are applied to investigate the sensitivity of loading parameters on fretting behavior. Conclusions on the relative influence of these microstructure attributes and loading parameters are drawn based on the deformation response and analysis using shear strain-based fatigue indicator parameters (FIPs).

3.2 Material

Duplex Ti-6Al-4V considered in this study contains a mixture of primary hcp α phase and secondary α plus bcc β phase arranged in a lamellar structure. As described in Chapter 2, the key first order microstructure attributes of Ti-6Al-4V include average globular (primary) α size, lamellar colony size, volume fraction of the primary α phase, and mean thicknesses of the secondary α and β phases in the lamellar colonies.

Table 3.1. Microstructure attributes considered in this study.

	Group I	Group II	Group III	Microstructure IV
Studied attribute	Texture	Grain size	Grain size distribution	
Average grain size, d (micron)	30	25, 30, 35	30	30
Grain size distribution (d_c/d)	1	1	0.3, 0.5, 0.8, 1	1
Vol. Fraction of Globular α V_f (%)	60	60	60	60
Texture	Basal Transverse Basal/Trans. Random	Basal	Basal	Basal
Mean thickness of α lath (micron)	1.5	1.5	1.5	1.5
Mean thickness of β lath (micron)	0.5	0.5	0.5	0.5

Three microstructure attributes are considered in the microstructure sensitivity study: average grain size d, grain size distribution, and texture. Other important microstructure attributes are assumed unchanged. These include maintaining the volume fraction of primary α phase (60%) and the lath thicknesses of secondary α and β phases (1.5 μm and 0.5 μm, respectively). Table 3.1 summarizes the microstructure attributes of

three groups of Ti-6Al-4V considered in the simulations corresponding to three studied microstructure attributes. Four textures are used in Group I: basal, transverse, basal/transverse, and random textures, as shown in Fig. 2.2. It should be noted that, owing to lack of detailed stereological information on lamellar colony size, the average primary α size and lamellar colony size are assumed to be identical. To investigate the influence of loading parameters on fretting behavior, various combinations of normal and tangential forces are applied on Microstructure IV.

The three-dimensional crystal plastic constitutive relations developed by Mayeur and McDowell (2007) are used to describe the deformation behavior of Ti-6Al-4V. The description of the model has been given in Chapter 2.

3.3 Finite Element Model

The finite element model for fretting fatigue simulations consists of the contact of a rigid cylinder with radius of 5 mm on infinite half space shown in Fig. 3.1(a). A cylindrical domain is used for the lower half space, with infinite elastic elements comprising the outmost layer. Infinite elements are generally used when the region of interest is small compared to the surrounding medium (ABAQUS, 2005). The half space is fully constrained by assuming the infinite direction is normal to the outmost layer. In this model, the thickness of the indenter is smaller than that of the half space and the lateral boundaries normal to the z-direction are assumed to be free of constraint.

The upper cylindrical body is first subjected to a normal force P in the y-direction, and then the fretting motion is applied by prescribing a cyclic tangential force Q parallel to the x-direction. The friction coefficient between the two bodies is set to 1.5 based on previous work (Goh et al., 2003). Only partial slip conditions are considered to prohibit the complete sliding between two bodies, which would be unconstrained in this force

control analysis. It should be noted that the length of the rigid cylinder is finite. Therefore, a substantial contact edge effect is expected at the regions where the end of the rigid cylinder contacts the half space, as shown in Fig. 3.1(b). Since a sharp contact edge would result in a stress singularity at the edge of contact that could lead to the computational difficulties, the contacting edge is rounded with a radius of 0.01 mm. The finite sliding option in ABAQUS (2005) is assumed between two bodies to avoid possible computational divergence, especially when the tangential force is high.

As shown in Fig. 3.1(b), the half space is separated into four parts. The inner part is defined as a crystal plasticity region; contact with the upper rigid cylinder occurs entirely within this region. The polycrystal Ti-6Al-4V is oriented in the way that the normal and rolling directions are parallel to the z- and y-axes, respectively, corresponding to the considered textures shown in Fig. 2.2. The domains shaded as blue and yellow colors represent the primary α phase and lamellar colonies, respectively. Each $3\times3\times3$ element block denotes a grain. The number of grains in the x-, y-, and z-directions is 12, 7, and 10, respectively. Thus, there is a total 22680 elements in the crystal plasticity region. The size of the crystal plasticity region is chosen to include all elements that undergo plastic deformation during the simulations. Outside of the crystal plasticity region is the initially isotropic J_2 plasticity region, rendered with dark gray color. For all simulations, pure linear isotropic elastic behavior is assigned to the elastic and infinite elastic regions beyond. To allow for transitions in mesh density, two neighboring regions are "glued" together by using "tie" surface constraints (ABAQUS, 2005). To decrease the computational costs, three-dimensional 8-node solid linear elements with reduced integration (C3D8R) (ABAQUS, 2005) are used in all regions.

Various grain size distributions are realized by using Voronoi tessellation. The descriptions of the Voronoi tessellation algorithm employed in this study are given in Chapter 2. It should be noted that the size of the crystal plasticity region is related to the average grain size and number of grains via Eq. (2.7). Three different grain size

distributions are obtained by setting the grain size distribution parameter d_c/d = 0.3, 0.5 and 0.8. The idealized structure with the cubic grains of identical size is a special case with d_c/d = 1. Various grain size distributions are simulated with simulated annealing method described in Chapter 2.

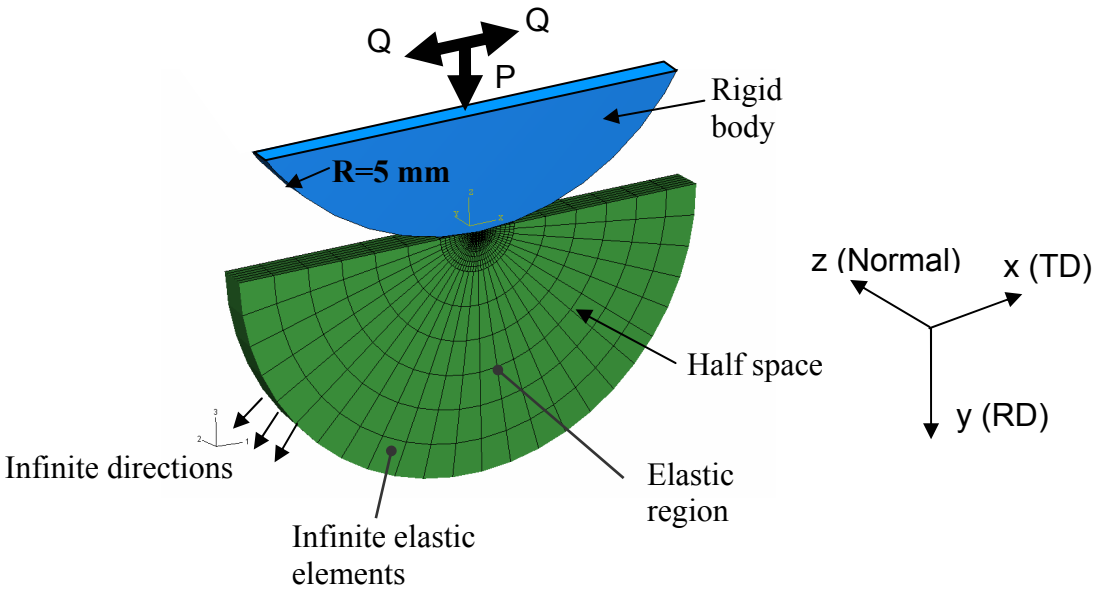

(a)

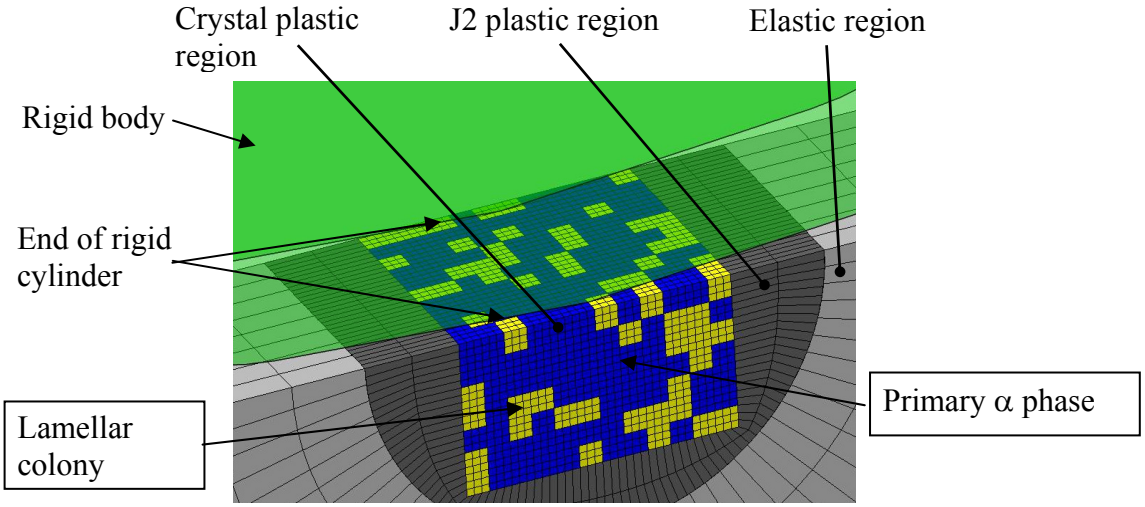

(b)

Figure 3.1. Three-dimensional finite element model for simulating fretting: (a) contact geometry and (b) close-up view of contact region, including the crystal plasticity zone.

3.4 Simulation Results

For purposes of the microstructure sensitivity study, the normal force $P = P_y$ and amplitude of alternating tangential force $Q = 0.1P_y$ are prescribed, where reference force P_y is defined as the force required to initiate yield in the subsurface, assuming homogenous and isotropic elastic behavior of duplex Ti-6Al-4V and ideal two-dimensional frictionless Hertzian contact. After applying the normal force P, the cyclic tangential force Q is applied for three cycles due to the intense nature of the computations. Both P and Q are set to be zero at the last unloading step. For the cases involving texture, the direction of the normal force is parallel to the rolling direction (RD).

To validate the finite element model, fretting simulations are conducted using elastic and J_2 plasticity material models under the same prescribed fretting conditions. These simulations are compared to a crystal plasticity simulation on Microstructure IV having basal texture with $d = 30$ μm and $d_c/d = 1.0$, as shown in Table 3.1. Contours of the von Mises effective stress in the crystal plasticity region after the application of initial normal force P are shown in Fig. 3.2. All contours are shown in x-y midsection view, as illustrated by Fig. 3.2(d). The x-y plane passes through the center of the model. Both the elastic and J_2 plasticity simulations show continuous and homogeneous distribution of the von Mises stress at the surface and subsurface regions. The crystal plasticity simulation displays a heterogeneous distribution. The stress in some grains is much higher than that of the neighboring grains. Such phenomena can be attributed to the highly anisotropic behavior of Ti-6Al-4V.

As expected, a strong edge effect is observed where the end of the cylinder contacts the half space. However, the response on the x-y plane (midsection plane) closely approximates line contact, since the edge effect is limited to the regions near the end of the contacting cylinder. The elastic simulation predicts the largest von Mises

stress because no yield is assumed. The slightly higher von Mises stress of the crystal plasticity simulation at certain locations can be attributed to the relatively high elastic modulus and yield strength of certain grains of Ti-6Al-4V having unfavorable orientations.

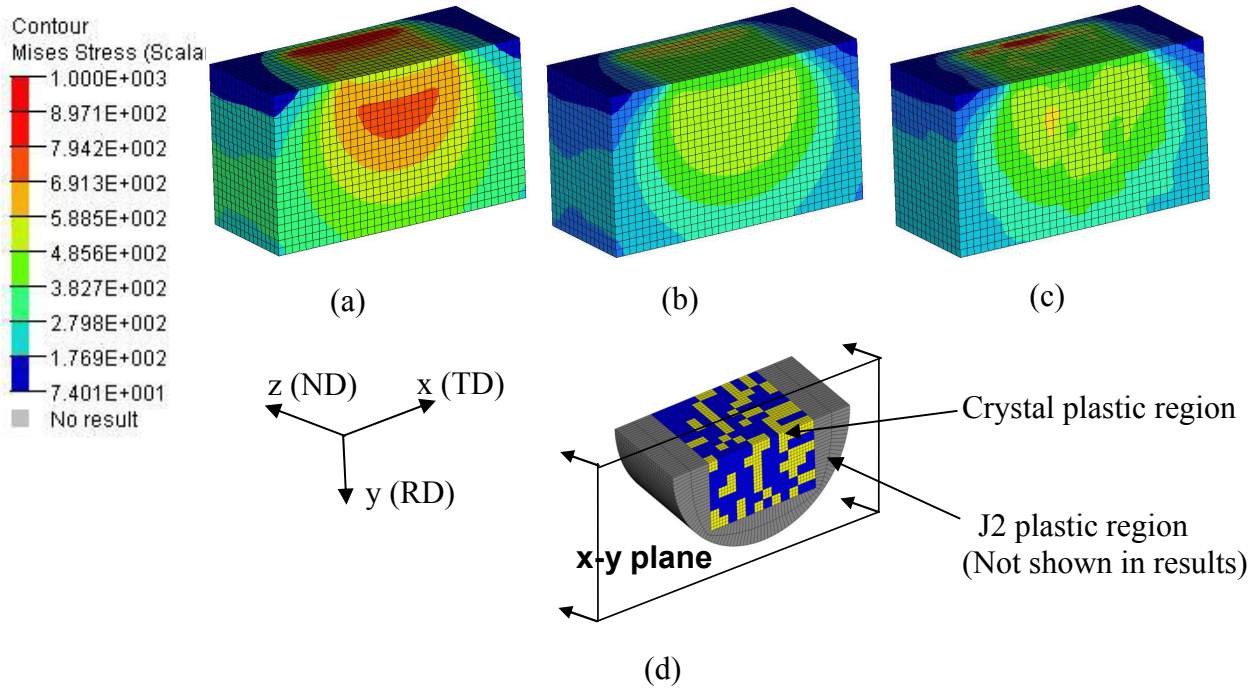

Figure 3.2. Contours of von Mises stress at crystal plasticity region after initial normal force is applied for different material models, (a) elastic, (b) J_2 plasticity, and (c) crystal plasticity with basal texture and uniform grain size and distribution, and (d) illustration of x-y cross-section (midsection of the model).

The contact pressure of three simulations in x-y plane (center plane) after initial normal load is shown in Fig. 3.3. The ideal frictionless Hertzian solution of the contact pressure for two-dimensional line contact with plane strain condition is also shown. The contact pressure of the elastic simulation is very close but slightly lower than that of the Hertzian solution. The frictionless, plane strain conditions assumed in the Hertzian solution are believed to account for the higher contact pressure. The slightly different

contact pressure at the trailing edge is caused by the low mesh density at the surface. The length of the contact half space of the elastic simulation is also very close to that of the Hertzian solution. It is concluded that the stress-strain state in x-y plane of the three-dimensional model is very close to that of the two-dimensional solution, thereby validating the finite element model used in this study. Comparing with the elastic simulation and the Hertzian solution, a lower contact pressure is observed for the J_2 plasticity simulation which can be attributed to the yielding of material in the subsurface region. It is noted that the smooth contact pressure are observed for the Hertzian solution and the elastic and J_2 plasticity simulations. On the contrary, the contact pressure of the crystal plasticity simulation is not smooth due to the anistropic behavior of Ti-6Al-4V and discrete grains. Both J_2 and crystal plasticity simulations predict larger size of the contacting half-space than the Hertzian solution and the elastic simulation for which no material yielding is assumed.

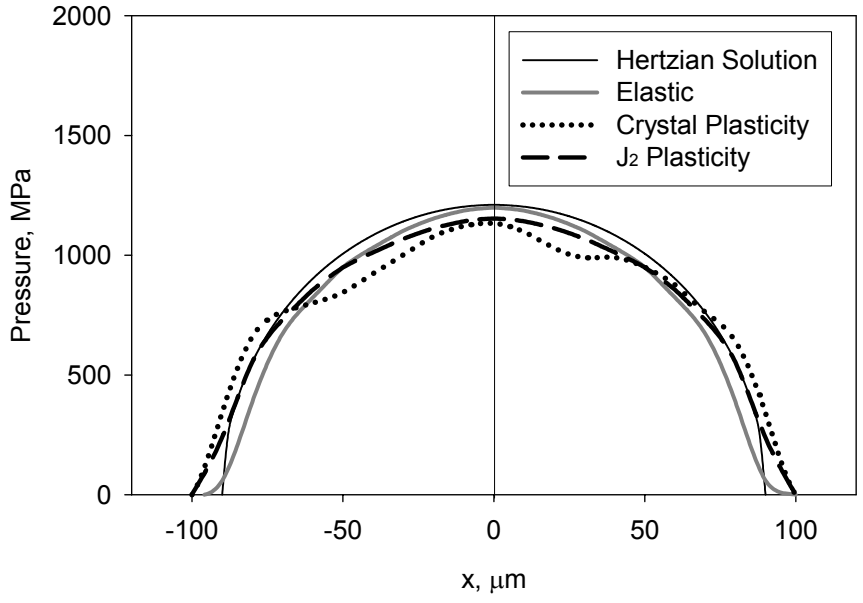

Figure 3.3. Contact pressure at x-y plane after initial normal load.

Figure 3.4 shows the relation between applied normal forces and corresponding normal displacements of the rigid body during the initial loading step and the unloading step after three tangential loading cycles. For $P = P_y$, the macroscopic normal displacement minimally depends on the material model used, increasing from 4.88 μm for purely linear isotropic elastic to 5.01 μm for crystal plasticity. For elastic simulations, the force-displacement curves of loading and unloading steps coincide. For J_2 and crystal plasticity simulations, an apparent difference between these two curves is shown. At the same time, the non-zero displacement corresponding to zero normal load is observed at the unloading step. The plastic deformation behavior has a noticeable effect on the normal loading behavior.

The tangential force and displacement responses of the rigid body during the third tangential loading cycle are presented in Fig. 3.5. The macroscopic tangential displacement response does not significantly depend on the material model, suggesting relatively low accumulation of plastic strain during the tangential loading cycle, as expected.

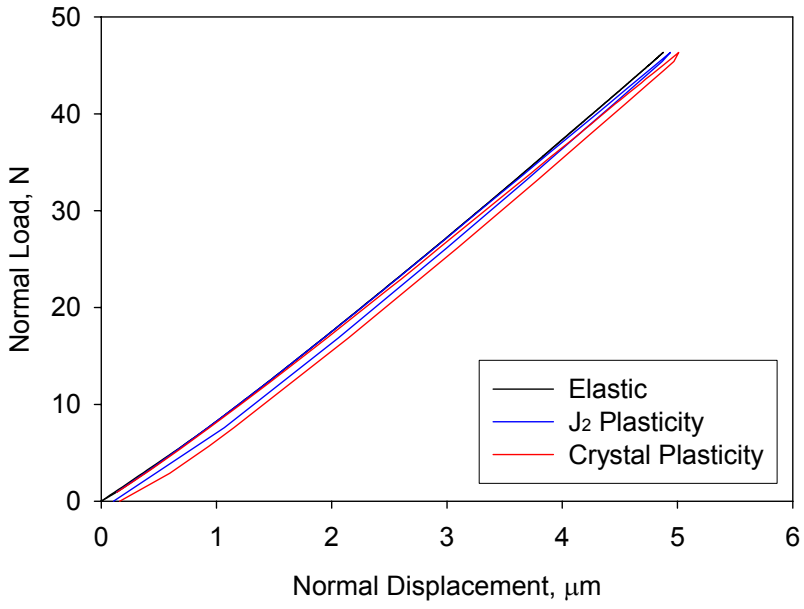

Figure 3.4. Normal force-displacement responses during loading and unloading steps.

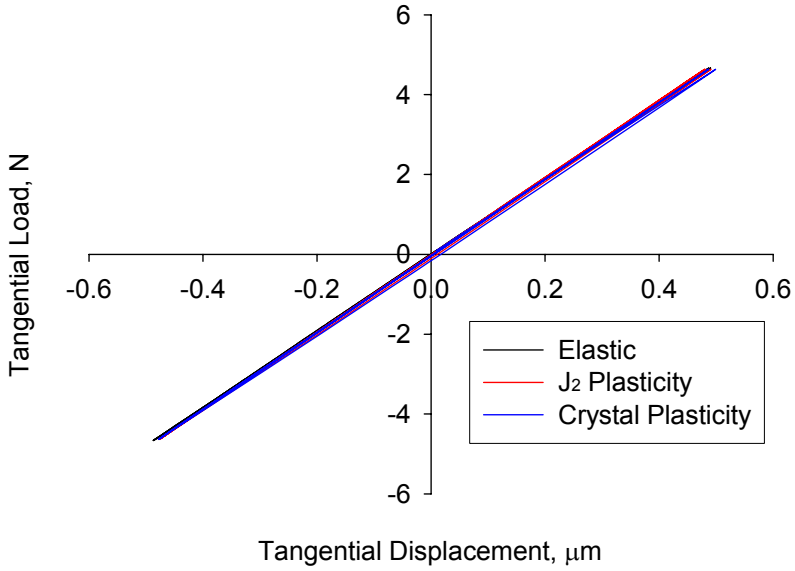

Figure 3.5. Tangential force-displacement responses over the 3rd tangential loading cycle.

As shown in Table 3.1, three groups of Ti-6Al-4V simulations are used to investigate the effects of texture, grain size, and grain size distribution d_c/d on the fretting fatigue behavior. The simulation results are summarized in Figs. 3.6-3.8 and Table 3.2. Since previous studies suggest that ratcheting plays a major role in fretting fatigue crack formation (Goh, 2002), it is most relevant to compare the cumulative plastic strains generated by fretting in the different microstructures. There are several ways this can be done. One is to view the effective plastic strain, defined by $\bar{\boldsymbol{\varepsilon}}^p = \sqrt{(2/3)\varepsilon_{ij}^p \varepsilon_{ij}^p}$, where $\boldsymbol{\varepsilon}^p = \sum_\alpha \gamma^\alpha \left(\mathbf{s}_0^\alpha \otimes \mathbf{m}_0^\alpha\right)_{sym}$, after three tangential loading cycles for various microstructures, as shown in Figs. 3.6-3.8. As one might expect, the values and distributions of $\bar{\boldsymbol{\varepsilon}}^p$ vary with different microstructures. Relatively large $\bar{\boldsymbol{\varepsilon}}^p$ is observed where the end of the cylinder contacts the half space. At the x-y plane section cut representing near two-dimensional loading conditions (i.e., line contact), the value of $\bar{\boldsymbol{\varepsilon}}^p$ at the center of contact is much lower than that at the edges of contact where microslip occurs due to fretting.

This is also the location where fatigue cracks are usually observed to form in experiments.

The contours of $\bar{\boldsymbol{\varepsilon}}^p$ for four microstructures of Group I simulations with different textures are shown in Fig. 3.6. The maximum pointwise $\bar{\boldsymbol{\varepsilon}}^p$ at the x-y plane (midsection plane), $\bar{\varepsilon}^p_{\max}\big|_{x-y}$, are given in Table 3.2 for all simulations. The overall features and nature of the effective plastic strain distributions for the various textures are similar. The basal and random textures have much higher $\bar{\varepsilon}^p_{\max}\big|_{x-y}$ than transverse and basal/transverse textures. Hence, the basal and random textures are softer textures, at least for the particular relative orientation of the fretting loading and texture axes considered here. The basal texture considered in this study is characterized by a "ring" shape in the pole figure as shown in Fig. 2.2. The angles between the c-axis of grains and normal direction range from 15 to 30 degrees. Consequently, several basal and prismatic slip systems have relatively high Schmid factors under these fretting loading conditions, resulting in low yield strength.

As shown in Fig. 3.7, the overall distributions of $\bar{\boldsymbol{\varepsilon}}^p$ for Ti-6Al-4V of Group II simulations with several average grain sizes are similar. The values of $\bar{\boldsymbol{\varepsilon}}^p$ as shown in Table 2 increase with increasing average grain size. This is in part due to the reduction of threshold stress according to Eq. (2.3). It is also due to the strength of the gradient of stress and strain at the notch relative to grain size as function of grain size, for fixed contact dimensions. Therefore, fretting fatigue resistance decreases as average grain size increases.

No clear trend can be obtained between $\bar{\varepsilon}^p_{\max}\big|_{x-y}$ and d_c/d (Group III simulations of Table 3.1). Therefore, the sensitivity of the deformation behavior of Ti-6Al-4V to grain size distribution under these particular fretting loading is relatively small in comparison effects of other microstructure attributes considered. It likely suggests that many more

realizations of grain size distributions and crystal orientations need to be considered to determine the extremal values of $\bar{\varepsilon}^p_{\max}\big|_{x-y}$. The case of d_c/d = 0.3 is shown in Fig. 3.8. Here, the grain size ranges from 0.3d to 3d for d_c/d = 0.3. This case can be compared to Fig. 3.6(a), which is at the same conditions except for d_c/d = 1.

Table 3.2 $\bar{\varepsilon}^p_{\max}\big|_{x-y}$ and maximum F_{PS} for different microstructures.

Microstructure attributes		$\bar{\varepsilon}^p_{\max}\big\|_{x-y}$	Max. F_{PS}
Texture (Group I)	Random	3.4×10^{-3}	2.2×10^{-5}
	Basal/ Transverse	2.3×10^{-3}	1.1×10^{-5}
	Transverse	2.7×10^{-3}	1.3×10^{-5}
	Basal	4.0×10^{-3}	3.2×10^{-5}
Average Grain size, d (Group II)	25 μm	3.6×10^{-3}	2.6×10^{-5}
	30 μm	4.0×10^{-3}	3.2×10^{-5}
	35 μm	4.3×10^{-3}	4.0×10^{-5}
Grain size distribution d_c/d (Group III)	0.3	4.6×10^{-3}	2.6×10^{-5}
	0.5	3.9×10^{-3}	2.0×10^{-5}
	0.8	4.5×10^{-3}	2.7×10^{-5}
	1.0	4.0×10^{-3}	3.2×10^{-5}

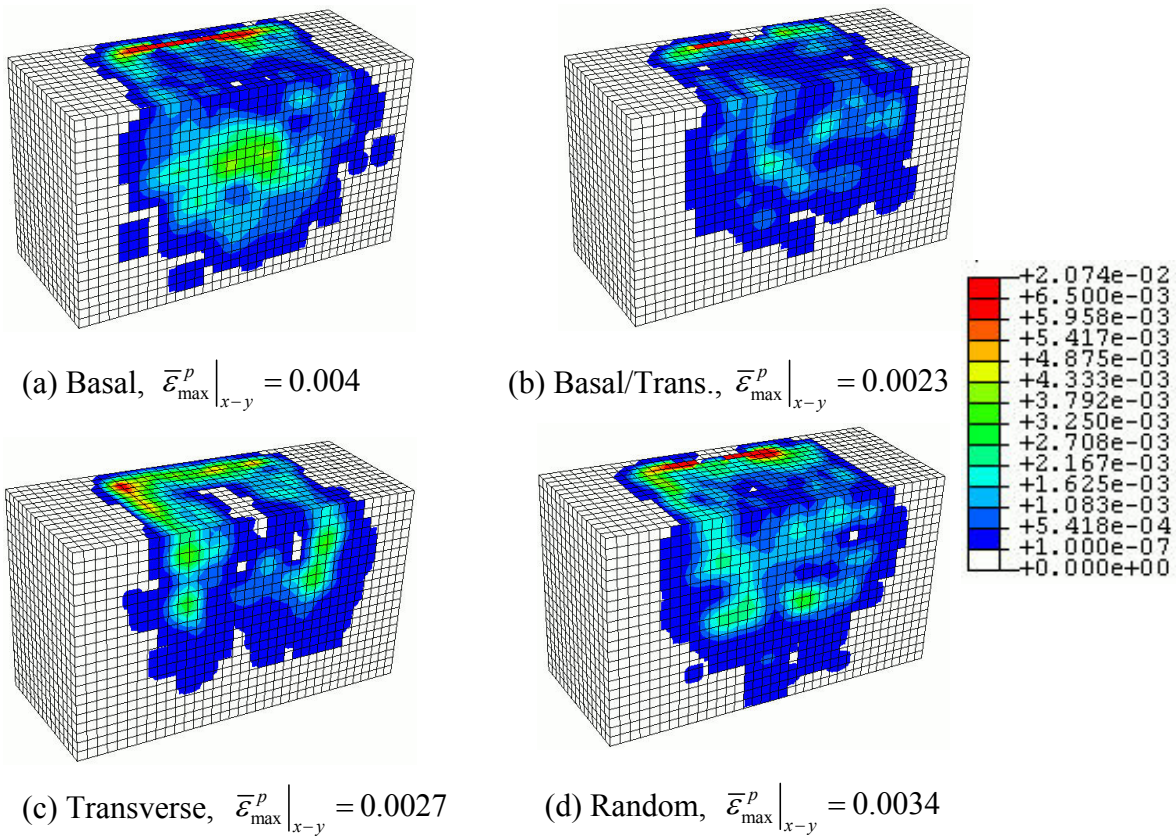

(a) Basal, $\bar{\varepsilon}^{p}_{\max}\big|_{x-y} = 0.004$ (b) Basal/Trans., $\bar{\varepsilon}^{p}_{\max}\big|_{x-y} = 0.0023$

(c) Transverse, $\bar{\varepsilon}^{p}_{\max}\big|_{x-y} = 0.0027$ (d) Random, $\bar{\varepsilon}^{p}_{\max}\big|_{x-y} = 0.0034$

Figure 3.6. Distribution of effective plastic strain after three tangential loading cycles for Ti-6Al-4V with various textures with d = 30 μm and d_c/d = 1 (Group I).

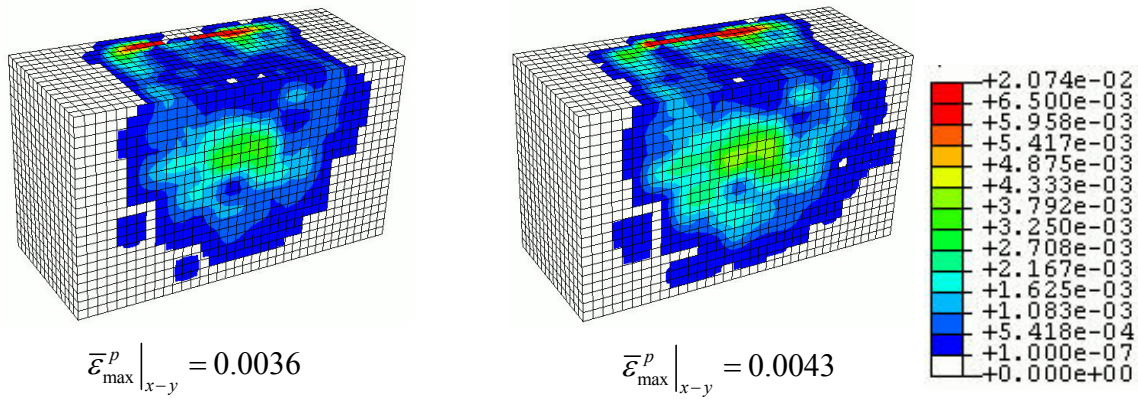

$\bar{\varepsilon}^{p}_{\max}\big|_{x-y} = 0.0036$ $\bar{\varepsilon}^{p}_{\max}\big|_{x-y} = 0.0043$

(a) d = 25 μm (b) d = 35 μm

Figure 3.7. Distribution of effective plastic strain after three tangential loading cycles for Ti-6Al-4V with basal texture with grain size of (a) 25 μm and (b) 35 μm (Group II).

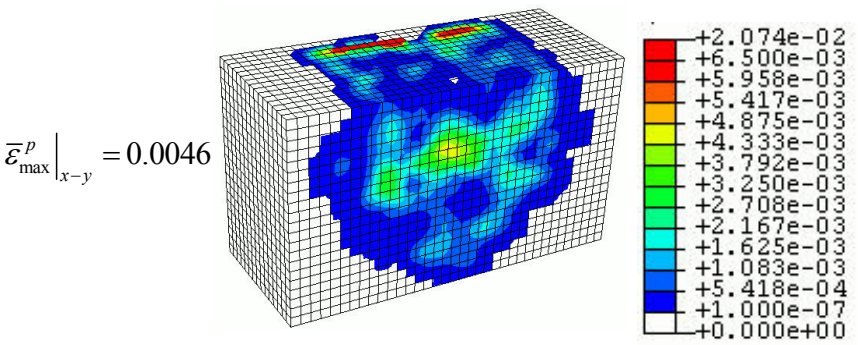

Figure 3.8. Distribution of effective plastic strain after three tangential loading cycles for Ti-6Al-4V with basal texture, $d = 30$ μm, and $d_c/d = 0.3$ (Group III).

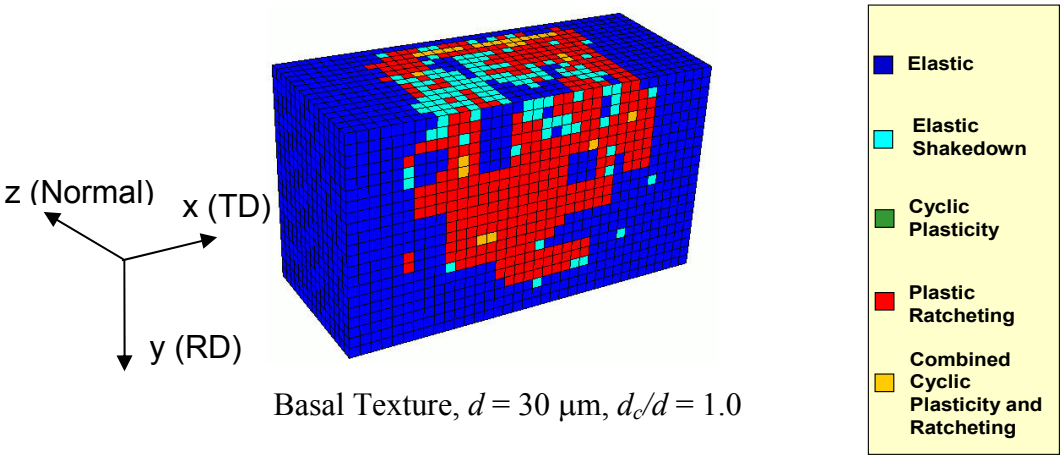

Basal Texture, $d = 30$ μm, $d_c/d = 1.0$

Figure 3.9. Distribution of effective plastic strain of Microstructure IV after three tangential loading cycles (midsection view).

For fretting simulations, it is desired to know how strain accumulates in the contact region. Strain behaviors are decomposed into five regimes: elastic, elastic shakedown, reversed cyclic plasticity, combined cyclic plasticity and ratcheting, and plastic ratcheting, as defined in Chapter 2. For all simulations, strain behaviors are calculated over the 3rd tangential loading cycle. The distribution of plastic strain behaviors for the basal textured Ti-6Al-4V with $d = 30$ μm and $d_c/d = 1.0$ (Microstructure IV) is shown in Fig. 3.9. Various colors are used to represent the different plastic strain

behaviors. Ratcheting is the dominant plastic strain behavior in the subsurface region. On the contact surface, the ratcheting elements are generally found near the edges of contact. The majority of elements at the center of surface reach elastic shakedown. Very few elements are found to have combined cyclic plasticity and ratcheting behavior and most of these are located at the edge of contact. No element undergoes just reversed cyclic plasticity.

Table 3.3. Plastic strain behavior for different microstructures over the 3rd tangential loading cycle.

Microstructure attributes		N_p (% of elements)	Elastic shakedown (% of N_p)	Reversed cyclic plasticity (% of N_p)	Combined cyclic and ratcheting (% of N_p)	Ratcheting (% of N_p)
Texture (Group I)	Random	6131 (27%)	22.2	0	6.2	71.6
	Basal/ Transverse	4793 (21.1%)	30.3	0	2.3	67.4
	Transverse	4470 (19.7%)	28.4	0	3	68.6
	Basal	7176 (31.6%)	18	0	7.5	74.4
Average Grain size, *d* (Group II)	25 μm	6381 (28.1%)	18.9	0	6.4	74.7
	30 μm	7176 (31.6%)	18	0	7.5	74.4
	35 μm	7883 (34.8%)	17.8	0	8.5	73.7
Grain size distribution d_c/d (Group III)	0.3	7697 (33.9%)	16.6	0	6.9	76.5
	0.5	7484 (33%)	18.8	0	7.4	73.8
	0.8	7247 (32%)	18.8	0	8.1	73.1
	1.0	7176 (31.6%)	18	0	7.5	74.4

Table 3.3 summarizes the plastic strain behavior of Ti-6Al-4V for three groups of microstructures considered in this study (Table 3.1). In Table 3.3, N_p denotes the number of elements that plastically deform. The number of plastically deformed elements for softer basal and random textures is significantly higher than that for harder basal/transverse and transverse textures. Hence, assuming fatigue crack formation is associated with effective plastic strain, the transverse and basal/transverse textures have

higher resistance to fretting fatigue since there are fewer numbers of plastically deformed elements and lower values of maximum effective plastic strain. N_p increases with increasing grain size. At the same time, the percentage of elements undergo plastic ratcheting marginally decreases. There is no clear trend on the effect of grain size distribution on the plastic deformation behavior. For all microstructures considered under this fretting loading, over 2/3 of the plastically deformed elements are dominated by ratcheting, consistent with the previous results (Goh et al., 2001, 2003; Mayeur et al., 2007).

The magnitude and distribution of plasticity among grains plays a key role in fatigue crack formation and early growth (McDowell, 2007). A direct measure of cyclic microplasticity is the maximum cyclic plastic shear strain $\Delta\gamma^{p}_{\max}/2$ over all possible shear strain planes for a given loading condition in individual grains (Bennett and McDowell, 2003). Same as that described in Chapter 2, a volume averaged $\Delta\gamma^{p^*}_{\max}/2$ is chosen to quantify the driving force for fatigue crack nucleation. The average grain size is considered as the scale of the averaging volume.

The distributions of $\Delta\gamma^{p^*}_{\max}/2$ computed over the 3rd cycle of the tangential loading history for microstructures of Group I simulations (texture), Group II simulations (average grain size) and Group III simulations (grain size distribution) are shown in Fig. 3.10 (a), (b) and (c) respectively. In Fig. 3.10(a), it is noted that for basal and random textures, a larger number of grains have high $\Delta\gamma^{p^*}_{\max}/2$. It is clear that basal and random textured materials are "soft" compared to the transverse and basal/transverse textured materials, which is consistent with the results in Tables 3.2 and 3.3. With increasing average grain sizes shown in Fig. 3.10(b), both the maximum $\Delta\gamma^{p^*}_{\max}/2$ and number of grains with higher $\Delta\gamma^{p^*}_{\max}/2$ increase, indicating a reduction of fatigue resistance with increasing grain size. In Fig. 3.10(c), basal textured materials with different d_c/d show

similar frequency distributions of $\Delta\gamma^{p^*}_{\max}/2$, and there is no clear trend among these cases. Therefore, compared to texture and average grain size, the grain size distribution has weaker influence on the plastic deformation behavior of Ti-6Al-4V. Texture has substantially the strongest influence.

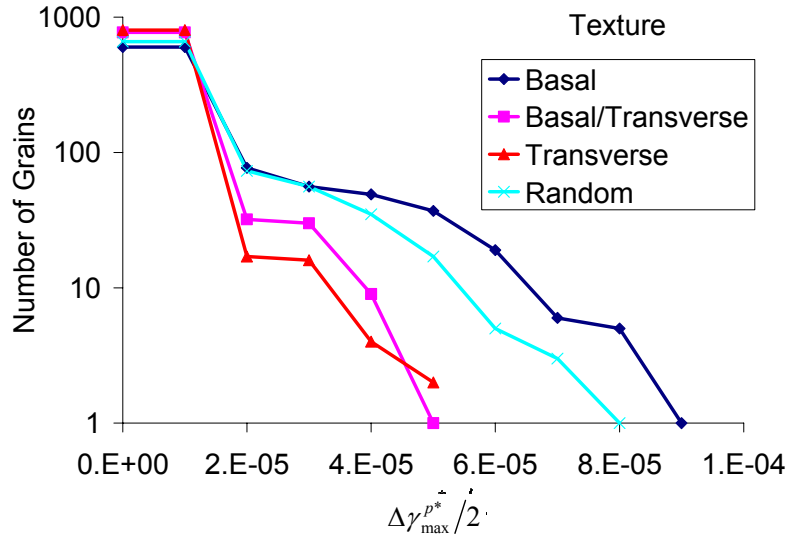

(a) Texture (Group I)

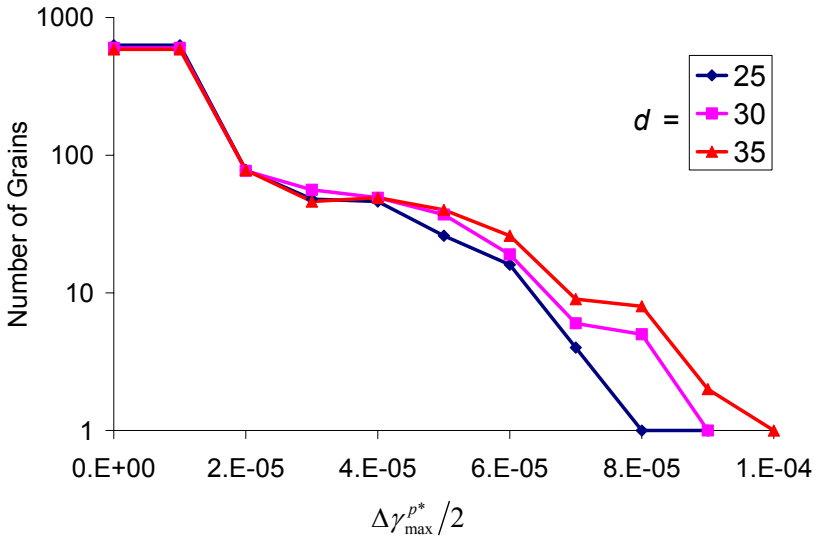

(b) Average grain size (Group II)

Figure. 3.10. Influence of microstructure attributes on the distribution of $\Delta\gamma^{p^*}_{\max}/2$ showing the relative effects of (a) texture, (b) average grain size, and (c) grain size distribution.

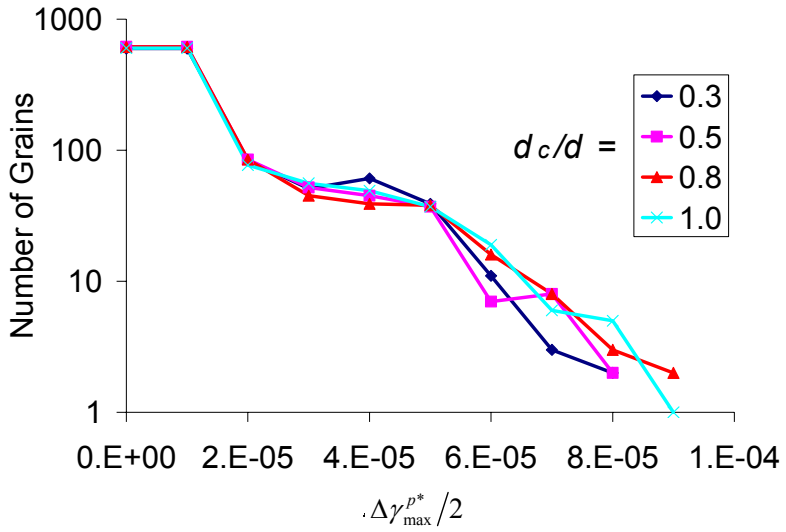

(c) Grain size distribution (Group III)

Figure. 3.10. Influence of microstructure attributes on the distribution of $\Delta\gamma^{p*}_{max}/2$ showing the relative effects of (a) texture, (b) average grain size, and (c) grain size distribution (cont.).

As in Chapter 2, P_{FS} is used to quantify the driving force for crack formation in this study. Figure 3.11 shows the distribution of P_{FS} for the basal textured Ti-6Al-4V with d = 30 μm and d_c/d = 1.0. It is found that in the subsurface region, the grains with high effective plastic strain have higher value of P_{FS}. At the surface, grains with larger P_{FS} are found at the edge of contact where fretting fatigue cracks usually nucleate. The possibility of crack nucleation at the center of contact is extremely low since P_{FS} is close to zero. The maximum P_{FS} on the contact surface is found at the edge of contact near the end of the cylinder, as indicated by arrow in Fig. 3.11.

Figure 3.12 (a), (b) and (c) respectively display the variations of distribution of P_{FS} for microstructures of Groups I (texture), II (average grain size) and III (grain size distribution) simulations, as summarized in Table 3.1. The maximum P_{FS} over the entire crystal plasticity region are given in Table 3.2 for all simulations. In Table 3.2, transverse

and basal/transverse textures have lower maximum P_{FS} and therefore have greater fretting fatigue crack formation resistance than basal and random texture. Same tendency can be observed from Fig. 3.12(a). The fatigue resistance increases with reduction of the average grain size as shown in Fig. 3.12(b). An approximate linear relation between average grain size and maximum P_{FS} is obtained in Table 3.2. Variation of the maximum P_{FS} with grain size distribution parameter d_c/d is relatively low. From Fig. 3.12(c) and Table 3.2, no clear correlation can be found between d_c/d and distribution and maximum P_{FS}. Therefore, it is concluded that comparing with the effects of texture and average grain size, the effect of d_c/d of on the fretting fatigue behavior of Ti-6Al-4V is relatively weak for the considered fretting loading condition. It is certainly possible that grain size distribution will have more significance as the normal force is decreased and the tangential force amplitude is increased, resulting in a majority of the plastically deforming elements being located at the edge of contact.

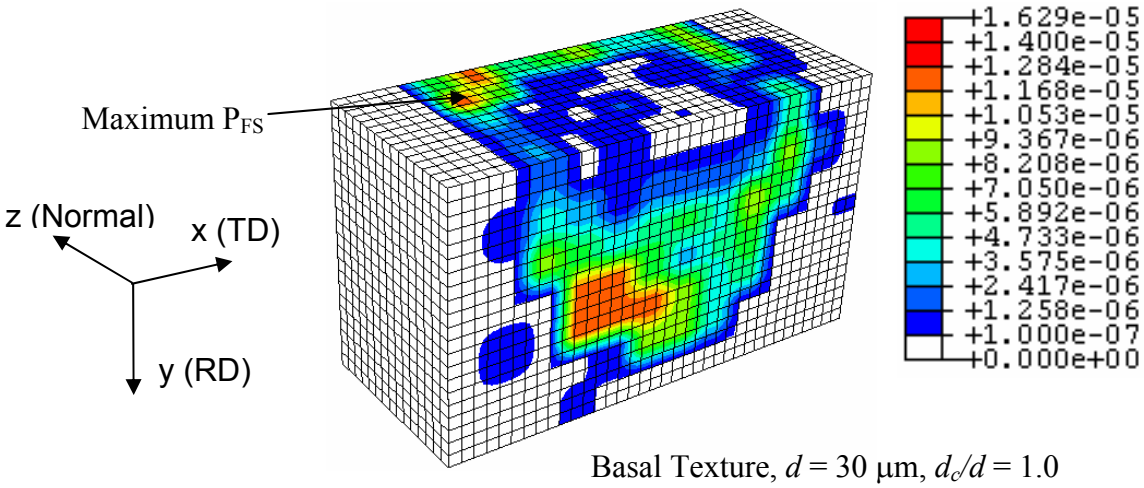

Figure 3.11. Distribution of P_{FS} (cross section view).

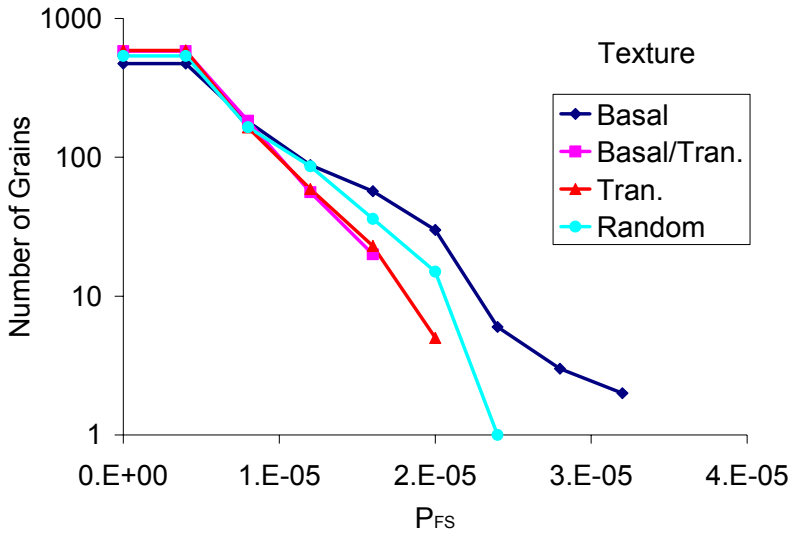

(a) Texture (Group I)

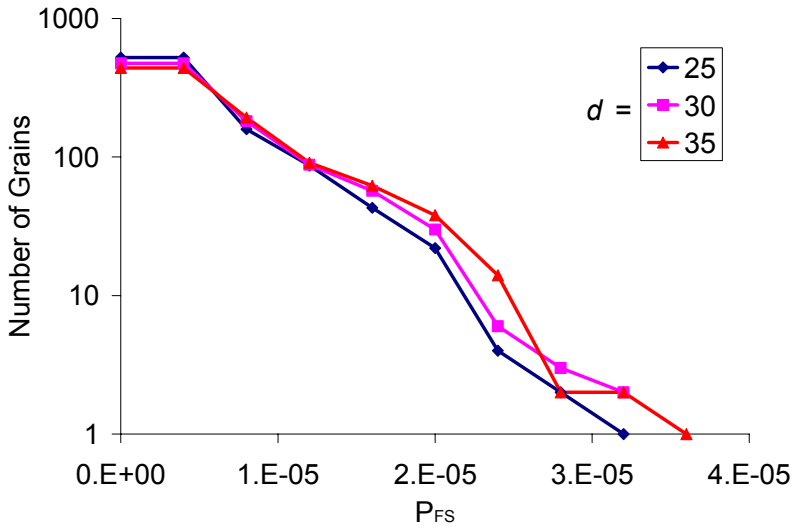

(b) Average grain size (Group II)

Figure 3.12. Variation of distribution of P_{FS} with respect to variation of microstructure attributes showing the relative effects of (a) texture, (b) average grain size, and (c) grain size distribution.

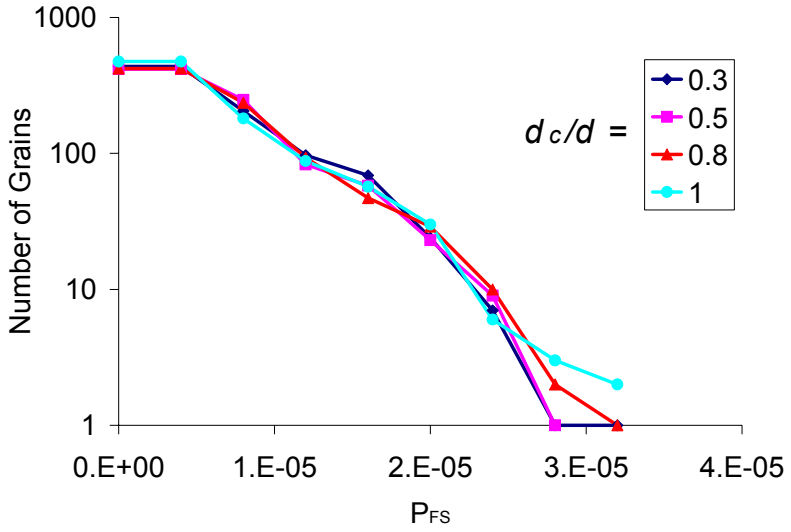

(c) Grain size distribution (Group III)

Figure 3.12. Variation of distribution of P_{FS} with respect to variation of microstructure attributes showing the relative effects of (a) texture, (b) average grain size, and (c) grain size distribution (cont.).

Table 3.4. Combinations of normal and tangential forces.

	$P = 0.3P_y$	$P = 0.5P_y$	$P = 0.75P_y$	$P = 1.0P_y$
$Q = 0.03P_y$	O			
$Q = 0.1P_y$	O	O	O	O
$Q = 0.15P_y$	O			O
$Q = 0.2P_y$				O

Group A

Group B

Group C

To study the effects of normal and tangential loads on the fretting fatigue of Ti-6Al-4V, various combinations of normal and tangential forces are applied on

Microstructure IV. These combinations are divided into three groups: A, B and C, as summarized in Table 3.4. To explore the influence of tangential force, same normal force $P = 0.3P_y$ and $P = P_y$ are used in Groups A and C, respectively. Groups A and C are respectively shown with red and green ovals. Four loading combinations, as shown by the blue oval, with normal force ranging from $0.3P_y$ to $1.0P_y$ and tangential force $Q = 0.1P_y$ are used to explore the effect of the normal load on the fretting fatigue behavior.

Figure 3.13 shows the distribution of the effective plastic strain $\bar{\varepsilon}^p$ of simulations of Group B after three tangential loading cycles. All contours are shown in section view, as illustrated in Fig. 3.2(d). The maximum $\bar{\varepsilon}^p$ at the x-y plane, $\bar{\varepsilon}^p_{\max}\big|_{x-y}$, are given in Table 3.5 for all simulations. For all four cases, it is noted that the value of $\bar{\varepsilon}^p$ at the center of contact is much lower than that at the edges of contact where microslip occurs due to fretting. Strong contact edge effects are observed where the end of the cylinder contacts the half space. It is shown that both the size of the plastically deformed region and $\bar{\varepsilon}^p_{\max}\big|_{x-y}$ significantly increase with increasing normal force P. As shown in Fig. 3.13(a), for $P = 0.3P_y$, plastic deformation mainly occurs at the edge of the contact. As P increases to $0.5P_y$, plastic strain begins to accumulate at the subsurface region. Substantial plastic deformation at the subsurface region is observed in Fig. 3.13(c) for $P = 0.75P_y$. It is noted that $\bar{\varepsilon}^p_{\max}\big|_{x-y}$ at surface is higher than that at subsurface for $P = 0.75P_y$. In case of $P = P_y$, subsurface region undergo significant plastic deformation. Value of $\bar{\varepsilon}^p_{\max}\big|_{x-y}$ at the subsurface region is higher than that at the edge of contact as shown in Fig. 3.13(d), suggesting the potential crack formation at this region.

Figures 3.14 and 3.15 show the contours of $\bar{\varepsilon}^p$ of simulations of Groups A and C, respectively. It is shown that the overall distributions of $\bar{\varepsilon}^p$ for various tangential forces Q are close. A significant increase of $\bar{\varepsilon}^p$ at the edge of contact is observed in Fig. 3.14 for $P = 0.3P_y$. These cases can be compared to Fig. 3.13(a) which is at the same normal

force with Q = 0.1P_y. In Group A, $\bar{\varepsilon}^p_{\max}\big|_{x-y}$ increases by about twenty times when Q increases from 0.03P_y to 0.15P_y. A much larger increase of $\bar{\varepsilon}^p_{\max}\big|_{x-y}$ is observed when Q increases from 0.1P_y to 0.15P_y. For P = P_y, the size of plastically deformed region slightly increases with increasing Q. The value of $\bar{\varepsilon}^p_{\max}\big|_{x-y}$ increases moderately, as shown in Table 3.5. Tangential force is observed to have larger influence on the fretting behavior when normal force is significantly lower than P_y.

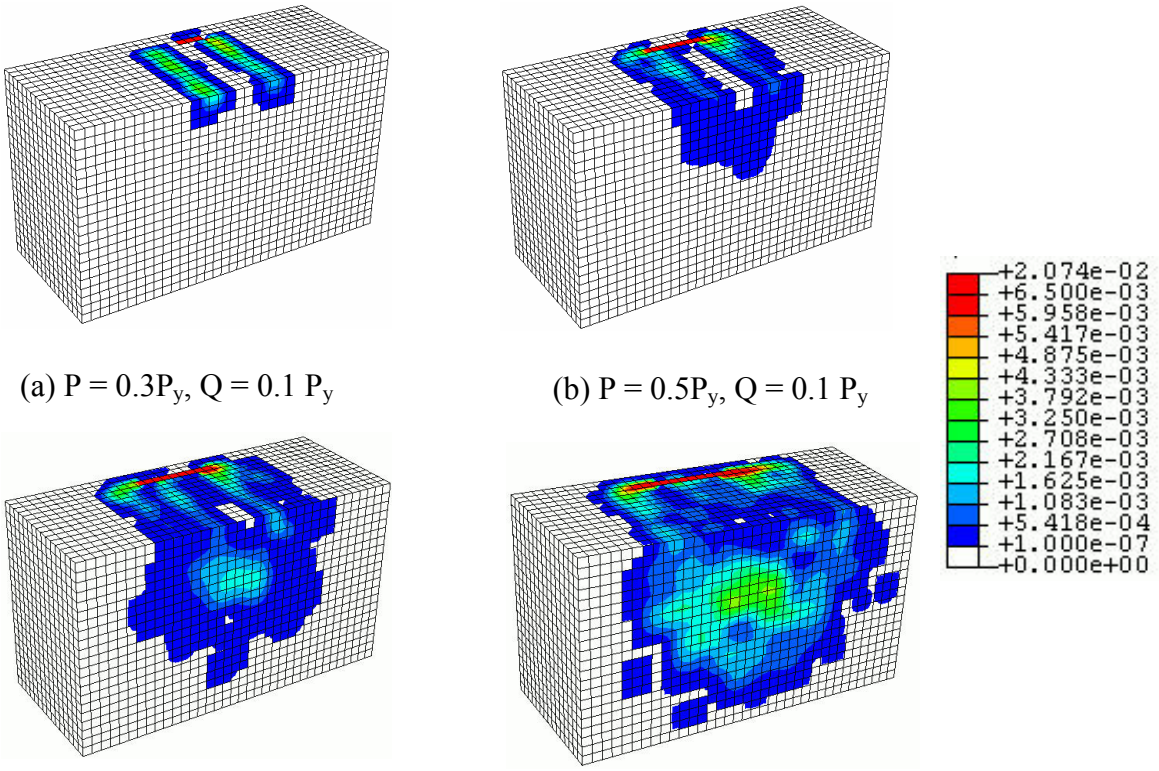

(a) P = 0.3P_y, Q = 0.1 P_y

(b) P = 0.5P_y, Q = 0.1 P_y

(c) P = 0.75P_y, Q = 0.1 P_y

(d) P = P_y, Q = 0.1 P_y

Figure 3.13. Distribution of $\bar{\boldsymbol{\varepsilon}}^p$ after three tangential loading cycles for Q = 0.1P_y (Group B).

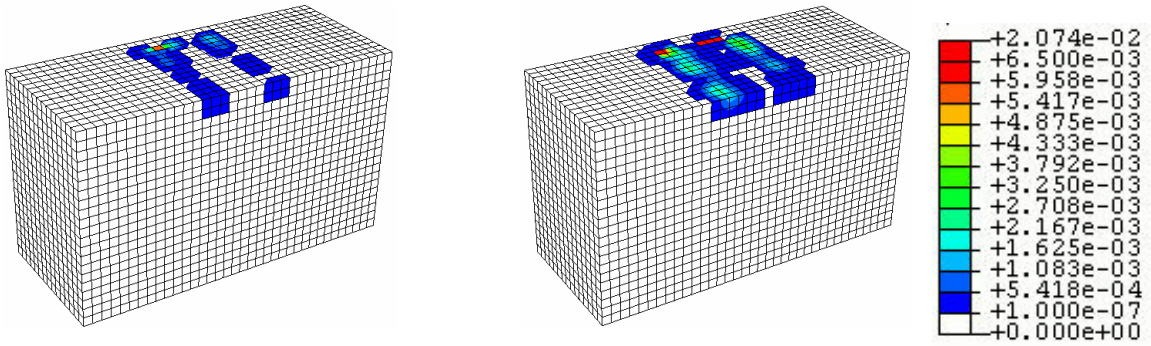

(a) $P = 0.3P_y$, $Q = 0.03P_y$ (b) $P = 0.3P_y$, $Q = 0.15P_y$

Figure 3.14. Distribution of $\bar{\varepsilon}^p$ after three tangential loading cycles for $P = 0.3P_y$ (Group A).

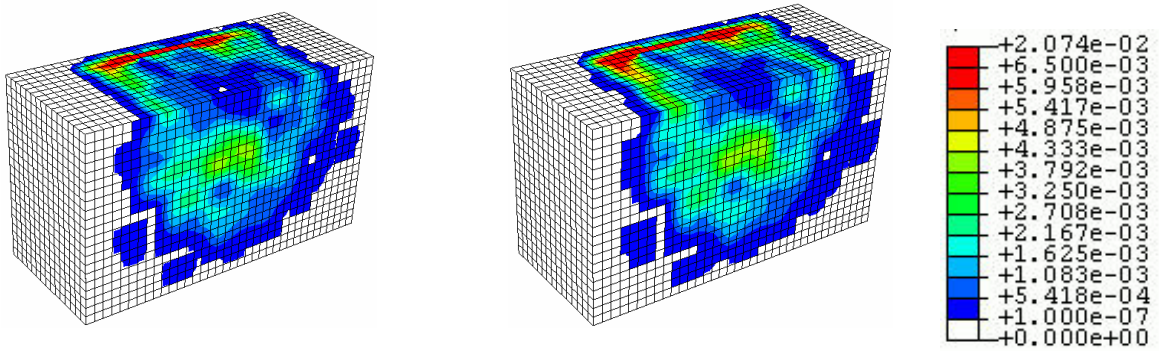

(a) $P = P_y$, $Q = 0.15P_y$ (b) $P = P_y$, $Q = 0.2P_y$

Figure 3.15. Distribution of $\bar{\varepsilon}^p$ after three tangential loading cycles for $P = P_y$ (Group C).

The plastic strain behaviors of simulations of Groups A, B and C are summarized in Table 3.5. It is shown that the number of elements undergoing plastic deformation significantly increases with increasing normal load P in Group B. When P is smaller than $0.5P_y$, only a few surface elements plastically deformed. A large percentage of elements undergo plastic deformation at $P = P_y$. This observation is consistent with the distributions of the effective plastic strain shown in Fig. 3.13. The plastic deformation behaviors change substantially with normal force. Ratcheting plasticity is the dominant plastic deformation mechanism when $P = 1.0P_y$. Elastic shakedown becomes increasingly

important with decreasing normal load. For a normal load $P = 0.3P_y$, elastic shakedown is equally important as the ratcheting plasticity.

The number of elements undergoing plastic deformation increases with increasing Q for Groups A and B. It is noted that the percentage of elements undergoing ratcheting plasticity among all plastically deformed elements increases with reducing Q for both Group A ($P = 0.3P_y$) and Group B ($P = 1.0P_y$). The percentages of elements undergoing cyclic plasticity and combined cyclic and ratcheting plasticity are negligible for all loading cases.

Table 3.5. Summary of plastic strain behavior for different combinations of normal and tangential forces.

	Load	$\bar{\varepsilon}^p_{\max}\big\|_{x-y}$	N_p (% of total elements)	Elastic shakedown (% of N_p)	Cyclic plasticity (% of N_p)	Combined cyclic and ratcheting (% of N_p)	Ratcheting (% of N_p)
Group A	$P = 0.3P_y$ $Q = 0.03P_y$	1.3×10^{-4}	90 (0.4%)	45.6	0	0	54.4
	$P = 0.3P_y$ $Q = 0.1P_y$	5.3×10^{-4}	135 (0.6%)	50.4	0	0	49.6
	$P = 0.3P_y$ $Q = 0.15P_y$	2.5×10^{-3}	302 (1.3%)	56	0.3	0.3	43.4
Group B	$P = 0.3P_y$ $Q = 0.1P_y$	5.3×10^{-4}	135 (0.6%)	50.4	0	0	49.6
	$P = 0.5P_y$ $Q = 0.1P_y$	1.1×10^{-3}	1049 (4.6%)	39.1	0	0	60.9
	$P = 0.75P_y$ $Q = 0.1P_y$	2.1×10^{-3}	3359 (14.8%)	24.5	0	0	75.5
	$P = P_y$ $Q = 0.1\ P_y$	4.9×10^{-3}	7176 (31.6%)	18	0	0	81.9
Group C	$P = P_y$ $Q = 0.1\ P_y$	4.9×10^{-3}	7176 (31.6%)	18	0	0	81.9
	$P = P_y$ $Q = 0.15\ P_y$	5.1×10^{-3}	7768 (34.3%)	19.4	0	0	80.6
	$P = P_y$ $Q = 0.2\ P_y$	5.7×10^{-3}	8267 (36.5%)	21	0	0.2	78.9

The distributions of the $\Delta\gamma^{p^*}_{\max}/2$ computed over the 3rd cycle of tangential loading history for simulations of Group B are shown in Fig. 3.16. The number of grains with large $\Delta\gamma^{p^*}_{\max}/2$ greatly increases with increasing normal force P. The peak value of the $\Delta\gamma^{p^*}_{\max}/2$ also significantly increase which agrees with previous results. Figure 3.17 shows that the value of $\Delta\gamma^{p^*}_{\max}/2$ increases with increasing tangential force Q when P = $0.3P_y$. The maximum $\Delta\gamma^{p^*}_{\max}/2$ increases significantly when Q increases from $0.1P_y$ to $0.15P_y$. Comparing Fig. 3.17 with Fig. 3.18, it is noted that Q has larger the influence on distribution of $\Delta\gamma^{p^*}_{\max}/2$ at lower normal force.

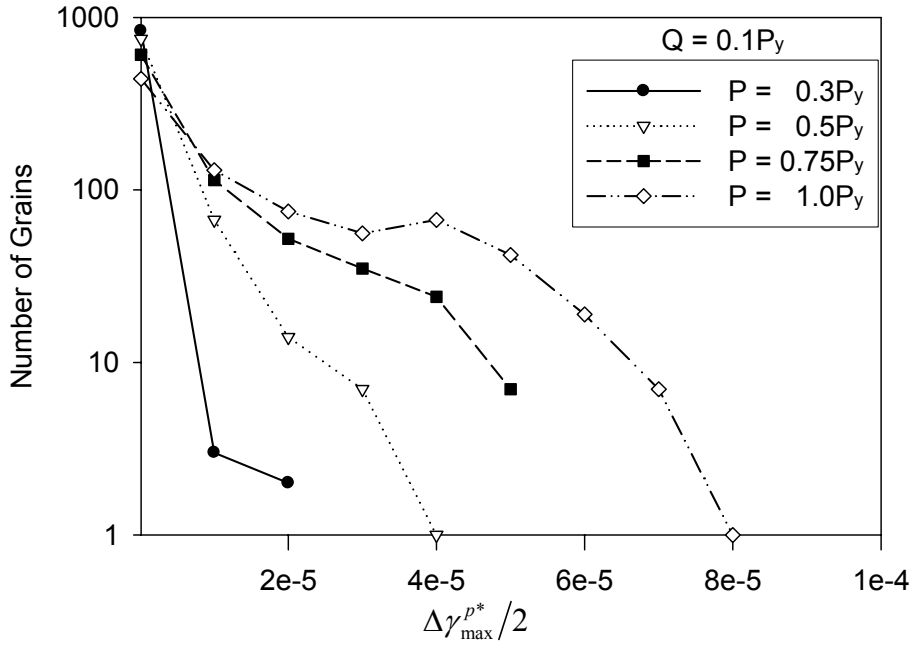

Figure 3.16. Variation of distribution of $\Delta\gamma^{p^*}_{\max}/2$ with respect to various P with Q = $0.1P_y$ (Group B).

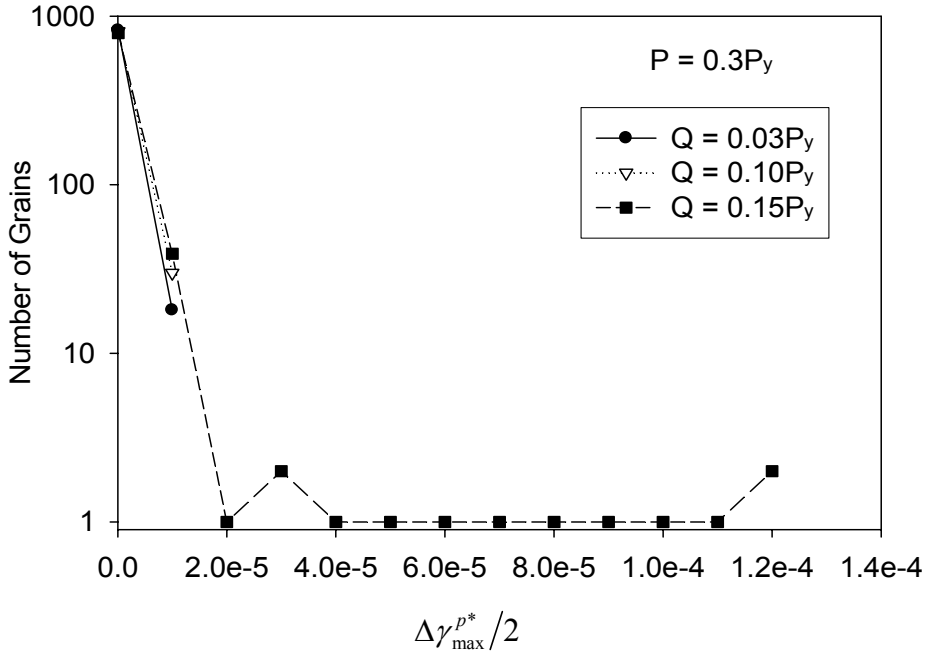

Figure 3.17. Variation of distribution of $\Delta\gamma_{\max}^{p*}/2$ with respect to various Q with P = $0.3P_y$ (Group A).

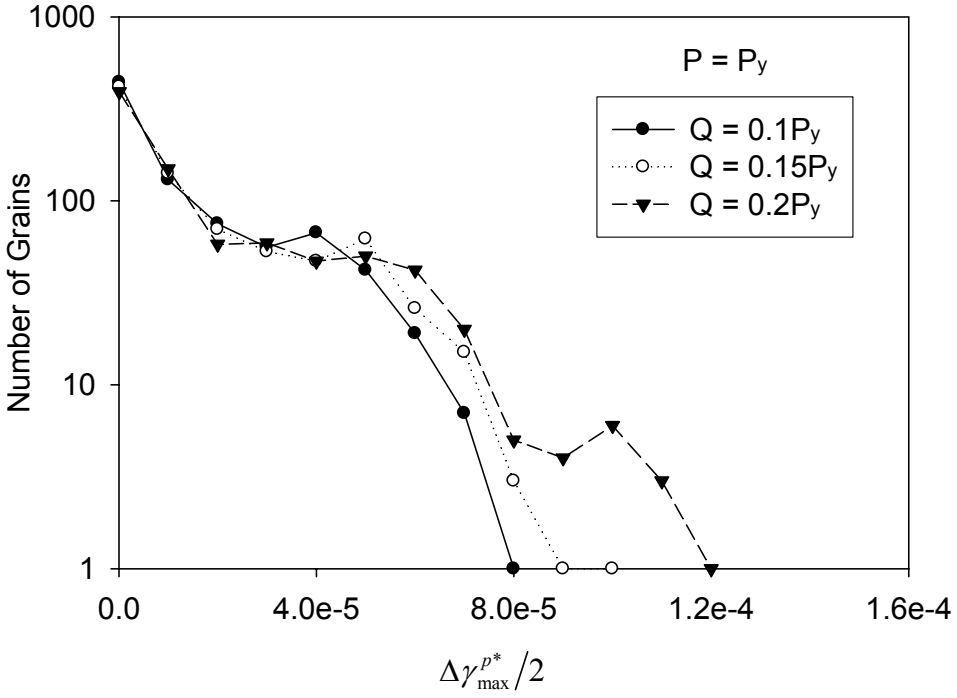

Figure 3.18. Variation of distribution of $\Delta\gamma_{\max}^{p*}/2$ with respect to various Q with P = P_y (Group C).

The FIP P_{FS} is calculated over the 3rd tangential loading cycle. The contours of P_{FS} of simulations of Groups B, A and C are shown in Figs. 3.19, 3.20 and 3.21, respectively. It is shown that the cracks will most likely form at the edge of contact where the large value of P_{FS} is found for $P = 0.3P_y$, as shown in Fig. 3.19(a). The non-zero P_{FS} is found at both edge of contact and subsurface region as P increases to $0.5P_y$. As shown in Fig. 3.19(b), the value of P_{FS} in the subsurface is lower than that at edge of contact. Therefore, it is concluded that cracks will most likely form at the edge of contact regions when the normal load is significantly lower than P_y. This result agrees with the observations that the cracks are generally found at the trialing edge in fretting experiments at relatively low normal load P (Araujo and Nowell, 2002). In the fretting experiments conducted by Cortez, et. al (1999), fatal cracks were found to propagate near the location of the trailing edge of contact when the applied normal load is around 20% of the force required to initiate yield of the tested Ti-6Al-4V. As P increases to $0.75P_y$ and P_y, the value of P_{FS} at both contact surface and subsurface region greatly increase and become close. This result suggests that the fatigue cracks may simultaneously form at the surface and subsurface regions when P is close to P_y.

Figure 3.20 shows that the overall distributions of P_{FS} are close for Groups A simulations. At the same time, value of P_{FS} significant increases with increasing Q. The same trend is observed in Fig. 3.21 for Group C simulations. Therefore, the tangential force Q significantly influences the fatigue crack formation life.

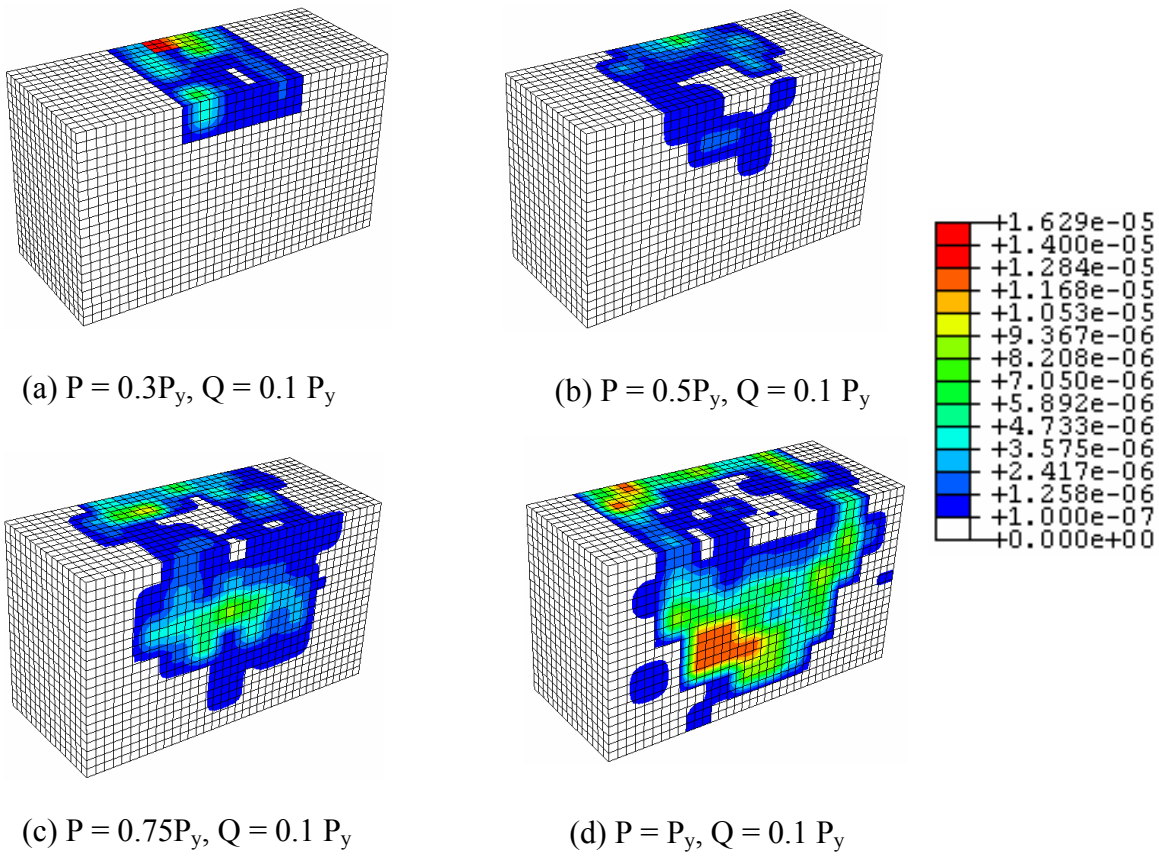

(a) $P = 0.3P_y$, $Q = 0.1\ P_y$

(b) $P = 0.5P_y$, $Q = 0.1\ P_y$

(c) $P = 0.75P_y$, $Q = 0.1\ P_y$

(d) $P = P_y$, $Q = 0.1\ P_y$

Figure 3.19. Contour of P_{FS} with respect to various P for $Q = 0.1P_y$ (Group B).

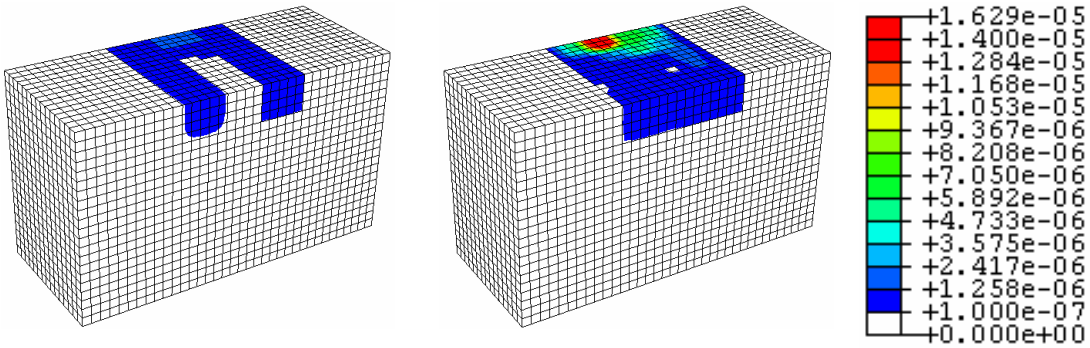

(a) $P = 0.3P_y$, $Q = 0.03P_y$

(b) $P = 0.3P_y$, $Q = 0.13P_y$

Figure 3.20. Contour of P_{FS} with respect to various Q for $P = 0.3P_y$ (Group A).

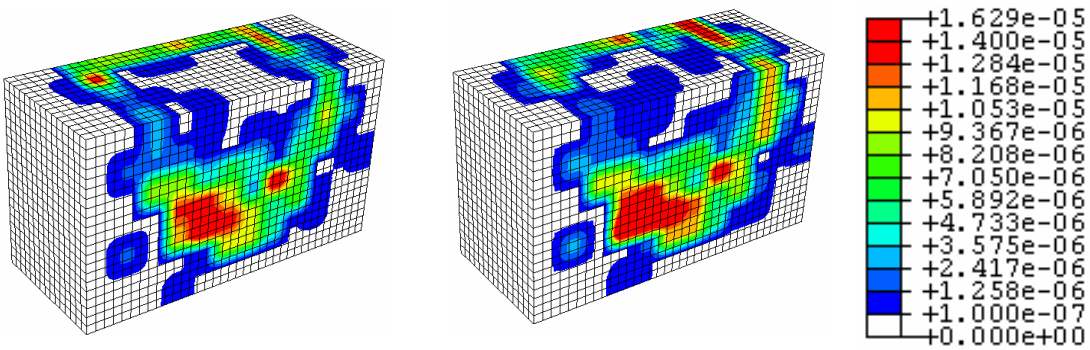

(a) $P = P_y$, $Q = 0.15P_y$ (b) $P = P_y$, $Q = 0.2P_y$

Figure 3.21. Contour of P_{FS} with respect to various Q for $P = P_y$ (Group C).

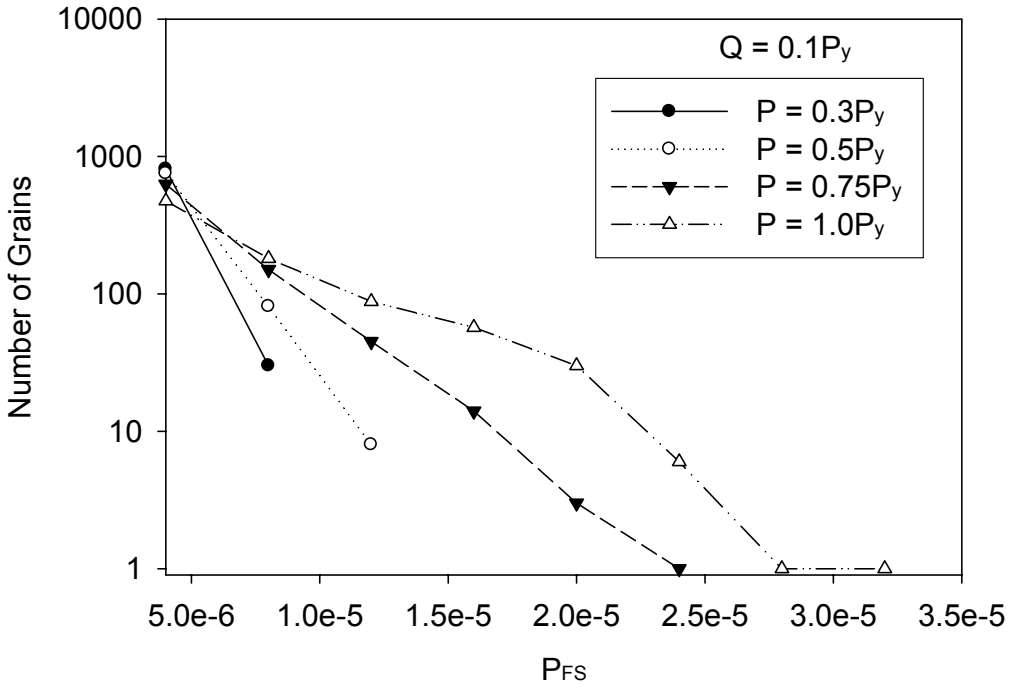

Figure 3.22. Variation of distribution of P_{FS} with respect to various P for $Q = 0.1P_y$ (Group B).

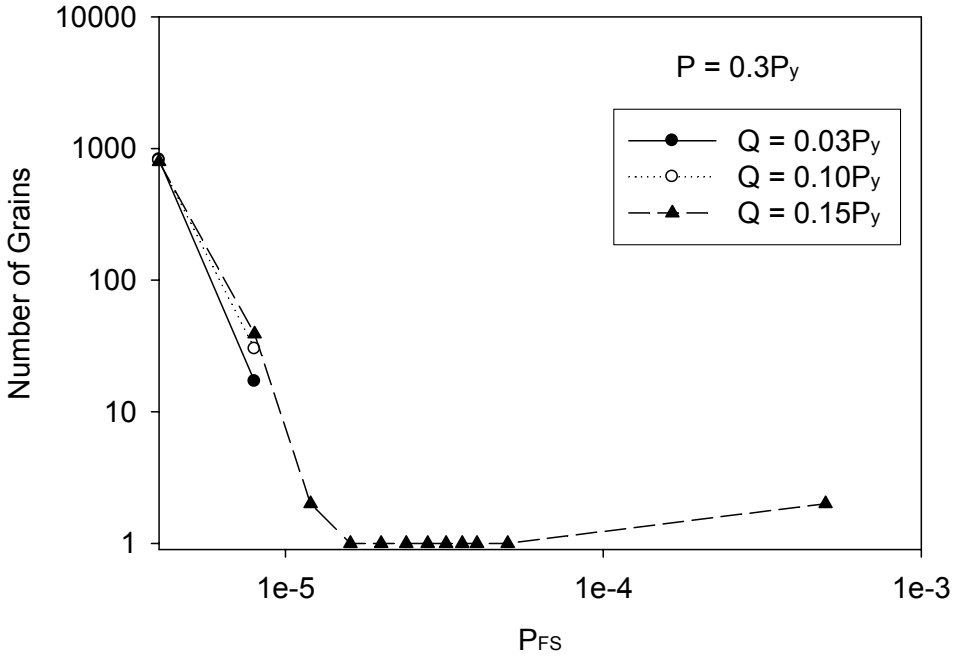

Figure 3.23. Variation of distribution of P_{FS} with respect to various Q for $P = 0.3P_y$. (Group A).

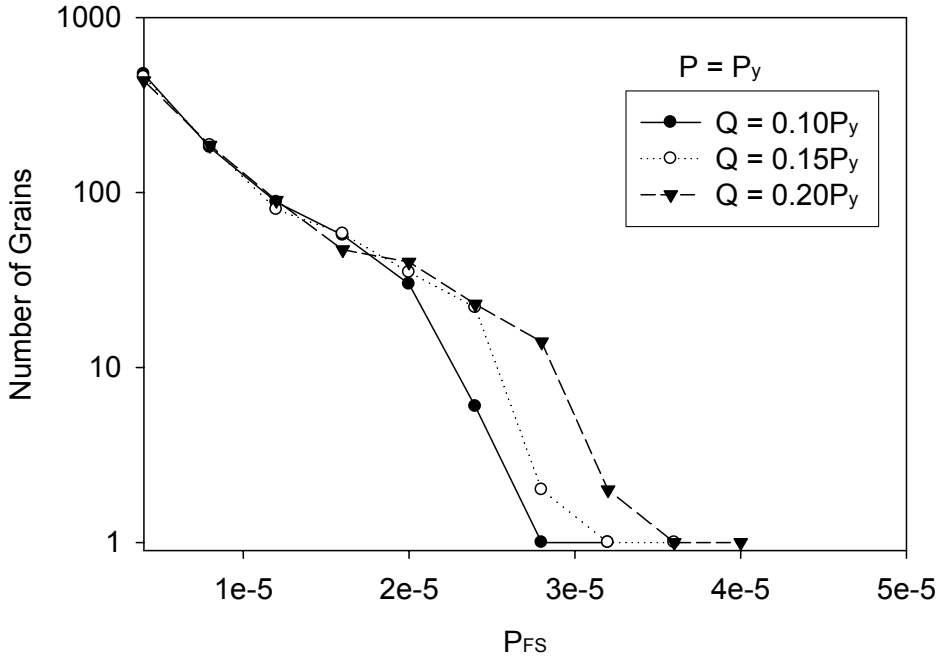

Figure 3.24. Variation of distribution of P_{FS} with respect to various Q for $P = P_y$ (Group C).

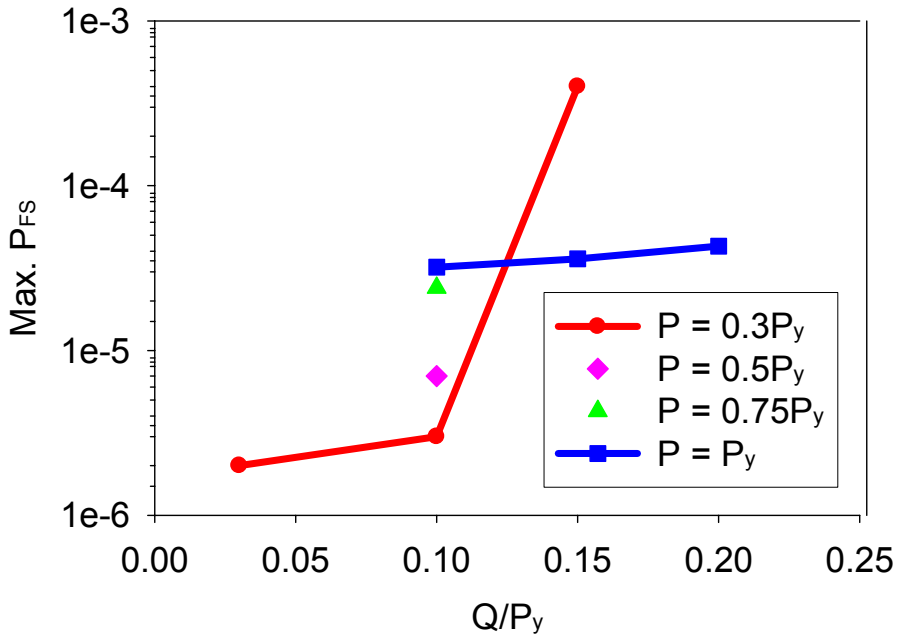

Figure 3.25. Variation of maximum P_{FS} with respect to loading parameters.

Distributions of P_{FS} of simulations of Groups B, A and C are shown in Fig. 3.22, 3.23 and 3.24, respectively. The maximum P_{FS} versus tangential force is shown in Fig. 3.25 for all simulations. Figure 3.22 shows that the number of grains with higher P_{FS} increases with increasing normal force. In Fig. 3.25, the maximum P_{FS} moderately increase with increasing normal force. These observations are consistent with the previous result that the fatigue crack formation life decrease with increasing normal force. Figures 3.23 and 3.24 show that the driving force for crack formation increases with increasing tangential force at both $P = 0.3P_y$ and $P = P_y$. In Fig. 3.25, a significant increase of P_{FS} is observed when Q increases from $0.1P_y$ to $0.15P_y$ at $P = 0.3P_y$. Tangential force Q is shown to have a much larger influence on the driving force for crack formation at low normal force. It is thus concluded that fretting fatigue of Ti-6Al-4V is dominated by the tangential force Q.

3.5 Summary

A methodology for using crystal plasticity to explore the sensitivity of fretting fatigue to microstructure and loading parameters was presented and demonstrated for duplex Ti-6Al-4V at room temperature. The crystal plasticity material model captures the crystallographic orientation dependence of the deformation behavior for both primary α phase and the lamellar colonies. A three-dimensional finite element model is constructed to simulate the fretting contact in the partial slip regime between the two bodies. A Voronoi tessellation procedure is used to render grain size distributions in the contact region.

Three microstructure attributes are considered in this sensitivity study: crystallographic texture, average grain size, and grain size distribution. The distribution and maximum value of the effective plastic strain and related fatigue indicator parameters are all shown to depend on the microstructure. Moreover, the sensitivity of several other microstructure attributes can potentially be considered using this methodology. These include volume fraction of phases, differences in the distribution of primary α and lamellar colony sizes, thicknesses of the α and β lathes, as different spatial distributions of microstructural features.

To study the effects of normal and tangential forces on the fretting fatigue behavior of Ti-6Al-4V, various combinations of normal and tangential forces are applied to each microstructure. The influence of tangential force on the fretting behavior is examined at both low and high normal force.

Based on the relatively limited range of conditions considered in this demonstration study, the effect of microstructure attributes and loading parameters on the resistance to fretting fatigue can be summarized as:

1. Smaller average grain size results in increased fretting fatigue resistance.

2. In this study, the polycrystal Ti-6Al-4V is oriented in the way that the rolling and transverse directions are parallel to the y- and x-axes, respectively, corresponding to the considered textures shown in Fig. 2.2. The normal and tangential forces are respectively applied in the y- and x- directions. For this loading condition, transverse and basal/transverse textured material exhibit greater fretting fatigue resistance, and the effect of texture on subsurface plasticity and FIP was more pronounced than that of the other two microstructure attributes.
3. The effect of grain size distribution is minimal.
4. Normal force has significant influence on the fretting fatigue of Ti-6Al-4V. The driving force for crack formation increases with increasing normal force. When the normal force is substantially lower than P_y, cracks are most likely formed at the edge of contact. With increasing normal force, the possibility of crack formation at subsurface region increase.
5. The driving force for crack formation increases with increasing tangential force at both low and high normal force. The tangential force has a larger influence on the driving force for crack formation at low normal force and dominates the fretting fatigue behavior of Ti-6Al-4V.

CHAPTER 4

CRYSTAL PLASTICITY MODELING OF CYCLIC DEFORMATION OF TI-6AL-4V

4.1 Introduction

Considerable work has been done to develop suitable constitutive relations to model the mechanical behavior of Ti-6Al-4V. In Chapter 1, it is shown that the homogenized plasticity model, such as J_2 plasticity, is unable to capture the effects of microstructure on mechanical behavior (Goh, 2002). Thus, application of those models is limited to length scales much larger than microstructure scales. Due to the lack of the microstructure sensitivity of the macroscopic models, they must be calibrated for each material with different microstructure. The calibrations usually require the experimental stress-strain responses of the materials, which are sometimes very expensive to obtain. To overcome these limitations, three-dimensional crystal plasticity constitutive relations have been developed by Mayeur and McDowell (2007) to model duplex Ti-6Al-4V. This model has been used in Chapters 2 and 3 for microstructure-sensitive cyclic and fretting simulations to explore driving forces for formation of fatigue cracks.

In this study, a crystal plasticity constitutive model of Ti-6Al-4V relevant to room temperature behavior is calibrated using the finite element method by fitting the measured stress-strain response of a heat treated Ti-6Al-4V alloy subjected to a complex cyclic loading history. The descriptions of material and constitutive model are given in Sections 4.2 and 4.3, respectively. Section 4.4 introduces three-dimensional finite element models that can precisely represent the microstructures of the test material. The fitting process and results are discussed in Section 4.5. The microstructure sensitivity of

the model is examined in Section 4.6 by comparing the experimental data with simulation results in terms of material yield strength. Discussion and summary are given in the last two sections.

4.2 Material

Depending on the thermomechanical process path and recrystallization, the microstructure of Ti-6Al-4V at room temperature can range from bimodal to fully lamellar structures. In this study, a duplex Ti-6Al-4V provided by Pratt & Whitney Company (PW1215) is considered which contains a primary HCP α phase, and secondary α plus bcc β phase arranged in a lamellar structure, as shown in Fig. 4.1. The key first order microstructural parameters of Ti-6Al-4V under consideration include average globular (primary) α size, lamellar colony size, volume fraction of the primary α phase, and mean thicknesses of the secondary α and β phases in the lamellar structure, as summarized in Table 4.1. Owing to lack of detailed stereological information on lamellar colony size, the average primary α size and lamellar colony size are assumed to be identical based on qualitative observation. The orientation and disorientation distributions are also important due to the highly anisotropic behavior of hcp crystals and lamellar colonies, which can either be reflected in a macroscopic yield function (Cazacu et al., 2006) or can be addressed explicitly using crystal plasticity. The basal plane pole figure and disorientation distribution of the tested material are shown in Figs. 4.2 and 4.3, respectively.

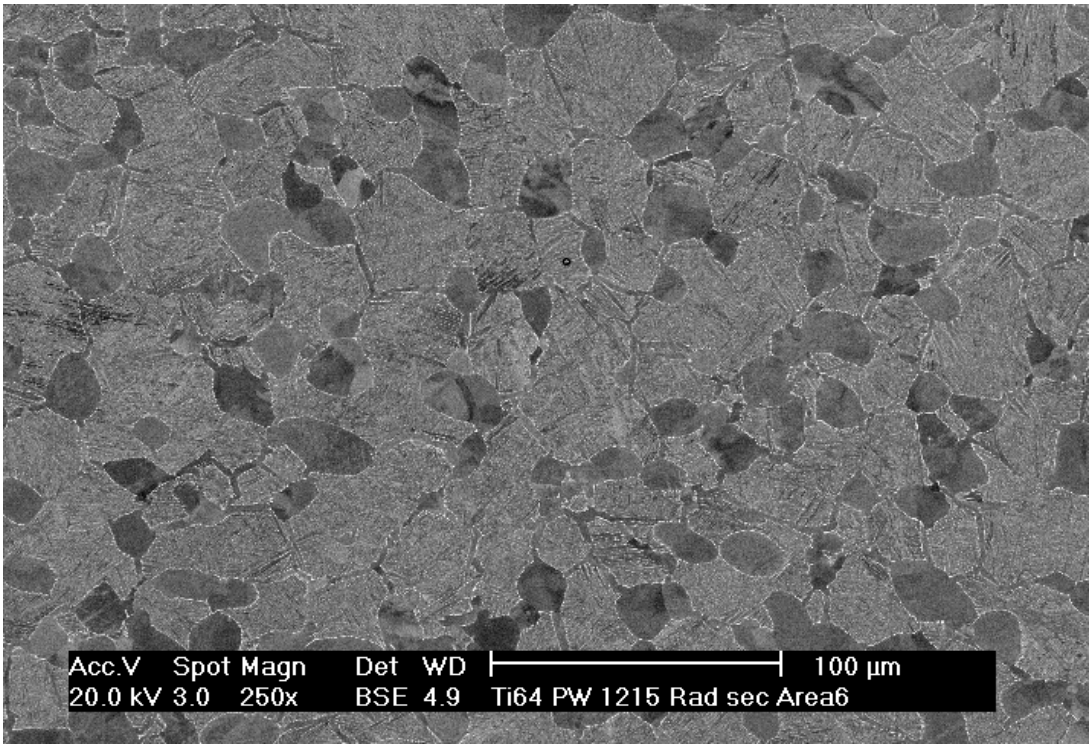

Figure 4.1. Microstructure of duplex Ti-6Al-4V (PW1215).

Table 4.1 Microstructure parameters of duplex Ti-6Al-4V (PW1215).

Globular α size (μm)	lamellar colony size (μm)	Vol. Fraction of Globular α (%)	Vol. Fraction of Total α (%)	Mean thickness of α lath (μm)	Mean thickness of β lath (μm)
7.74	7.74	24.09	91	0.30	0.03

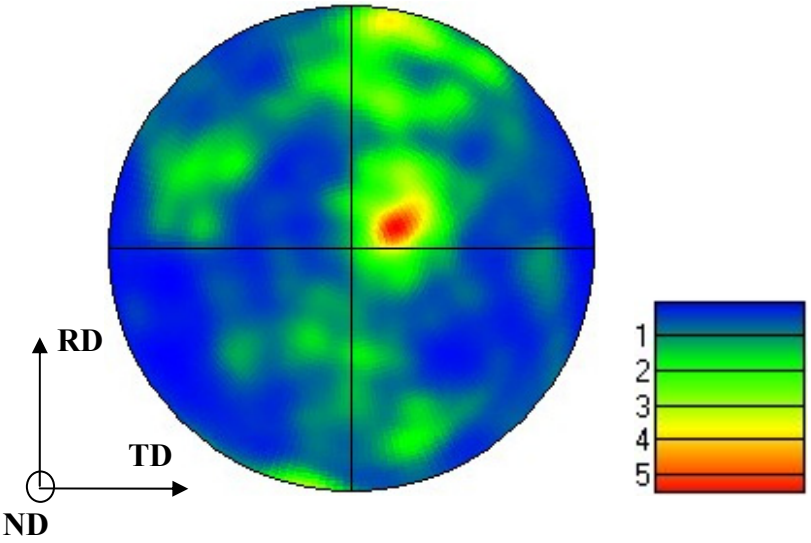

Figure 4.2. Basal plane pole figure of the orientation distribution of tested material (PW1215).

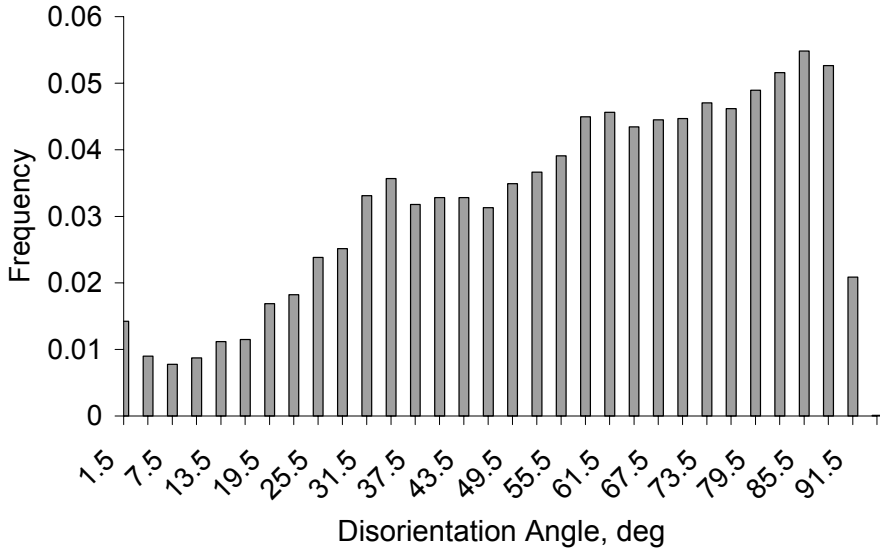

Figure 4.3. Disorientation distribution of tested material (PW1215).

4.3 Crystal Plasticity Modeling of Ti-6Al-4V

The basic concept of crystal plasticity has been given in Chapter 1. Chapter 2 described the slip system of the primary α phase and lamellar colonies.

In a rate dependent formulation, all slip systems are considered to be active for stresses above the threshold, and the shearing rates are related to the resolved shear stress and the current state of the microstructure according to

$$\dot{\gamma}^{\alpha} = \dot{\gamma}_{o} \left\langle \frac{\left|\tau^{\alpha} - \chi^{\alpha}\right| - \kappa^{\alpha}}{D^{\alpha}} \right\rangle^{m} \operatorname{sgn}\left(\tau^{\alpha} - \chi^{\alpha}\right) \tag{4.1}$$

Here, τ^{α} is the resolved shear stress, D^{α} is the drag stress, m is the inverse strain rate sensitivity exponent, χ^{α} is the kinematic harding variable or back stress on the α^{th} slip system, κ^{α} is the scalar threshold stress, and $\dot{\gamma}_{o}$ is the reference shearing rate. The Macauley bracket in Eq. (4.1) is defined by <x> = xH(x), where H(x) is the Heaviside function.

The drag stress of the primary α- phase is taken as a constant, i.e., $\dot{D}^{\alpha} = 0$. For the HCP slip systems of secondary α+β lamellar phase, the drag stresses are taken to be the same as their counterparts in the primary α phase ($D_{\alpha}^{prism} = D_{\alpha+\beta}^{prism}$, $D_{\alpha}^{basal} = D_{\alpha+\beta}^{basal}$, etc.), whereas the drag stress for the bcc systems is taken to be slightly lower than the drag stress for prismatic systems ($D_{\alpha+\beta}^{\langle 111\rangle\{110\}} = 0.9 D_{\alpha}^{prism}$) to represent the mechanically softer nature of β-Ti alloys. They are also assumed to be constant at a given temperature.

The initial value of back stress is set to be zero for all slip systems in both phases. The back stress evolves according to a modified Armstrong-Fredrick direct

hardening/dynamic recovery relation (Goh et al., 2001, 2002, 2003; Mayeur and McDowell, 2007). Asymmetry in tension and compression has been reported for α/β titanium alloys such that the yield strength is higher in compression than in tension (Mayeur and McDowell, 2007). It was suggested that the asymmetry of slip resistance for <c+a> (Williams et al., 2002) and <a> (Neeraj , et al., 2005) slip induces the tension-compression asymmetry. In addition, differences in lattice rotation in finite tension and compression deformation can induce some asymmetry, and are of course included in our model. However, we describe the additional tension-compression asymmetry that arises both from slip interaction under current loading with prior long transient planar slip accumulation of screw dislocations (bands) at room temperature and from short transient non-planar dislocation core spreading in the α phase. Accordingly, with regard to the former mechanism the evolution law of back stress is given by

$$\dot{\chi}^{\alpha} = \mathrm{B}\dot{\gamma}^{\alpha} - \mathrm{C}\psi\left(x^{\alpha}\right)\chi^{\alpha}\left|\dot{\gamma}^{\alpha}\right| = \mathrm{B}\left(\mathrm{sgn}\left(\dot{\gamma}^{\alpha}\right) - \psi\left(x^{\alpha}\right)\frac{\mathrm{C}}{\mathrm{B}}\chi^{\alpha}\right)\left|\dot{\gamma}^{\alpha}\right| \tag{4.2}$$

$$\psi(x^{\alpha}) = \begin{cases} \exp\left(\eta_1 x^{\alpha}\right) & \text{for } x^{\alpha} < 0 \\ 1.0 & \text{for } x^{\alpha} \geq 0 \end{cases} \tag{4.3}$$

$$x^{\alpha} = \mathrm{sgn}(\tau^{\alpha} - \chi^{\alpha})\, p^{\alpha}, \textit{with} \quad \dot{p}^{\alpha} = \left|\dot{\gamma}^{\alpha}\right| \mathrm{sgn}(\tau^{\alpha} - \chi^{\alpha}) \tag{4.4}$$

Here, $\eta_1 > 0$ is a constant, B and C are direct hardening and dynamic recovery coefficients, respectively. The additional term $\psi(x^{\alpha})$ is introduced in the dynamic recovery coefficient to reflect the slip band interaction mechanism described above, with x^{α} conjugate to a strain-like internal state variable p^{α} that represents a slip history-weighted sign of the slip system overstress ($\tau^{\alpha} - \chi^{\alpha}$); the sign of x^{α} depends on the sign

of the current overstress times p^{α}. Physically, we associate the asymmetry described by this term as the interaction of slip in a set of bands associated with current reversed loading with a distinct set of planar bands of screw dislocations in the interior of α grains established during prior loading. In other words, different slip bands are assumed activated in tension and compression, an effect outside the realm of the kinematics of the local crystal plasticity continuum treatment. It should be noted that p^{α} may increase or decrease during a cycle of tensile and compressive loading. A stable cyclic trajectory of p^{α} can be achieved after several loading cycles. For the primary α phase, a component of the threshold stress in Eq. (4.6), κ^{α}, is used to incorporate the non-Schmid behavior for prismatic systems and associated tension-compression asymmetry that arises from the non-planar dislocation core structure (Naka et al., 1988; Bassani et al., 2001) of dislocations on prismatic and basal slip systems, described below.

The threshold stress does not evolve, i.e., $\dot{\kappa}^{\alpha} = 0$, for pyramidal slip systems of the primary α- phase and the hard slip systems of α+β colony. One component of threshold stress for each slip system manifests scale effects, i.e.,

$$\kappa_1^{\alpha} = k_y \left(d^{\alpha} \right)^{-0.5} \tag{4.5}$$

where k_y is the Hall-Petch slope and d^{α} is the microstructural dimension relating to the free slip length of the slip system. The threshold stress for prismatic and basal slip systems of the primary α- phase is given by

$$\kappa^{\alpha}{}_{prism} = \kappa_1^{\alpha}\Big|_{prism} + A(\tau_{Pyr1} - \tau_{Pyr2}) + \kappa_s^{\alpha}\Big|_{prism} \tag{4.6}$$

$$\kappa^{\alpha}{}_{basal} = \kappa_1^{\alpha}\Big|_{basal} + \kappa_s^{\alpha}\Big|_{basal} \tag{4.7}$$

where $\kappa_1^{\alpha}\Big|_{prism}$ and $\kappa_1^{\alpha}\Big|_{basal}$ are defined by Eq. (4.5), and k_y is the same value as for pyramidal slip systems. Slip length d^{α} for prismatic and basal systems in the primary α-phase corresponds to the mean α grain size. Shear stresses τ_{pyr1} and τ_{pyr2} in Eq. (4.6) are non-Schmid resolved shear stresses on pyramidal planes that share the $<11\bar{2}0>$ burgers vector with each prismatic plane and promote recombination of the dissociated core (Mayeur and McDowell, 2007). The second term in Eq. (4.6) corresponds to the non-Schmid effect and will either increase or decrease the threshold stress, depending on the sense of the applied load with respect to the crystal orientation. This non-Schmid term is included only for prismatic systems and leads to tension/compression yield asymmetry for these systems. $\kappa_s^{\alpha}\Big|_{basal}$ and $\kappa_s^{\alpha}\Big|_{prism}$, respectively, incorporate softening of basal and prismatic slip systems associated with breakdown of short range order due to dislocation glide at low to moderate homologous temperatures (planar dislocation arrays) that promote a nearly elastic-perfectly plastic behavior of the material. These initial softening terms decay rapidly, approximated by the evolution laws

$$\dot{\kappa}_s^{\alpha}\Big|_{basal} = -\mu\,\kappa_s^{\alpha}\Big|_{basal}\left\|\dot{\gamma}\right\| \tag{4.8}$$

$$\dot{\kappa}_s^{\alpha}\Big|_{prism} = -\mu\,\kappa_s^{\alpha}\Big|_{prism}\left\|\dot{\gamma}\right\| \tag{4.9}$$

where μ is a constant and $\left\|\dot{\gamma}\right\|$ is defined as

$$\left\|\dot{\gamma}\right\| = \sum_{\alpha=1}^{N} \left|\dot{\gamma}^{\alpha}\right| \tag{4.10}$$

where N is the number of slip systems. The initial value of $\kappa_s^{\alpha}\Big|_{prism,basal}$ is given by

$$\kappa_s^{\alpha}\Big|_{prism,basal}(0) = \kappa_s(0) \tag{4.11}$$

The threshold stress for soft slip systems of the α+β colony also includes an initial softening term, i.e.,

$$\kappa^{\alpha}{}_{soft} = \kappa_1^{\alpha} + \kappa_s^{\alpha}\Big|_{soft} \tag{4.12}$$

The softening term evolves according to the evolution law

$$\dot{\kappa}_s^{\alpha}\Big|_{soft} = -\mu\,\kappa_s^{\alpha}\Big|_{soft}\left\|\dot{\gamma}\right\| \tag{4.13}$$

The initial value of $\kappa_s^{\alpha}\Big|_{soft}$ is given by

$$\kappa_s^{\alpha}\Big|_{soft}(0) = \kappa_s(0) \tag{4.14}$$

The constitutive equations are summarized in Table 4.2.

This crystal plasticity algorithm is applied to both the primary α phase and lamellar colonies via implementation into a UMAT subroutine in ABAQUS (2005).

Table 4.2 Constitutive equations for Ti-6Al-4V.

Flow Rule:

$$\dot{\gamma}^{\alpha} = \dot{\gamma}_o \left\langle \frac{\left|\tau^{\alpha} - \chi^{\alpha}\right| - \kappa^{\alpha}}{D^{\alpha}} \right\rangle^{m} \operatorname{sgn}\left(\tau^{\alpha} - \chi^{\alpha}\right) \quad \text{for all slip systems}$$

Evolution Equations for Hardening Variables:

Back stress (primary α phase and lamellar colony)

$$\dot{\chi}^{\alpha} = \mathrm{B}\dot{\gamma}^{\alpha} - \mathrm{C}\psi\left(x^{\alpha}\right)\chi^{\alpha}\left|\dot{\gamma}^{\alpha}\right| = \mathrm{B}\left(\operatorname{sgn}\left(\dot{\gamma}^{\alpha}\right) - \psi\left(x^{\alpha}\right)\frac{\mathrm{C}}{\mathrm{B}}\chi^{\alpha}\right)\left|\dot{\gamma}^{\alpha}\right|$$

$$\psi(x^{\alpha}) = \begin{cases} \exp\left(\eta_1 x^{\alpha}\right) & \text{for } x^{\alpha} < 0 \\ 1.0 & \text{for } x^{\alpha} \geq 0 \end{cases}$$

$$x^{\alpha} = \operatorname{sgn}(\tau^{\alpha} - \chi^{\alpha})\, p^{\alpha}, \textit{with} \quad \dot{p}^{\alpha} = \left|\dot{\gamma}^{\alpha}\right| \operatorname{sgn}(\tau^{\alpha} - \chi^{\alpha})$$

Threshold stress

Primary α phase

$$\kappa^{\alpha}{}_{prism} = \kappa_1^{\alpha}\Big|_{prism} + A(\tau_{Pyr1} - \tau_{Pyr2}) + \kappa_s^{\alpha}\Big|_{prism} \qquad \dot{\kappa}_s^{\alpha}\Big|_{prism} = -\mu\kappa_s^{\alpha}\Big|_{prism}\left\|\dot{\gamma}\right\|$$

$$\kappa^{\alpha}{}_{basal} = \kappa_1^{\alpha}\Big|_{basal} + \kappa_s^{\alpha}\Big|_{basal} \qquad \dot{\kappa}_s^{\alpha}\Big|_{basal} = -\mu\kappa_s^{\alpha}\Big|_{basal}\left\|\dot{\gamma}\right\|$$

$$\kappa^{\alpha}{}_{pry} = \kappa_1^{\alpha}\Big|_{pry} \qquad \dot{\kappa}^{\alpha}_{pry} = 0$$

Lamellar colony

$$\kappa^{\alpha}{}_{soft} = \kappa_1^{\alpha}\Big|_{soft} + \kappa_s^{\alpha}\Big|_{soft} \qquad \dot{\kappa}_s^{\alpha}\Big|_{soft} = -\mu\kappa_s^{\alpha}\Big|_{soft}\left\|\dot{\gamma}\right\|$$

$$\kappa^{\alpha}{}_{hard} = \kappa_1^{\alpha}\Big|_{hard} \qquad \dot{\kappa}^{\alpha}\Big|_{hard} = 0$$

$$\kappa_1^{\alpha} = k_y\left(d^{\alpha}\right)^{-0.5} \qquad \kappa_s^{\alpha}\Big|_{prism}(0) = \kappa_s^{\alpha}\Big|_{basal}(0) = \kappa_s^{\alpha}\Big|_{soft}(0) = \kappa_s(0) \qquad \left\|\dot{\gamma}\right\| = \sum_{\alpha=1}^{N}\left|\dot{\gamma}^{\alpha}\right|$$

Drag stress

$$\dot{D}^{\alpha} = 0 \qquad D_{\alpha}^{prism} = D_{\alpha+\beta}^{prism} \qquad D_{\alpha}^{basal} = D_{\alpha+\beta}^{basal} \qquad D_{\alpha+\beta}^{\langle 111\rangle\{110\}} = 0.9D_{\alpha}^{prism}$$

4.4 **Finite Element Model**

The microstructure of the tested Ti-6Al-4V is simulated by a finite element model. Microstructure attributes are given in Table 4.1 for this material. The low symmetry of the hcp crystal structure and the anisotropy of slip system strengths result in material behavior for α-Ti and α/β Ti-Al alloys that depends strongly on the polycrystalline texture, as well as disorientation at grain/phase boundaries. Therefore, it is essential to address crystallographic texture in the constitutive model and finite element realizations of polycrystals.

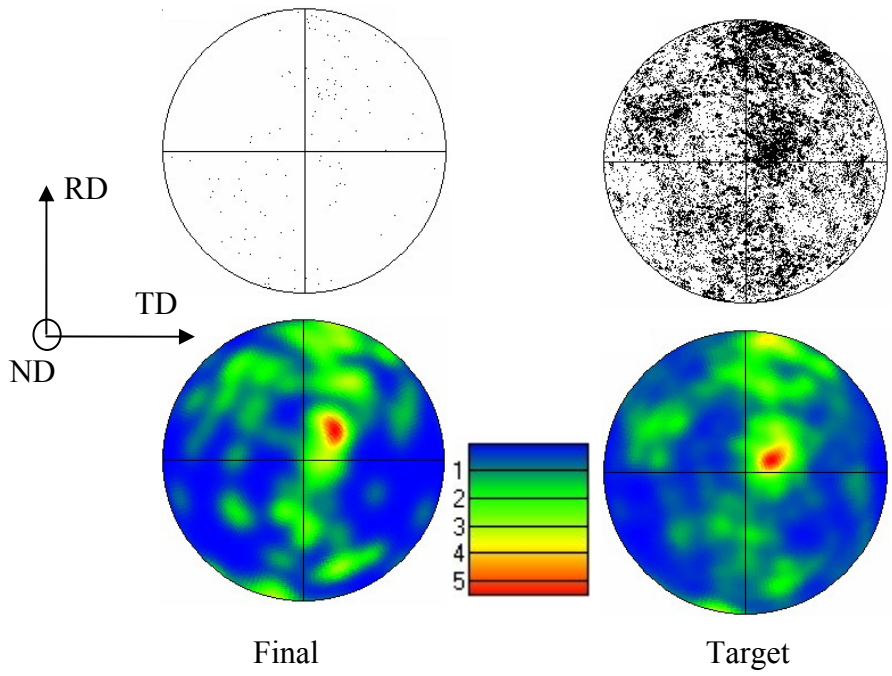

Figure 4.4. Basal plane pole figure of the initial, target and final orientation distributions.

For simplicity, in this study the target orientation distribution in the Rodriguez space and disorientation angle distribution of the polycrystalline material are extracted directly from EBSD (electron back scatter diffraction) scanning data (provided by Prof.

M. Mills, OSU), taking the crystal symmetry into consideration (Randel and Engler, 2000; Sztwiertnia et al., 1999; Saylor et al., 2004). The orientation distribution of grains is simulated by using the approach described in Chapter 2. Figure 4.4 shows the basal plane pole figures of fitting and target orientation distribution of grains. It should be noted that 125 grains are used to fit the target orientation distribution in Fig. 4.4.

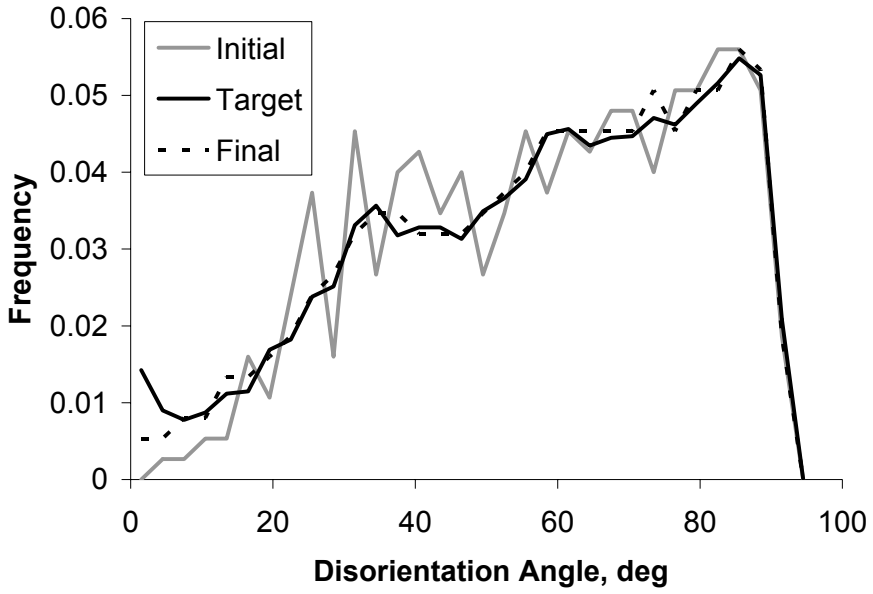

Figure 4.5. Initial, target and final disorientation distributions for 125 grains.

The simulated annealing method is used to fit the disorientation angle distribution (Miodownik, 1999). In this method, the domain that includes all possible grain disorientations is divided into M sub-domains. To simulate the disorientation distribution while maintaining the target orientation distribution, the resulting orientations from previous fitting processes are randomly assigned to a cluster of cubic grains arranged in a cubic space. The error ω of the disorientation distribution is obtained by

$$\omega = \sum_{j=1}^{M} [f^s(\Delta g_j) - f^t(\Delta g_j)]^2 \tag{4.15}$$

where $f^s(\Delta g_j)$ and $f^t(\Delta g_j)$ are the simulated and target frequencies of disorientation distributed in the sub-domain j. The variation of error $\Delta\omega$ is calculated after the orientations of two randomly selected grains are swapped. Then, $\Delta\omega$ is used to determine whether this operation is acceptable based on a probability criterion $p(\Delta\omega)$ which, following the Metropolis algorithm, is given by

$$p(\Delta\omega) = \begin{cases} 1 & (\Delta\omega < 0) \\ \exp(-\Delta\omega / T) & (\Delta\omega > 0) \end{cases} \tag{4.16}$$

Here, T is a control parameter (analogous to temperature) used to define an annealing schedule. The operation is accepted if $\Delta\omega < 0$ or $\Delta\omega > 0$ but $p(\Delta\omega) \geq \rho$, where ρ is a random number; otherwise, the operation is rejected. The operations continue until the error is less than a preset critical value (e.g., $\omega = 10^{-5}$). The initial, target and final disorientation distribution functions for an ensemble of 125 grains are shown in Fig. 4.5.

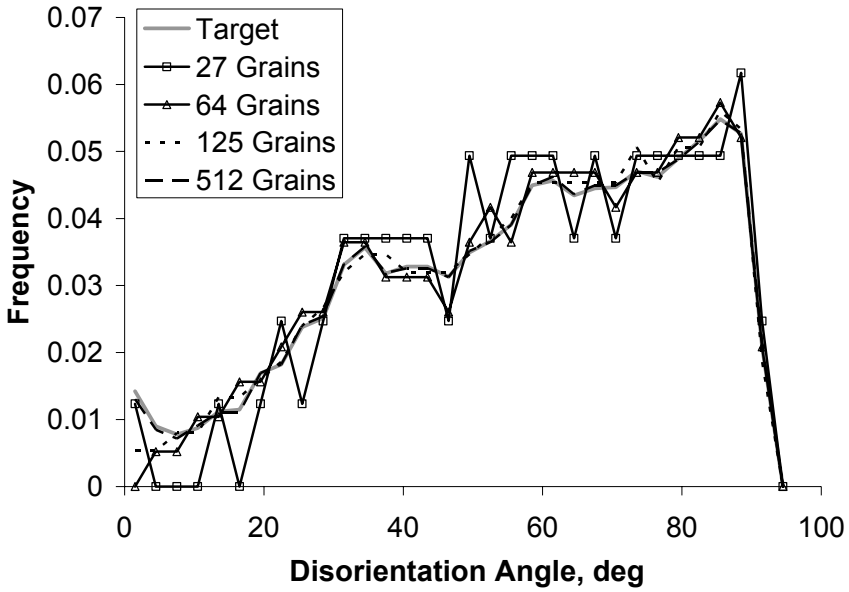

Figure 4.6. Fit for the disorientation distribution with 27, 64, 125 and 512 grains.

It should be noted that the fitting results depend strongly on the number of grains in the finite element mesh. During the EBSD scanning (provided by Prof. M. Mills, OSU), the orientations of over 10,000 grains were recorded. Finite element meshes with very few grains cannot precisely simulate the orientation and disorientation distributions of such a large number of grains. Figure 4.6 shows the fitting results of disorientation frequency functions with 27, 64, 125 and 512 grains. Clearly, at least 125 grains are needed to accurately fit the target disorientation distribution. The basal plane pole figures of target and simulated textures with 125 and 512 grains are shown in Fig. 4.7. The fitting result with 125 grains is shown to be sufficient to represent the target texture. A larger number of grains (512 grains) would result in a more accurate fit, as shown in Fig. 4.7. However, computational cost will significantly increase with addition of more grains.

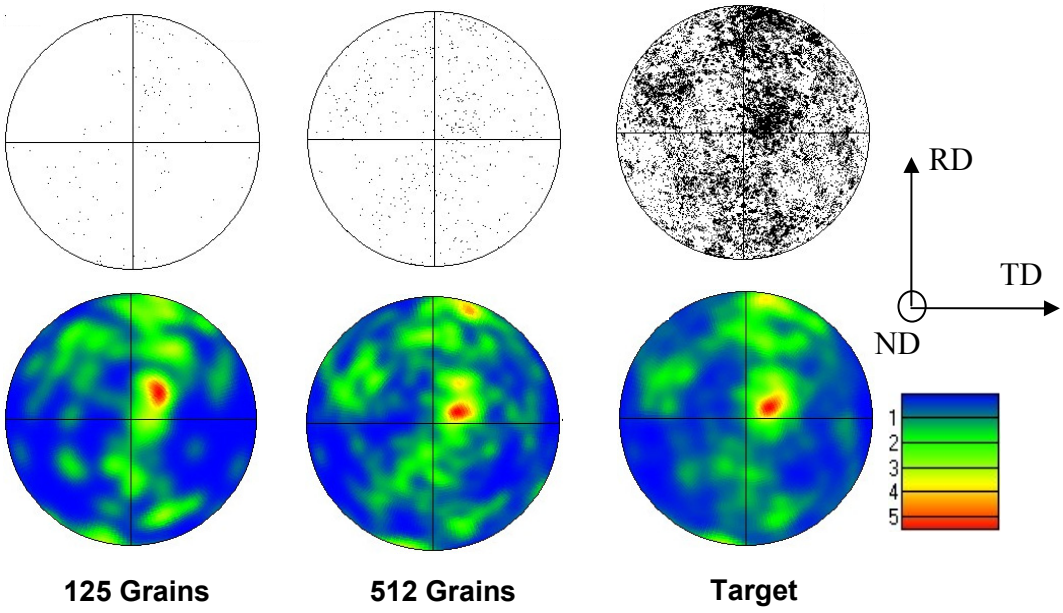

Figure 4.7. Basal plane pole figures of fit orientation distribution with 125 and 512 grains, compared to target orientation distribution.

The number of grains of each phase is defined by the volume fraction of that phase, since all grains in the finite element model considered here are assumed to have same size. It is noted the phases of each grain are randomly distributed due to the lack of information regarding the spatial characteristics of the phase distribution. However, certain constraints are introduced to avoid large clusters of either phase. In this study, the phase of each grain is initially randomly assigned according to the volume fraction and then adjusted to avoid substantial clustering of each phase, while maintaining the target volume fraction.

In this study, a cubic grain finite element model was used. The edge size L of the model is defined by

$$L = n^{1/3} d \tag{4.17}$$

where n is the number of grains and d is the average grain size. The tested polycrystalline material is idealized as an aggregate of cubic crystals of identical size, as shown in Fig. 4.8. Such an idealization represents a highly idealized, uniform grain size distribution of two phases. The finite element mesh was created using a Fortran code and implemented in ABAQUS (2005). As discussed before, a minimum of 125 grains are required to simulate the orientation and misorientation distributions of tested material. Thus, the statistical volume element (SVE) FE model consists of $5 \times 5 \times 5$ cubic grains, with each grain having $2 \times 2 \times 2$ elements, as shown in Figure 4.12. There are a total of 1000 8-node linear cubic elements. All elements employ reduced integration. Each reduced integration element has one integration point, therefore significantly reduce computational cost. To simulate the behavior of bulk material with only hundreds of grains, random periodic boundary conditions are applied to all three directions: RD, TD, and the normal direction shown in Fig. 4.8, in view of the strong heterogeneity of the

SVE. This boundary condition imposes constraints on the sides such that the opposite edges deform in the same manner (cf. (Smit, et al., 1998; Van der Sluis et al., 2000; Ostoja-Starzewski et al., 1994; Kumar, et al., 2006). The displacements are enforced (specified) in the normal direction to correspond to strains imposed in the experiments. It is noted that when the displacement is specified on an upper boundary, as in uniaxial loading, the sides of the mesh (other two directions) experience approximately zero net traction, in accordance with the axial loading condition.

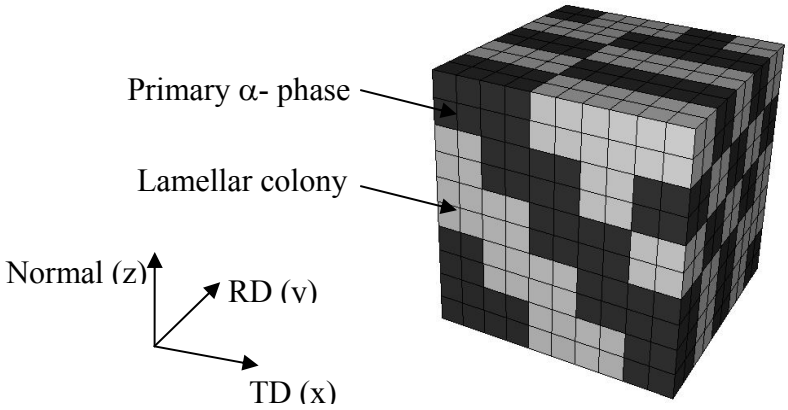

Figure 4.8 Finite element model of periodic polycrystal.

4.5 **Fitting Procedure**

All experimental data were obtained from Pratt & Whitney Company. In all mechanical tests of the heat treated Ti-6Al-4V (PW1215) conducted at room temperature, the loading direction was aligned with the normal direction of the material shown in Fig. 4.8. Relatively complex uniaxial strain-controlled loading histories were employed with and without strain hold periods interspersed throughout. In tests with hold periods, four

strain rates of 10^{-3} s^{-1}, 10^{-4} s^{-1}, 3×10^{-5} s^{-1}, and 10^{-5} s^{-1} were employed to explore the strain rate sensitivity of the material. Another type of test enforced a complex uniaxial strain-controlled cyclic history at a constant strain rate of 10^{-4} s^{-1}, without hold periods. Also, a load-controlled uniaxial creep test was performed at room temperature with a nominal (engineering) stress of 827 MPa and the creep strain was recorded. Several materials parameters such as the inverse strain-rate sensitivity exponent m in Eq. (4.1) are amenable to estimation by virtue of the variation of strain rates and stress relaxation during strain hold periods or by uniaxial creep tests. However, creep tests alone are unable to calibrate the parameters that control the cyclic behavior, such as the direct hardening and dynamic recovery coefficients of the kinematic hardening. Therefore, in this study, the crystal plasticity model is calibrated by fitting the stress-strain response of the strain-controlled tests at different strain rates with strain hold periods. The results of constant strain rate strain-controlled experiments and creep tests are then used in a predictive sense to validate the calibrated constitutive model.

Table 4.3 Material constants for various microstructures at room temperature (Mayeur, 2004).

Property	Value	Reference
C_{11}	162,400 MPa	Simmons and Wang, 1971
C_{12}	92,000 MPa	
C_{13}	69,000 MPa	
C_{33}	180,700 MPa	
C_{44}	46,700 MPa	
$\dot{\gamma}_o$	0.001 s^{-1}	Goh, 2002
k_y	17 MPa-$mm^{0.5}$	Picu and Majorell, 2002, Kalidindi et al., 2003

It should be noted that several material constants of the crystal plasticity model can be obtained from the literature or directly from characterized microstructure features. These constants, shown in Table 4.3, include the elastic constants for the α-phase and lamellar colony (C_{ij}), reference shearing rate and Hall-Petch constant; they can be applied to the same nominal composition with different microstructures arising from different thermomechanical process routes.

The relationship between Miller-Bravais indices of HCP crystal and Cartesian coordinate system is shown in Fig. 4.9. The elasticity tensor *C* of an HCP crystal is given by

$$\boldsymbol{C} = \begin{bmatrix} C_{11} & C_{12} & C_{13} & 0 & 0 & 0 \\ C_{12} & C_{11} & C_{13} & 0 & 0 & 0 \\ C_{13} & C_{13} & C_{33} & 0 & 0 & 0 \\ 0 & 0 & 0 & C_{44} & 0 & 0 \\ 0 & 0 & 0 & 0 & C_{44} & 0 \\ 0 & 0 & 0 & 0 & 0 & 0.5\left(C_{11} - C_{12}\right) \end{bmatrix} \tag{4.18}$$

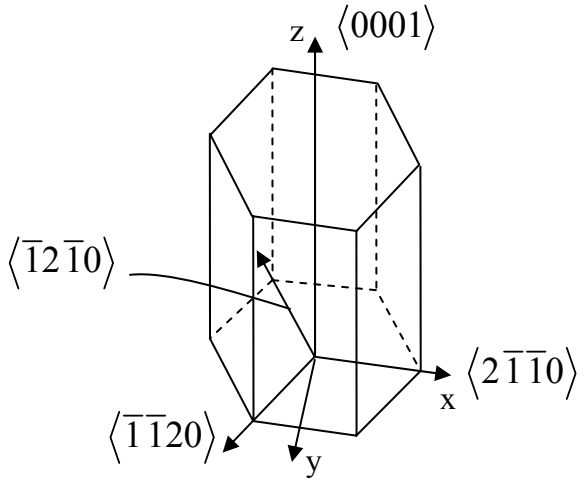

Figure 4.9. Coordinate relationship between the Cartesian system and the Miller-Bravais system.

The threshold stress depends on average grain size via the Hall-Petch slope. The value of other constants must be found by fitting the experimental data. These constants include the inverse rate sensitivity exponent m, coefficient for tension-compression asymmetry of the back stress η_1, the drag stress of each slip system D^{α}, the initial value of the softening term $\kappa_s(0)$, and degree of softening of the threshold stress of basal and prismatic slip systems μ, etc.

The fitting process is as follows. For a given loading history, some material constants are first determined based on the microstructure attributes; then the values of fitting parameters are estimated within a reasonable range based on previous works (Mayeur, 2004). After running simulations, the resulting stress values at each strain point are compared with those of the experimental data. This estimation, simulation and comparison loop can be run until the error is minimized.

The fitting process can be rendered more efficient by conducting a sensitivity analysis of variables with respect to the stress-strain response in the first stage of calibration. Given all of the crystal plasticity parameters that needed to be calibrated, it is known that some of them have more influence on the response, such as inverse material rate sensitivity exponent m and the initial value of the softening term $\kappa_s(0)$. In the fitting process, the material rate sensitivity m can be initially approximated by only fitting the stress relaxation response during strain hold periods. Although a small change of m is needed to obtain the best fit of the entire relaxation curve, this approximation was shown to be very accurate. The initial value of the softening term $\kappa_s(0)$ in the threshold stress, which has an effect on initial yield behavior, decays rapidly (breakdown of short range order at low to moderate homologous temperatures), which means this term will have almost no effect on the long range cyclic stress-strain behavior. Therefore, the softening term can be fit by comparing the stress-strain response during the first few loading cycles and can then be held constant thereafter.

Table 4.4 Relative CRSS of slip systems at room temperature reported in the literature for α-titanium and α/β Ti-Al alloys, normalized to CRSS for prismatic slip (Mayeur, 2004).

$\tau_{CRSS}^{basal} / \tau_{CRSS}^{prism}$	$\tau_{CRSS}^{pyr\langle a \rangle} / \tau_{CRSS}^{prism}$	$\tau_{CRSS}^{pyr\langle c+a \rangle} / \tau_{CRSS}^{prism}$	Reference
0.93 - 1.3	1	1.1 - 1.6	Medina et al., 1995
1.25	-	2.625	Paton et al., 1973
5	5	8.0 - 15.0	Fundenberger et al., 1997
1.5	1	3	Dunst and Mecking, 1996
1	-	8	Lebensohn and Canova, 1997
1.43	-	4.23	Bieler and Semiatin, 2001

The estimation of material constants involves certain constraints. Such constraints can be imposed as ranges of target values based on the literature. For example, it is well known that the CRSS of pyramidal slip systems is much larger than that of the basal and prismatic slip systems for α-titanium and α/β Ti-Al alloys (Dunst and Mecking, 1996). Therefore, the drag stresses of these slip systems are estimated in proportion to relative ratios of estimated CRSS for various slip systems presented in Table 4.4.

In Fig. 4.10, the stress-strain curves resulting from the fitting procedure are compared against the corresponding experimental data for an imposed uniaxial strain history with various strain rates and strain hold periods. Clearly, the model simulations agree well with data in terms of the flow stress at both low and high strain rate. The tension-compression asymmetry behaviors are also simulated well, as is stress relaxation during strain hold periods (e.g., $\varepsilon = 0.032$). Material constants are reported in Table 4.5. The same constants are used to conduct predictive simulations for cyclic uniaxial strain-controlled histories at a constant strain rate of 10^{-4} s^{-1} without hold times and for creep histories. The resulting stress-strain-time predictions are all in reasonable agreement with

experimental data, as shown in Figs. 4.11 and 4.12, thereby validating the model for purpose of this study.

The κ_1 values for all slip systems in the globular alpha phase are calculated based on the Hall-Petch relation in Eq. (4.5) with grain size of 7.74 μm, giving κ_1 =193 MPa. For lamellar colonies, $\kappa_1^{(\alpha+\beta)\text{basal}}$ and $\kappa_1^{(\alpha+\beta)\text{easy glide systems}}$ of soft slip modes are also calculated based on the Hall-Petch relation with grain size of 7.74 μm; following Mayeur (2004), $\kappa_1^{(\alpha+\beta)basal}$ is assumed to be 30 MPa lower than $\kappa_1^{(\alpha+\beta)\text{easy glide systems}}$. Both $\kappa_1^{(\alpha+\beta)prism}$ and $\kappa_1^{(\alpha+\beta)\text{pyr}}$ are determined using the alpha lath thickness as the characteristic length scale in Eq. (4.5), as 981 MPa. The value of $\kappa_1^{(\alpha+\beta)\text{bcc}}$ is capped at 800 MPa.

Table 4.5 Material constants for PW1215 at room temperature.

D_0^{basal}	95 MPa	κ_1^{basal}	193 MPa	μ	40
D_0^{prism}	95 MPa	κ_1^{prism}	193 MPa	η_1	800
$D_0^{\text{pyr}\langle a\rangle}$	200 MPa	$\kappa_1^{\text{pyr}\langle a\rangle}$	193 MPa	A	-0.1
$D_0^{\text{pyr}\langle c+a\rangle}$	200 MPa	$\kappa_1^{\text{pyr}\langle c+a\rangle}$	193 MPa	m	15
$D_0^{(\alpha+\beta)\text{basal}}$	95 MPa	κ_1^{prism}	193 MPa	$B^{\alpha,\alpha+\beta}$	40000
$D_0^{(\alpha+\beta)\text{prism}}$	95 MPa	$\kappa_1^{(\alpha+\beta)\text{basal}}$	163 MPa	$C^{\alpha,\alpha+\beta}$	8000
$D_0^{(\alpha+\beta)\text{pyr}}$	200 MPa	$\kappa_1^{(\alpha+\beta)\text{prism}}$	981 MPa		
$D_0^{(\alpha+\beta)\text{bcc BOR}}$	85.5 MPa	$\kappa_1^{(\alpha+\beta)\text{pyr}}$	981 MPa	$\kappa_1^{(\alpha+\beta)\text{bcc}}$	800 MPa
		$\kappa_1^{(\alpha+\beta)\text{easy glide systems}}$	193 MPa	$\kappa_s(0)$	140 MPa

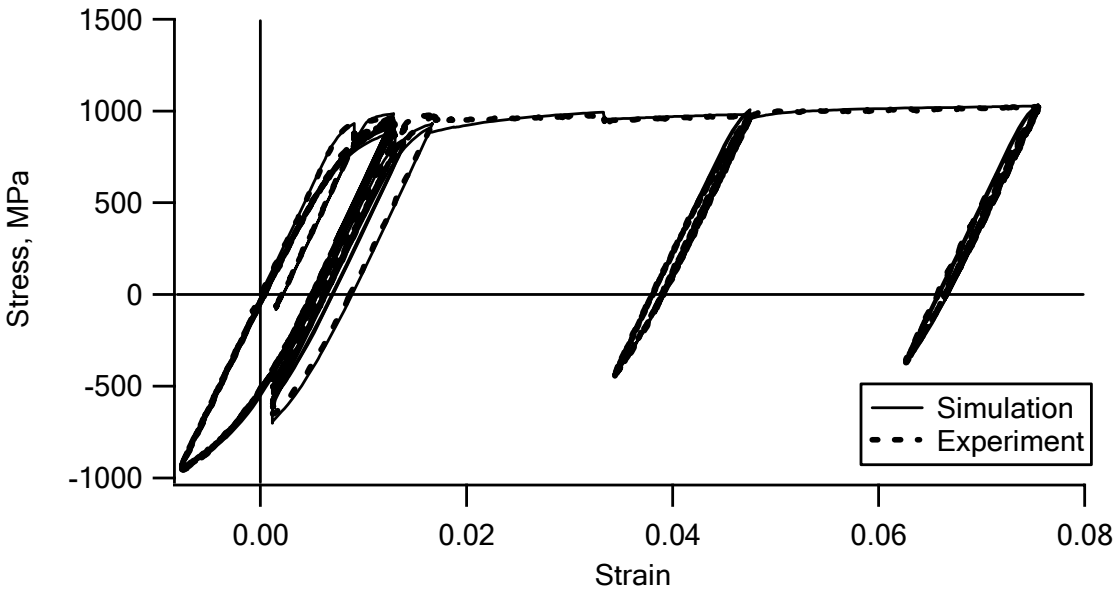

Figure 4.10. Fit for stress-strain curve of tested Ti-6Al-4V for the room temperature uniaxial strain history with multiple strain rates of 10^{-3} s^{-1}, 10^{-4} s^{-1}, 3×10^{-5} s^{-1}, and 10^{-5} s^{-1} and strain hold periods (note corresponding stress relaxation events at several points in history).

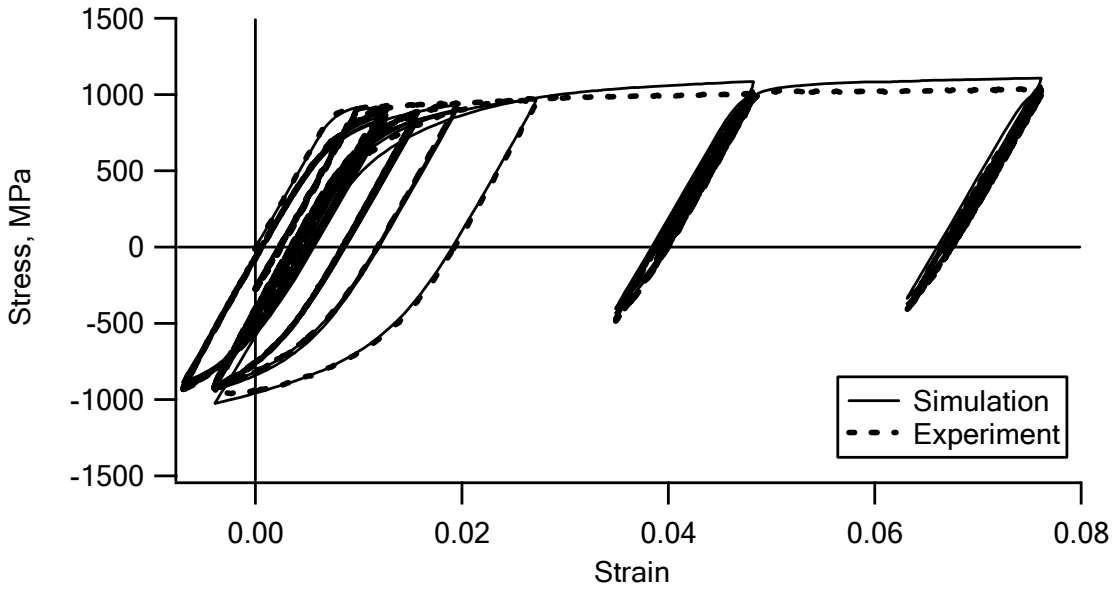

Figure 4.11. Comparison of model simulation of stress-strain curve with experimental results for Ti-6Al-4V at room temperature. for the uniaxial strain history with constant strain rate of 10^{-4} s^{-1} and with no hold periods.

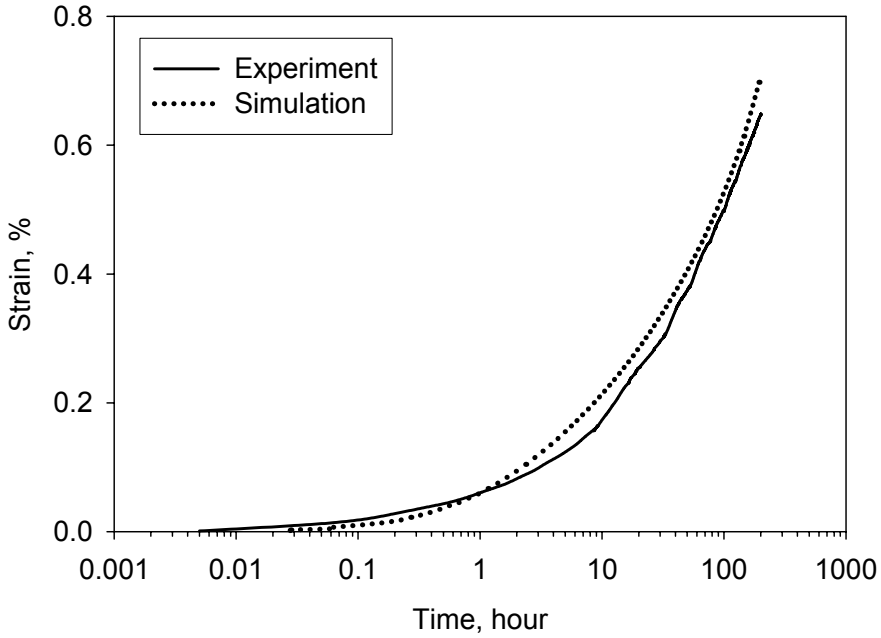

Figure 4.12. Comparison of simulation with experiment for uniaxial creep strain versus time response of Ti-6Al-4V at room temperature for an initial applied stress of 827 MPa.

4.6 **Validation of the Crystal Plasticity Model: Other Microstructures**

The good agreement between simulated results and experimental data obtained by the crystal plasticity model for these complex histories ensures the utility of this model for the Ti-6Al-4V material characterized and tested. Since the model is sensitive to the length scales of various microstructure features, it is important to investigate the microstructural sensitivity of this model to see if trends match experiments. In this way, the predictive character of the mechanistic model can be explored.

Experimental data exist to examine the sensitivity of two specific microstructural features, average globular α grain size, d, and volume fraction of the globular α phase, V_f. These two features are known to have significant influence on the deformation behavior

of Ti-6Al-4V. To avoid the influence of other microstructural features on the sensitivity study, the tested samples should be processed in a way that only the considered features vary, which is generally not possible due to thermodynamic and kinetic constraints. Therefore, efforts were made to choose experimental data associated with microstructures for which only d and V_f vary substantially.

The simulations are conducted using finite element models similar to the ones used for fitting parameters. To investigate the effect of average grain size, a range of d values between 6 μm to 10 μm were considered, holding $V_f = 0.5$ fixed. In the studies of the influence of volume fraction of globular α-phase, V_f ranged from 0.2 to 0.6, holding d = 8.5 μm fixed. In all simulations, the lath thickness of secondary α phase is 0.5 μm, β lath thickness is 0.03 μm, and a constant strain rate of 8.33×10^{-5} s^{-1} is applied. The results of the simulations are compared with experimental data in terms of the 0.2% offset-defined yield strength of the material. The variation of material yield strength with regard to the variation of the square root of average grain size and V_f of the simulations and tests are in reasonably good agreement, as respectively shown in Figs. 4.13 and 4.14. The Hall-Petch relation between average grain size and yield strength shown in the simulations can be attributed to the length scale effects of threshold stress defined in Eq. (4.5). The area per unit volume of interfaces between primary α grains and lamellar colonies deceases with increasing V_f, thereby decreasing incompatibility strains of these low symmetry phases and reducing material strength with increasing V_f. Clearly, similar trends are shown by the experimental data and the polycrystal plasticity model.

The deviation of experimental data from the results of simulations can be attributed to lack of independent control over microstructural parameters in the experimental microstructures. For example, experimental samples with V_f ranging from 0.486 to 0.515 and lath thicknesses of secondary α phase ranging from 0.377 to 0.674 μm were used to consider the influence of average grain size. Furthermore, neither the orientation or disorientation distributions of grains can be considered due to the lack of

companion experimental data, so we assume a random texture for the simulated microstructures.

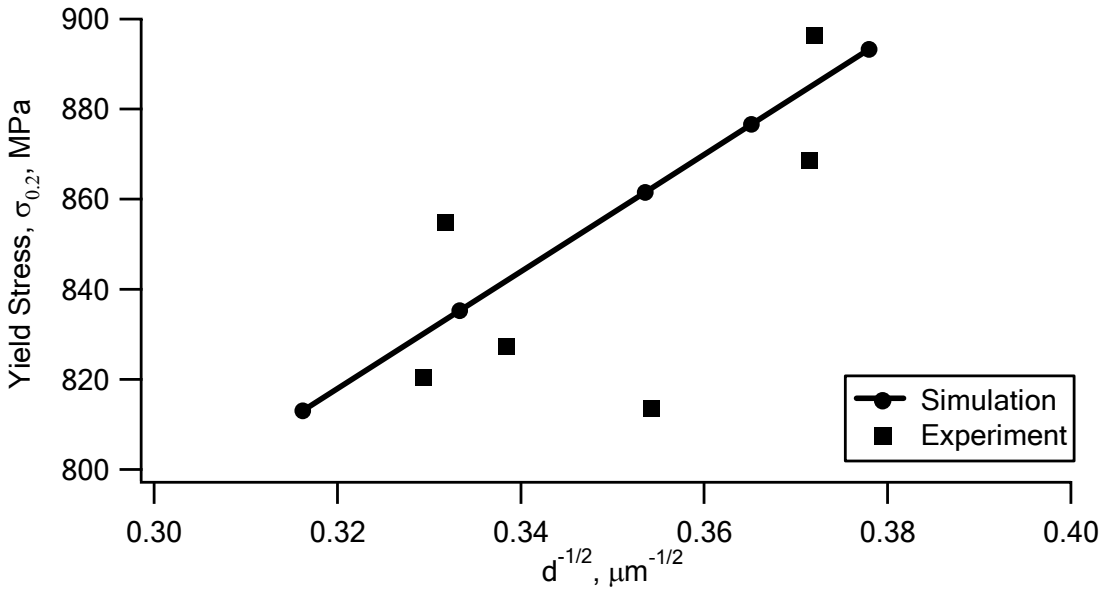

Figure 4.13. Variation of material strength with regard to the inverse square root of average grain size.

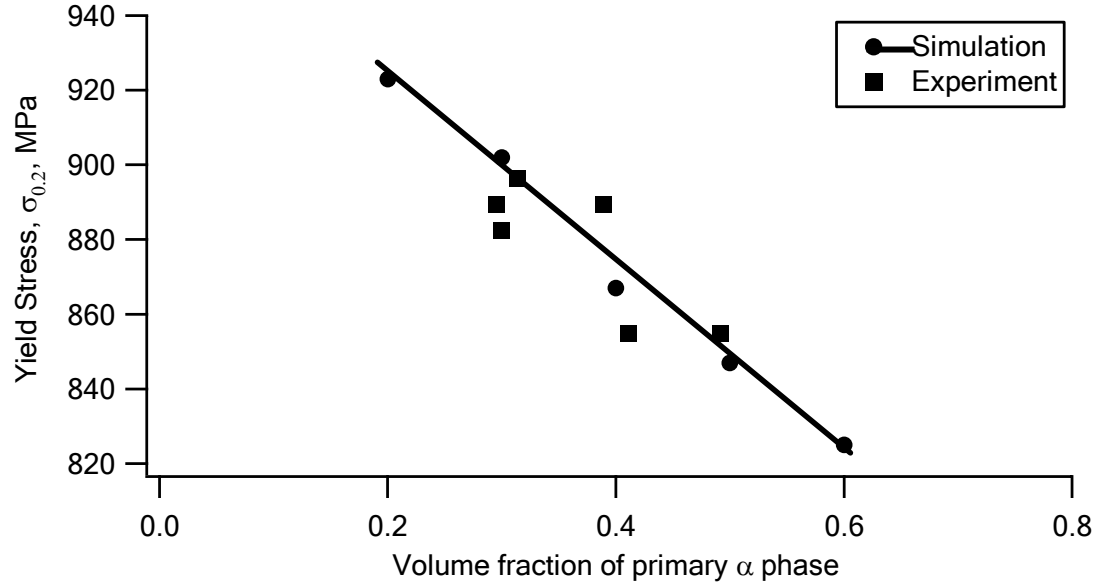

Figure 4.14. Variation of yield strength with regard to the volume fraction of primary α phase.

The goals of the constitutive model and polycrystal simulations considered here have something in common with artificial neural network (ANN) models used to recognize patterns of dependence of macroscopic responses on individual microstructure features such as d and V_f (Kar, 2005; Kar et al., 2006). Both approaches explore sensitivity of the representative polycrystalline response to variation of microstructure features. Both approaches permit assessment of variation of individual microstructure features to explore sensitivity, holding other features fixed, something that is not generally possible in physical experiments. In work of Kar et al. (2006) at The Ohio State University, an extensive experimental microstructure-response database was used to train and test an ANN model; this neural network approach was chosen for its capability to address a large number of variables with complex interdependencies, without prior knowledge of the physics of the problem. It should be noted that ANN approaches are relatively expensive due to the requirements of a sufficiently large experimental database over a sufficiently wide range of microstructures necessary to train and validate the pattern identification. An advantage of the present framework, of course, is that the crystal plasticity model applies to general loading histories and stress states, an aspect ANN cannot really addresses.

4.7 Discussion

It is well known that formation of fatigue cracks in metals is dominantly related to the cyclic plastic shear strain (slip) range within the microstructure, as well as the local stress or strain state. A homogenous macroscopic plasticity model is unable to provide this kind of information for heterogeneous microstructures. The microstructure-scale model proposed in this study is shown to have value in capturing orientation (texture), complex cyclic viscoplastic behavior, and scale effects of some key microstructure

features in duplex Ti-6Al-4V. The nature of microstructural sensitivity of this model enables its application to microstructure-sensitive fatigue analysis (McDowell, 2005) with an aim to predict the variation of fatigue behavior with regard to variation of microstructure in actual materials. In this study, the crystal plasticity model of Ti-6Al-4V follows that described in Mayeur and McDowell (2007). Compared with the parameters obtained therein (Mayeur, 2004) by fitting experimental data from uniaxial loading, a relatively low value of inverse strain rate sensitivity exponent m is obtained in this study, indicative of significant strain rate sensitivity of this material, consistent with the observations of substantial creep at room temperature (Neeraj et al., 2000).

In this study, only the material yield strength is used to validate the sensitivity of the proposed model to variation of microstructure. Of course, the fact that the model was capable of describing quite complex cyclic strain histories indicates that it may be useful in a broader context. A more comprehensive study should include the investigation of the strain hardening and stress relaxation behaviors as a function of microstructure as well.

4.8 **Summary**

Ti-6Al-4V is a dual phase material with range of possible complex microstructures. It is well known that mechanical behavior of Ti-6Al-4V is significantly affected by its texture and microstructure morphology. A three-dimensional scale-dependent model of the duplex Ti-6Al-4V is proposed in this study. The model includes length scale effects associated with dislocation interactions with different microstructure features, and is calibrated using polycrystalline finite element simulations to fit the measured macroscopic responses (overall stress-strain behavior) of a duplex heat treated Ti-6Al-4V alloy subjected to a complex cyclic loading history. The finite element

models are established to adequately represent the microstructures of the tested material. Equivalent orientations with similar probability density distributions of the crystallographic orientations are assigned to the finite element mesh. The simulated annealing method is used to fit the disorientation distributions of the sample. For a given Ti-6Al-4V alloy, it is shown that its mechanical deformation behavior can be correctly predicted by conducting the simulations on the finite element model using the proposed material modeling. Effects of microstructural features are examined and compared with the experimental data in terms of their influence on the material yield strength. The results are shown to agree with the experimental observations. The microstructure sensitivity of the model enables its application to microstructure-sensitive fatigue analysis of duplex Ti-6Al-4V.

CHAPTER 5

EFFECT OF GRAIN SIZE DISTRIBUTION ON MONOTONIC TENSION BEHAVIOR OF TI-6AL-4V

5.1 Introduction

As discussed before, microstructure has significant influence on the various properties of crystalline materials. Experimental approaches have been widely used in industry to study the dependence of the mechanical behavior on the microstructure. However, experimental studies are usually expensive and time-consuming to study effects of varying microstructure. The systematic study of microstructure sensitivity is difficult due to the fact that only a limited range of microstructures can be achieved by heat treatment and thermomechanical processing.

A computational approach was developed by McDowell (2005) to systematically investigate the variation of material properties with respect to variation of microstructure. Such approach can greatly reduce the cost for developing new material and is important for robust material design (McDowell et al., 2007). Extensive studies have been conducted to explore the sensitivity of tensile, cyclic and fatigue behaviors to microstructure by using the computational approach. Gall and coworkers (2001) investigated the effect of size and distribution of inclusions and voids in a cast A356-T6 aluminum alloy on fatigue crack formation. In the study conducted by Morrissey et al. (2003), the cyclic behavior of Ti–6Al–4V was shown to depend on the phase morphology and grain orientation distribution. In Chapter 2, the effects of three microstructure attributes, texture, average grain size and grain size distribution, on tensile and cyclic deformation behaviors of Ti-6Al-4V were examined. Fretting simulations (Chapter 3)

were conducted to investigate the effect of various microstructural features on fretting fatigue behavior (Mayeur et al., 2006; Zhang et al., 2006). In Chapter 4 (Zhang et al., 2007), effects of two microstructure attributes are examined and compared with the experimental data in terms of their influence on the material yield strength of Ti-6Al-4V. It is shown that the material strength increases with decreasing grain size and volume fraction of the primary α phase. In Chapters 2 and 3, a relatively simple variant of Voronoi tessellation was used to create various grain size distributions. It was shown that this modeling parameter (d_c/d) has relatively small influence on the tensile and cyclic deformation and fretting behaviors of Ti-6Al-4V.

The macroscopic monotonic tension behavior could be affected by both mean and scatter of grain size (Kurzydlowski et al., 1990). A numerical study of the effects of grain size distribution was conducted by Ghosh and Raj (1981) by using the Taylor assumption. Berbenni et al. (2007) systematically investigated the effect of grain size on the macroscopic yield strength of heterogeneous material by using the representative volume element (RVE) containing a large number of spherical homogeneous and isotropic grains; self-consistent method was used to simulate the monotonic deformation behavior of polycrystal. The material strength was shown to increase with decrease of average grain size and grain size dispersion. It is noted that the interaction between grains with various sizes and orientations cannot be precisely captured in this work since the realistic polycrystalline structure and heterogeneous and anistropic deformation behavior of grains was not considered.

The intrinsic inhomogeneity of polycrystals requires realistic representation of polycrystal structure with finite element mesh. The two-dimensional views of polycrystalline microstructure can be directly obtained from SEM with EBSD. Two-dimensional finite element meshes can then be created directly from these observations. However, three-dimensional real microstructure is generally unavailable or requires considerable effort by using SEM and EBSD. It should be noted that a sufficient number

of grains are required to construct the representing microstructures which would be highly computationally expensive. Several tessellation models, such as homogeneous Johnson-Mehl model (HJM), nonhomogeneous Johnson-Mehl (NHJM) model and Voronoi tessellation (Horalek, 1990), for approximating 3D realistic structures from two dimensional observations have been proposed. Among them, Voronoi tessellation has been extensively used in materials science to model polycrystal (Nygards, 2003; Zhang et al., 2006), intergranular cracks (Cizelj and Riesch-Oppermann, 2002) and composites (Winterfeld et. al, 1981) and is used in this study. Li and Gross (2002) showed that the log-normal grain size distribution can be achieved by using Voronoi tessellation with a sequence of minimization procedures (simulated annealing methods). It should be noted that orientation and disorientation distributions were not considered in Gross and Li (2002). We maintain that use of simulated annealing methods to impose such distributions can modify Voronoi tessellation to produce more realistic microstructures. Ultimately, the grain boundary character distribution should also be enforced.

The aim of this study is to develop a computational approach that can capture the effects of the grain size distribution on deformation behavior of Ti-6Al-4V. The elastic-viscoplastic deformation behavior of Ti-6Al-4V is described by a fully three-dimensional crystal plasticity constitutive relation developed by Zhang et al. (2007), which has been described in Chapter 4. The key component of this approach is to develop a numerical tool for microstructure modeling. Simulated annealing method has been used in previous chapters to fitting the microstructure attributes (orientation and disorientation distributions) of Ti-6Al-4V. In this chapter, a comprehensive modeling tool is developed to simultaneously simulate microstructure attributes, such as average grain size, grain size distribution, orientation distribution, minimum misorientation (i.e., disorientation) distribution, volume fraction of lamellar colonies and so on. A series of microstructures with various grain size distributions are created by using this modeling tool. All other important microstructure attributes are assumed unchanged. Monotonic tension

simulations are then performed on these microstructures. Variations of elastic modulus and yield strength with respect to variation of grain size distribution are computed. It should be noted that the computational approach developed here can be easily used to examine the sensitivity of other microstructure attributes of Ti-6Al-4V. Extension of this approach to other heterogeneous materials can be carried out by introducing the corresponding material models and appropriate microstructure attributes.

5.2 Material

Duplex Ti-6Al-4V considered in this study is a dual phase material with a primary HCP α phase, and secondary α plus bcc β phase arranged in lamellar structure. Microstructures with various grain size distributions are used. Other microstructural parameters, including average globular (primary) α size, lamellar colony size, volume fraction of the primary α phase, thickness of secondary α and β phases, and texture, are assumed unchanged. In this study, the material under consideration consists of 60% primary α phase and 40% lamellar colonies. The average primary α size and lamellar colony size is assumed to be the same, at $d = 10$ μm. The lath thicknesses of secondary α and β phases of the material are 1.5 μm and 0.5 μm, respectively. The orientation and disorientation distributions are extremely important due to the highly anisotropic behavior of low symmetry hcp crystals. The orientation and disorientation distributions of microstructures considered in this study are identical to those of PW1215 in Chapter 4. Figures 4.2 and 4.3 shows the basal pole figure of orientation distribution and misorientation distribution, respectively, of duplex Ti-6Al-4V.

The grain size of the single phase polycrystalline materials, such as Cu, follows the log-normal distribution (Gross and Li, 2002). For duplex Ti-6Al-4V, grain size

distributions of the primary α grains and lamellar colonies are unknown due to the lack of the experimental data. For simplicity, we assume that the sizes of primary α grains and lamellar colonies of Ti-6Al-4V follow the same log-normal distribution.

Table 5.1 Parameters of the log-normal distributions of grain size.

	d (μm)	*Var* (μm)	μ	σ
Microstructure 1	10	0	2.302	0
Microstructure 2	10	3	2.288	0.172
Microstructure 3	10	5	2.278	0.221
Microstructure 4	10	8	2.264	0.277
Microstructure 5	10	10	2.255	0.309
Microstructure 6	10	15	2.233	0.374
Microstructure 7	10	20	2.211	0.427
Microstructure 8	10	25	2.191	0.472
Microstructure 9	10	30	2.171	0.512

The probability density function of the log-normal distribution is written as

$$f\left(l;\mu,\sigma\right)=\frac{1}{l\sigma\sqrt{2\pi}}e^{-\left(\ln l-\mu\right)^2/2\sigma^2} \tag{5.1}$$

where μ and σ are mean and standard deviation of the natural logarithm of the variable l (grain size). The expected value or average of the grain size d is given by

$$d=e^{\left(\mu+\sigma^2\right)/2} \tag{5.2}$$

and the variance is

$$Var = \left(e^{\sigma^2} - 1\right) e^{2\mu+\sigma} \tag{5.3}$$

Correspondingly, the values of μ and σ can be obtained from the average grain size, d, and variance, Var, i.e.,

$$\mu = \ln\left(d\right) - \frac{1}{2}\ln\left(1 + \frac{Var}{d^2}\right) \tag{5.4}$$

$$\sigma^2 = \ln\left(1 + \frac{Var}{d^2}\right) \tag{5.5}$$

Various grain size distributions can be achieved by varying the mean d and variance Var of the probability density function. It is noted that this study focuses on the effect of grain size distribution. Therefore, nine microstructures with mean d = 10 μm and variance Var ranging from 0 to 30 μm are used. The parameters of distributions of grain size are summarized in Table 5.1. The possibility density functions can be obtained from the mean grain size d and variance of grain size Var through Eqs. (5.1), (5.4) and (5.5). Figure 5.1 shows the frequency distributions of grain size of microstructures used in this study. It should be noted that Microstructure 1 represents an idealized polycrystalline structure in which all grains have same cubic shape and identical size at 10 μm, as shown in Fig. 5.2.

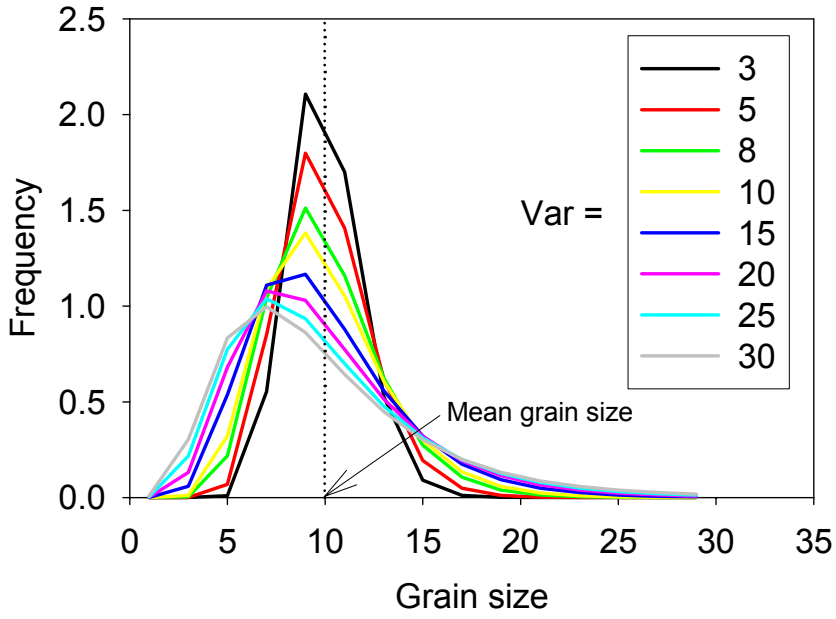

Figure 5.1 Frequency distributions of grain size for Microstructures 2-9 in Table 5.1.

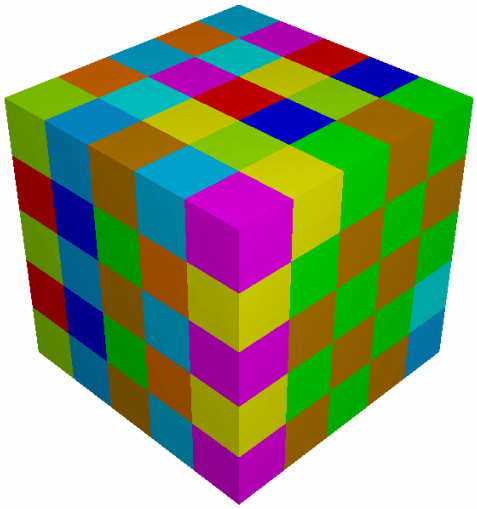

Figure 5.2 Polycrystalline structure of Microstructure 1.

5.3 Finite Element Model

The cubic model used in this study contains 125 grains with the average grain size d = 10 μm. The edge size L of the cubic model is dependent on average grain size d and number of grains n, i.e,

$$L = \sqrt[3]{n}d / 0.7 \tag{5.6}$$

Voronoi tessellation is used in this study to create microstructures with various grain size distributions (Microstructure 2-9). In the Voronoi tessellation algorithm employed here, the initial polycrystalline structure is created by randomly distributing 125 nuclei in the model space. A periodic cell structure is then constructed from a Poisson point process by introducing planar cell walls perpendicular to lines connecting neighboring nuclei. The cell walls near the surface of the cubic model are determined by the nuclei at the opposite surfaces. The distance between two neighboring nuclei should be smaller than a critical value, d_c. This critical distance can significantly influence the initial grain size distribution: the larger the critical distance, the lower the variance of the grain size distribution about its mean value (Chapter 2). Thus, polycrystal with high variance of grain size can be obtained by using lower critical value d_c. Gross and Li (2001) indicated that the grain size distribution of microstructures created via random Voronoi tessellation follow the Poisson distribution. On the other hand, grain sizes in most polycrystalline materials follow log-normal distribution. Therefore, adjustment of the nuclei is required to obtain the polycrystalline structure with log-normal grain size distributions given in Table 5.1.

The simulated annealing method is used to fit the grain size distribution (Miodownik, 1999). The grain size domain includes all possible grain sizes ranging from 0 to *3d*. The size of each grain is calculated from the Voronoi cells via a line section

algorithm. To calculate the grain size distribution function, the grain size domain is evenly divided into N_{gs} sub-domains. The possibility factor P_i for sub-domain i is defined as:

$$P_i = \frac{S_i}{S} \tag{5.7}$$

where S_i and S are the number of grains with grain size in sub-domain i and total number of grains, respectively. Then the error λ of the grain size distribution is obtained as

$$\lambda = \sum_{i=1}^{N_{gs}} [P_i^s - P_i^t]^2 \tag{5.8}$$

where P_i^s and P_i^t are the simulated and target grain size possibilities in sub-domain i, respectively. The variation of error, $\Delta\lambda$, is calculated after moving the center of a randomly selected grain for a random distance. Then, $\Delta\lambda$ is used to determine whether this operation is acceptable based on a probability criterion $p(\Delta\lambda)$ which, following the Metropolis algorithm, is given by

$$p(\Delta\lambda) = \begin{cases} 1 & (\Delta\lambda < 0) \\ \exp(-\Delta\lambda / T) & (\Delta\lambda > 0) \end{cases} \tag{5.9}$$

Here, T is a control parameter (analogous to temperature) used to define an annealing schedule. The operation is accepted if $\Delta\lambda < 0$ or $\Delta\lambda > 0$ but $p(\Delta\lambda) \geq \rho$, where ρ is a random number; otherwise, the operation is rejected. The operations continue until the error is less than a preset critical value (for example $\lambda = 10^{-5}$). Figure 5.3 shows fitted and target grain size frequency distributions for Microstructure 9.

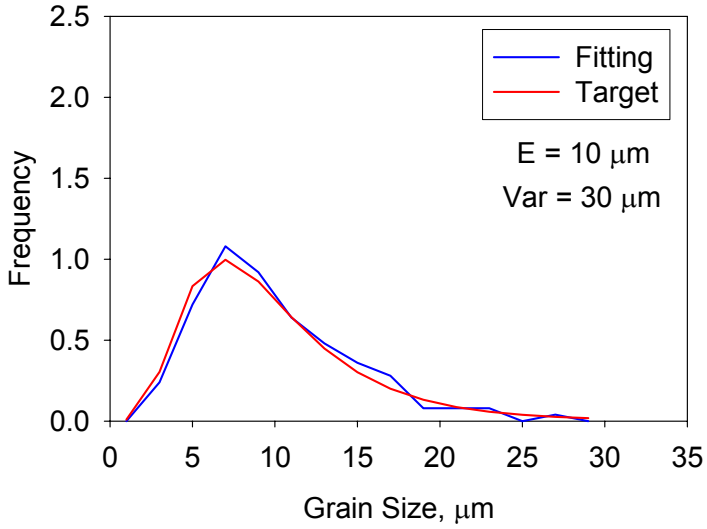

Figure 5.3. Fitting and target grain size distributions of Microstructure 9.

Microstructure 1 is an aggregate of cubic crystals of identical size. To assign the phase (α or β) for Microstructure 1, the number of grains of each phase is defined by the volume fraction V_f of primary α phase, i.e.,

$$M^{\alpha} = V_f K \tag{5.10}$$

$$M^{\alpha/\beta} = (1 - V_f) K \tag{5.11}$$

where M^{α} and $M^{\alpha/\beta}$ are the number of grains of primary α phase and lamellar phases, respectively. The total number of grains is K = 125. The phase of each grain is initially randomly assigned and then manually adjusted to avoid substantial clustering of each phase.

For microstructures other than Microstructure 1, all grains are divided into N_{phase} groups (bins) according to their grain size. The number of grains m_i of primary α phase in each group i is determined by

$$m_i = V_f n_i \qquad i = 1,2,....,15 \tag{5.12}$$

where V_f is the volume fraction of the primary α phase and n_i is the number of grains in the group i. It is assumed that the two phases of Ti-6Al-4V are randomly distributed and follow the same grain size distribution. To do so, the phase of each grain in a group is initially randomly assigned and then adjusted to avoid substantial clustering of each phase based on the qualitative observation.

To simulate the orientation distribution of grains, the Rodriguez space is evenly divided into N_{orien} sub-spaces. The probability of observing an orientation g_i in the sub-space i is determined by

$$f(g_i) = \frac{V_i}{V} \tag{5.13}$$

where V_i and V are the volume of crystals with the orientation in sub-space i and the total volume of all grains obtained from the scanning data, respectively. The domain that includes all possible grain disorientations is divided into $N_{misorien}$ sub-domains. The possibility of disorientation Δg_j distributed in the sub-domain j is written by

$$h(\Delta g_j) = \frac{R_j}{R} \tag{5.14}$$

where R_j and R are the area of grain boundaries with disorientation angle in sub-domain i and total area of grain boundaries.

The size of each grain of Microstructure 1 is the same. Thus, the orientation probability factor (P_i) for each orientation sub-space *i* can be obtained as

$$P_i = K\, f(g_i) \tag{5.15}$$

where *K* is total number of grains. The number of grains within each orientation sub-space *i* equals P_i, which sums over all sub-spaces to give

$$K = \sum_{i=1}^{N} P_i \tag{5.16}$$

Accordingly, *K* sets of orientation angles are then selected from the orientation population P and are randomly assigned to the different grains.

To simulate the disorientation distribution for Microstructure 1 while maintaining the target orientation distribution, the resulting orientations from previous fitting processes (Eq. 5.15 and 5.16) are randomly assigned to a cluster of cubic grains arranged in a cubic space. The error ω of misorientation distribution is obtained by

$$\omega = \sum_{j=1}^{N_{misorien}} [h^s(\Delta g_j) - h^t(\Delta g_j)]^2 \tag{5.17}$$

where $h^s(\Delta g_j)$ and $h^t(\Delta g_j)$ are the simulated and target frequencies of misorientation distributed in the sub-domain *j*. The variation of error $\Delta\omega$ is calculated after the orientations of two randomly selected grains are swapped. Similar to Eq. (5.9), a probability criterion $p(\Delta\omega)$ is given by

$$p(\Delta\omega) = \begin{cases} 1 & (\Delta\omega < 0) \\ \exp(-\Delta\omega / T) & (\Delta\omega > 0) \end{cases} \tag{5.18}$$

Same rule as described before is used to determine whether the operation is acceptable. The operations continue until the error is less than a preset critical value.

For microstructures other than Microstructure 1, random orientations are initially assigned to grains. Orientation and misorientation distributions are then simultaneously fitted by using the simulated annealing method. The error is given by

$$\pi = \sum_{i=1}^{N_{orien}} [f^s(g_i) - f^t(g_i)]^2 + \sum_{j=1}^{N_{misorien}} [h^s(\Delta g_j) - h^t(\Delta g_j)]^2 \tag{5.19}$$

where $f^s(g_i)$ and $f^t(g_i)$ are the simulated and target frequencies of orientation distributed in the sub-domain *i*. Two types of operations can be randomly performed: (i) change the orientation of a grain and (ii) swap orientation of two randomly selected grains. The variation of error $\Delta\pi$ is calculated after each operation. The probability criterion $p(\Delta\omega)$ is given by

$$p(\Delta\pi) = \begin{cases} 1 & (\Delta\pi < 0) \\ \exp(-\Delta\pi / T) & (\Delta\pi > 0) \end{cases} \tag{5.20}$$

The acceptance of operation is determined by the same rule as described before. A minimum error (10^{-5}) is set to terminate the operations. Figure 5.4 shows the basal plane pole figures of target and fitting orientation distributions for Microstructure 9. The target and fitting disorientation distributions for Microstructure 9 is shown in Fig. 5.5. Figure 5.6 shows the flow chart of the complete process for the modified Voronoi tessellation scheme.

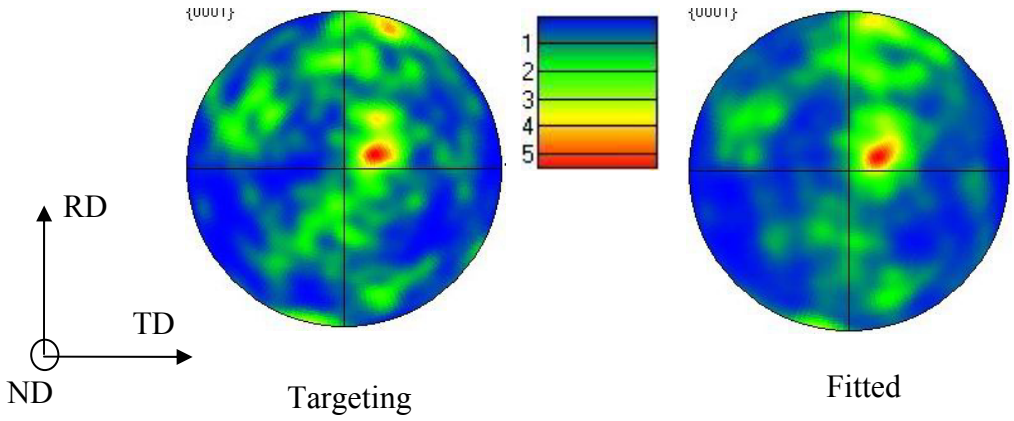

Figure 5.4 Basal plane pole figures of target and fitted minimum misorientation (disorientation) distributions for Microstructure 9.

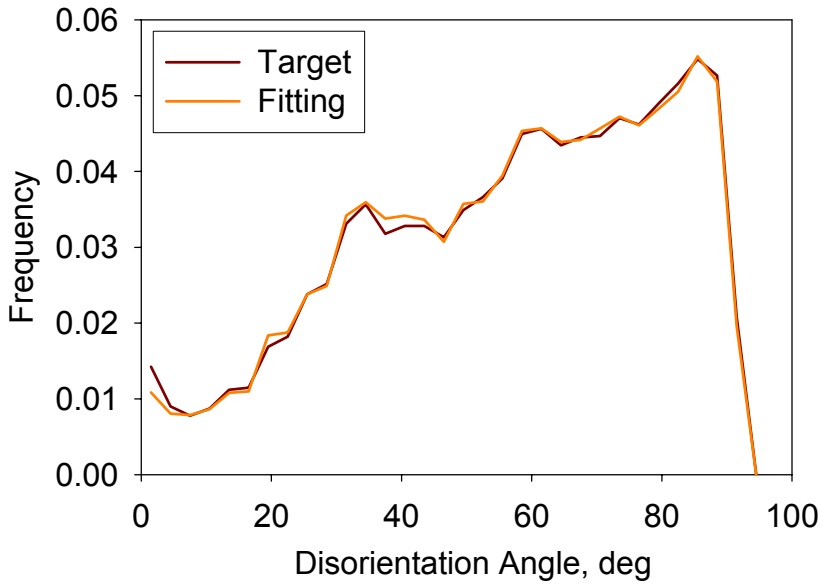

Figure 5.5. Target and fitting disorientation distributions for Microstructure 9.

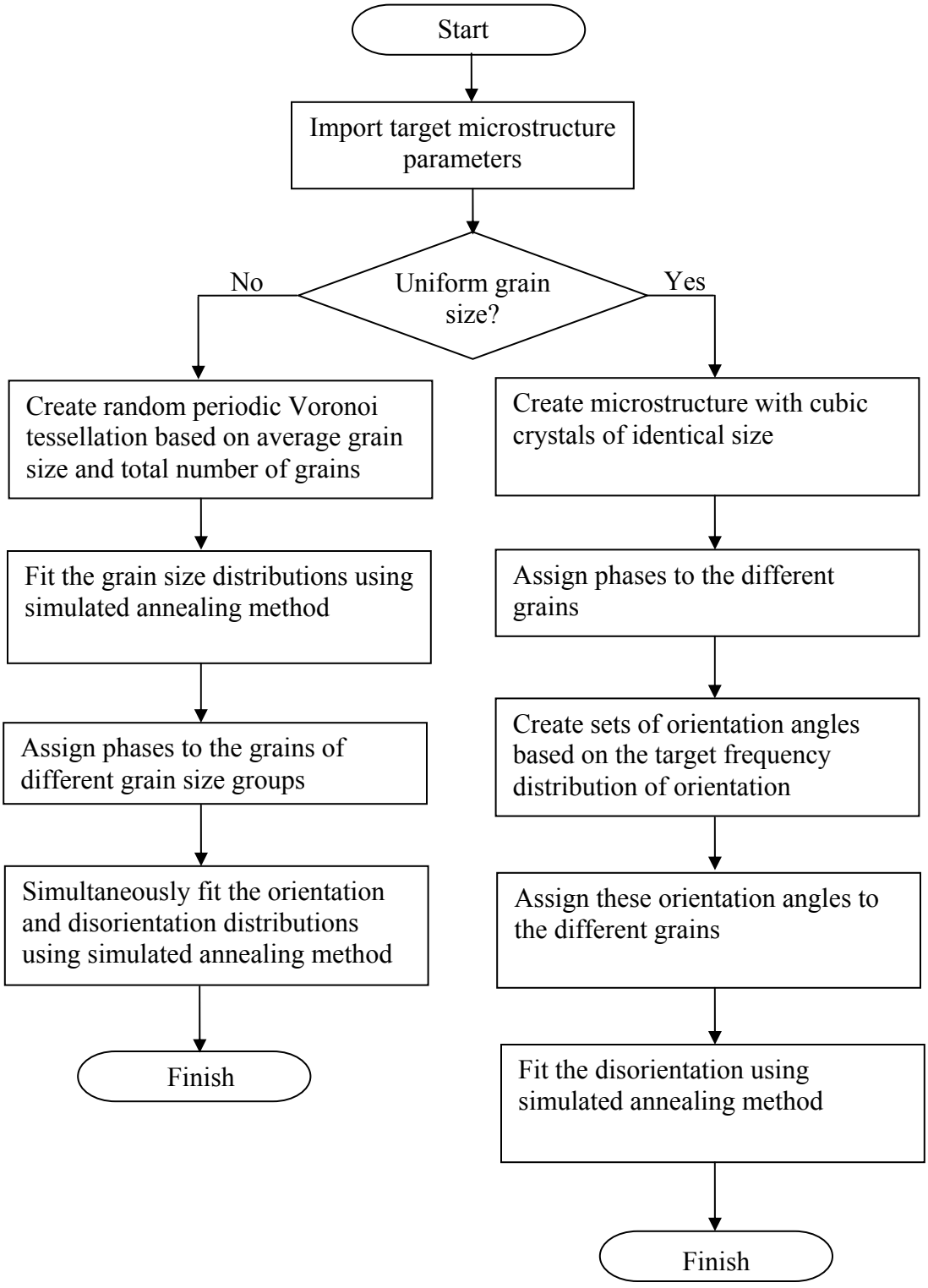

Figure 5.6. Flow chart of polycrystal fitting processes.

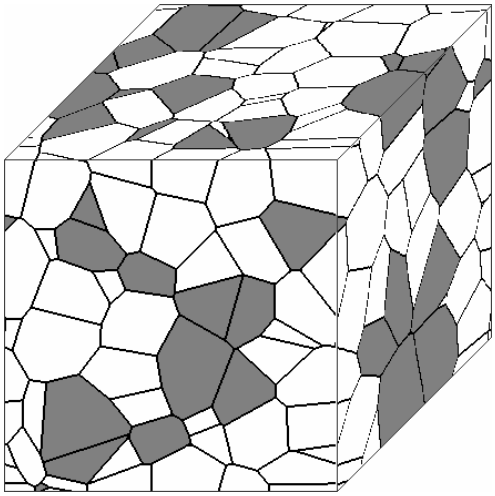

Figure 5.7 Polycrystal of Microstructure 9.

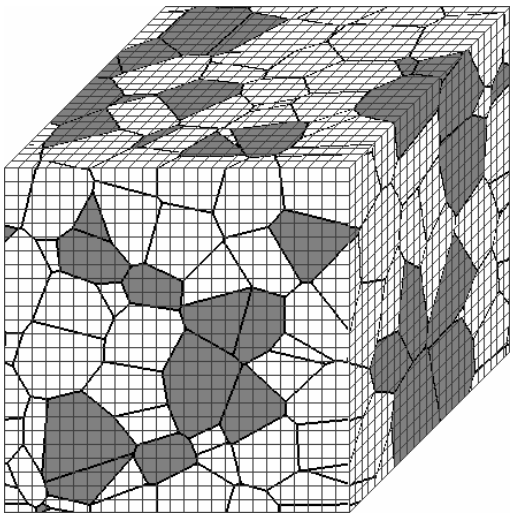

Figure 5.8. Mesh and polycrystal of Microstructure 9.

Figure 5.7 shows the tessellated Ti-6Al-4V polycrystal of Microstructure 9. The periodic tessellation contains white and grey cells representing primary α grains and lamellar colonies, respectively. The small regular cubic elements (C3D8R) are used to mesh the tessellation as shown in Fig. 5.8. The number of nodes on each edge of the

polycrystalline region is controlled by the mesh density. Based on the distance between the integration point of an element and the centroid of each grain, elements are assigned to grains. Figure 5.9 shows the finite element model corresponding to the microstructure in Fig. 5.8.

As discussed in Chapter 2, each microstructure may have multiple realizations. For example, two realizations may have the same grain size distribution but different grain structures. Multiple realizations result in the scatter of the mechanical properties such as the yield strength. For simplicity, in this study each microstructure has only one realization.

To simulate the behavior of bulk material with only hundreds of grains, periodic boundary conditions are applied to all three directions: RD, TD, and the normal direction (ND). For all finite element simulations, the tensile load is applied along the normal direction (z-axis) of material shown in Figs. 5.4 and 5.9.

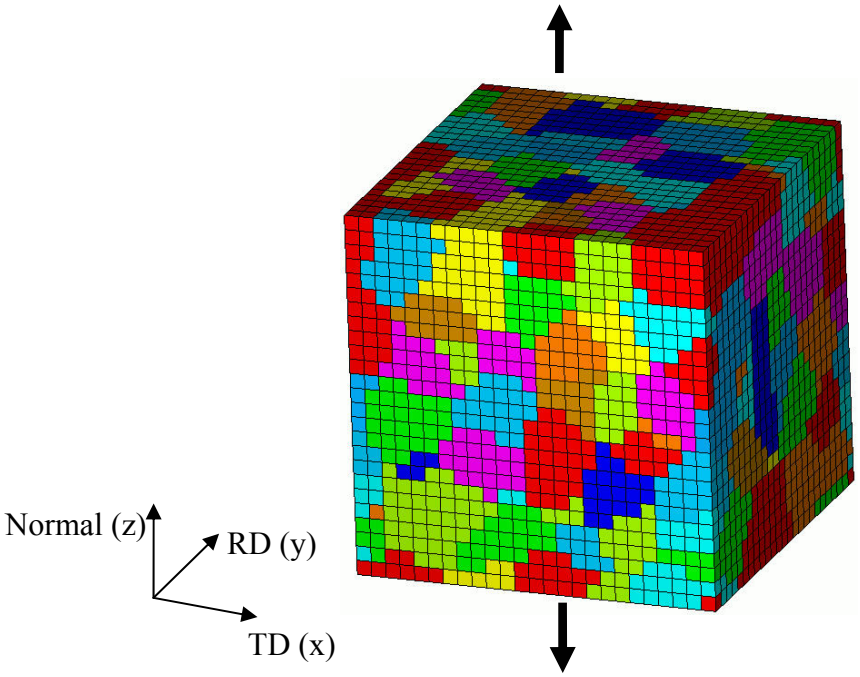

Figure 5.9. Finite element model corresponding to Microstructure 9.

5.4 Simulation Results

Tensile deformation is imposed up to 1.5% in all simulations. The strain rate is 10^{-3} s^{-1}. The stress-strain responses for Microstructures 1, 3, 7 and 9 are shown in Fig. 5.10. The tensile deformation behaviors are very close for these microstructures when the applied strain is lower than 0.8%. As shown in Fig. 5.11, the Young's modulus in the loading direction for various microstructures is very close. It is known that elastic property of a grain is mainly controlled by its orientation. Grain size does not appreciably affect the elastic modulus. The material strength slightly increases with decreasing *Var*. Figure 5.12 shows the variation of yield strength with respect to variation of grain size distribution. The stress at a plastic strain of 0.1% has been defined as yield stress σ_y in these simulations. Both yield strength σ_y and 0.2% offset-defined yield strength $\sigma_{0.2}$ (common in industry) are shown in Fig. 5.12. Approximate linear relations between σ_y and $\sigma_{0.2}$ and *Var* are shown. This result can be explained by the increasing number of large grains with lower strength as *Var* increase. Comparing with hard small grains, large soft grains with high plastic strain have larger influence on the deformation behavior of polycrystals. Thus, as *Var* increases, the yield strength decreases. It should be noted that compared to the effect of average grain size, shown in Chapter 2, the effect of grain size variance on yield strength is relatively low. This conclusion agrees with the simulation results obtained by Berbenni et al. (2007). Figure 5.13 shows variation of flow stress with respect to *Var* at 1.5% strain. The relation between σ_y and grain size distribution is repeated in Fig. 5.13. It is known that the room-temperature tensile deformation of Ti-6Al-4V exhibits nearly elastic-perfect plastic behavior. In this study, very low strain hardening is predicted for various microstructures. Differences of flow stresses among various microstructures increase with increasing applied strain as shown in Figure 5.10 and 5.13. Microstructure 1 has the highest flow stress at 1.5% strain. The grain size

distribution is shown to have larger influence on strain hardening behavior than initial yield strength. It is noted that each microstructure has only one realization. A small scatter of the monotonic tension behavior will be obtained if multiple realizations are used. However, the overall tendency between the grain size distribution and the monotonic tension behavior will not change.

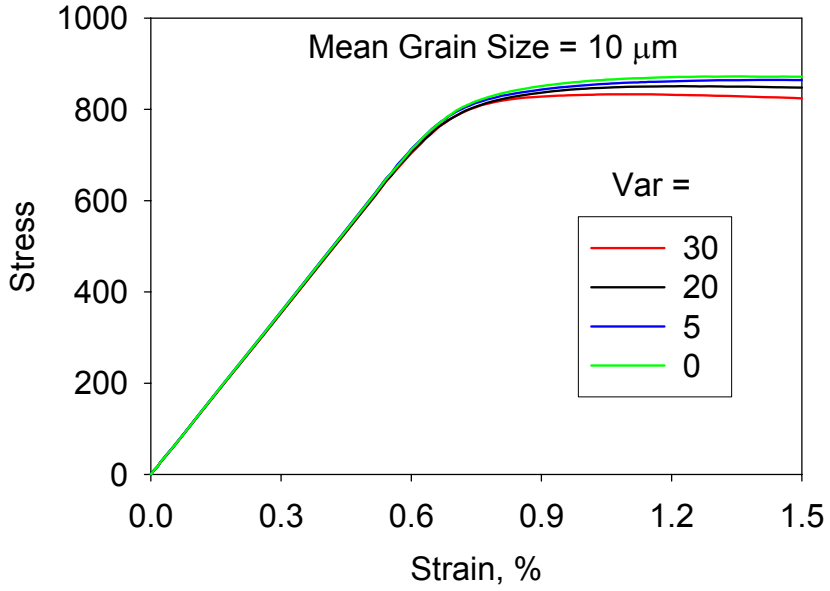

Figure 5.10 Stress-strain responses of Microstructure 1, 3, 7 and 9.

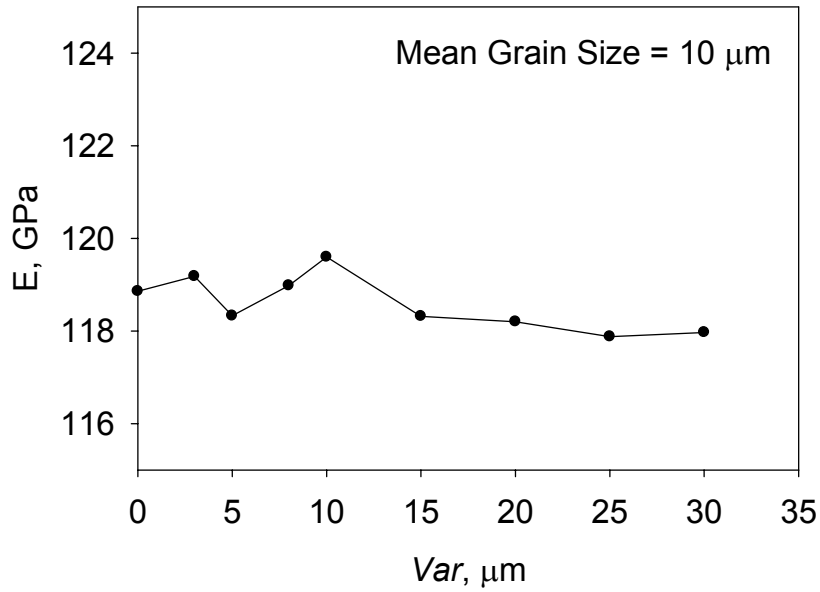

Figure 5.11. Variation of E with respect to *Var* for Microstructure 1-9.

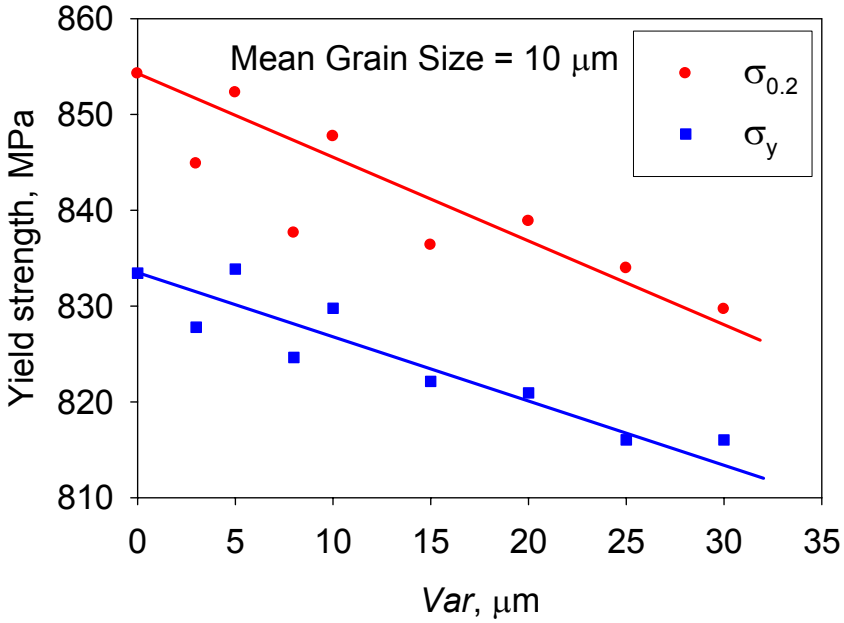

Figure 5.12. Variation of yield stress with respect to *Var*.

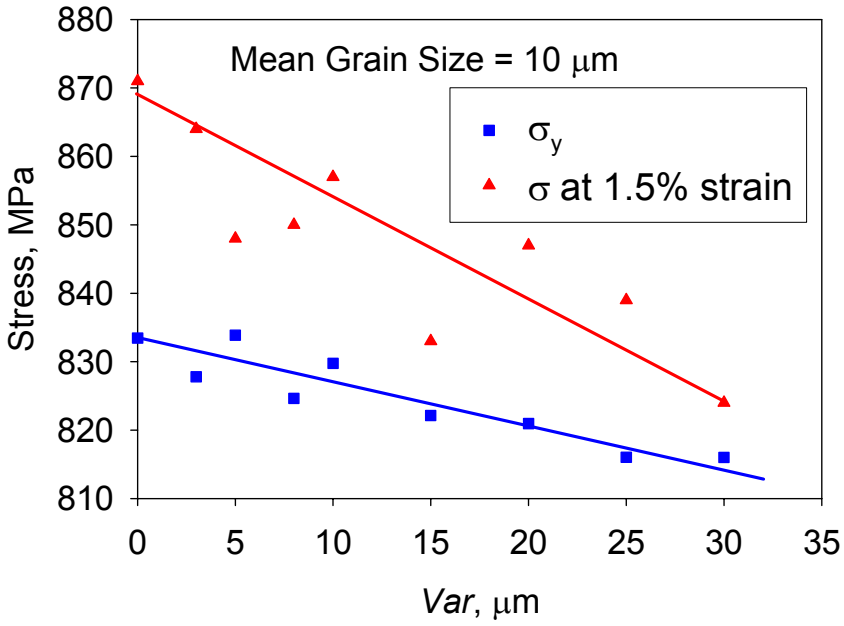

Figure 5.13 Variation of flow stress with respect to *Var*.

5.5 Summary

In this study, a computational approach is employed to study the effect of the grain size distribution on uniaxial tension deformation behavior of Ti-6Al-4V. The elastic-viscoplastic deformation behavior of Ti-6Al-4V is described by a fully three-dimensional, scale-dependent crystal plasticity constitutive relation described in Chapter 4. Microstructures with various grain size distributions are realized in FE meshes, using a sequence of error minimization operations (simulated annealing) performed on random Voronoi tessellations to fit microstructure attributes such as grain size distribution and orientation and disorientation distributions. A study of grain size distribution on tensile behavior of Ti-6Al-4V is carried out.

The results show that with increasing variance of grain sizes, the yield strength decreases slightly while the elastic modulus is unchanged. The grain size distribution has the most significant influence on tensile strain hardening behavior past initial yield.

CHAPTER 6

SIMULATIONS OF SINGLE CRYSTAL α TI-5AL SUBJECTED TO CYCLIC LOADING

6.1 Introduction

In Chapters 2-5, microstructure-sensitive studies for Ti-6Al-4V were performed. The deformation behaviors of primary α and α/β lamellar phases of Ti-6Al-4V at room temperature are described by a fully three-dimensional crystal plasticity constitutive relation.

As discussed in Chapter 1, dislocation substructures in the form of planar slip bands play an important role in the deformation and fatigue behaviors of α TiAl alloys. Many attempts have been made to simulate the deformation behavior of TiAl alloys, as summarized in Chapter 1. These studies showed that the crystal plasticity model is able to capture the significant microstructure and texture effects on the mechanical deformation behavior of Ti-6Al-4V which is important for microstructure sensitivity study and microstructure-scale fatigue analysis. However, conventional crystal plasticity theory is incapable of fully capturing the formation of intense shear in slip bands (see also Clayton et al., 2002), which is important for HCF modeling. Moreover, the dominance of single slip in grains for HCF cannot be accurately modeled with standard theory.

It is well known that the formation of a fatigue crack can comprise a large fraction of the HCF life of a material (Lankford and Kusenberger, 1973). For polycrystalline materials, two fatigue crack formation mechanisms are typically observed at low plastic strain amplitude: intense cyclic shear along slip bands and slip band impingement on the grain boundary (Morrison and Moosbrugger, 1997). Since there is no grain boundary in a

single crystal, the former mechanism is the dominant driving force for fatigue crack formation.

In this study, an approach is proposed which employ perturbation elements to initiate slip bands. Using a fully three-dimensional crystal plasticity constitutive model, finite element meshes for column grains are simulated for a cyclically deformed single crystal α Ti-5Al oriented for single and double prismatic slips at various completely reversed, strain-controlled cycling at room temperature at a strain rate of 3×10^{-4} s^{-1}. Several modeling and meshing parameters are examined in terms of their effects on the stress-strain responses, distribution of cyclic plastic strain and fatigue behavior. The simulation results are compared with the experimental data reported in Xiao and Umakoshi (2002, 2003). This Chapter is organized as follows. The crystal plasticity constitutive relation for α Ti-5Al is introduced in Section 6.2 and the FE model is described in Section 6.3. Section 6.4 presents simulation results. The simulated deformation and fatigue behaviors are compared with experimental data. The influence of two modeling parameters, mesh density and distribution of initial defects, on simulation results are examined in Section 6.5. Summary and Conclusions are given in the last section.

6.2 Crystal Plasticity Model

Single phase α Ti-5Al has the hexagonal-close-packed structure (HCP) at room temperature. There are four families of slip systems: 3 $<11\bar{2}0>(0001)$ basal, 3 $<11\bar{2}0>\{10\bar{1}0\}$ prismatic, 6 $<11\bar{2}0>\{10\bar{1}1\}$ first order pyramidal and 12 $<11\bar{2}3>\{10\bar{1}1\}$ second order pyramidal slip systems (Naka and Lasalmonie, 1982), illustrated in Figure 6.1. The dominant slip systems of the primary α phase are the basal

and prismatic slip due to their relatively low CRSS (critical resolved shear stress). The slip resistances of the first order pyramidal slip systems are about twice that of the basal and prismatic slip systems. The second order pyramidal systems have the highest CRSS of all slip systems.

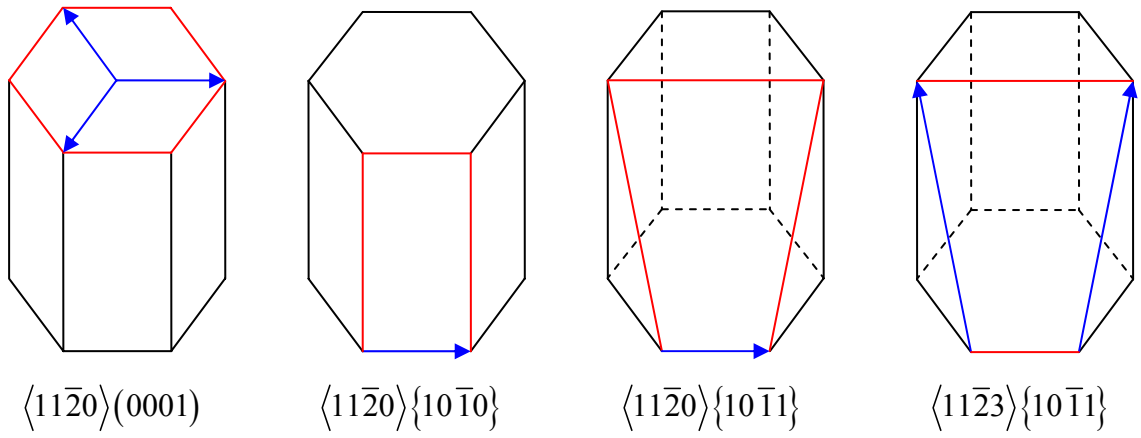

Figure 6.1. Slip systems for the α Ti-5Al.

The anisotropic elastic deformation behavior of each phase of α Ti-5Al is determined by an elasticity tensor C_{ijkl} with five independent components, as shown in Eq. (4.18). In the crystal plasticity framework, the shearing rate, $\dot{\gamma}^{\alpha}$, on the α^{th} slip system is given by

$$\dot{\gamma}^{\alpha} = \dot{\gamma}_0 \left\langle \frac{\left|\tau^{\alpha} - \chi^{\alpha}\right| - \kappa^{\alpha}}{D^{\alpha}} \right\rangle^{m} \operatorname{sgn}\left(\tau^{\alpha} - \chi^{\alpha}\right) \tag{6.1}$$

where D^{α} is the drag stress, m is the inverse strain-rate sensitivity exponent, χ^{α} represents the back stress on the α^{th} slip system, κ^{α} is the scalar threshold stress,

and $\dot{\gamma}_o$ is the reference shearing rate. The Macauley bracket in Eq. (6.1) is defined by <x> = xH(x), where H(x) is the Heaviside function.

The drag stress is taken as a constant, i.e., $\dot{D}^{\alpha} = 0$. The back stress is initially set to zero for all slip systems and evolves according to a nonlinear kinematic hardening rule of Armstrong-Frederick type, i.e.,

$$\dot{\chi}^{\alpha} = C\dot{\gamma}^{\alpha} - D\chi^{\alpha}\left|\dot{\gamma}^{\alpha}\right| \tag{6.2}$$

where C and D are direct hardening and dynamic recovery coefficients, respectively.

Cyclically deformed crystalline material with dislocation substructure often contains matrix and slip bands. Slip bands are the regions with intense shear. It was observed that plastic strains in persistent slip bands (PSBs) of Cu are as much as two orders of magnitude higher than in the matrix (Winter, 1974). For α TiAl at room temperature, a slip band is a 'soft' region with lower slip resistance due to breakdown of short range order (SRO) between Ti and Al atoms (Neeraj and Mills, 2001). This softening effect causes strong plastic strain localization in the slip band and should be considered in the crystal plasticity constitutive relations. In this study, a shear-enhanced evolution law of the threshold stress is employed to account for this softening effect to simulate the initiation and propagation of a slip band within single crystal α Ti-5Al. It should be noted that the elastic stiffness of the points within the slip band is assumed to be identical to that of the matrix. To incorporate the softening effect of the slip band, the threshold stresses for prismatic and basal systems are given by

$$\kappa^{\alpha}{}_{prism} = \kappa_1^{\alpha}\Big|_{prism} + A(\tau_{Pyr1} - \tau_{Pyr2}) + \kappa_s^{\alpha}\Big|_{prism} \tag{6.3}$$

$$\kappa^{\alpha}{}_{basal} = \kappa_1^{\alpha}\Big|_{basal} + \kappa_s^{\alpha}\Big|_{basal} \tag{6.4}$$

where $\kappa_1^{\alpha}\Big|_{basal} = \kappa_1^{\alpha}\Big|_{prism}$ are constants for single crystal α Ti-5Al, and $\kappa_s^{\alpha}\Big|_{basal}$ and $\kappa_s^{\alpha}\Big|_{prism}$ respectively incorporate softening of basal and prismatic slip systems associated with breakdown of short range order due to dislocation glide at room temperature. The second term of Eq. (6.3) corresponds to core spreading effects, as described in Chapter 2. A similar definition of the threshold stress has been used in Chapter 4 for α phase of Ti-6Al-4V. The softening terms in Eqs. (6.3) and (6.4) follow the evolution laws

$$\dot{\kappa}_s^{\alpha}\Big|_{prism} = -\mu\left(\xi\kappa_s^{\alpha}\Big|_{prism}\left|\dot{\gamma}^{\alpha}\right|\right) \tag{6.5}$$

$$\dot{\kappa}_s^{\alpha}\Big|_{basal} = -\mu\left(\xi\kappa_s^{\alpha}\Big|_{basal}\left|\dot{\gamma}^{\alpha}\right|\right) \tag{6.6}$$

where μ is a constant and ξ is the softening coefficient. Contrary to the uniform evolution law of threshold stress for all basal and prismatic slip systems used in Chapter 4 and Zhang et al. (2007), a softening criteria is employed here to trigger the softening of the threshold stress, i.e.,

$$\xi = \begin{cases} 1 & \gamma_{crit} \le \left|\gamma^{\alpha}\right| < \gamma_{saturate} \\ 0 & otherwise \end{cases} \qquad \gamma^{\alpha} = \int \dot{\gamma}^{\alpha} dt \tag{6.7}$$

where γ_{crit} and $\gamma_{saturate}$ are the threshold and saturated plastic shear strain, respectively. The magnitude of plastic shear $\left|\gamma^{\alpha}\right|$ for the α^{th} slip system is used to trigger the softening of κ_s^{α}. It is noted that the criteria is based on plastic shear strain due to the fact that the leading dislocations destroy the short range order (SRO), manifesting a softening effect

on the glide plane (Neeraj and Mills, 2001). As a result, further slip concentrates in the same glide plane. Following dislocations do not destroy or restore the SRO and therefore have no softening effect. Hence, saturated plastic shear strain $\gamma_{saturate}$ is used to prohibit further softening of the threshold stress with increasing slip. The initial value of $\kappa_s^\alpha\big|_{prism,basal}$ is given by

$$\kappa_s^\alpha\big|_{prism,basal} = \kappa_s\left(0\right) \tag{6.8}$$

The softening effect applies only to basal and prismatic slip systems. The threshold stress does not evolve (i.e., $\dot{\kappa}^\alpha = 0$) for pyramidal slip systems. The threshold stress for pyramidal systems is defined as

$$\kappa^\alpha\big|_{pry} = \kappa_1^\alpha \tag{6.9}$$

In this study, the same κ_1^α is assumed for all slip systems. To account for the higher slip resistance (CRSS) of pyramidal slip systems, larger drag stresses are assigned to the pyramidal systems.

The constitutive equations are summarized in Table 6.1. All material parameters are listed in Table 6.3. The material constants are obtained by fitting the stress-strain response of single crystal α Ti5Al as reported in Section 6.3.2. The crystal plasticity algorithm has been implemented into ABAQUS via a UMAT subroutine (ABAQUS, 2005).

Table 6.1 Constitutive equations for α Ti5Al.

Flow Rule:

$$\dot{\gamma}^{\alpha} = \dot{\gamma}_o \left\langle \frac{\left|\tau^{\alpha} - \chi^{\alpha}\right| - \kappa^{\alpha}}{D^{\alpha}} \right\rangle^{m} \operatorname{sgn}\left(\tau^{\alpha} - \chi^{\alpha}\right) \quad \text{for all slip systems}$$

Evolution Equations for Hardening Variables:

Back stress

$$\dot{\chi}^{\alpha} = B\dot{\gamma}^{\alpha} - C\chi^{\alpha}\left|\dot{\gamma}^{\alpha}\right|$$

Threshold stress

$$\kappa^{\alpha}{}_{prism} = \kappa_1^{\alpha}\Big|_{prism} + A(\tau_{Pyr1} - \tau_{Pyr2}) + \kappa_s^{\alpha}\Big|_{prism} \qquad \dot{\kappa}_s^{\alpha}\Big|_{prism} = -\mu\left(\xi\kappa_s^{\alpha}\Big|_{prism}\left|\dot{\gamma}^{\alpha}\right|\right)$$

$$\kappa^{\alpha}{}_{basal} = \kappa_1^{\alpha}\Big|_{basal} + \kappa_s^{\alpha}\Big|_{basal} \qquad \dot{\kappa}_s^{\alpha}\Big|_{basal} = -\mu\left(\xi\kappa_s^{\alpha}\Big|_{basal}\left|\dot{\gamma}^{\alpha}\right|\right)$$

$$\kappa^{\alpha}{}_{pry} = \kappa_1^{\alpha}\Big|_{pry} \qquad \dot{\kappa}^{\alpha}_{pry} = 0$$

$$\kappa_s^{\alpha}\Big|_{prism}(0) = \kappa_s^{\alpha}\Big|_{basal}(0) = \kappa_s(0)$$

$$\xi = \begin{cases} 1 & \gamma_{crit} \le \left|\gamma^{\alpha}\right| < \gamma_{saturate} \\ 0 & otherwise \end{cases} \qquad \gamma^{\alpha} = \int \dot{\gamma}^{\alpha} dt$$

Drag stress

$$\dot{D}^{\alpha} = 0$$

6.3 Single Crystal α Ti5Al Oriented for Double Prismatic Slip

Finite element simulations are performed to simulate the cyclic deformation behavior of single crystal α Ti-5Al oriented for double prismatic slip. Completely-reversed strain-controlled deformation is applied. The simulation results are then compared with the experimental data reported by Xiao and Umakoshi (2002) in terms of stress-strain response and slip bands.

6.3.1 Finite Element Model

To simulate the cyclic deformation behavior of single crystal α Ti-5Al oriented for double prismatic slip at various strain amplitudes, a finite element model containing 19×60 4-node square elements with reduced integration (CPEG4R) (ABAQUS, 2005) was created, as shown in Fig. 6.2. Each reduced integration element has one integration point, therefore significantly reduce computational cost. For first-order reduced integration elements (e.g., CPEG4R), the uniform strain (one integration point) is assumed for the element which equals to the average strain over the element volume (ABAQUS, 2005). The constitutive model is fully 3D. To incorporate deformation in the third (z) direction, generalized plane strain elements are used. Generalized plane strain implementation used in ABAQUS assumes that the model lies between two bounding planes, which may move parallel with respect to each other, thus causing strain of the "thickness direction" fibers of the model (ABAQUS, 2005). The two bounding planes are free of traction. Generalized plane strain elements are typically used to model a section of a long structure that is free to expand.

For all simulations, displacement is specified along the y direction on edges AB and CD with a strain rate of 3×10^{-4} s^{-1}. The crystallographic orientation angles are

assigned to the model such that $\left[2\bar{1}\bar{1}0\right]$ is parallel to the loading direction, as shown in Fig. 6.2, which is consistent with the experimental setup (Xiao and Umakoshi, 2002).

It is generally accepted that slip bands are triggered by material instabilities such as material defects, microvoid nucleation (Steninger and Melander, 1982), hard or soft inclusions (Sukumar et al., 2001), and so on. In previous modeling works on slip bands, prescribed perturbations were used as material defects to initiate the localized deformation in single crystal (Dao and Asaro, 1993; Sluys and Estrin, 2000; Zhou et al., 2005). The perturbations can be material imperfections, boundary constraints, inhomogeneities of the FE model, etc. In this study, lower initial threshold stress for prismatic and basal systems is used as a perturbation at selected integration points to trigger the slip band, i.e.,

$$\kappa^{\alpha}_{defects}\Big|_{prism,basal} = \kappa^{\alpha}_{1} \tag{6.10}$$

consistent with

$$\kappa^{\alpha}_{s(defects)}\Big|_{prism,basal}(0) = 0 \tag{6.11}$$

All other material parameters at perturbed integration points are identical to that of regular elements. This means that these points have already been pre-softened. It is noted that the regular elements have the same limiting threshold stress as the slip band softening saturates, i.e., $\kappa^{\alpha}_{s}\Big|_{prism,basal} \to 0$.

In Xiao and Umakoshi (2002), it was shown that the width of slip bands is close to 1.5 μm for cyclic strain amplitudes ranging from 0.2% to 0.8%. For the mesh shown in Fig. 6.2, each slip band is triggered by one perturbation element. Simulations with various element sizes and distributions of perturbation element (Section 6.5) show that the slip band usually spans 2 to 3 elements. For simplicity, the size of each element is set

to 0.5×0.5 μm. To simulate the behavior of bulk material with a model of dimension 9.5×30 μm, periodic boundary conditions are applied in both x and y directions. This boundary condition imposes constraints on the sides such that the opposite edges deform in the same manner. This implies that deformation pattern of edge AB must be same as that of edge CD, and deformation pattern of edge AC must be same as that of edge BD, as shown in Fig. 6.2.

Table 6.2. Wavelength, width and spacing of slip bands of single crystal a Ti-5Al oriented for double prismatic slip

Applied strain amplitude, $\Delta\varepsilon_t/2$	Width, l_w (μm) *	Spacing, l_s (μm) *	Wavelength, l_d (μm)
0.2%	1.5	2	3.5
0.4%	1.5	1.5	3
0.6%	1.1	0.9	2
0.8%	1	0.5	1.5

* Data from Xiao and Umakoshi (2002)

By applying periodic boundary conditions, the finite element model represents a periodic cell which requires the slip band structure to be periodic as well. Therefore, all defects are located along the line of symmetry of the FE model. Uniformly distributed perturbation elements with wavelength l_d are assigned along the y direction in the middle of the FE model. The wavelength l_d sets the wavelength of the slip bands, i.e.,

$$l_d = l_w + l_s \tag{6.12}$$

where l_w and l_s are the width and spacing of slip bands, respectively, as illustrated in Fig. 6.3. Xiao and Umakoshi (2002) showed that l_w and l_d depend on the applied strain amplitude, as shown in Table 6.2.

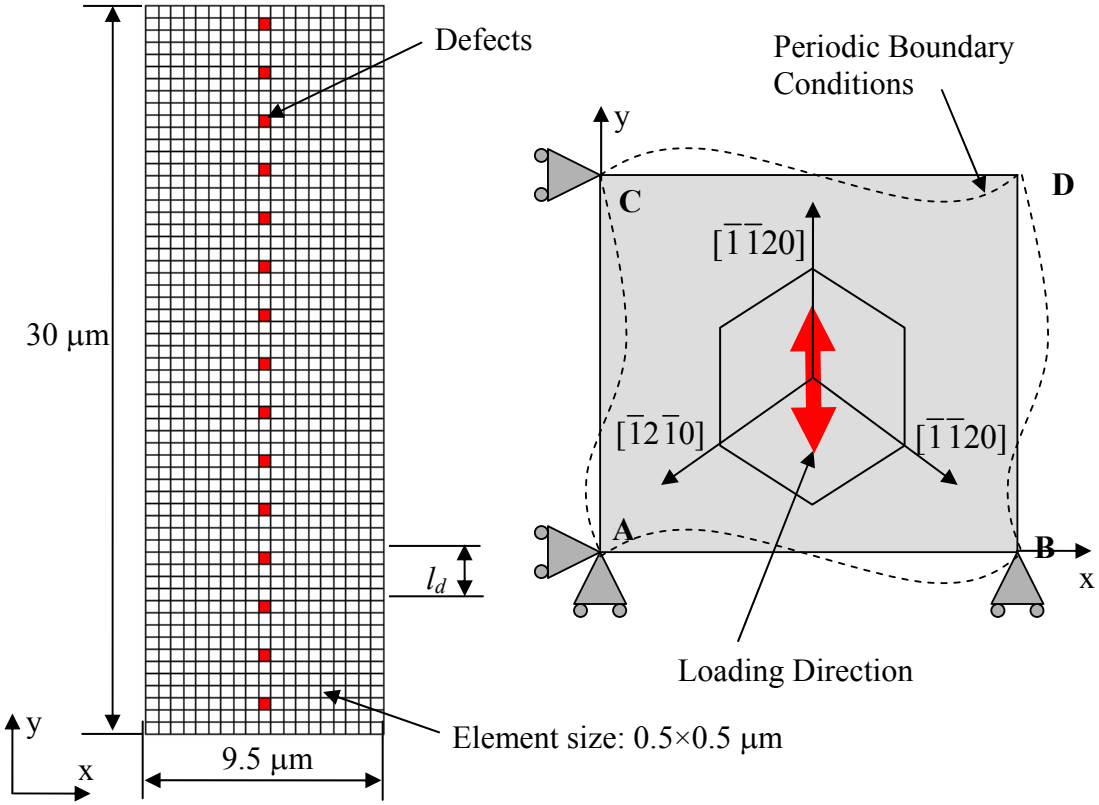

Figure 6.2. Finite element model.

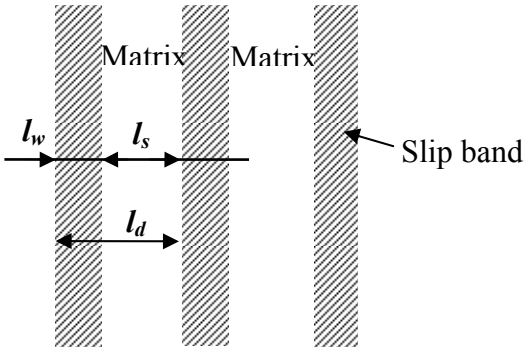

Figure 6.3. Illustration of slip band structure.

6.3.2 Simulation Results

Prior to performing the cyclic simulations, parameters of the crystal plasticity model are calibrated by fitting the stress-strain response for an applied cyclic strain amplitude at $\Delta\varepsilon_t/2 = 0.6\%$ of single crystal α Ti-5Al oriented for double prismatic slip as in Fig. 6.2 as reported in (Xiao and Umakoshi, 2002). It is noted that six hysteresis loops ranging from cycle 1 to cycle 2500 were given in Xiao and Umakoshi (2002). In this study, only the 1st, 5th and 50th loops are used to calibrate the model. The crystal plasticity model is then validated by comparing the simulation results and experimental data in terms of variation of the cyclic shear stress amplitude with number of loading cycles at different completely reversed applied strain amplitudes, $\Delta\varepsilon_t/2$.

Several material parameters, such as the elastic constants, can be obtained from the literature. It is noted that the direct hardening and dynamic recovery coefficients of the backstress only have a short range effect on the cyclic deformation behavior. Therefore, these two parameters can be determined by fitting the first hysteresis loop. The evolution of the threshold stress dominates the long range cyclic softening behavior of single crystal α Ti-5Al. The 5th and 50th loops can be used to calibrate the threshold plastic shear strain γ_{crit}, saturated plastic shear strain $\gamma_{saturate}$, and consistant μ.

The fitting results of the stress-strain responses at 1st, 5th and 50th cycles are shown in Figures 6.4 (a), (b) and (c), respectively. All material parameters are listed in Table 6.3. Following that described in Xiao and Umakoshi (2002), the cyclic shear stress amplitude $\Delta\tau_a/2$ was defined as the average of the absolute values of the maximum and minimum resolved shear stress on the $<1\bar{2}10>\{10\bar{1}0\}$ prismatic slip system. In Fig. 6.5, the simulation results of the variation of $\Delta\tau_a/2$ with number of loading cycles at $\Delta\varepsilon_t/2 =$ 0.2%, 0.4%, 0.6% and 0.8% are shown to be in good agreement with the corresponding experimental data during the first 50 loading cycles. The experimental data shows that a

saturation stage at $\Delta\tau_a/2 \approx 90$ MPa is reached for all loading cases after around 200 cycles. It is believed that the same result can be obtained from the simulations since the applied loading amplitude will not affect the minimum κ_s^α. The cyclic softening will cease as $\kappa_s^\alpha\big|_{\text{prism}} \to 0$ for all loading cases.

Figure 6.6 shows the contours of effective plastic strain at $\Delta\varepsilon_t/2 = 0.6\%$, defined by $\bar{\boldsymbol{\varepsilon}}^p = \sqrt{(2/3)\boldsymbol{\varepsilon}^p : \boldsymbol{\varepsilon}^p}$, where $\boldsymbol{\varepsilon}^p = \sum_\alpha \gamma^\alpha \left(\mathbf{s}_0^\alpha \otimes \mathbf{m}_0^\alpha\right)_{sym}$, at the 1st, 10th and 50th loading cycles. In Fig. 6.5, it is shown that the variation of the cyclic shear amplitude is relatively low for the first 5 cycles. This phenomenon can be attributed to the relatively homogeneous plastic deformation within the single crystal except the regions around the defects, as shown in Fig 6.6(a). Clearly, the slightly heterogeneous slip around the defect has insignificant influence on the macroscopic stress-strain responses of the initial several cycles. With increasing number of loading cycles, strongly heterogeneous slips develop due to softening of the threshold stress of elements within the slip band. In Fig. 6.6(c), it is shown that the effective plastic strain in the slip band is about 3 times larger than that in the matrix at the 50th cycle. Similar to the transmission electron microscopy (TEM) observations (Xiao and Umakoshi, 2002), two slip bands along prismatic slip planes can be seen from the Fig. 6.6(b) and 6.6(c) since the single crystal α Ti-5Al is oriented for double prismatic slip. The maximum effective plastic strain can be found at "defect elements" for which lower slip resistance is assumed. A larger effective plastic strain can also be found at the elements where slip bands cross. At the same time, $\Delta\tau_a$ significantly decreases with increasing number of loading cycles.

Figures 6.6(b) and 6.6(c) show that slip bands on two prismatic systems are equally developed, resulting in an interference pattern. Two slip bands can easily cross each other with relatively low resistance since these planar bands are dominantly populated by screw dislocations. The same phenomenon was observed in the experiments (Xiao and Umakoshi, 2002).

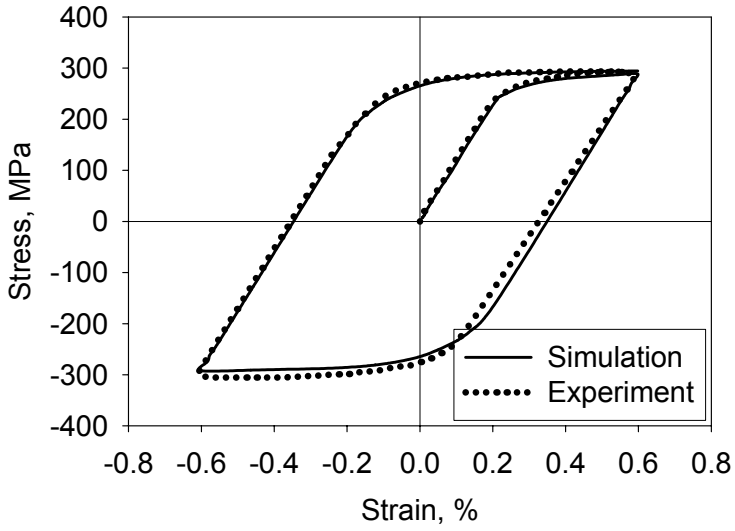

(a) 1st cycle

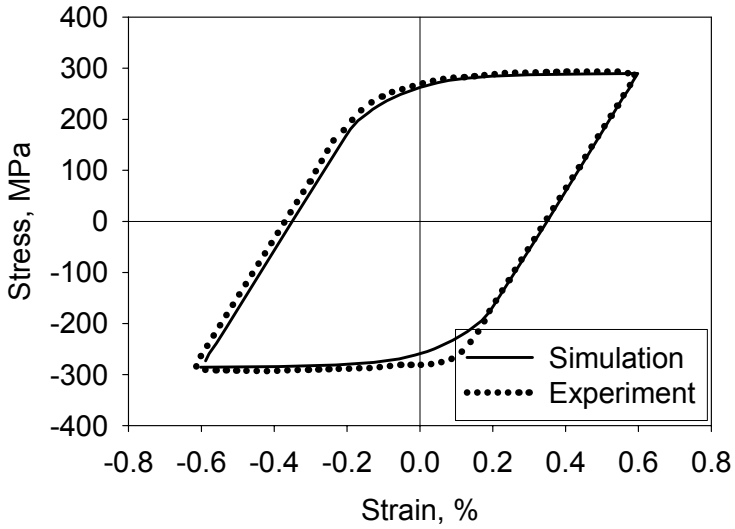

(b) 5th cycle

Figure 6.4. Hysteresis loops for different cycles.

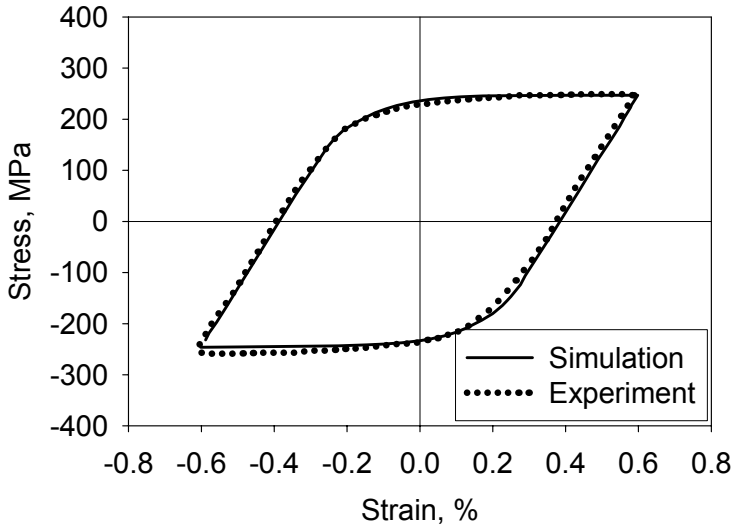

(c) 50th cycle

Figure 6.4. Hysteresis loops for different cycles (cont.).

Table 6.3. Material constants.

Property	Value	Property	Value	Property	Value
C_{11}	170,400 MPa	D_0^{basal}	40 MPa	C	1000
C_{12}	92,000 MPa	D_0^{prism}	40 MPa	D	50
C_{13}	69,000 MPa	$D_0^{pyr\langle a\rangle}$	100 MPa	m	15
C_{33}	180,700 MPa	$D_0^{pyr\langle c+a\rangle}$	200 MPa	γ_{crit}	0.0005
C_{44}	46,700 MPa	κ_1	30 MPa	$\gamma_{saturate}$	0.0015
$\dot{\gamma}_o$	0.001 s^{-1}	$\kappa_s^{\alpha}\big\vert_{prism,basal}(0)$	40 MPa	μ	5

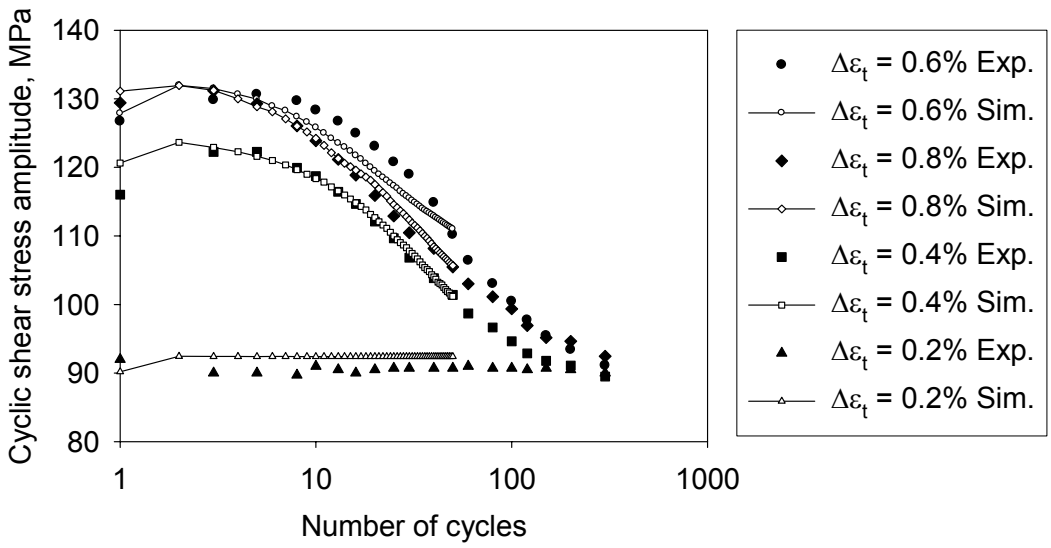

Figure 6.5. Variation of $\Delta\tau_a/2$ with number of loading cycles.

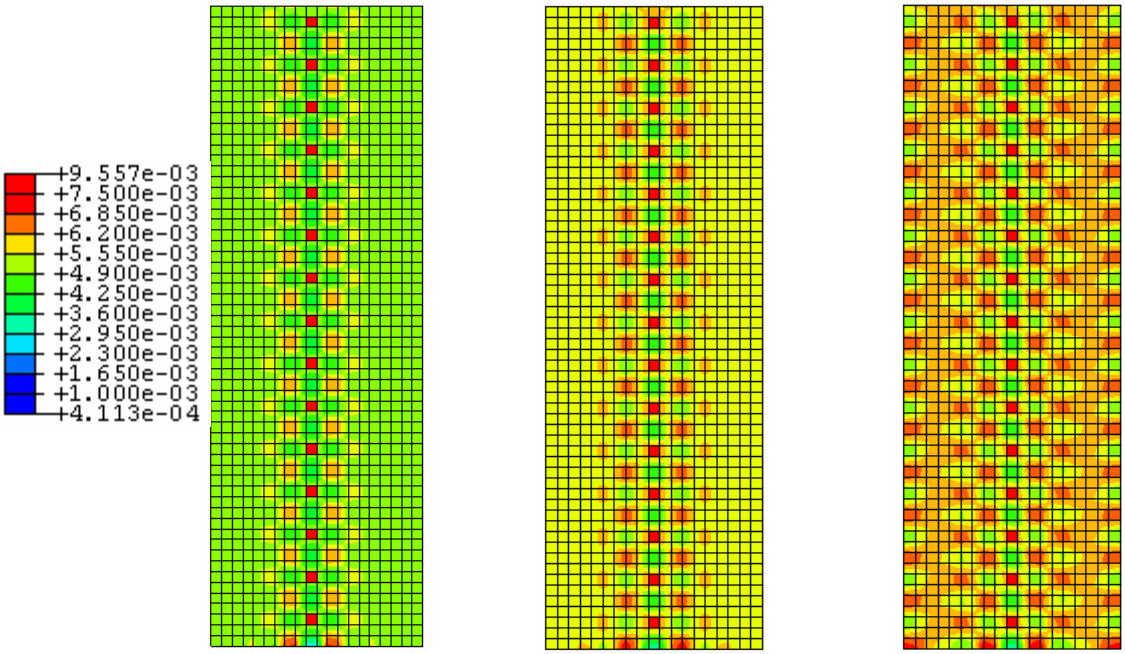

(a) 1st cycle (b) 10th cycle (c) 50th cycle

Figure 6.6. Distribution of the effective plastic strain at the peak of the cycle for $\Delta\varepsilon_t/2 = 0.6\%$.

6.3.3 Fatigue Indicator Parameters (FIPs)

In addition to the deformation behavior, the fatigue behavior of the single crystal α Ti-5Al is also investigated. Two nonlocal FIPs, Fatemi-Socie (FS) (1988) parameters P_{FS} and maximum plastic shear strain amplitude P_{γ}, are used, which are respectively given by Eqs. (1.22) and (1.23).

As discussed in Chapter 2, nonlocal FIPs are to capture crack formation driving force over a finite process zone size. In this study, four different averaging areas are used for the FIPs: 0.5×0.5 μm, 1×1 μm, 1.5×1.5 μm, and 2×2 μm, as illustrated in Fig. 6.7. FIPs calculated over each single element can be considered as the averaged FIPs over an area of 0.5×0.5 μm, since the size of each element is 0.5×0.5 μm. For averaging area larger than 0.5×0.5 μm, the FIPs of the black domain in Fig. 6.7 are calculated by averaging the stress and plastic strain over the grey areas with 4, 9 and 16 elements. Since periodic boundary conditions are used in the simulations, for the elements close to boundary, the averaging area contains the elements at the opposite boundary, as shown in Fig. 6.7.

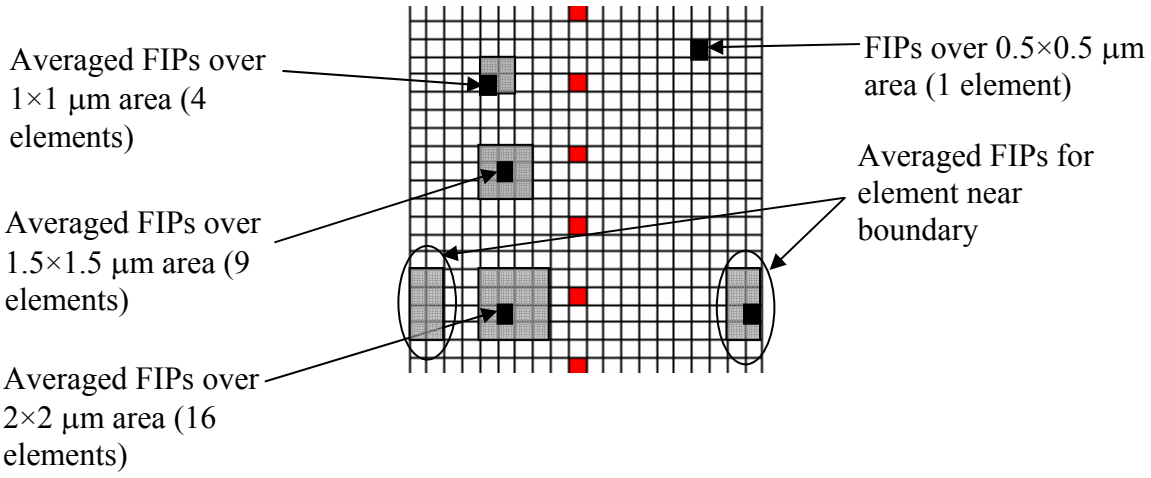

Figure 6.7. Scheme of averaged calculation of FIPs.

The frequency distributions of two nonlocal FIPs averaged over each single element (0.5×0.5 μm) at the 50th cycle for $\Delta\varepsilon_t/2 = 0.6\%$ are shown in Fig. 6.8. It should be noted that different scales are used for two parameters. It is shown that two parameters have similar "bimodal" distributions with two distinct peaks. For example, the frequency distribution of P_γ has peaks at $P_\gamma = 0.002$ and $P_\gamma = 0.005$. This observation is contrary to the uni-modal distribution of the FIPs obtained in pervious works on polycrystalline Ni-based alloy and Ti-6Al-4V (Shenoy, 2006; Zhang et al., 2006a). Clearly, two distinct deformation regions in the model, slip bands and matrix, result in the bi-modal distribution of the FIPs. The FIPs in the slip band are much larger (2 to 3 times) than in the matrix.

Figure 6.8 shows that only a few percent of elements have the highest fatigue indicator parameters. For example, about 5% elements have a FS parameter larger than 0.013. It is believed that the maximum FIPs can generally be found at the material defects and/or the elements where the slip bands cross and reinforce. For material defects and the elements where the slip bands cross, both the effective plastic strain and the resolved plastic shear strain significantly increase due to double prismatic slip. Thus, for the given loading condition, the microscopic crack can nucleate from the material defects and/or regions where slip bands cross and then propagate along the slip band.

Crack formation of α Ti-5Al is related to irreversible to and fro slip in slip bands. The overall distributions of two shear-dominated FIPs are somewhat similar. Among these shear-dominated FIPs, the FS parameter includes the maximum normal stress to the critical plane and therefore is considered to be more suitable than P_γ for purposes of correlating fatigue crack formation and early growth (McDowell, 1996).

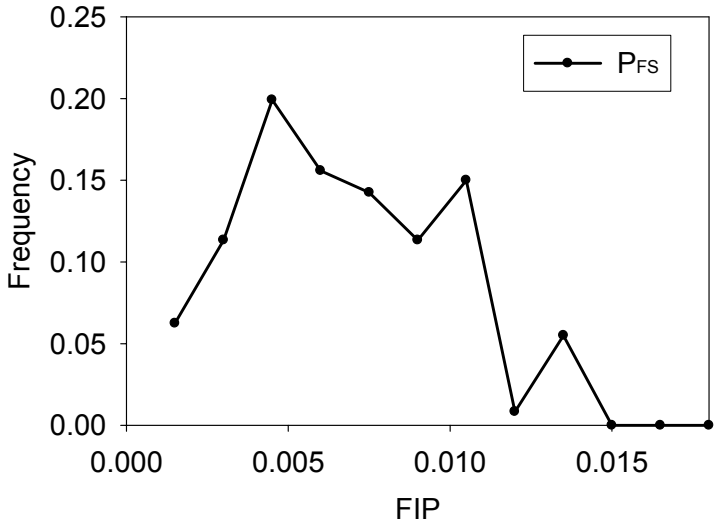

(a) Fatemi-Socie parameter

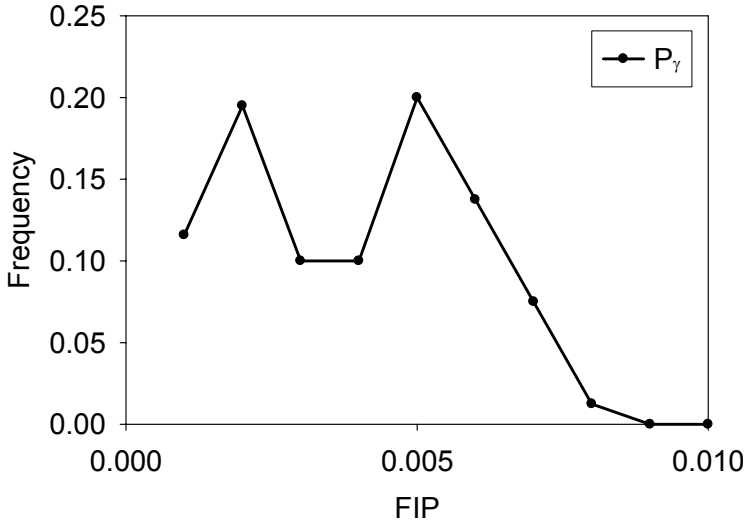

(b) Maximum plastic shear strain amplitude

Figure 6.8. Frequency distribution of nonlocal FIPs at the 50th cycle for $\Delta\varepsilon_t/2 = 0.6\%$, with 0.5×0.5 μm averaging area.

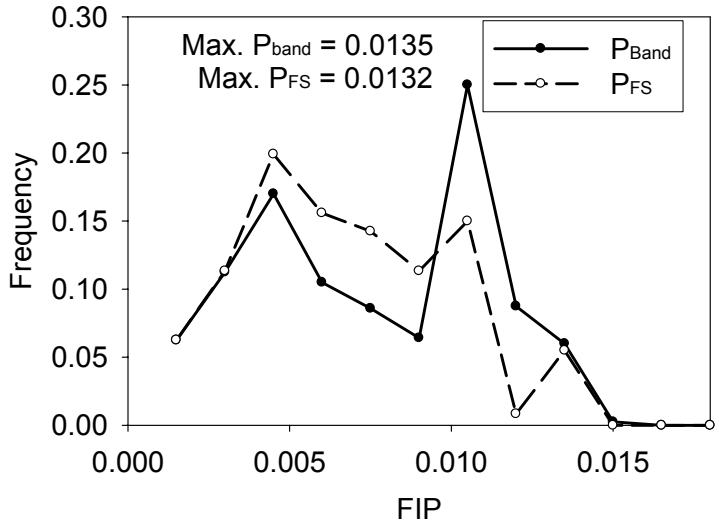

Figure 6.9. Frequency distributions of nonlocal P_{FS} and P_{band} at the 50th cycle for $\Delta\varepsilon_t/2 = 0.6\%$, with 0.5×0.5 μm averaging area.

Experimental observations show that cracks generally form along slip bands. Equation (6.13) shows that the FS parameter, P_{FS}, is calculated on the critical plane on which the maximum range of the plastic shear strain is found; P_{FS} does not consider the influence of the possible dislocation structures within the crystals that organize in accordance with crystallographic planes. Therefore, another nonlocal FIP, P_{band}, is proposed in this study to account for the intense shear along crystallographic slip planes, i.e.,

$$P_{band} = \frac{\Delta\gamma_{band}^{p*}}{2}\left(1 + K'\frac{\sigma_{band}^{\max*}}{\sigma_y}\right) \tag{6.13}$$

where $\Delta\gamma_{band}^{p*}$ is the nonlocal amplitude of the maximum plastic shear strain along all possible slip bands and $\sigma_{band}^{\max*}$ is the nonlocal maximum normal stress acting on the slip

band during a loading cycle. The constant *K'* is assumed to equal to *K* of Eq. (6.15). It is noted that the definition of P_{band} is nearly identical to that of P_{FS}.

Figure 6.9 compares the frequency distributions of nonlocal P_{FS} and P_{band} at the 50^{th} cycle for $\Delta\varepsilon_t/2 = 0.6\%$, with $0.5\times0.5\mu m$ averaging area. These two parameters display a similar bimodal distribution, but the values of P_{band} are larger than those of P_{FS} for most elements. P_{band} will be used in this study to investigate the variation of the fatigue crack formation life with respect to applied strain amplitude.

As shown in Fig. 6.6, the effective plastic strain of slip bands increases with increasing number of loading cycles. At the same time, Figure 6.5 shows that the cyclic shear stress amplitude decreases with increasing number of loading cycles due to the cyclic softening of the single crystal. Thus, P_{band} evolves with number of loading cycles. Figure 6.10 shows the frequency distribution of P_{band} calculated over single element at 1^{st}, 5^{th}, 30^{th} and 50^{th} cycles. It is shown that the frequency distribution of P_{band} is almost unchanged while the value of P_{band} slightly increases during the first 10 loading cycles. At the 30^{th} and 50^{th} cycle, bimodal distributions of P_{band} develop. The maximum value of P_{band}, P_{band}^{max}, increases with number of loading cycles. In Fig. 6.10, a small change of P_{band}^{max} occurs after 30^{th} cycle. The fraction of elements with higher P_{band} increases due to the development of the slip band, which affects probability of fatigue crack formation.

Figure 6.11 shows that the maximum P_{band} increases with number of loading cycles as slip band intensifies. It is found that a nearly constant value of P_{band} is reached after about 40 cycles. The reason is believed to be the decrease of the normal stress on the slip band due to the cyclic softening. At the same time, the increase of cyclic plastic shear strain within the slip band is much slower as $\kappa_s^{\alpha}\big|_{prism,basal} \to 0$. Therefore, the stable maximum P_{band} after the 40^{th} cycle should be used for purposes of correlating fatigue crack formation and early growth. In this study, P_{band} at 50^{th} cycle is used since only 50 loading cycles are applied.

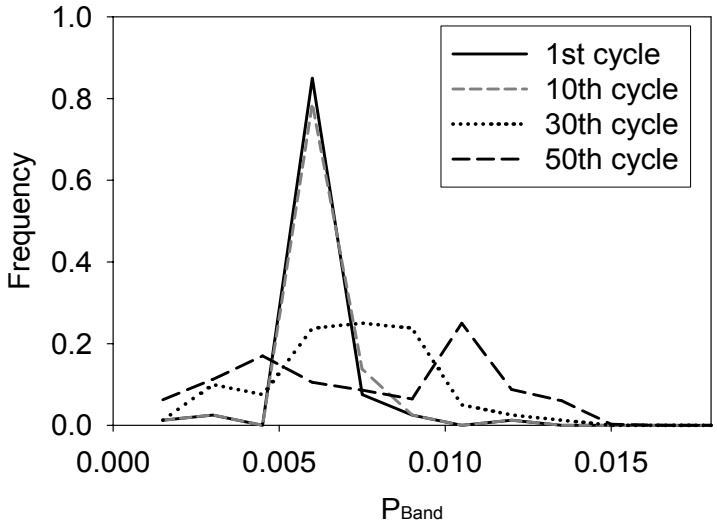

Figure 6.10. Frequency distribution of P_{band} with number of loading cycles for $\Delta\varepsilon_t/2$ = 0.6%, with 0.5×0.5 μm averaging area.

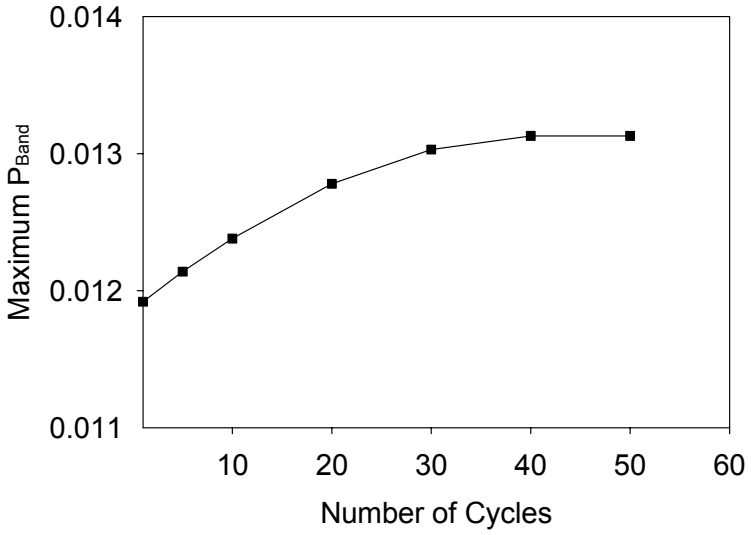

Figure 6.11. Variation of maximum P_{band} with number of loading cycles for $\Delta\varepsilon_t/2$ = 0.6%, with 0.5×0.5 μm averaging area.

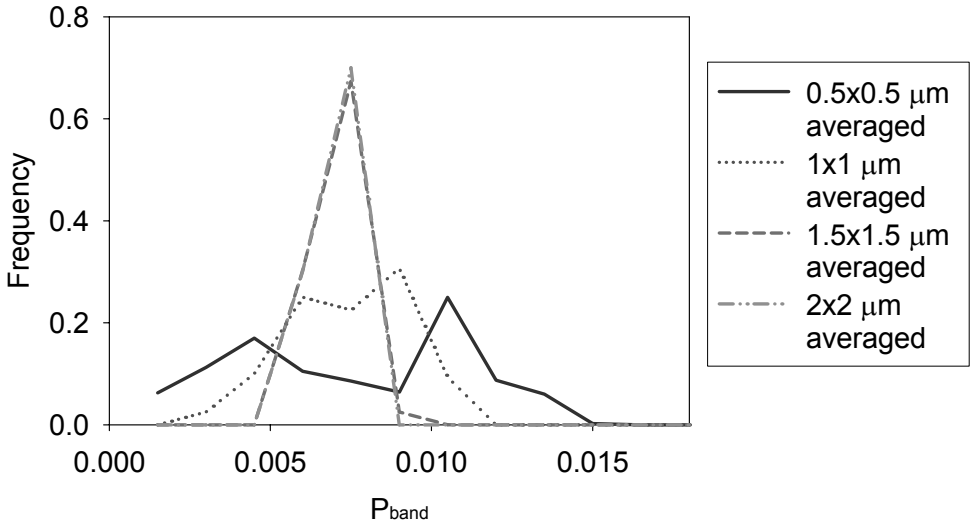

Figure 6.12. Frequency distribution of averaging P_{band} at the 50th cycle for $\Delta\varepsilon_t/2 = 0.6\%$.

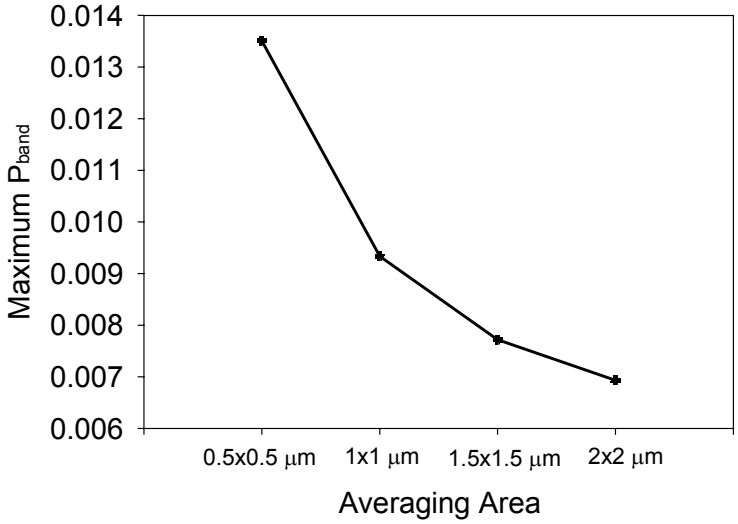

Figure 6.13. Variation of maximum P_{band} with averaging area at the 50th cycle for $\Delta\varepsilon_t/2 = 0.6\%$.

The nonlocal FIPs reported to this point have been obtained from the single element calculation with averaging size of 0.5×0.5 μm. To explore effects of averaging volume size, three other different averaging areas are used: 1×1 μm, 1.5×1.5 μm, 2×2 μm, as illustrated in Fig. 6.7. Figure 6.12 shows the frequency distributions of nonlocal P_{band} calculated over various averaging area at the 50th cycle for $\Delta\varepsilon_t/2$ = 0.6%. The 0.5×0.5 μm averaging P_{band} shows a bi-modal type of distribution which spread over a large range. With increasing averaging area, uni-modal distributions of P_{band} are displayed with peak P_{band} of about 0.007. The strong contrast between slip band and matrix can be effectively removed by this averaging process. Figure 6.13 shows that the maximum P_{band} decreases with increasing averaging area. Thus, the prediction of the crack formation life depends on the averaging area. It is noted that for the amplitude of applied strain ranging from 0.2% to 0.8%, the minimum wavelength of the slip bands is 1.5 μm, as shown in Table 6.1. We may assert that the proper averaging length scale should respect both characteristic length of crack embryos at nucleation and intensification of slip in the slip bands. Accordingly, we suggest an averaging area of 1/2 the slip band width as a characteristic averaging length scale. In this case, it is approximately the element size.

6.3.4 Prediction of Fatigue Crack Formation

The maximum P_{band} values averaged over 0.5×0.5 μm, 1×1 μm, and 1.5×1.5 μm area at the 50th cycle are referred to as $P^{0.5}_{fatigue}$, $P^{1}_{fatigue}$ and $P^{1.5}_{fatigue}$, respectively. The finite element simulations are carried out at various amplitude of the applied strain $\Delta\varepsilon_t/2$. Approximate linear relations between $P^{0.5}_{fatigue}$, $P^{1}_{fatigue}$ and $P^{1.5}_{fatigue}$ and $\Delta\varepsilon_t/2$ are shown in Fig. 6.14. $P^{0.5}_{fatigue}$ is much larger than $P^{1}_{fatigue}$ and $P^{1.5}_{fatigue}$ for $\Delta\varepsilon_t/2 > 0.4\%$ due to the intense

plastic shear within the slip band. $P^{1}_{fatigue}$ and $P^{1.5}_{fatigue}$ average over both slip band and matrix, and therefore are unable to distinguish the shear localization of the slip band. The FIP $P^{0.5}_{fatigue}$ can be related to the crack formation life using Coffin-Manson relation

$$P^{0.5}_{fatigue} = \gamma_f^{'}(2N_f)^{c'} \tag{6.14}$$

where $\gamma_f^{'}$ and c' can be obtained by fitting the fatigue lives at various $\Delta\varepsilon_t/2$ as reported in (Xiao and Umakoshi, 2002). In this study, fatigue lives at $\Delta\varepsilon_t/2$ = 0.4%, 0.6% and 0.8% are used to determine the constants of Coffin-Manson relation. A constraint is imposed on the constant c', which is known to lie in the range from -0.5 to -0.7 for most metals. For Ti-6Al-4V deformed at room temperature, c' is reported to range from -0.51 to -0.67 when various FIPs were used to fit biaxial test data (Gallagher et al., 2005). Figure 6.15 shows results of fitting with two constants $\gamma_f^{'} = 0.95$ and $c' = -0.51$. The correlated fatigue lives agree well with experimental data. It should be noted that the arrow in Fig. 6.15 indicates run-out of the fatigue life at $\Delta\varepsilon_t/2$ = 0.2%, means that no failure was observed during applied loading cycles with the test stopped at 10^4 cycles.

As discussed before, the averaging length scale should respect the critical length of crack embryos at nucleation. However, critical crack length corresponding to failure used in fatigue tests was not given in (Xiao and Umakoshi, 2002). Therefore, two constants obtained here should not be directly used for other loading histories. Although not offering a prediction per se, this exercise demonstrates that this methodology can be used for other amplitudes to correlate fatigue life.

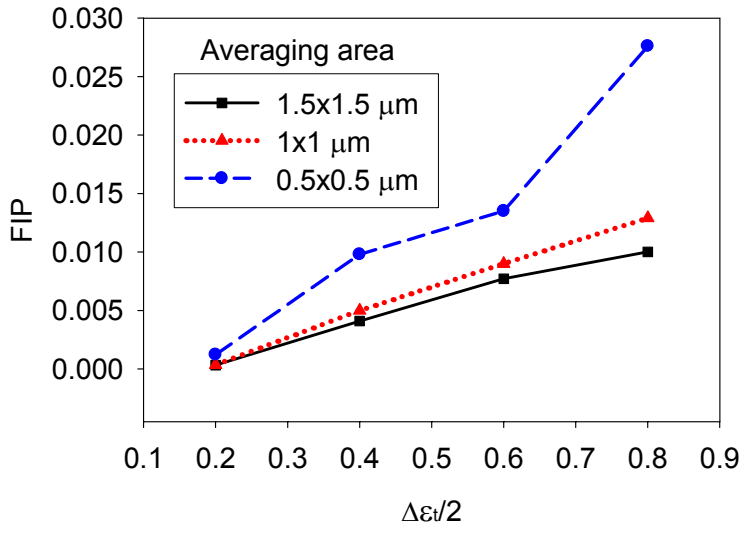

Figure 6.14. Variation of maximum $P_{fatigue}$ at the 50th cycle with applied strain amplitude $\Delta\varepsilon_t/2$.

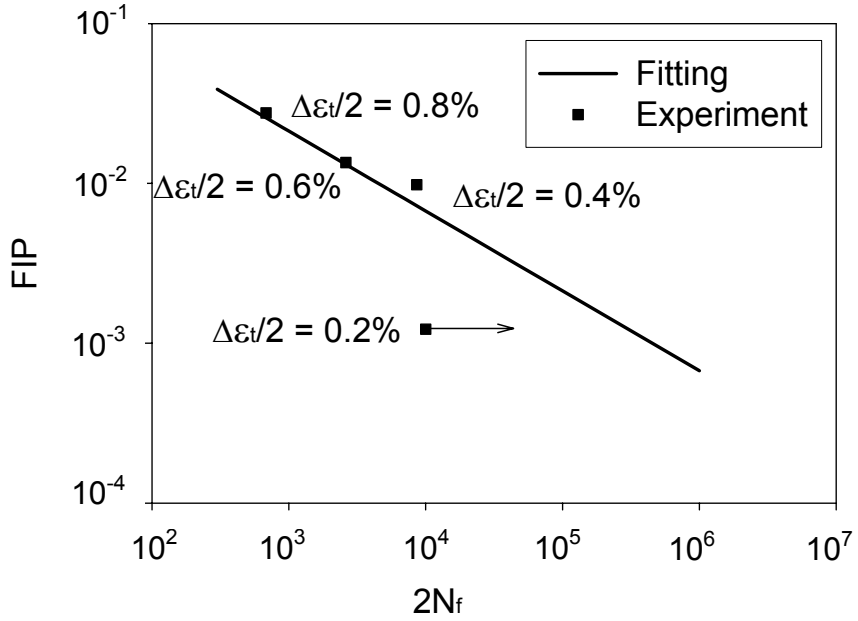

Figure 6.15. Fitting for Coffin-Manson relation with $P_{fatigue}^{0.5}$ for single crystal α Ti5Al orientated for double prismatic slip.

6.4 Single Crystal α Ti-5Al Oriented for Single Prismatic Slip

In the last section, finite element simulations are performed to simulate the cyclic deformation behavior of single crystal α Ti-5Al oriented for double prismatic slip. The simulation results are shown to calibrate well with the experimental data reported by Xiao and Umakoshi (2002). In this section, the same methodology and material constants will be used to predict the deformation and fatigue of single crystal α Ti-5Al oriented for single prismatic slip, a geometry not used to calibrate any aspects of the model. To validate the approach and material constants reported in last section, the simulation results are compared with the experimental data reported in Xiao and Umakoshi (2003).

6.4.1 Finite Element Model

The generalized plane strain finite element model for single prismatic slip is shown in Fig. 6.16. The model contains 4-node square elements with reduced integration (CPEG4R) (ABAQUS, 2005), as described in last section. Periodic boundary conditions are applied in both x and y directions. Fully-reversed strain-controlled deformation is applied along the y direction at a strain rate of 3×10^{-4} s^{-1} at room temperature. To enforce single prismatic slip, the crystal is oriented in such way that the Schmid factor of the most favored (1100) prismatic slip system is 0.5, as shown in Fig. 6.16.

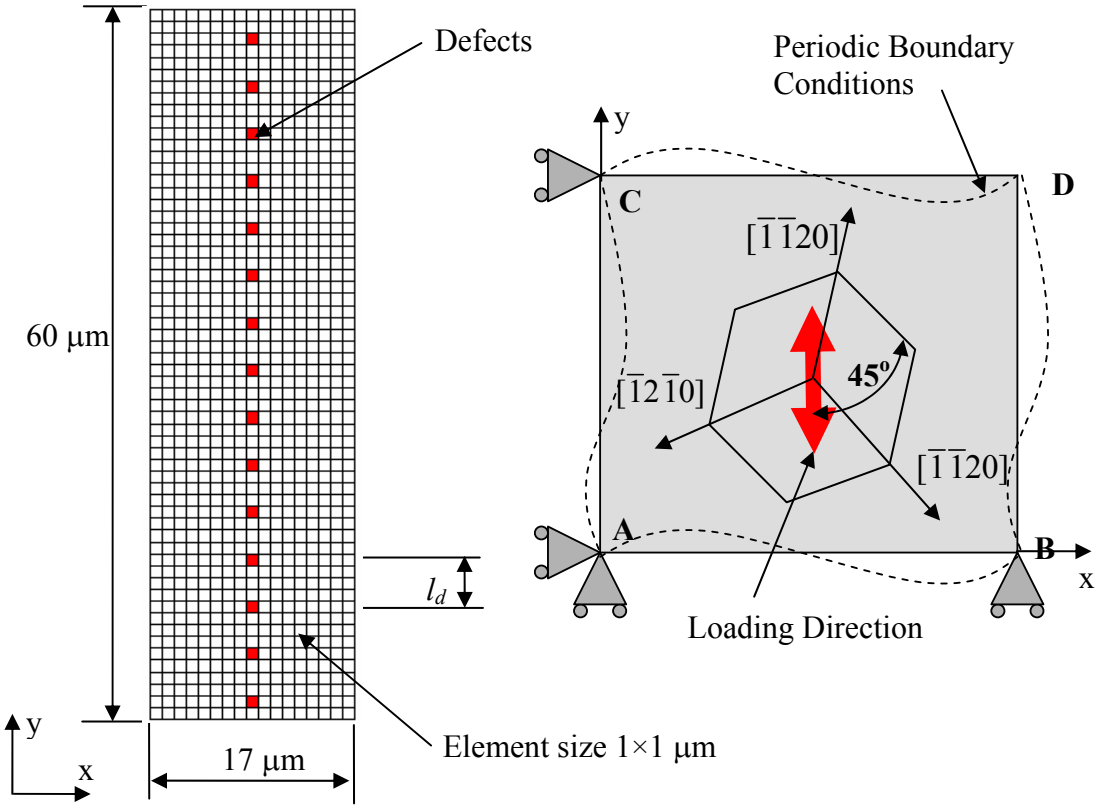

Figure 6.16. Finite element model for single prismatic slip.

Table 6.4. Wavelength, width and spacing of slip bands of single crystal a Ti5Al oriented for single prismatic slip.

Applied strain amplitude	Width, l_w (μm) *	Spacing, l_s (μm) *	Wavelength, l_d (μm)
0.2%	2.5	1.5	4
0.3%	2.6	1.4	4
0.4%	2.7	1.3	4
0.6%	2.8	1.2	4
0.8%	3	1	4
1.0%	3	1	4

* Data from Xiao and Umakoshi (2003)

In Xiao and Umakoshi (2003), the amplitudes of completely-reversed strain range from 0.2% to 1.0%. The width, spacing and wavelength of slip bands for $\Delta\varepsilon_t/2$ = 0.2%, 0.3%, 0.4%, and 0.6% reported by Xiao and Umakoshi (2003) are summarized in Table 6.3. The parameters of slip bands for $\Delta\varepsilon_t/2$ = 0.8% and 1.0% in Table 6.3 are assumed based on the tendency of reported parameters. The widths of slip bands are shown to range from 2.5μm to 3μm. The size of each element is set to 1×1 μm. To enforce the periodic structure of slip bands, the width of the model (17μm) is determined by the wavelength of slip bands, as shown in Fig.6.16.

6.4.2 Simulation Results

Figure 6.17 shows the variation of $\Delta\tau_a/2$ with number of loading cycles at $\Delta\varepsilon_t/2$ ranging from 0.2% to 1.0%d 0.8%. The simulation predictions are shown to agree fairly well with the experimental data during first 50 loading cycles. This observation validates the crystal plasticity constitutive relations and material constants outlined in last Section.

Figure 6.18 shows the contours of effective plastic strain at $\Delta\varepsilon_t/2$ = 0.6 at the 1st, 10th and 50th loading cycles. The material defects are shown to have large value of $\bar{\boldsymbol{\varepsilon}}^p$ at the 1st cycle, as shown in Fig. 6.18(a). Relatively homogeneous plastic deformation within the single crystal is observed except the regions around the defects. This observation is close to the contour of $\bar{\boldsymbol{\varepsilon}}^p$ of a single crystal oriented for double prismatic slip, as shown in Fig. 6.6(a). In Fig. 6.17(a), the variation of the cyclic plastic shear strain amplitude is relatively low for the first few cycles. Combined with the simulations of double prismatic slip, it is concluded that the slightly heterogeneous slip around the defect has insignificant influence on the macroscopic stress-strain responses of the initial several cycles.

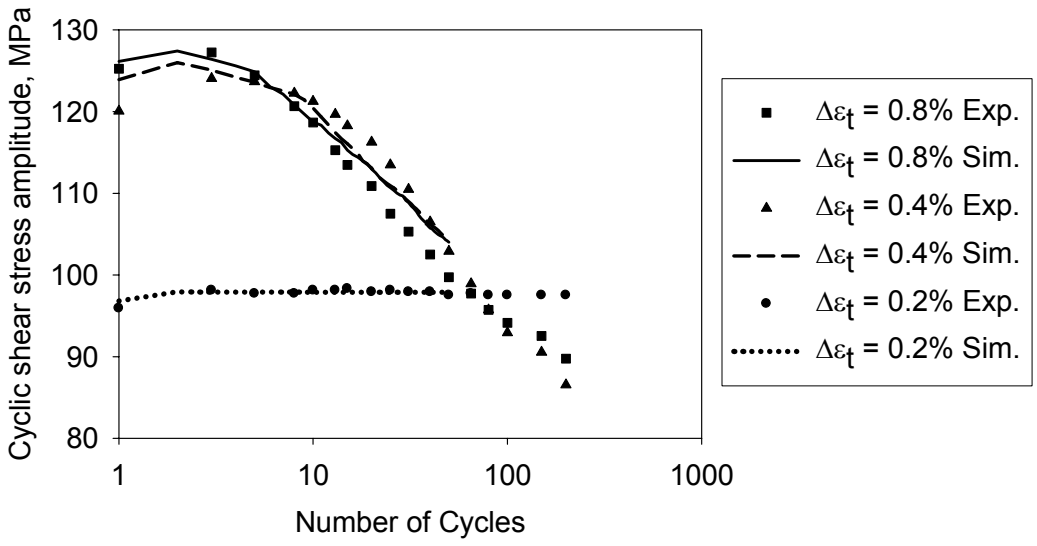

(a)

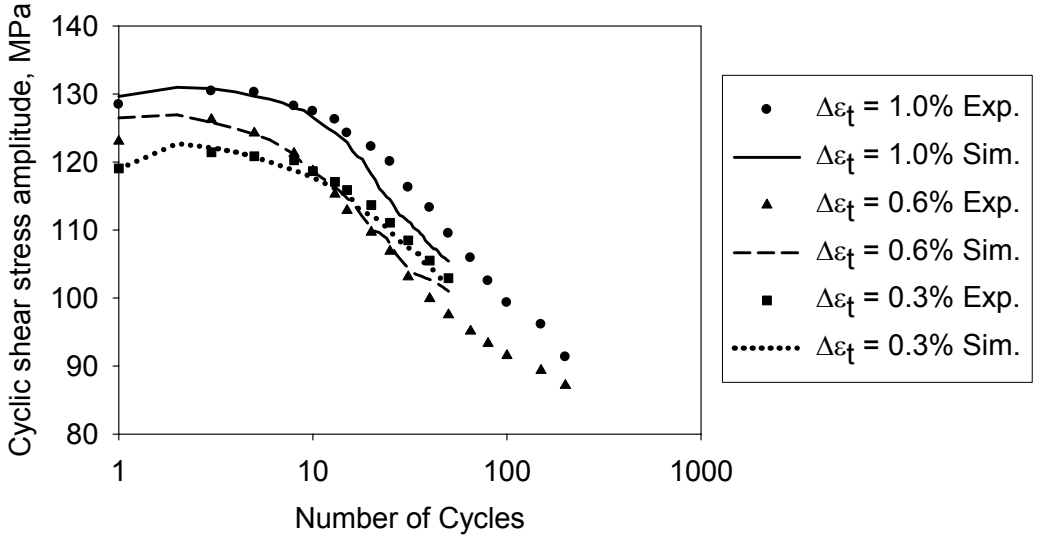

(b)

Figure 6.17. Variation of $\Delta\tau_a/2$ with number of loading cycles for (a) $\Delta\varepsilon_t/2$ = 0.2%, 0.4%, and 0.8% and (b) $\Delta\varepsilon_t/2$ = 0.3%, 0.6%, and 1.0%.

With increasing number of loading cycles, a single slip band system initiates and develops from the material defects, aligned with the favorable prismatic slip plane. The observation agrees with the TEM observations of Xiao and Umakoshi (2003). The

strongly heterogeneous slip is attributed to the softening of the threshold stress within the slip band. In Fig. 6.18(b), the slip band is shown to initiate and $\bar{\varepsilon}^p$ in slip band is about twice as higher as that of the matrix. The value of $\bar{\varepsilon}^p$ in slip band increases with increasing number of loading cycles. At the same time, $\bar{\varepsilon}^p$ in matrix does not change. At the 50th cycle, $\bar{\varepsilon}^p$ in slip band is about 3 times higher than that in matrix, as shown in Fig. 6.18(c). At the same time, $\Delta\tau_a$ significantly decreases with increasing number of loading cycles. Similar to the case of double prismatic slip, the maximum effective plastic strain can be found at "defect elements" for which lower slip resistance is assumed.

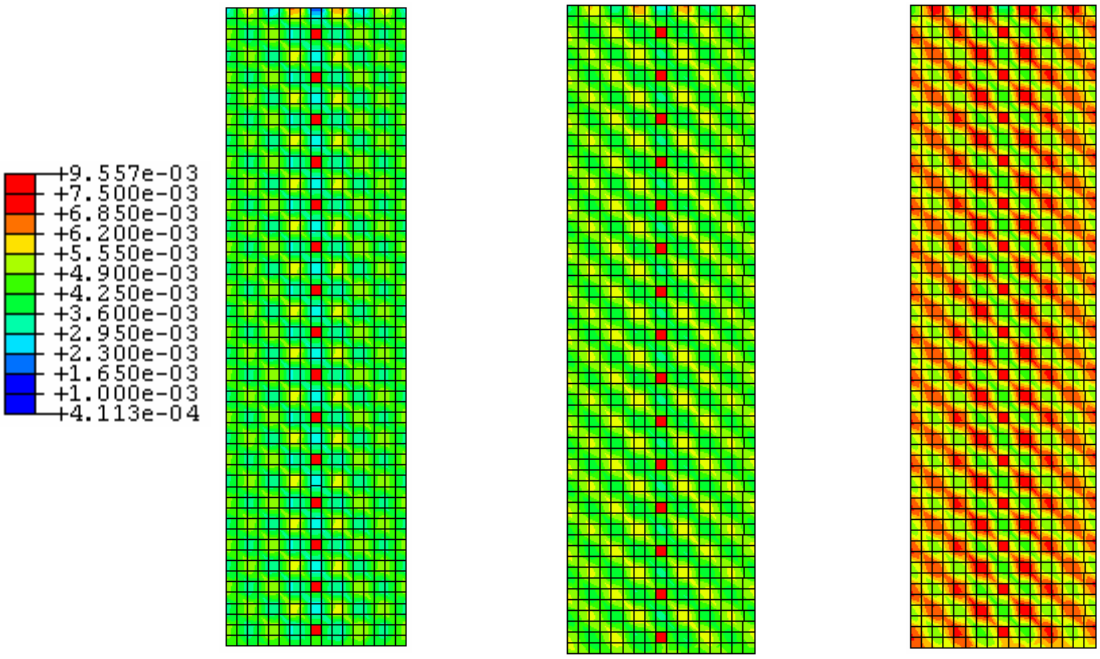

(a) 1st cycle (b) 10th cycle (c) 50th cycle

Figure 6.18. Distribution of the effective plastic strain at the peak of the cycle for $\Delta\varepsilon_t/2 = 0.6\%$.

6.4.3 Prediction of Crack Formation

In Section 6.3, the FIP P_{band} is proposed to account for the driving force for crack formation in single crystal Ti-5Al subjected to cyclic loading. The maximum nonlocal P_{band} averaged over a 0.5×0.5 μm area at the 50th cycle, hereafter referred as $P_{fatigue}$ is used for fatigue life prediction. The Coffin-Manson relation is calibrated by fitting the fatigue lives at various $\Delta\varepsilon_t/2$ as reported in (Xiao and Umakoshi, 2002). Two constants $\gamma_f^{'} = 0.95$ and $c' = -0.51$ of the Coffin-Manson relation (6.14) are employed in Section 6.3.4. However, it was shown in Section 6.3.4 that these two constants should not be directly used for other loading histories, since the critical crack length corresponding to failure was not reported in (Xiao and Umakoshi, 2002).

In this Section, the same methodology as used in Section 6.3.4 is used to correlate the fatigue lives of single crystal α Ti-5Al oriented for single prismatic slip. In Section 6.3.3, we suggested an averaging area of 1/2 the slip band width as a characteristic averaging length scale. Table 6.4 shows that for single prismatic slip, the width of slip band ranges from 2.5 to 3 μm, 1/2 of the slip band width is close to the element edge size (1 μm). Therefore, the maximum nonlocal P_{band} averaged over 1×1 μm area at the 50th cycle is referred as $P_{fatigue}^{1\times1}$ and is plotted versus fatigue lives reported in Xiao and Umakoshi (2003) in Fig. 6.19. It should be noted that the critical crack length corresponding to failure used in the fatigue tests was not also reported in Xiao and Umakoshi (2003).

The characteristic length scale of the averaging area corresponds to the scale of the process for fatigue crack formation. Therefore, for a different averaging area, the constants of Coffin-Manson relation are different. Thus, two constants $\gamma_f^{'} = 0.95$ and $c' = -0.51$ cannot be used here, since the averaging area of 0.5×0.5 μm is used in Section 6.3.4. In this Section, fatigue lives at $\Delta\varepsilon_t/2$ = 0.4% and 0.6% are used to calibrate

the Coffin-Manson relation which is plotted in Fig. 6.19. Two constants $\gamma_f^{'} = 0.75$ and $c' = -0.5$ are obtained. It should be noted that the arrows in Fig. 6.19 indicate run-out of the fatigue life at $\Delta\varepsilon_t/2 = 0.2\%$, meaning that no failure was observed during applied loading cycles with the test stopped at 10^4 cycles. Fatigue lives at $\Delta\varepsilon_t/2 = 0.3\%$ and 0.8% are used to validate the Coffin-Manson relation. The calibrated Coffin-Manson relation agrees fairly well with the crack formation lives for $\Delta\varepsilon_t/2 = 0.3\%$, 0.8%. This result validates the approach reported in Section 6.3 based on correlation for double prismatic slip. However, two constants obtained here should not be directly used for other loading histories due to the lack of the critical crack length used in fatigue tests.

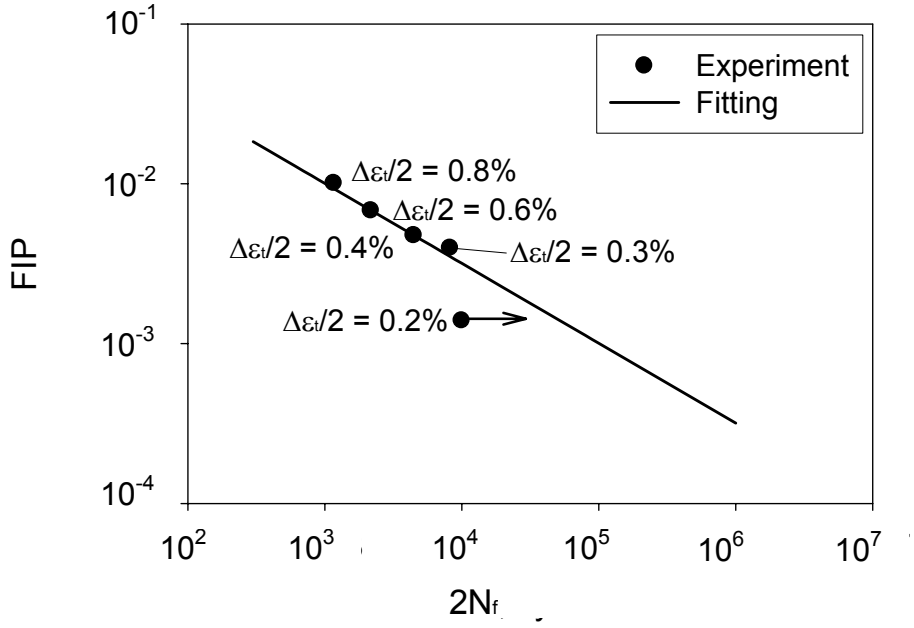

Figure 6.19. Fit for Coffin-Manson relation with $P_{fatigue}^{1\times1}$ for single crystal α Ti5Al orientated for single prismatic slip.

6.5 Discussion

6.5.1 Mesh sensitivity

It is noted that both the finite element method and the crystal plasticity model employed here are local approaches, thereby giving rise to mesh sensitivity. Strongly heterogeneous deformation such as a slip band in the single crystal is a nonlocal phenomenon. To address this, we employ a minimum mesh refinement scale relative to expected slip band width and spacing, as well as nonlocal FIPs to incorporate driving force for fatigue crack formation. It is necessary to investigate the influence of the mesh density on the simulation results to ensure that our strategy is robust.

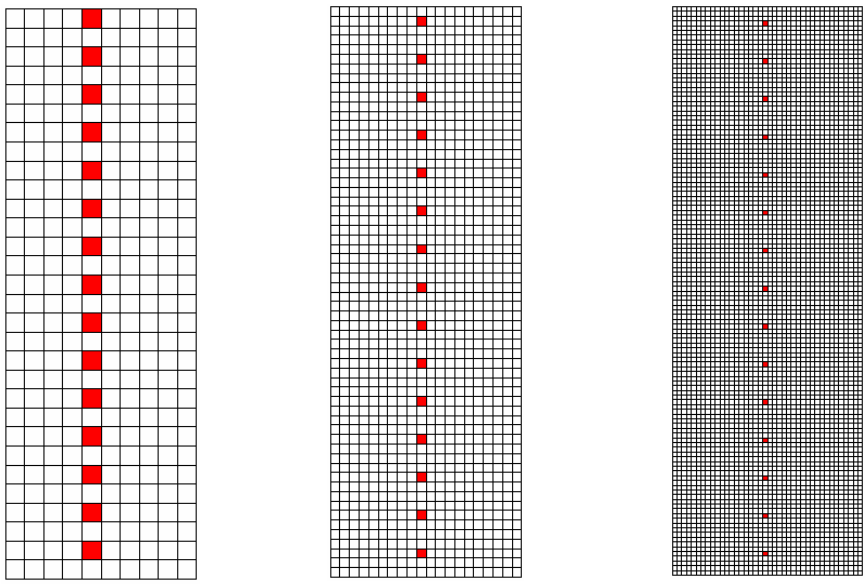

(a) Coarse mesh (b) Fine mesh (c) Finer mesh

Figure 6.20. Finite element models with various mesh densities.

In this study, three meshes containing 300, 1200 and 4800 two-dimensional generalized plane strain elements with reduced integration (CPEG4R) (ABAQUS, 2005) are used to examine the mesh sensitivity. These meshes are referred as coarse, fine and finer meshes and have the same overall size of 9.5×30 μm, as shown in Fig. 6.20. The element sizes of the coarse, fine and finer meshes are 1×1 μm, 0.5×0.5 μm and 0.25×0.25 μm, respectively. The identical orientation (for double prismatic slip) and boundary conditions as shown in Fig. 6.2 are used for the three models. The perturbation elements that serve as material defects are assigned in three models such that the wavelength of shear band, l_d, is unchanged.

Finite element simulations are carried out on three models with completely reversed load strain amplitude of $\Delta\varepsilon_t/2 = 0.6\%$ at a strain rate of 3×10^{-4} s^{-1} at room temperature. A significant effect of the mesh density on the plastic strain distribution is shown in Fig. 6.21. The slip bands are clearly demarcated in the finer mesh model. The coarse mesh model displays a rather homogenous distribution of the plastic strain. No clear slip band structure is developed. The fine and finer mesh models show that the slip band width refines to the scale of a single element. Thus, the width of the slip band decreases with increasing mesh density while the plastic strain within the slip band increases. This means that one key constraint of this approach is to limit the mesh refinement in accordance with the characteristic length scales of slip band width and spacing, as experimentally observed.

The variation of macroscopic $\Delta\tau_a$ over the entire mesh with number of loading cycles for different mesh densities is shown in Fig. 6.22. It is shown that the three curves are very close. During the first 10 cycles, the finer the mesh, the higher the cyclic shear stress amplitude, $\Delta\tau_a$. This phenomenon can be explained as the lower volume fraction of the defects for the finer mesh. Since the defect is assumed as the material point with lower slip resistance, the high volume fraction of the defects would result in the lower τ_a. After the 10^{th} cycle, three curves are close. Clearly, the mesh density has only small

effect on the macroscopic stress-strain response, especially after the slip bands develop, even in the softening regime.

As described before, the averaging area for P_{band} should be properly chosen based on the physical phenomenon of interest. Crack formation in single crystal with dislocation substructures results from decohesion of the interface between slip band and matrix. Therefore, the proper averaging areas should be determined by the width and wavelength of the slip band.

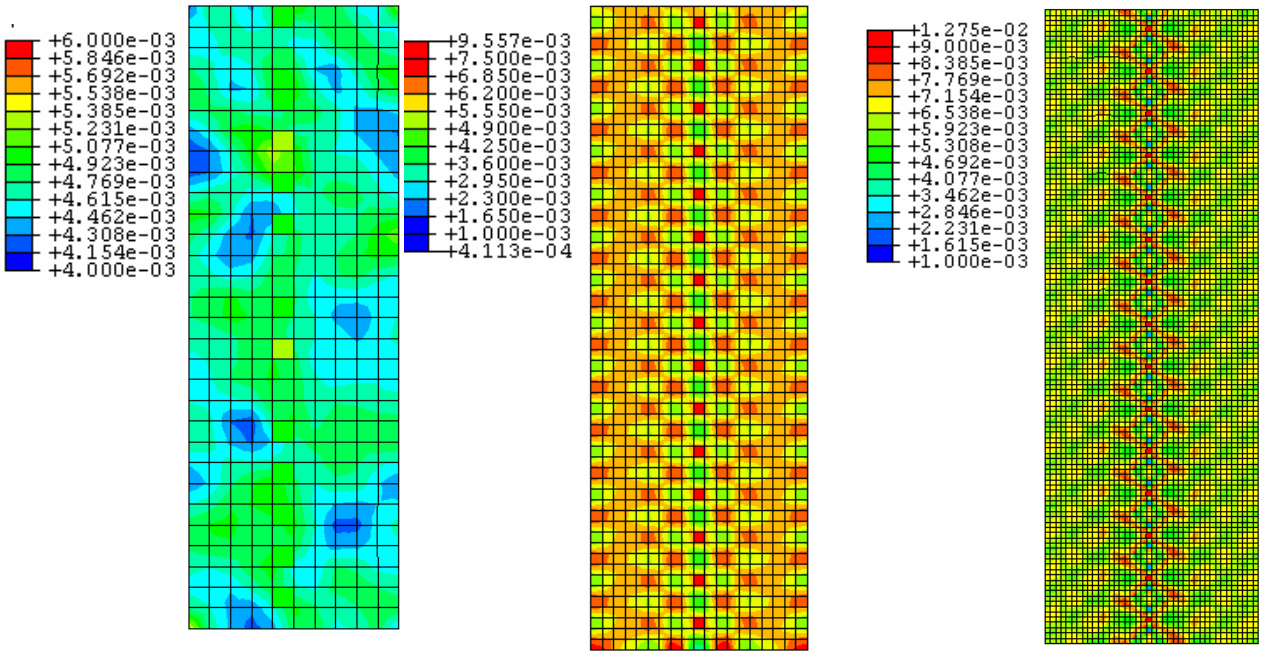

(a) Coarse mesh (b) Fine mesh (c) Finer mesh

Figure 6.21. Distribution of the plastic strain at $\Delta\varepsilon_t/2 = 0.6\%$ for different mesh densities at the 50^{th} cycle.

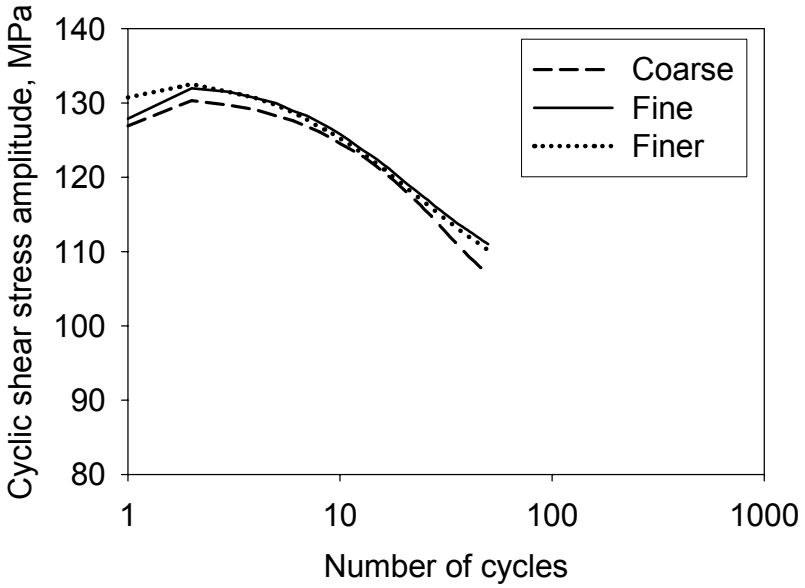

Figure 6.22. Variation of $\Delta\tau_a$ with number of loading cycles for different mesh densities.

6.5.2 Slip Band Wavelength

The slip band wavelength, l_d, has strong effects on the fatigue behavior of crystalline material. It is interesting to understand the variation of deformation and fatigue behavior of single crystal α Ti-5Al with respect to various l_d via finite element analysis. Experimental observations (Xiao and Umakoshi, 2002, 2003) showed that the detailed structure of the slip bands is determined by the crystallographic orientation and strain amplitude. In this study, slip bands are triggered by the material defects. Thus, various structures of the slip bands can be obtained by varying the wavelength of the defects, l_d, in the finite element model.

Figure 6.24(a) and (b) show the finite element meshes for defects spacing of 2 μm and 4 μm, respectively. The identical orientation (for double prismatic slip) and boundary conditions as shown in Fig. 6.2 are used for the two models. The overall sizes of two

meshes are also identical. All simulations are carried out at fully reversed, strain-controlled history at $\Delta\varepsilon_t/2 = 0.6\%$ for 50 cycles.

The significant influence of the distribution of defects on contours of the effective plastic stain at 50th cycle is shown in Fig. 6.25. The overall shape and orientation of slip bands are same for two models. Increasing l_d leads to fewer slip bands in the model. The effective plastic strain within each slip band increases. Although the material defects in the model trigger the formation of slip bands, their distribution controls the degree of intensification of plastic strain within the slip band.

Variation of $\Delta\tau_a$ with number of loading cycles for these two l_d value is shown in Fig. 6.26. Two curves are close over the first 50 cycles, indicating a relatively small effect of l_d on the macroscopic stress-strain response of the model.

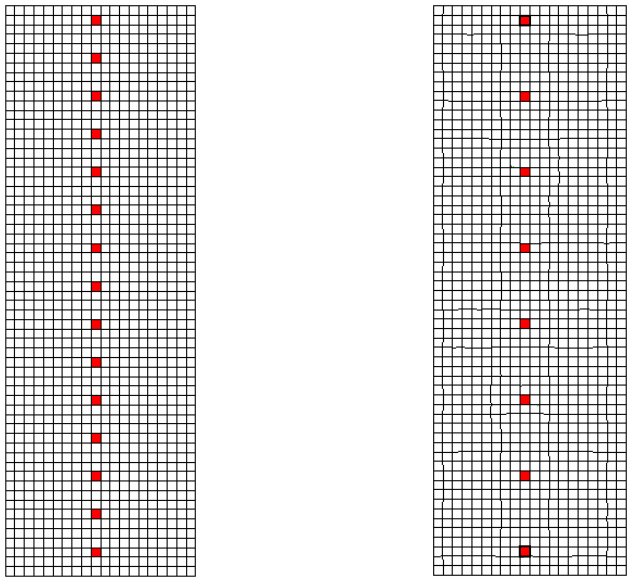

(a) $l_d = 2$ μm (b) $l_d = 4$ μm

Figure 6.24. Finite mesh with various l_d.

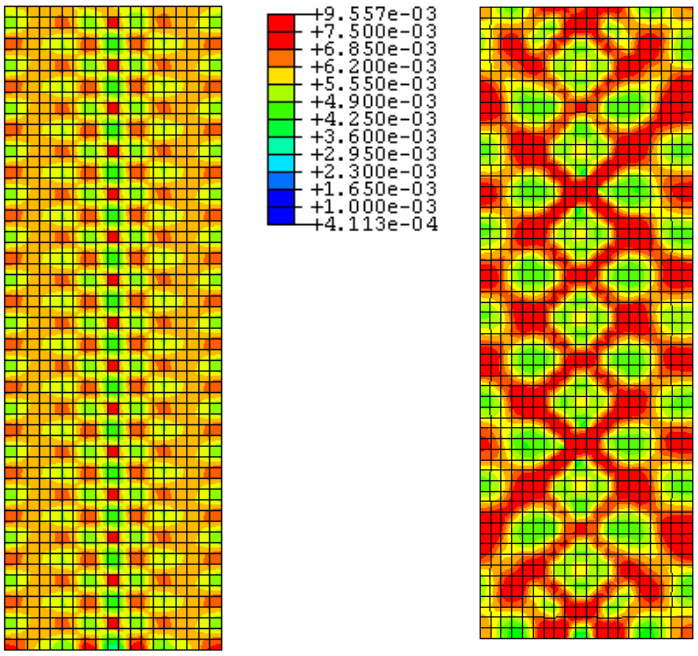

(a) $l_d = 2$ μm (b) $l_d = 4$ μm

Figure 6.25. Distribution of the plastic strain at $\Delta\varepsilon_t/2 = 0.6\%$ for different l_d.

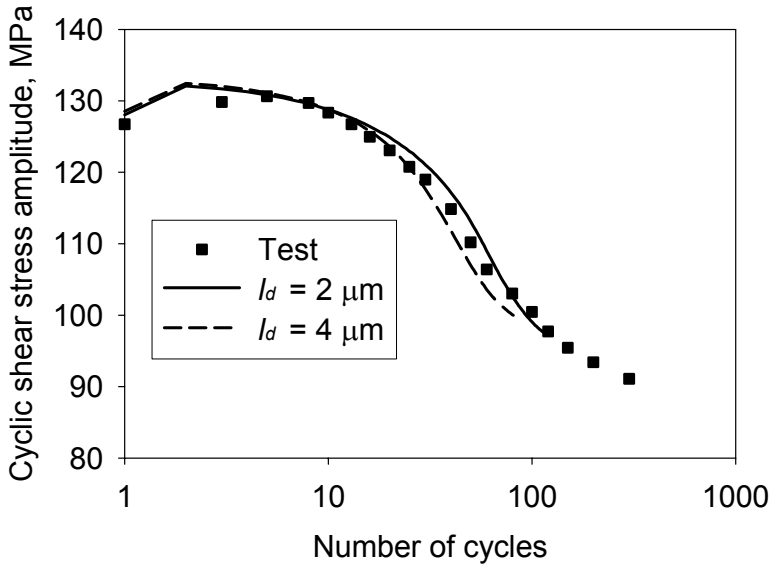

Figure 6.26. Variation of $\Delta\tau_a$ with number of loading cycles for different l_d.

Figure 6.27 shows the maximum P_{band} averaged over 0.5×0.5 μm area at the 50th cycle for different l_d. The maximum P_{band} significantly increases with increasing l_d due to the increasing intensification of plastic strain within the slip band. The simulation results predict a significant effect of the wavelength of the slip band on the deformation and fatigue behavior of single crystal α Ti-5Al. The sensitivity of the FIP to l_d cannot be removed with the averaging method. Therefore, the wavelength l_d is a key modeling parameter that must be determined through experimental observations (Xiao and Umakoshi, 2002, 2003) or theoretical calculations (Venkataraman, et. al., 1991a, 1991b) before any meaningful fatigue analysis can be carried out.

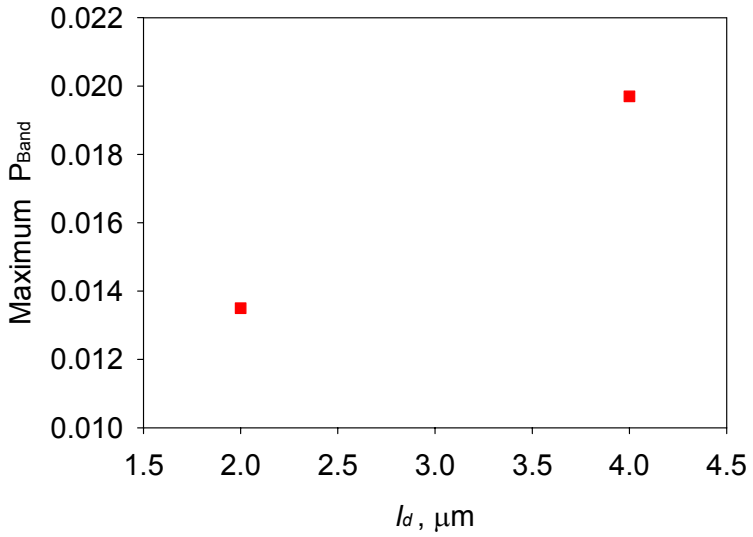

Figure 6.27. Variation of maximum P_{Band} with 0.5×0.5 μm averaging area at the 50th cycle for $\Delta\varepsilon_t/2 = 0.6\%$ for different l_d.

6.6 Summary

In this study, a shear-enhanced crystal plasticity model is used to model the deformation behavior of the single crystal α Ti-5Al oriented for single and double prismatic slip. Softening of the threshold stress is introduced to incorporate the cyclic

strain softening observed in the experiments. The cyclic strain softening is associated with highly planar slip of α Ti-5Al at room temperature. Finite element models are established to simulate the deformation and fatigue behaviors of the α Ti-5Al. In order to model the slip band effect, the element size and the distribution of the defects within the model are determined by the experimentally observed slip band structure. The simulated stress-strain responses are shown to be in good agreement with the experimental results at different orientations and various amplitudes of completely reversed cyclic strain at room temperature.

A new FIP, P_{band}, is proposed to correlate fatigue crack formation along the slip band. An averaging procedure for the FIP over integration points is employed to incorporate the crack formation mechanism over a physically representative scale on the order of slip band width. The nonlocal Coffin-Manson law is used to correlate the fatigue life and the FIP and is calibrated by fitting the fatigue lives of single crystal α Ti-5Al oriented for double prismatic slip. Predicted fatigue lives are shown to be in good agreement with the experimental data of single crystal α Ti-5Al oriented for single prismatic slip.

Two modeling parameters, mesh density and spacing of defects, are investigated in terms of their effects on the deformation and fatigue behavior of α Ti-5Al. It is found that these two parameters have minor effect on the macroscopic stress-strain response. However, the distribution of the effective plastic strain and FIP vary substantially with variation of these two parameters. The mesh size should be assigned to less than the slip band width. Parameter l_d is an important material length scale that must be determined before conducting simulations.

CHAPTER 7

SIMULATION OF SLIP BAND BASED ON SHEAR ENHANCED CRYSTAL PLASTICITY MODEL

7.1 Introduction

Extensive studies summarized in Chapters 1 and 6 have been conducted to simulate the slip localization in crystalline materials. Many of those works explicitly model the slip bands using macroscopic plasticity or crystal plasticity models combined with the finite element method. In those works on explicitly modeling the slip bands in crystalline metals, the prescribed perturbations were necessary to trigger the localized deformation.

Simulations of slip bands in single crystal α-Ti5Al subjected to cyclic loading have been carried out in Chapter 6. The simulation results are shown to agree with the experimental observations of single crystals oriented for single and double prismatic slip in terms of macroscopic stress-strain responses and deformation behavior (Xiao and Umakoshi, 2002, 2003). The fatigue analyses were performed by calculating fatigue indicator parameters. A modified Coffin-Manson relation was calibrated and used to correlate the FIPs with fatigue lives. It was shown that the predicted fatigue lives for various loading histories are in good agreement with the experimental data.

The works reported in Chapter 7 and 8 will focus on the simulation of slip bands in polycrystalline Ti-6Al-4V. The objectives of this study are as follows:

- Develop a physically-based crystal plasticity constitutive model that can simulate the development of slip band in the primary α phase of Ti-6Al-

4V deformed at room temperature. This microstructure-scale model can be used to study the effects of microstructure on the deformation and fatigue behaviors of Ti-6Al-4V.

- Develop physically-based FIPs that can reflect driving forces for various mechanisms for fatigue crack formation.
- Conduct simulations demonstrating the role of microstructure in cyclic deformation and fatigue behaviors.
- Develop a computational approach for microstructure-scale material modeling and fatigue analyses.

Emphasis is placed on the developing and using the computational tools and frameworks to study the effect of microstructure of Ti-6Al-4V on deformation and fatigue behavior while considering the slip localization in the primary α phase.

In Chapter 6, perturbation elements with lower slip resistance are used to trigger slip localization in single crystal α-Ti5Al. The distribution of perturbation elements is determined from experimental observations. It is shown that the slip bands gradually propagate from the perturbation elements. This approach is unsuccessful in simulating slip band in polycrystal. It is found that the slip band cannot initiate from the perturbation elements. A rather homogenous slip is observed due to the strong heterogeneity of the grain boundary. In order to enforce the localized slip in polycrystal, a new strategy is developed in Section 7.2. In this strategy, the crystal is divided into two regions representing slip band and matrix based on the experimental observations and orientation of slip planes. Different material constants are assigned to each of the two regions to model different deformation behaviors of slip band and matrix. The simulations are conducted on a 2D finite element model obtained from the EBSD observation of the polycrystalline structure of a Ti-6Al-4V subjected to monotonic tension history, as shown in Section 7.3. In Section 7.3, the simulated slip band structures are shown to be in qualitative agreement with the experimental observations.

7.2 Crystal Plasticity Model

The kinematics of crystal plasticity theory has been explained comprehensively in Chapter 1 and the slip systems of primary α phase and lamellar colony are given in Chapter 2. Same flow rule as shown in Eq. (4.1) is used. The evolution laws for drag stress and backstress for primary α phase and lamellar colonies follow that described in Chapter 4.

The threshold stress does not evolve, i.e., $\dot{\kappa}^{\alpha} = 0$, for pyramidal slip systems of the primary α phase and the hard slip systems of α+β colony. The threshold stresses for basal and prismatic slip systems of primary α phase are given by

$$\kappa^{\alpha}{}_{prism} = \kappa_1^{\alpha}\Big|_{prism} + A(\tau_{Pyr1} - \tau_{Pyr2}) + \kappa_s^{\alpha}\Big|_{prism} \tag{7.1}$$

$$\kappa^{\alpha}{}_{basal} = \kappa_1^{\alpha}\Big|_{basal} + \kappa_s^{\alpha}\Big|_{basal} \tag{7.2}$$

where $\kappa_1^{\alpha}\Big|_{prism}$ and $\kappa_1^{\alpha}\Big|_{basal}$ are defined by Eq. (4.5). The second term in Eq. (7.2) corresponds to the non-Schmid effect (core spreading effects), as described in Chapter 2.

It is noted that breakdown of SRO causes strong planar slip and results in slip localization in primary α phase. As a result, slip bands develop when polycrystal is deformed at room temperature. Same as in the Chapter 6, the magnitude of plastic shear $|\gamma^{\alpha}|$ for the α^{th} slip system is used to trigger the softening of κ_s^{α}. Therefore, the evolution laws of the softening terms of Eqs. (7.2) and (7.3) is written as

$$\dot{\kappa}_s^{\alpha}\Big|_{prism} = -\mu\left(\xi^{\alpha}\kappa_s^{\alpha}\Big|_{prism}\left|\dot{\gamma}^{\alpha}\right|\right) \tag{7.3}$$

$$\dot{\kappa}_s^{\alpha}\big|_{basal} = -\mu\left(\xi^{\alpha}\kappa_s^{\alpha}\big|_{basal}\left|\dot{\gamma}^{\alpha}\right|\right) \tag{7.4}$$

where μ is a constant and ξ^{α} is the softening coefficient for α^{th} slip system. The initial value of $\kappa_s^{\alpha}\big|_{prism}$ and $\kappa_s^{\alpha}\big|_{basal}$ are given by

$$\kappa_s^{\alpha}\Big|_{prism}(0) = \kappa_s(0) \tag{7.5}$$

$$\kappa_s^{\alpha}\Big|_{basal}(0) = \kappa_s(0) \tag{7.6}$$

A slip band is the region in which cyclic plastic shear strain is localized. The matrix, on the other hand, contains very low plastic shear strain. The differential slip in slip band and matrix shows that the threshold stress does not soften uniformly in all material points. In effect, the softening only occurs at the material points that are located within the slip band. A new strategy is proposed to create banded slip in primary α grains, as illustrated in Fig. 7.1.

In Fig. 7.1, multiple slip bands are assumed to have the same thickness t and be separated by uniform distance l. The wavelength of the slip band is $w = t + l$. For a material point, the value of the softening coefficient ξ^{α} for α^{th} slip system is determined by the distance ϖ between the slip plane and a remote reference point, i.e.,

$$\begin{cases} \xi^{\alpha} = 1 & \text{if} \quad nw - t/2 \geq \varpi \geq nw + t/2 \\ \xi^{\alpha} = 0 & \text{otherwise} \end{cases} \qquad n = 1,2,3... \tag{7.7}$$

With this strategy, only the material points that reside within the slip bands will soften, as shown in Fig. 7.1. Thus, the plastic shear will concentrate in the slip band regions due to relatively low slip resistance.

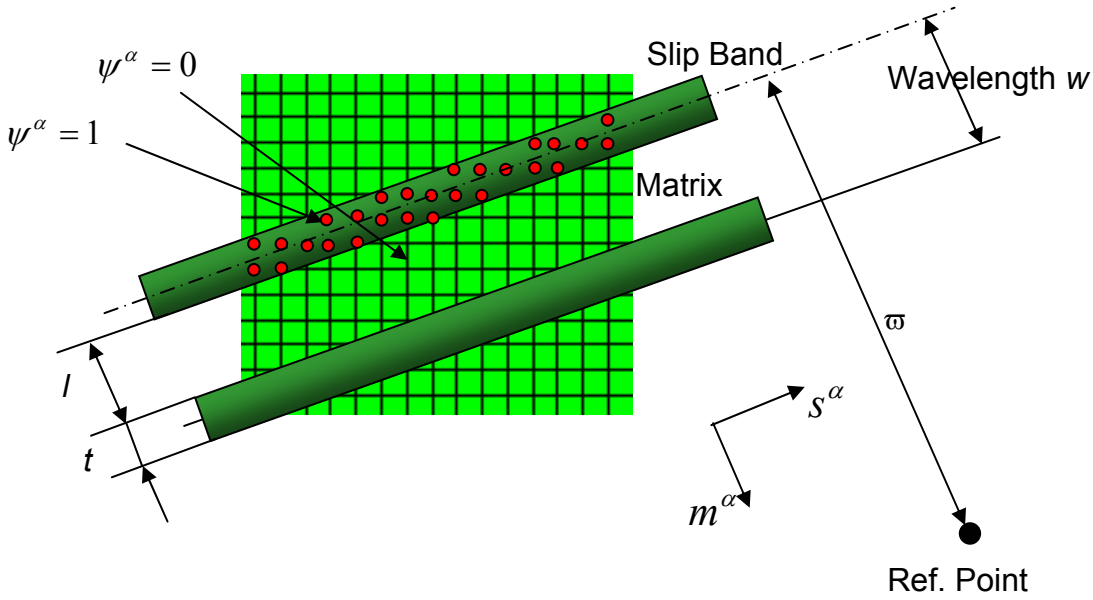

Figure 7.1 Illustration of softening strategy for primary α phase.

The thickness and spacing of slip bands are important characteristic material length scales that need to be determined before conducting simulations. It is well known that t and l of slip bands are dependent on material, loading conditions, temperature, and so on. However, a theoretical formulation that allows calculation of slip band thickness and spacing in α TiAl alloys is lacking. Experimental observations on cyclically deformed single crystal α Ti5Al showed that for various loading histories, variation of spacing and thickness of slip band was relatively low (Xiao and Umakoshi, 2002, 2003). Table 7.1 summarizes the value of t and w for various α TiAl alloys subjected to various loading conditions. Most experiments were conducted at room temperature except the experiment carried out by Williams et al. (2002). The values of t and w are obtained based on the SEM images provided in the literatures. Table 6.1 shows that the thickness

of slip band ranges from 0.3 μm to 2 μm and the wavelength ranges from 1 μm to 3 μm. For simplicity, uniform slip band thickness t = 0.8 μm and slip band wavelength w = 1.5 μm are assumed for all primary α grains. It is assumed that no new slip bands will be formed during the deformation.

Table 7.1 Thickness and wavelength of slip band reported and observed in literature for α Ti-Al alloys.

Thickness of slip band t, (μm)	Wavelength of slip band, w (μm)	Material	Loading Condition	Reference (based on TEM observations)
0.8	2.8	α Ti-6Al	Creep at 552 MPa	Brandes and Mills, 2004
0.8~1	1.5~2	Various heat treated Ti-6Al	Creep at 552 MPa	Neeraj and Mills, 2001
0.3 *	1.2 *	Single crystal Ti-6.6Al	Compressive load at 77K	Williams et al., 2002
0.5	1	Ti-6Al	Creep at 716 MPa	Neeraj et al., 2000
1~2	1~1.5	Single crystal Ti-5Al	Double prismatic slip, strain amplitude 0.2% ~ 0.8%	Xiao, Umakoshi, 2003
1~3	2~3	Single crystal Ti-5Al	Single prismatic slip, strain amplitude 0.2% ~ 1.0%	Xiao, Umakoshi, 2003
0.5~2	0.8~1.8	Single crystal Ti-5Al	Various orientation, strain amplitude 0.4%	Xiao, Umakoshi, 2002
0.3-0.8	1	IMI834, Ti-5.8Al-4Sn-3.7Zr	Strain amplitude 0.8% ~ 1.5%	Singh et al., 2002
<1	1~2	Ti-6Al-4V	6% tensile strain	Le Biavant et al., 2001
0.5	1	Ti-6Al	Creep and compressive load	Neeraj and Mills, 2002

Table 7.2 Constitutive equations for Ti-6Al-4V.

Flow Rule:

$$\dot{\gamma}^{\alpha} = \dot{\gamma}_o \left\langle \frac{\left|\tau^{\alpha} - \chi^{\alpha}\right| - \kappa^{\alpha}}{D^{\alpha}} \right\rangle^{m} \operatorname{sgn}\left(\tau^{\alpha} - \chi^{\alpha}\right) \qquad \text{for all slip systems}$$

Evolution Equations for Hardening Variables:

Back stress (primary α phase and lamellar colony)

$$\dot{\chi}^{\alpha} = \mathrm{B}\dot{\gamma}^{\alpha} - \mathrm{C}\psi\left(x^{\alpha}\right)\chi^{\alpha}\left|\dot{\gamma}^{\alpha}\right| = \mathrm{B}\left(\operatorname{sgn}\left(\dot{\gamma}^{\alpha}\right) - \psi\left(x^{\alpha}\right)\frac{\mathrm{C}}{\mathrm{B}}\chi^{\alpha}\right)\left|\dot{\gamma}^{\alpha}\right|$$

$$\psi(x^{\alpha}) = \begin{cases} \exp\left(\eta_1 x^{\alpha}\right) & \text{for } x^{\alpha} < 0 \\ 1.0 & \text{for } x^{\alpha} \geq 0 \end{cases}$$

$$x^{\alpha} = \operatorname{sgn}(\tau^{\alpha} - \chi^{\alpha})\, p^{\alpha}, \textit{with} \quad \dot{p}^{\alpha} = \left|\dot{\gamma}^{\alpha}\right| \operatorname{sgn}(\tau^{\alpha} - \chi^{\alpha})$$

Threshold stress

Primary α phase

$$\kappa^{\alpha}{}_{prism} = \kappa_1^{\alpha}\Big|_{prism} + A(\tau_{Pyr1} - \tau_{Pyr2}) + \kappa_s^{\alpha}\Big|_{prism} \qquad \dot{\kappa}_s^{\alpha}\Big|_{prism} = -\mu\left(\xi^{\alpha}\kappa_s^{\alpha}\Big|_{prism}\left|\dot{\gamma}^{\alpha}\right|\right)$$

$$\kappa^{\alpha}{}_{basal} = \kappa_1^{\alpha}\Big|_{basal} + \kappa_s^{\alpha}\Big|_{basal} \qquad \dot{\kappa}_s^{\alpha}\Big|_{basal} = -\mu\left(\xi^{\alpha}\kappa_s^{\alpha}\Big|_{basal}\left|\dot{\gamma}^{\alpha}\right|\right)$$

$$\kappa^{\alpha}{}_{pry} = \kappa_1^{\alpha}\Big|_{pry} \qquad \dot{\kappa}^{\alpha}_{pry} = 0$$

Lamellar colony

$$\kappa^{\alpha}{}_{soft} = \kappa_1^{\alpha}\Big|_{soft} + \kappa_s^{\alpha}\Big|_{soft} \qquad \dot{\kappa}_s^{\alpha}\Big|_{soft} = -\mu\,\kappa_s^{\alpha}\Big|_{soft}\left|\dot{\gamma}^{\alpha}\right|$$

$$\kappa^{\alpha}{}_{hard} = \kappa_1^{\alpha}\Big|_{hard} \qquad \dot{\kappa}^{\alpha}\Big|_{hard} = 0$$

$$\kappa_1^{\alpha} = k_y\left(d^{\alpha}\right)^{-0.5} \qquad \kappa_s^{\alpha}\Big|_{prism}(0) = \kappa_s^{\alpha}\Big|_{basal}(0) = \kappa_s^{\alpha}\Big|_{soft}(0) = \kappa_s(0)$$

Drag stress

$$\dot{D}^{\alpha} = 0 \qquad D_{\alpha}^{prism} = D_{\alpha+\beta}^{prism} \qquad D_{\alpha}^{basal} = D_{\alpha+\beta}^{basal} \qquad D_{\alpha+\beta}^{\langle 111\rangle\{110\}} = 0.9 D_{\alpha}^{prism}$$

The threshold stress for soft slip systems of the α+β colony also includes an initial softening term, i.e.,

$$\kappa^{\alpha}{}_{soft} = \kappa_1^{\alpha} + \kappa_s^{\alpha}\Big|_{soft} \tag{7.8}$$

Since the slip band is generally not formed in the lamellar phase, the softening strategy is not applied to lamellar colonies. The softening term $\kappa_s^{\alpha}\big|_{soft}$ evolves according to the evolution law

$$\dot{\kappa}_s^{\alpha}\Big|_{soft} = -\mu\left(\xi^{\alpha}\kappa_s^{\alpha}\Big|_{sfot}\left|\dot{\gamma}^{\alpha}\right|\right) \tag{7.9}$$

where the softening coefficient for the lamellar colony is ξ^{a} = 1. The constitutive equations are summarized in Table 7.2. The described crystal plasticity algorithm is applied to both the primary α phase and the lamellar colony via implementation into a UMAT subroutine in ABAQUS (2005).

7.3 Calibration of Crystal Plasticity Model of Ti-6Al-4V

The calibration of the crystal plasticity model of Ti-6Al-4V is carried out by fitting the macroscopic stress-strain responses of a duplex Ti-6Al-4V subjected to a complex loading history at the room temperature. The same material (PW1215) and loading history as described in Chapter 4 (also in Zhang et al. 2007) is used. The microstructure of the duplex Ti-6Al-4V is shown in Figure 4.1. Table 4.1 summarizes the microstructure parameters. The detailed calibration process can also be found in Chapter 4. A brief description is given in below.

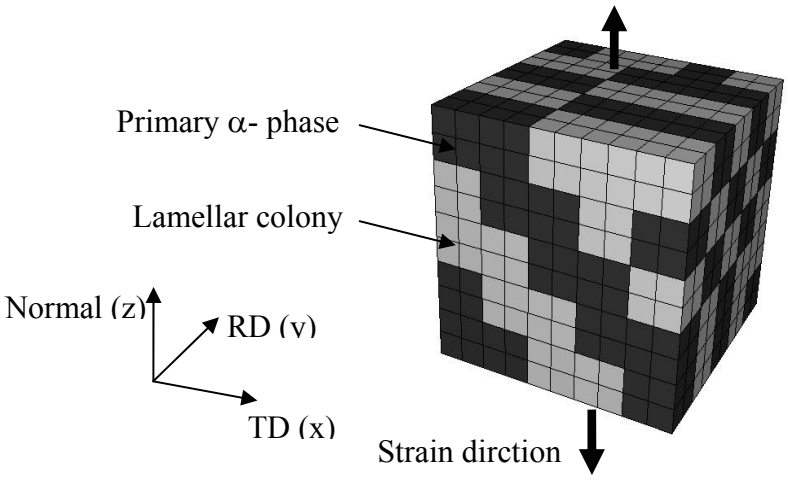

Figure 7.2 Finite element model of periodic polycrystal.

The microstructure of the tested Ti-6Al-4V is simulated by a finite element model as shown in Fig. 7.2. To adequately represent the microstructures of the tested material by the finite element mesh, microstructure attributes such as average grain size, volume fraction of primary α phase are simulated. A serious of simulated annealing processes is performed to fit the orientation and disorientation distributions, as described in Chapter 4.

The same finite element model as described in Chapter 4 is used here. In this model, the polycrystalline material is idealized as an aggregation of cubic crystals of identical size, as shown in Fig. 7.2. Such an idealization represents a highly idealized, uniform grain size distribution of two phases. The finite element model consists of $5\times5\times5$ cubic grains, with each grain containing $2\times2\times2$ elements.

To simulate the behavior of bulk material with only hundreds of grains, random periodic boundary conditions are applied to all three directions: RD, TD, and the normal direction shown in Fig. 7.2. The displacements are enforced (controlled) in the normal direction, consistent with the experiments in which strains are controlled in this direction.

A detailed description of the finite element model is given in Chapter 4 and (Zhang et. al, 2007).

It should be noted that several material constants of the crystal plasticity model can be obtained from the literature or directly from characterized microstructure features, as shown in Table 4.3. The value of other constants must be found by fitting the experimental data.

Certain constraints on the slip resistance are applied. For example, the slip resistance of the basal system is known to be close to that of the prismatic system. The CRSS of the pyramidal slip systems is much larger than that of the basal and prismatic slip systems for α-titanium and α/β Ti-Al alloys. Therefore, the drag stresses of these slip systems are estimated in proportion to relative ratios of estimated CRSS for various slip systems presented in Table 4.4.

In this study, only part of the loading history that was used in Chapter 4 is applied in this work to calibrate the crystal plasticity model. The computational cost will be greatly reduced by using the loading history up to 2.5% applied strain. This loading history includes four strain rates 10^{-3} s^{-1}, 10^{-4} s^{-1}, 3×10^{-5} s^{-1}, and 10^{-5} s^{-1} and hold periods, and it is adequate for calibrating the rate sensitivity exponent, coefficient for tension-compression asymmetry of the back stress, the drag stress of each slip system, the value of the softening term, and the degree of softening of the threshold stress of basal and prismatic slip systems, etc.

The simulated stress-strain responses are in good agreement with the experimental data up to 2.5% applied strain, as shown in Fig. 7.3. Material constants are reported in Table 7.3. Compared with the material constants reported in Chapter 4, a lower drag stress for prismatic and basal slip systems of primary α phase is obtained. At the same time the drag stress of the pyramidal slip system significantly increases. Thus, each primary α grain will undergo single slip when the applied load is relatively low, which is consistent with the experimental observations (Bridier et al., 2005).

Table 7.3 Material constants for PW1215 at room temperature.

D_0^{basal}	65 MPa	κ_1^{basal}	193 MPa	μ	70
D_0^{prism}	65 MPa	κ_1^{prism}	193 MPa	η_1	500
$D_0^{pyr\langle a\rangle}$	400 MPa	$\kappa_1^{pyr\langle a\rangle}$	193 MPa	A	-0.1
$D_0^{pyr\langle c+a\rangle}$	800 MPa	$\kappa_1^{pyr\langle c+a\rangle}$	193 MPa	m	15
$D_0^{(\alpha+\beta)basal/soft}$	65 MPa	κ_1^{prism}	193 MPa	$B^{\alpha,\alpha+\beta}$	40000
$D_0^{(\alpha+\beta)prism/soft}$	65 MPa	$\kappa_1^{(\alpha+\beta)basal}$	163 MPa	$C^{\alpha,\alpha+\beta}$	8000
$D_0^{(\alpha+\beta)hard}$	400 MPa	$\kappa_1^{(\alpha+\beta)prism}$	981 MPa		
$D_0^{(\alpha+\beta)bcc\ BOR}$	58.5 MPa	$\kappa_1^{(\alpha+\beta)pyr}$	981 MPa	$\kappa_1^{(\alpha+\beta)bcc}$	800 MPa
		$\kappa_1^{(\alpha+\beta)easy\ glide\ systems}$	193 MPa	$\kappa_s(0)$	140 MPa

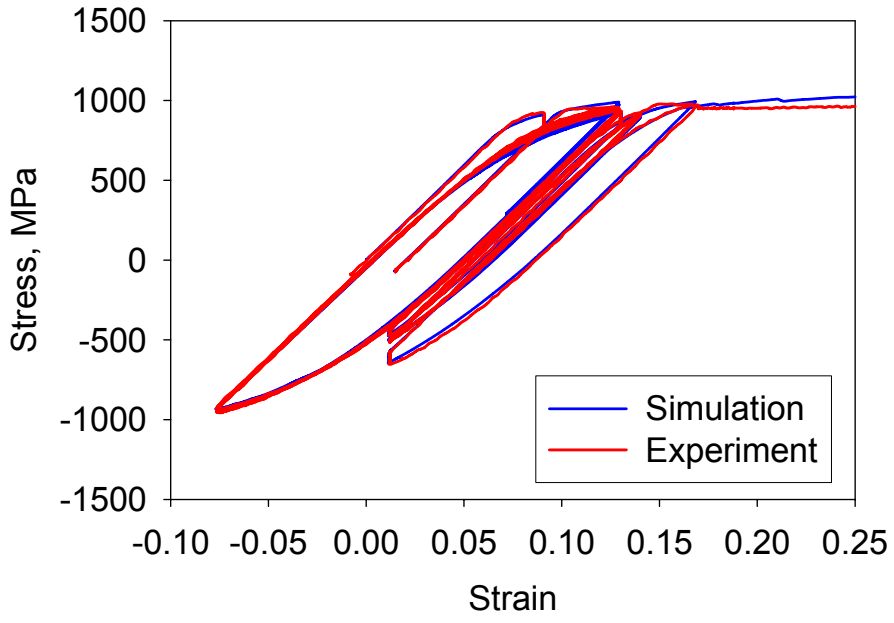

Figure 7.3. Fit for stress-strain curve of tested Ti-6Al-4V (PW1215) for the room temperature uniaxial strain history.

7.4 Simulation of the Slip Behavior of Ti-6Al-4V

In the last section, it was shown that the proposed crystal plasticity model can simulate the macroscopic stress-strain response of a polycrystalline Ti-6Al-4V subjected to a complex loading history at the room temperature. The finite element model used in the last section can adequately represent the microstructure of the test material. It is noted that this finite element model has a relatively coarse mesh. The edge length of each element is about 3.5 μm. Apparently, such a coarse mesh is unable to simulate the formation and propagation of the slip bands.

Bridier and co-workers (2005, 2007) investigated the slip behavior of Ti-6Al-4V subjected to monotonic tension strain-controlled history. Electron back-scatting diffraction (EBSD) measurement of the polycrystalline structure at a 48×52 μm zone centered on the gauge length was reported. The slip activity within this zone for various applied strain level were recorded. In this study, a two-dimensional finite element mesh is created based on the EBSD map to represent the microstructure of the measured zone. Finite element simulations are carried out by using the proposed crystal plasticity model and softening strategy for the primary α phase. The simulation results are then compared with the experimental observations.

The EBSD map and corresponding scanning electron microscope (SEM) image of the measured zone are shown in Figs. 7.4 and 7.5, respectively. Figure 7.6 shows the corresponding finite element model used in this study. It is noted that the periodic boundary conditions are applied in the x and y directions. These boundary conditions impose constraints on the sides such that the opposite edges deform in the same manner. The displacements are enforced (specified) in the y direction to correspond to strains imposed in the experiments. It is noted that when the displacement is specified on an upper boundary, as in uniaxial loading, the x side of the mesh experiences approximately zero net traction, in accordance with the axial loading condition. It is noted that the

experimentally measured zone is not a periodic cell of the tested material. In other words, this zone does not repeat itself in the x and y directions. Direct application of the periodic boundary conditions on the EBSD zone may impose incorrect constraints. To relax the extra constraints imposed on the EBSD zone by periodic boundary condition, a simple expansion of the EBSD zone is applied in both the x and y directions such that the expanded region has the same orientation as the boundary grains. As shown in Fig. 7.6, the size of the finite element mesh is 60×60 μm, and it consists of two regions: EBSD zone and expanded zone. The orientation of the elements at the expanded zone is same as that of the nearest elements at the boundary of EBSD zone.

The finite element mesh was created using a FORTRAN code and implemented in ABAQUS (2005). There are a total of 57600 two-dimensional generalized plane strain elements (CPEG4R). The size of each element is 0.25×0.25 μm. The generalized plane strain element allows for the slip in the z direction, i.e., 3D crystal plasticity relations. The generalized plane strain theory used in ABAQUS assumes that the model lies between two bounding planes, which may move as rigid bodies with respect to each other, thus causing strain of the "thickness direction" fibers of the model (ABAQUS, 2005). The two bounding planes are free of traction. Generalized plane strain elements are typically used to model a section of a long structure that is free to expand. In order to reduce execution time, all elements employ reduced integration.

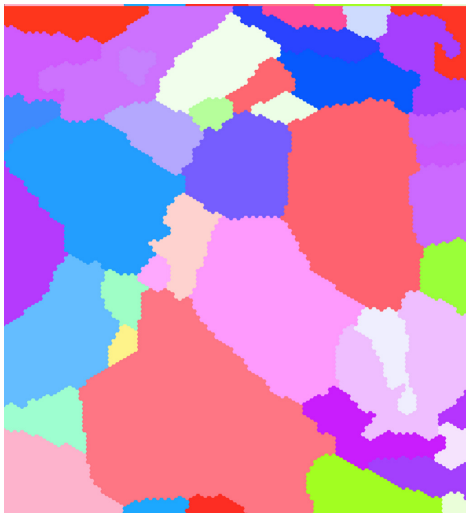

Figure 7.4 EBSD image of the measured zone.

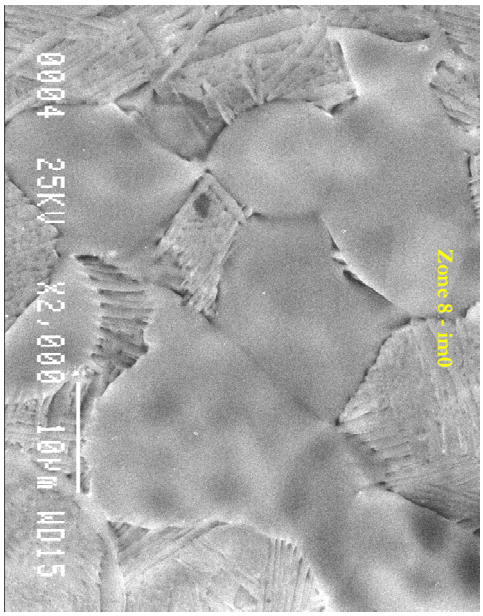

Figure 7.5 SEM image of the measured zone.

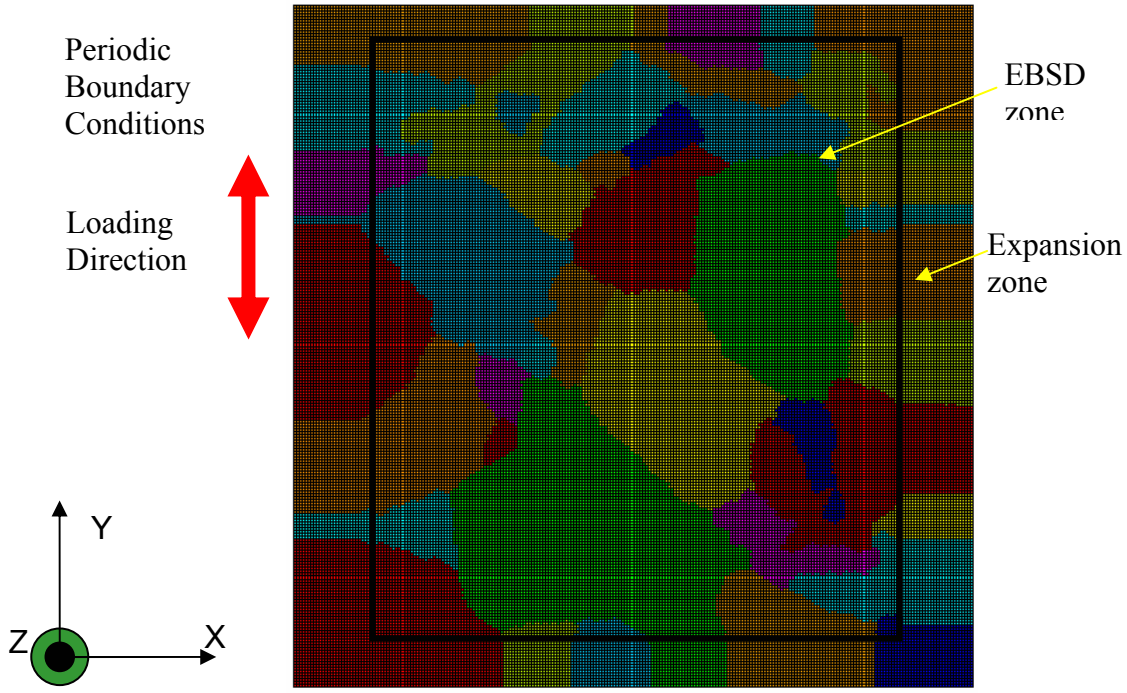

Element size 0.25×0.25 μm

Figure 7.6 Finite element model.

The EBSD zone consists of 43 grains. Among these grains, there are 7 primary α grains labeled from 1 to 7, as shown in Fig. 7.7. The orientation angles of these grains in Bunge-Roe convention are given in Table 7.4. Table 7.4 also lists the Schmid Factors of basal and prismatic slip systems of each primary α grain when the loading direction is parallel to the y direction. In Table 7.4, B1, B2 and B3 represent basal slip systems $\langle \bar{1}2\bar{1}0 \rangle (0001)$, $\langle \bar{1}\bar{1}20 \rangle (0001)$ and $\langle 2\bar{1}\bar{1}0 \rangle (0001)$, respectively; P1, P2 and P3 denote prismatic slip systems $\langle \bar{1}2\bar{1}0 \rangle (10\bar{1}0)$, $\langle \bar{1}\bar{1}20 \rangle (\bar{1}100)$ and $\langle 2\bar{1}\bar{1}0 \rangle (0\bar{1}10)$, respectively. It should be noted that the grain size d^{α} is determined by the area of each grain due to the lack of the microstructure information in the third direction.

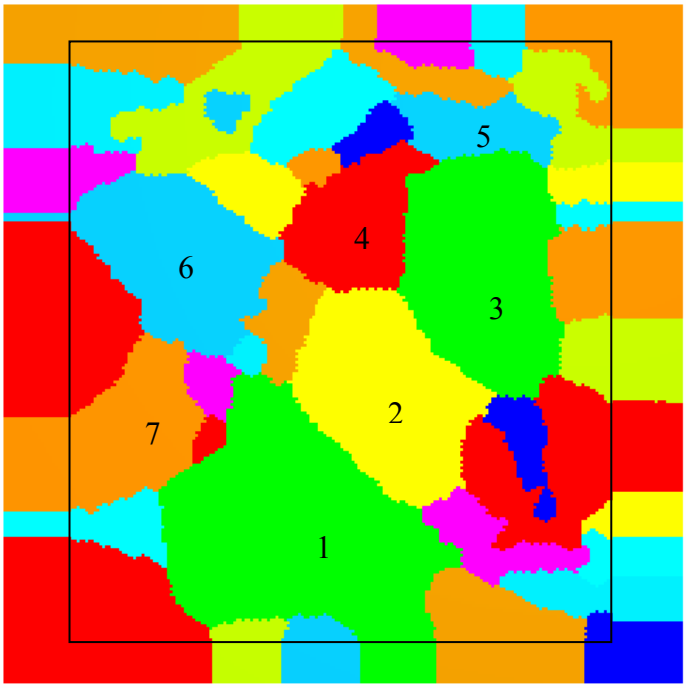

Figure 7.7 Primary α grains at EBSD zone.

Table 7.4 Schmid factors and orientation angles in Bunge-Roe convention of primary α grains.

Grain	Orientation angle, degree			Schmid factors for basal and prismatic slip systems					
	φ_1	Φ	φ_2	B1	B2	B3	P1	P2	P3
1	105	65	249	0.31	0.41	0.097	0.12	0.065	0.05
2	88	38	280	0.38	0.45	0.073	0.3	0.21	0.08
3	80	69	283	0.34	0.26	0.08	0.04	0.07	0.03
4	143	24	217	0.19	0.21	0.01	0.43	0.37	0.06
5	179	19	177	0.01	0.01	0.0004	0.39	0.46	0.07
6	1	71	351	0.01	0.01	0.002	0.34	0.49	0.15
7	8	77	9	0.10	0.13	0.02	0.48	0.30	0.18

(a) Basal system

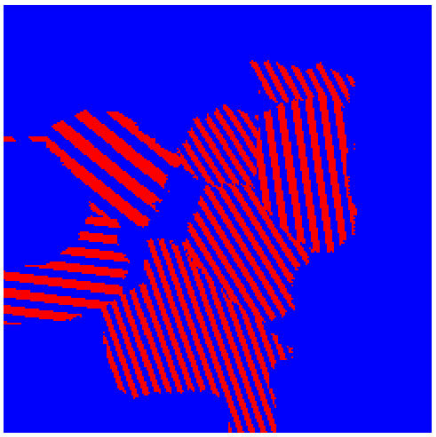

(b) P1 slip system

(b) P2 slip system

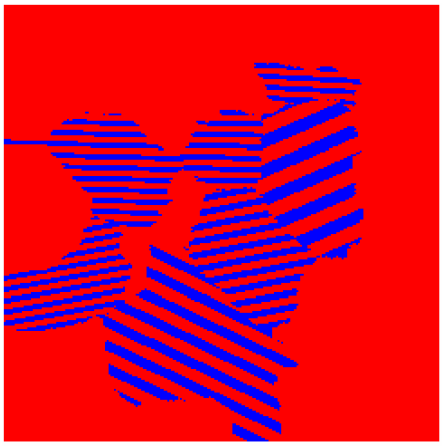

(c) P3 slip system

Figure 7.8 Distribution of ξ^{α}.

The distributions of the softening coefficient ξ^{α} for basal and prismatic systems are shown in Fig. 7.8. The red and blue colors denote $\xi^{\alpha} = 1$ and $\xi^{\alpha} = 0$, respectively. The softening coefficient distributes in a band structure at primary α phase. Such structure allows for softening of threshold stress of the elements at the slip band only and in turn enforces shear localization. The contours of the softening coefficient effectively show the structure of the possible slip bands viewed at the x-y plane. It is noted that all three

basal slip bands have the same configuration since they share the same slip plane. Three prismatic slip bands corresponding to slip systems $\langle \bar{1}2\bar{1}0 \rangle (10\bar{1}0)$, $\langle \bar{1}\bar{1}20 \rangle (\bar{1}100)$ and $\langle 2\bar{1}\bar{1}0 \rangle (0\bar{1}10)$ have different orientations. It is noted that the x-y section view of slip bands for different grains are different, even though the same thickness and wavelength of slip band are assumed for all primary α grains. The discrepancy is caused by the various orientation angles of the slip planes. When the angle between the slip plane and the x-y plane decreases from 90 degree to 0 degree, the thickness and wavelength of slip band shown in the x-y plane increase.

The softening coefficient for the basal system of lamellar phase is $\xi^{\alpha} = 1$ since the basal system belongs to soft system. Similarly, $\xi^{\alpha} = 1$ for P3 slip system which is also a soft system. The hard systems P1 and P2 have the value $\xi^{\alpha} = 0$.

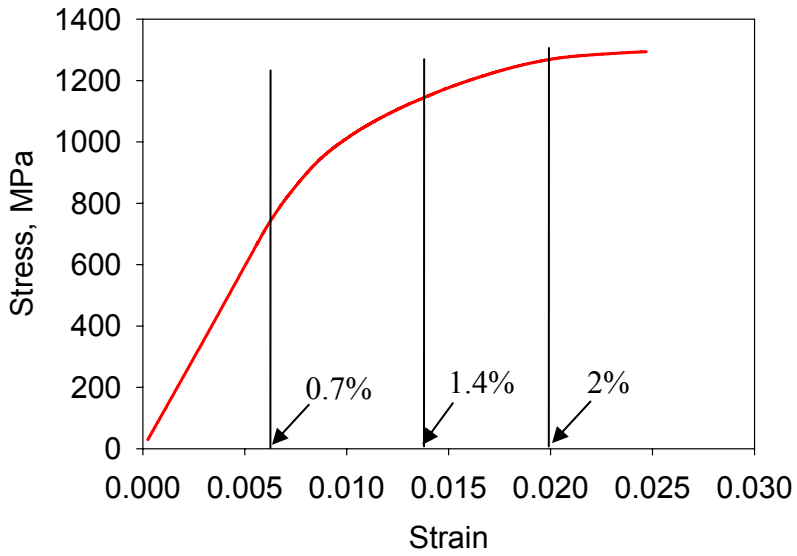

Figure 7.9 Simulated stress-strain responses.

Figure 7.9 shows the simulated stress-strain responses for a monotonic tension strain-controlled history up to 2.5%. The strain rate is 10^{-3} s^{-1}. It is noted that the size of

the simulated zone is relatively small (48×52 μm). Such a small zone is inadequate to statistically represent the microstructure of the bulk material. Furthermore, the EBSD observation provides 3D lattice orientation and 2D grain structure of polycrystal. Thus, direct comparison of the simulated stress-strain curve with experimental data is not performed.

The strong plastic shear localization can be viewed from the contour of effective plastic strain, defined by $\bar{\boldsymbol{\varepsilon}}^p = \sqrt{(2/3)\varepsilon_{ij}^p \varepsilon_{ij}^p}$, where $\boldsymbol{\varepsilon}^p = \sum_\alpha \gamma^\alpha \left(\mathbf{s}_0^\alpha \otimes \mathbf{m}_0^\alpha\right)_{sym}$, at various applied strain ε_t. Figure 7.10 compares SEM images and contours of the effective plastic strain. When the applied strain is relatively low at 0.7%, no clear slip trace can be seen from the SEM image at Fig. 7.10 (a). This strain level is lower than the macroscopic yield strain as shown in Fig. 7.9. However, the contours of the effective plastic strain show that there are a few grains with favored orientations undergoing plastic deformation and the effective plastic strain is relatively low. The banded structure of effective plastic strain is shown for grains 1, 2 and 7. Both grains 1 and 2 undergo basal slip while grain 7 undergoes prismatic slip. The active slip system of each grain has the highest Schmid factor, as shown in Table 7.4. It is noted that the effective plastic strain at the slip band is close to that that of matrix. It is believed that the threshold stress of slip band is close to that of the matrix at low applied load.

When the applied strain increases to 1.4%, the plastic deformation is shown in the macroscopic stress-strain curve in Fig. 7.9. In Fig. 7.10(b), clear slip traces are shown in the SEM image in grains 1, 2, 3 and 6. Within these four grains, basal slip is the main slip mode for grains 1 and 3. Grain 6 mainly undergoes prismatic slip. Both basal and prismatic slip bands are developed in grain 2 due to relatively high Schmid factor for slip systems B2 and P1. In the SEM image, large wavelengths are observed in the slip bands for grains 3 and 6; the wavelengths of the slip bands in grains 1 and 2 are relatively small. The finite element simulation at the right of Fig. 7.10(b) shows that most grains undergo

plastic deformation at ε_t = 1.4%. The effective plastic strain distributed in clearly banded structure for all primary α grains. The orientations of the simulated slip bands of grains 1, 2, 3 and 6 are same as that of the observed slip traces. The finite element model can correctly predict the active slip system. The wavelength of the simulated slip band is generally close to the experimental observation. However, a clear discrepancy of wavelength can be seen from grain 3 which is resulted from the assumption of uniform wavelength of the slip band in the model. In grain 2, the simulated plastic shear in the prismatic slip system is stronger than that in the basal system which is opposite to the SEM observation. Such discrepancy can be attributed to the 2D generalized plane strain elements and periodic boundary conditions used in the finite element simulation.

The SEM image in Fig. 7.10(c) shows significant plastic deformation of primary α grains when ε_t = 2%. The wavelength of the slip band decreases with increase of plastic deformation. Grains 4 and 7 begin to develop prismatic slip bands. The orientations of the slip bands in grains 4 and 7 are in agreement with the simulation results. As shown in Table 7.4, the active slip systems (P1 for grain 4, P2 for grain 7) have the highest Schmid factors among all basal and prismatic systems. The contours of effective plastic strain show strong plastic deformation in both primary α grains and lamellar colonies when ε_t = 2%. It is noted that different legends are used for Fig. 7.10(b) and 7.10(c). In comparison with Fig. 7.10(b), Fig. 7.10 (c) shows that the effective plastic strain within the slip band significantly increases while $\bar{\boldsymbol{\varepsilon}}^p$ of matrix does not change. The slip localization is apparently caused by relatively low threshold stress of the elements within slip bands.

In Fig. 7.10, it is shown that the simulated slip bands structure is in qualitative agreement with the experimental observations. The finite element simulation correctly predicts the orientations of the slip bands. The wavelength of the slip bands is also close to the experimental observations. For all primary α grains, the first activated slip system

is the system with the highest Schmid factor. Most grains undergo single slip at different applied strain level. Only a few grains can undergo multiple slips when load is high, such as grain 2. Both experimental observations and simulations show that basal and prismatic slips are the most active slip systems for primary α grains.

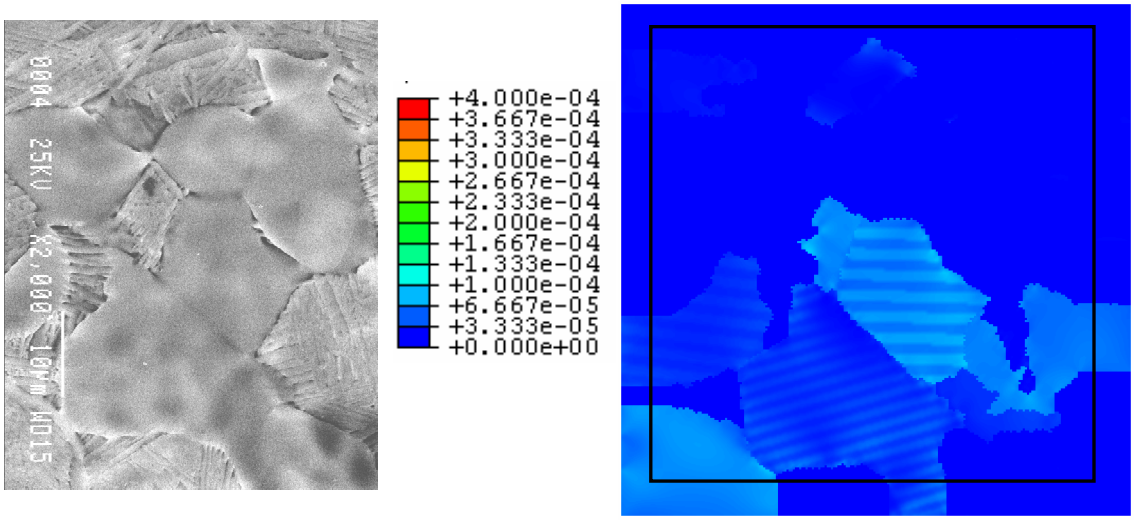

Experiment Simulation

(a) $\varepsilon_t = 0.7\%$

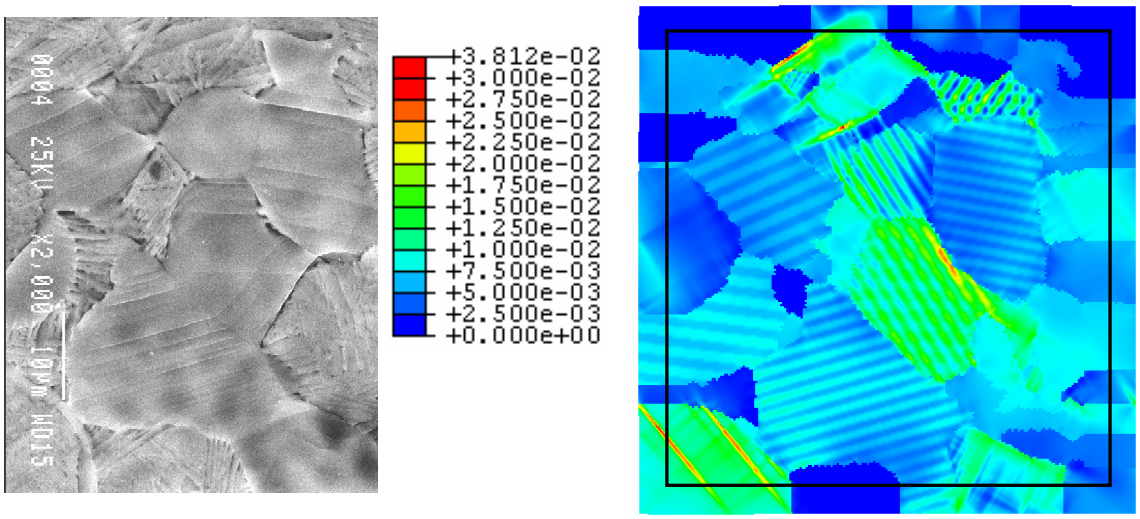

Experiment Simulation

(b) $\varepsilon_t = 1.4\%$

Figure 7.10 Comparison of slip behaviors at various applied strain ε_t.

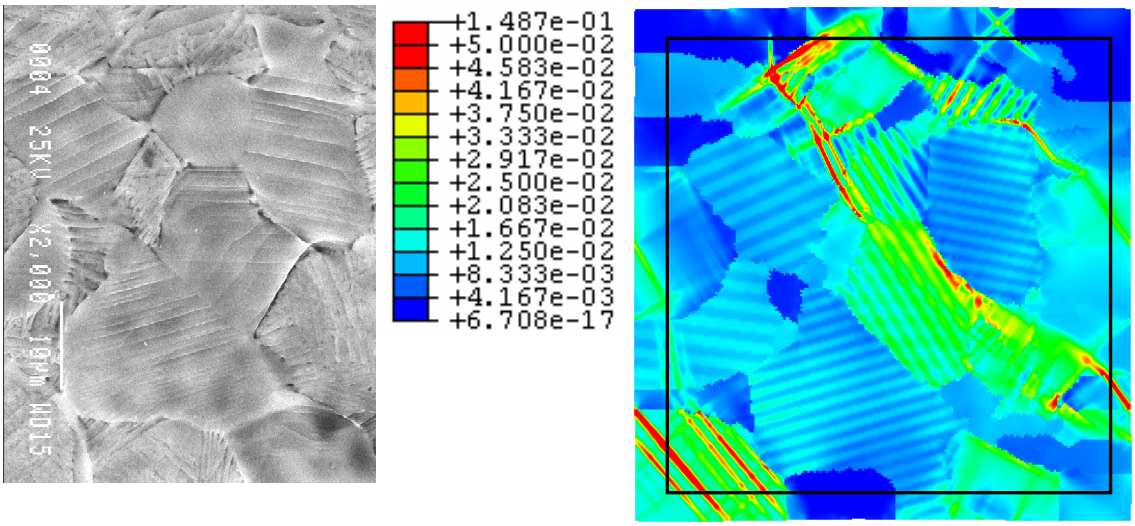

Experiment

Simulation

(c) $\varepsilon_t = 2\%$

Figure 7.10 Comparison of slip behaviors at various applied strain ε_t (Cont.).

Experimental observations show that the wavelength of the slip bands decrease with increasing plastic deformation. At the same time, the thicknesses of the slip bands increase (Xiao and Umakoshi, 2002, 2003). In finite element simulations, constant slip band thickness and wavelength are assumed for all primary α grains at various plastic strains. This assumption results in the discrepancy in the structure of slip bands between experiment and simulation. The finite element simulation is unable to fully capture the slip behavior of primary α grains. For example, the simulation shows stronger prismatic slip than basal slip in grain 2 which contradict to the experimental observations. From the contour of effective plastic strain at $\varepsilon_t = 2\%$, both grains 4 and 5 are shown to undergo significant plastic deformation. However, the SEM image shows slight slip traces in grain 4 and no slip trace in grain 5. Such a discrepancy can be in part attributed to the periodic boundary conditions used in this study. Lack of microstructure information in the z direction can also lead to discrepancies between simulation and experiment.

In this Section, it is shown that the proposed crystal plasticity model and softening strategy can be used to simulate the development of slip bands in the primary α phase of Ti-6Al-4V deformed at room temperature. The proposed crystal plasticity model can simulate the softening of slip resistance due to breakdown of the short range order between titanium and aluminum atoms.

The development of slip bands in crystalline material is a nonlocal phenomenon. That is, the slip and deformation behaviors of a material point are influenced by both the surrounding material points and the remote material points. In this study, the slip band is modeled with a local approach (conventional finite element method) combined with the experimental observations regarding characteristic length scale of the slip bands. It is possible that the nonlocal approach such as certain forms of strain gradient crystal plasticity can be used to model slip bands. However, compared to the strain gradient crystal plasticity model, the approach used in this study is simpler, more robust for fatigue simulation, and less computationally expensive. Furthermore, the strain gradient approach faces the similar issues as the nonlocal approach. For example, the wavelength of slip band effectively needs to be determined a priori by assignment of a suitable gradient coefficient.

7.5 Summary

In this Chapter, shear enhanced crystal plasticity constitutive relations are proposed to account for the slip softening due to breakdown of the short range order between titanium and aluminum atoms. In the primary α phase, the threshold stress evolves according to softening restricted to slip band only. Thus, slip concentrates in the slip bands due to their relatively low slip resistance. In this softening strategy, uniform thickness and wavelength of slip bands are assumed for all grains during deformation

since the theoretical calculations of these two parameters are unavailable. This study employs a combination of typical values of thickness and wavelength obtained from experimental observations. The proposed model is calibrated by performing finite element simulations on a polycrystalline Ti-6Al-4V (PW1215). The 3D finite element model is constructed to precisely represent the microstructure of the polycrystalline Ti-6Al-4V as described in Chapter 4. The simulated stress-strain response is shown to be in good agreement with the experimental data provided by Pratt & Whitney up to 2.5% strain.

The slip behavior of a Ti-6Al-4V subjected to monotonic tension history is investigated. The two-dimensional finite element mesh is obtained from the EBSD observation (Bridier et al., 2005). The finite element simulation is performed with the proposed shear enhanced model and softening strategy. The contours of effective plastic strain are compared with the SEM images at various stain levels. It is shown that the proposed approach for slip band simulation can qualitatively capture the slip behavior measured in experiments. The slip bands often form on the basal or prismatic slip system with the highest Schmid factor. The thickness and wavelength of the simulated slip bands are close but are often not same as the SEM observations. Such a discrepancy can be attributed in part to the constant thickness and wavelength of slip bands assumed in this approach.

This approach provides a useful computational tool to study the effect of slip bands on the deformation behavior of Ti-6Al-4V, particularly grain scale shear localization and stresses related to fatigue crack formation. It is also noted that slip bands play an important role in fatigue crack initiation in Ti-6Al-4V. Therefore, the approach can add value to the study of the microstructure-scale fatigue behavior of Ti-6Al-4V.

CHAPTER 8

MICROSTRUCTURE-SCALE FATIGUE ANALYSIS OF TI-6AL-4V BASED ON SHEAR ENHANCED CRYSTAL PLASTICITY MODEL

8.1 Introduction

Fatigue is a complex process that depends significantly on the temperature/environment, loading history, and microstructure of the material. It is desired to understand scatter in fatigue as a function of microstructure in order to tailor microstructure to improve fatigue resistance. Moreover, we can gain some understanding of dependence of mean fatigue behavior on microstructure. An engineering approach to fatigue life estimation for components requires a large number of fatigue tests for various microstructural materials which are generally expensive and which require significant amounts of time to conduct.

The formation of fatigue cracks is a highly localized process that occurs at various microstructure inhomogeneities. For Ti-6Al-4V, fatigue cracks can initiate from primary α grains, lamellar colonies and grain boundaries. During high cycle fatigue (HCF) life, the formation of a fatigue crack can take a large fraction of the fatigue life of a material (Lankford and Kusenberger, 1973). Consequently, it is important to quantify the relative driving force for fatigue crack formation at various microstructure inhomogeneities.

Various models have been proposed to predict the crack incubation life (fatigue crack formation) of materials under multiaxial fatigue load. Among them, the critical plane approaches such as Fatemi-Socie (FS) (1988) and maximum cyclic plastic shear strain have demonstrated superior predictive capabilities in modeling fatigue crack

formation at the microstructure level (McDowell, 1996a). It should be noted that these fatigue indicator parameters (FIPs) are calculated over a finite volume since the crack formation operates over a finite domain. Crack formation in Ti-6Al-4V was shown to be a shear-dominated phenomenon (Goh, 2002). Among the shear-dominated FIPs, the Fatemi-Socie FIP includes the maximum normal stress to the critical plane and therefore is considered to be more suitable than the maximum cyclic plastic shear strain for the predication of fatigue life of Ti-6Al-4V (Mayeur et. al, 2006). The FIPs can be related to the crack formation life according to modified Coffin-Manson relations.

Slip banding plays an important role in fatigue crack initiation in crystalline materials. Intense shear along the persistent slip band causes formation of protrusions at the surface in Cu (Ma and Laird, 1989). Protrusion consists of many small intrusions and extrusions, and cracks often nucleate at or close to protrusions, as shown in Fig. 8.1 (Ma and Laird, 1989). Cracks can also initiate along internal slip bands in primary α grain due to to-and-fro slip, as shown in Fig. 8.2.

Fatigue crack formation due to the impingement of slip bands on the grain boundary has been reported for crystalline materials such as Ni (Morrison and Moosbrugger, 1997) and Ti alloys (Neal and Blenkinsop, 1975; Evans and Bache, 2003). The impingement mechanism of crack formation was first proposed by Hollomon and Zener (1946). It was shown that high normal stress concentrated at the region where the slip band impinged on the grain boundary due to the dislocation pile-up. Stroh (1954) shows that the tensile stress σ_{inten} that developed on the slip band normal to the slip plane was a function of the resolved shear stress τ and the distance r from the head of the pile-up, i.e.,

$$\sigma_{inten} = \frac{3}{2}\eta\tau\left(\frac{L}{r}\right)^{1/2} \tag{8.1}$$

where η is a constant that depends on the orientation of the slip band and L is the distance over which the leading dislocation in the pile-up has traveled from the source. This distance can be assumed to be equal to the grain size. Clearly, the highest tensile stress due to impingement occurs at the grain boundary where r is minimal. Slip band impingement on grain boundary can lead to formation and propagation of small cracks in the microstructure (McDowell, 2005). Figure 8.3 shows cracks that have formed at grain boundary due to slip band impingement of a single crystal Ni cycled at $\Delta\varepsilon/2 = 2.5\times10^{-4}$ at room temperature.

Another important crack formation mechanism is decohesion of α/β interface in lamellar colony (Neal and Blenkinsop, 1975). It is believed that the intense shear along the interface causes decohesion of lamellar layers, possibly enhanced by residual dislocation content at the interface.

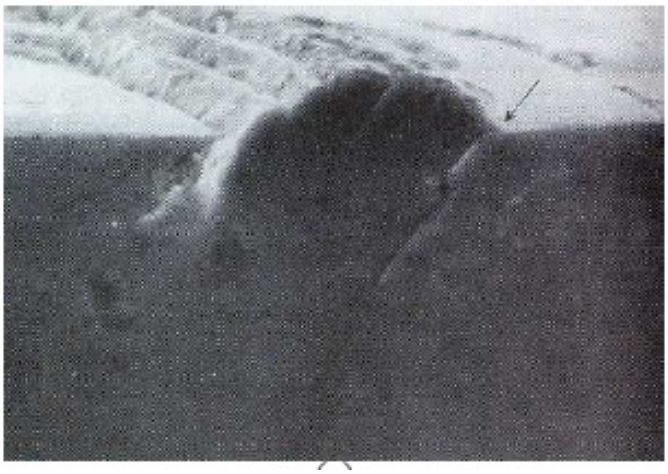

Figure 8.1 Crack nucleate at protrusion of single crystal copper deformed at room temperature (Ma and Laird, 1989).

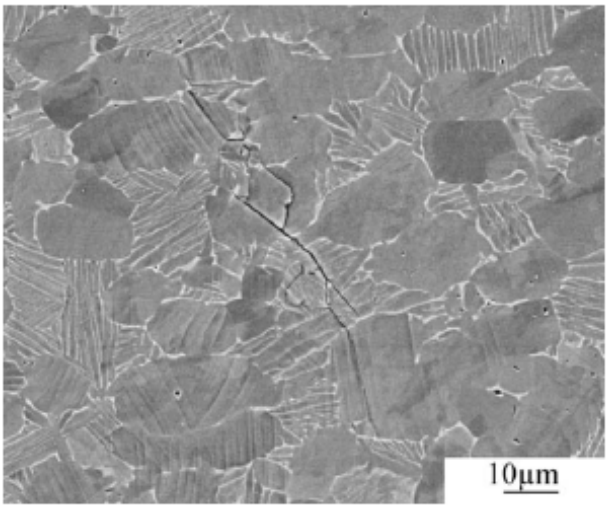

Figure 8.2 Crack initiate along a slip band on Ti-6Al-4V subjected to a cyclic bending test at room temperature (Le Biavant et al., 2002).

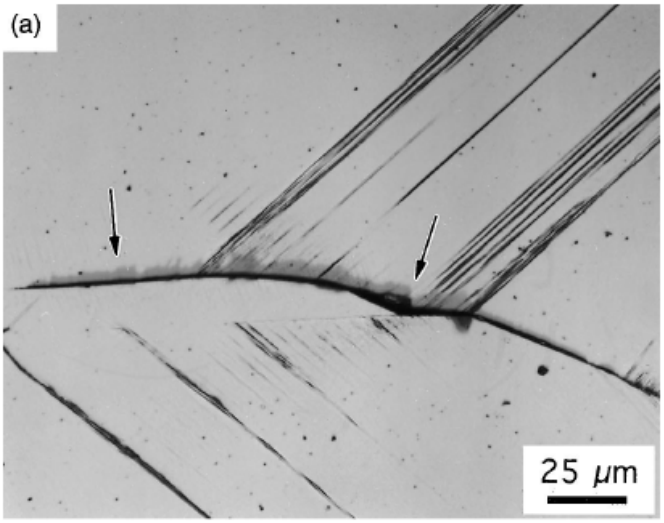

Figure 8.3 Crack formation at grain boundaries of Ni where slip band impinged, arrows identify the location of crack (Morrison and Moosbrugger, 1997).

A simulation-based microstructure sensitive approach to fatigue has been developed by McDowell (1996b) using the measured microstructural attributes to quantify the statistical distribution of fatigue responses. In addition to microstructure parameters, sensitivity of fatigue to loading parameters such as the amplitude of the applied strain, the load ratio, and multiaxiality can also be explored using computational methods (McDowell, 2005). This approach involves the following steps (McDowell, 2005):

1. Identify controlling microstructural features for crack formation and early growth.
2. Conduct numerical analyses (e.g. finite element) of various microstructures for representative loading cases.
3. Calculate the fatigue indicator parameter as a function of applied strain amplitude, mean stress or strain, and variable amplitude loading, as appropriate.
4. Apply microstructure-scale crack formation/incubation relations based on simple Coffin-Manson forms to model crack formation life.
5. Calibrate constants of Coffin-Manson and small crack propagation relations to the results for experimentally characterized microstructure(s) and then use these constants to predict results for other microstructures.

This approach can be applied to investigate the microstructure sensitivity of fatigue crack formation life of Ti-6Al-4V as previous shown.

In previous chapters, shear-dominated fatigue indicator parameter (Fatemi-Socie parameter) was used to quantify the driving force for crack formation in Ti-6Al-4V at the microstructure level. Apparently, the Fatemi-Socie FIP is unable to account for all crack formation mechanisms, as previously discussed. Additional FIPs are needed to account for slip bands. In last Chapter, a new approach containing shear enhanced crystal plasticity constitutive relations and softening strategy is proposed to simulate the formation of slip bands in primary α grains of duplex Ti-6Al-4V. Fatigue analysis of Ti-6Al-4V is performed by combining this new approach with additional FIPs. The aim of

this study is to provide a new computational approach that can quantify the various driving forces for crack formation in primary α grains, grain boundaries and lamellar colonies.

Quasi-cleavage is an important failure mechanism of TiAl alloys subjected to loading history with "cold-dwell" (Bache and Evans, 2003; Evans and Bache, 1994). This is not a brittle phenomenon. The term ''quasi-cleavage'' is used in recognition of the fact that the facets are found to have a near basal plane crystallographic orientation. It is found that quasi-cleavage results from the presence of "hard" and "soft" grains. The grain with c-axis parallel to the loading direction is the "hard grain". The slip band forms in neighboring "soft" grain and impinges on the grain boundary between the "soft" and "hard" grains. The strong stress intensification on the grain boundary causes facets in "hard" grains in spite of their unfavorable orientation.

To investigate the quasi-cleavage phenomenon, Dunne et al. (2007) introduced a "rogue" gain combination in which the basal plane of the hard grain is perpendicular to the loading direction. The c-axis of the adjacent grain made an angle of about 20 degree to the loading direction. By using a strain-gradient crystal plasticity model (Dunne et al., 2007), it was shown that the rogue grain combination causes very high basal normal stress on the hard grain.

The works reported in this Chapter will focus on the simulation of slip band in polycrystal Ti-6Al-4V. The objectives of this study are as follows:

- Apply the physically-based crystal plasticity constitutive model developed in the last Chapter to various microstructures.
- Develop physically-based fatigue indicator parameters that can account for various crack formation mechanisms.
- Simulate the role of microstructure in deformation and fatigue behavior.
- Develop a computational approach for microstructure-scale material modeling and fatigue analyses.

More emphasis is placed on the developing and using computational tools and frameworks to study the effects of microstructure of Ti-6Al-4V on deformation and fatigue behaviors while considering the slip localization in α TiAl.

In this study, cyclic loading is applied on the microstructure that was used in Chapter 7. A second microstructure is established to introduce a rogue grain combination, as shown in Section 8.2. The new fatigue indicator parameters are described in Section 8.3. The monotonic tension behaviors of the two microstructures are shown in Section 8.4. Section 8.5 shows the fatigue behaviors of these two microstructures. A summary is given in the last Section.

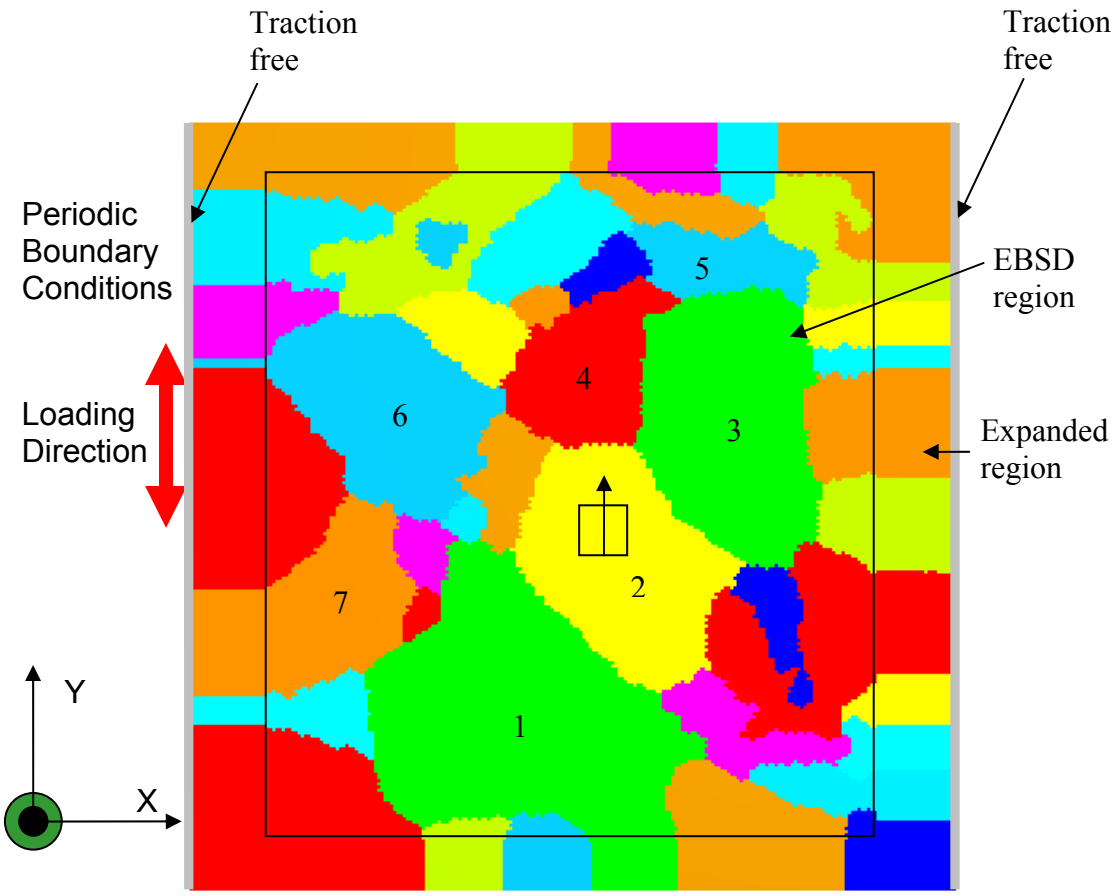

Figure 8.4 Microstructure II.

8.2 Finite Element Model

Two microstructures characterized by EBSD, along with expanded regions are used in this study to identify the effect of a rogue grain combination on resistance to crack formation of Ti-6Al-4V. The first microstructure (Microstructure I) is the same as that used in Chapter 7, which contains 7 primary α grains. To introduce the hard grain in Microstructure II, the orientation of grain 2 is changed in such a way that its c-axis is parallel to loading direction (y direction), as shown in Fig. 8.4. The Schmid factors of the basal and prismatic systems of grain 2 are zero. Since the slip resistant of pyramidal system is relatively high, grain 2 of Microstructure II will mainly undergo elastic deformation.

8.3 Fatigue Indicator Parameters (FIPs)

Extensive study has been devoted to the development of robust fatigue models that are applicable to multiaxial stress states. The critical-plane approaches currently appear to be receiving the most attention among active researchers because of their good correlation with multiaxial test data (McDowell, 1996; Gallagher et al., 2004). In previous chapters, the shear dominated Fatemi-Socie FIP (P_{FS}), was used to quantify the driving force for crack formation in Ti-6Al-4V at the microstructure level. The critical plane defined in this model is the plane experiencing the maximum range of cyclic plastic shear strain. The Fatemi-Socie FIP is given by Eq. (1.22)

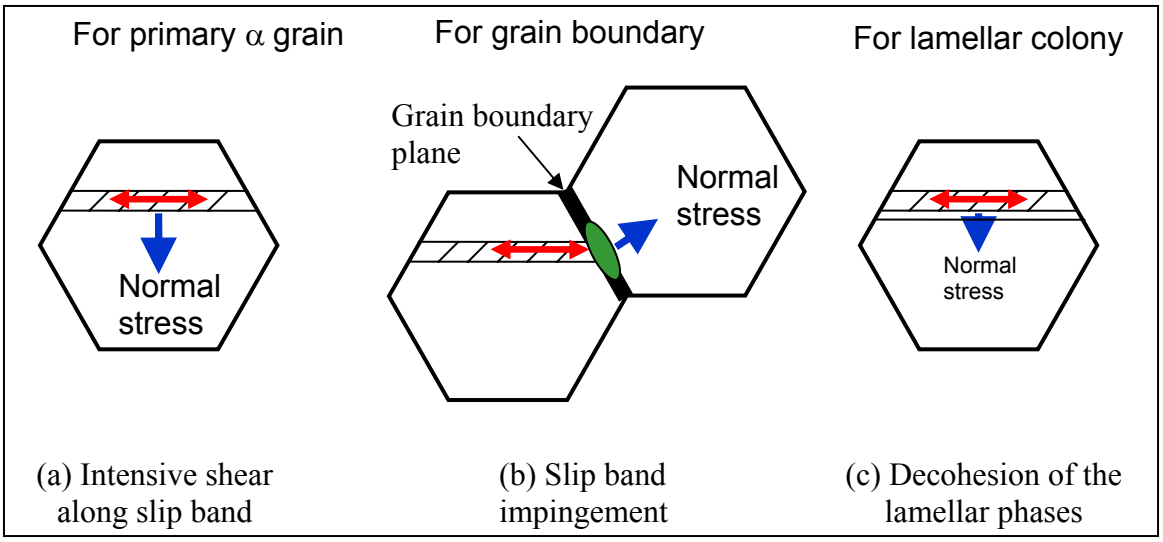

Figure 8.5 Crack formation mechanisms of Ti-6Al-4V.

As discussed before, two crack formation mechanisms of HCF α–TiAl need to be considered: decohesion of the slip band interface due to the intense shear along the slip band and slip band impingement on the grain boundary, as shown in Fig 8.5 (a) and (b). In this work, two FIPs are proposed, corresponding to these two mechanisms. A modified FS FIP can be used to account for the first crack formation mechanism, which is shear-dominated, i.e.,

$$P_{BAND} = \frac{\Delta\gamma_{BAND}^{p*}}{2}\left(1 + K_1 \frac{\sigma_n^{BAND*}}{\sigma_y}\right) \tag{8.2}$$

where $K_1 = 1$ is constant and $\Delta\gamma_{BAND}^{p*}$ is the plastic shear strain range along the slip band averaged over a finite volume, σ_n^{BAND*} and σ_y denote the averaged maximum normal stress acting on the slip band plane and the yield strength, respectively. Clearly, the

critical plane for this FIP is the slip band plane with the maximum range of plastic shear strain.

Slip band impingement on grain boundaries leads to stress intensification due to progressive slip. The critical plane is thus the grain boundary plane. The FIP accounting for the impingement mechanism is used for the grain boundary elements and is written as

$$P_{IMP} = \frac{\Delta\gamma_{BAND}^{p*}}{2}\left(1 + K_2 \frac{\sigma_n^{GB*}}{\sigma_y}\right) \tag{8.3}$$

where $\Delta\gamma_{BAND}^{p*}$ is the averaged maximum plastic shear strain range over a finite volume along the slip band at the grain boundary, K_2 = 1 is constant and σ_n^{GB*} is the averaged normal stress applied on the grain boundary.

For lamellar colonies, decohesion of lamellar phases is the dominant mechanism for crack formation as shown in Fig. 8.5(c). Therefore, the α/β interface is the critical plane for this FIP. The conventional form of the FS FIP can be used for the lamellar colonies as the driving force for fatigue crack nucleation, i.e.,

$$P_{LAMELLAR} = \frac{\Delta\gamma_{\max}^{p*}}{2}\left(1 + K_3 \frac{\sigma_n^{\max*}}{\sigma_y}\right) \tag{8.4}$$

where K_3 = 1 is constant and $\Delta\gamma_{\max}^{p*}$ and $\sigma_n^{\max*}$ denote the averaged maximum plastic shear strain range and the maximum normal stress on the corresponding critical plane, respectively.

These three proposed FIPs are the relevant FIPs and will be used to assess the relative potency of crack formation for Ti-6Al-4V as a function of microstructure under cyclic loading. The Fatemi-Socie parameter P_{FS} is also calculated and compared with the

proposed FIPs. It should be noted that the FIP is computed using a nonlocal volume averaging procedure over integration points. Its nonlocal range reflects the scale of crack formation and it is not mesh dependent. The frequency distributions of FIPs significantly depend on the size of averaging volume. In this study the edge size of the averaging volume is 0.5 μm which is about 1/2 of the width of slip band. There is also a consideration that averaging is performed over a minimum volume to reflect the scale of crack formation.

Both the maximum value and frequency distributions of FIPs are important to identify the variations of the fatigue behaviors with respect to variation of the microstructures and loading history. The crack formation life can be calculated from the maximum nonlocal FIPs. The frequency distribution of the nonlocal FIPs can be used to identify the distributed crack formation.

8.4 Monotonic Tension Simulations

The same periodic boundary conditions as shown in Chapter 7 are used to study of two microstructures in this Chapter. To examine the monotonic tension behavior of Microstructures I and II, strain-controlled tension is applied with the loading direction parallel to y direction. The simulated stress-strain responses are shown in Fig. 8.6. Two microstructures have the same elastic properties. Microstructure II has higher yield strength than Microstructure I for the considered loading direction. The yield strain and stress for these two microstructures are listed in Table 8.1. At the same total strain level, the plastic deformation of Microstructure I is larger than that of Microstructure II.

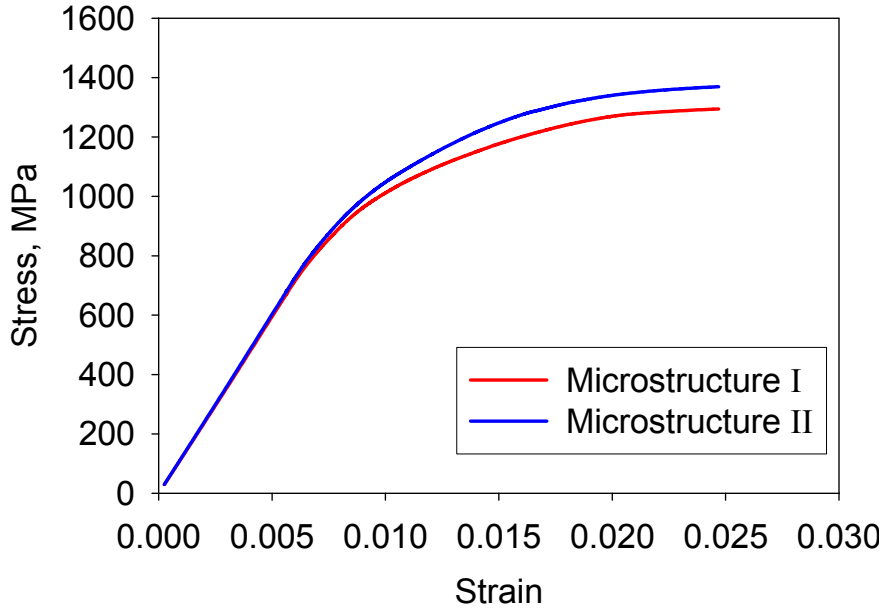

Figure 8.6 Tensile stress-strain responses of Microstructures I and II.

Table 8.1 Tensile properties of microstructure I and II.

	Yield strength (0.2% yield strength), MPa	Yield strain
Microstructure I	1010	0.98%
Microstructure II	1095	1.09%

8.5 Cyclic Loading Simulations

To calculate FIPs, a strain-controlled cyclic loading history with strain rate at 4.25×10^{-4} s^{-1} and load ratio at -1 is used, as shown in Fig. 8.7. The applied strain amplitude $\Delta\varepsilon_t/2$ is 0.85% which is lower than the yield strain of both microstructures I

and II. The loading direction is parallel to the y direction. Ten cycles are applied to achieve the stable cyclic behavior.

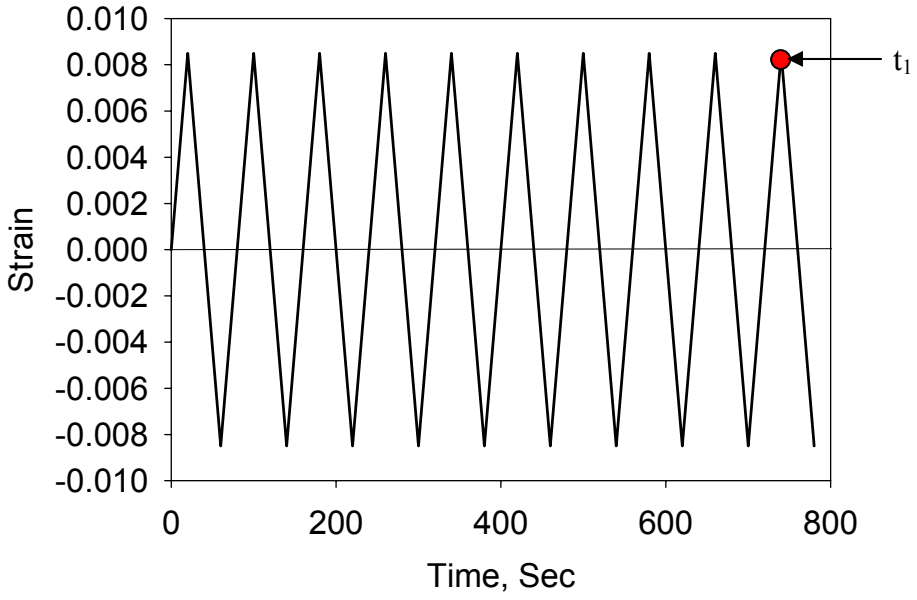

Figure 8.7 Applied loading history.

The stress-strain responses for the two microstructures are shown in Fig. 8.8. A significant drop of the maximum stress for the first loading cycle is shown. A slight reduction of stress is shown for the following 4 to 5 cycles. After that, the hysteresis loop is relatively stable. The cyclic softening can be attributed to the softening of the threshold stresses of the prismatic and basal systems of primary α grains and the soft system of lamellar colonies. It is noted that the threshold stress decreases rapidly according to a power law relation which causes the largest reduction of stress during the first cycle.

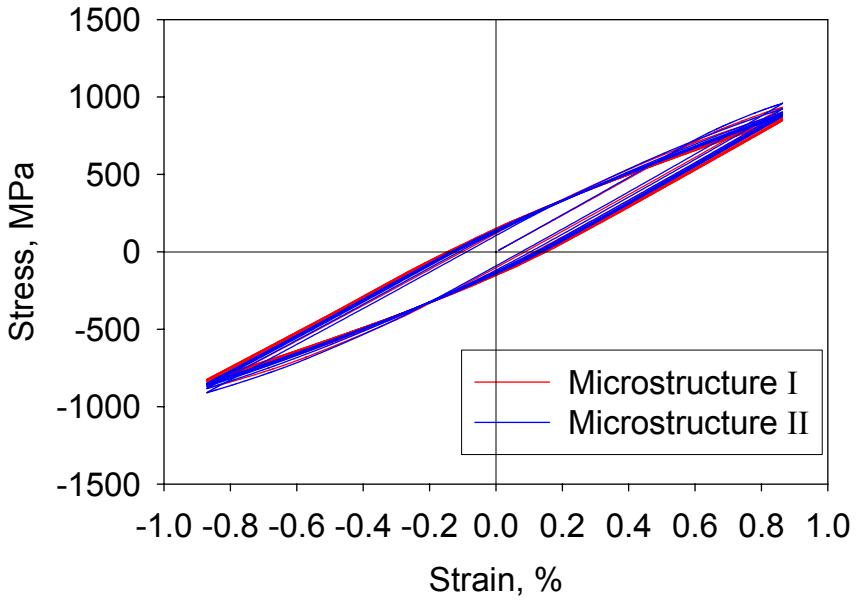

Figure 8.8 Stress-strain responses for two microstructures.

The cumulative plastic strains $\bar{\varepsilon}^p_{cum}$ can be effectively used to display the cumulative plastic deformation over loading cycles, defined as

$$\bar{\varepsilon}^p_{cum} = \int d\bar{\varepsilon}^p \tag{8.5}$$

where $\bar{\varepsilon}^p$ is the effective plastic strain as defined before. Figures 8.9(a) and (b) show the contours of the cumulative plastic strain of two microstructures at time $t = t_1$ as shown in Fig. 8.7. For Microstructure I, the clear band structure of $\bar{\varepsilon}^p_{cum}$ is shown for all primary α grains except grain 4. Grain 4 has relatively low cumulative plastic strain and thus mainly undergoes elastic deformation. The same band structure of $\bar{\varepsilon}^p_{cum}$ is found in grains 1, 3, 4, 6 and 7 of Microstructure II. No plastic deformation is found for grain 2, which has the c-axis parallel to the loading direction. Grain 4 of Microstructure II has much

higher cumulative plastic strain than that of Microstructure I. The significant yielding of grain 4 in Microstructure II is caused by high stress induced by the hard grain. The introduction of hard grain 2 in Microstructure II also affects the plastic deformation behavior of the neighboring grains 1 and 3. $\bar{\varepsilon}^{p}_{cum}$ of grain 1 of Microstructure II is higher than that of Microstructure I. The effect of hard grain on the plastic deformation behavior of remote grains 4, 6 and 7 is negligible.

Figures 8.10(a) and (b) show contours of von Mises stress of two microstructures at time $t = t_1$. It is noted that the von Mises stress is also distributed in a band structure for primary α grains. The von Mises stress in the slip band is much lower than that of matrix which is considered as "hard" region. Grain 2 of Microstructure II has von Mises stress about two times higher than that of Microstructure I. Introduction of a hard grain also causes stress intensification on the neighboring grains. The von Mises stress of grains 1, 2 and 5 increases. Comparing Fig. 8.10(a) with (b), it is shown that variation of von Mises stress in remote grains 4, 6 and 7 is relatively low.

Observation of the cumulative plastic strain and von Mises stress for the two microstructures shows that the introduction of a hard grain significantly affects the deformation behavior of the neighboring grains. Both plastic deformation and stress increase due to the stress intensification induced by the hard grain. At the same time, variation of deformation behavior of the remote grains is relatively low.

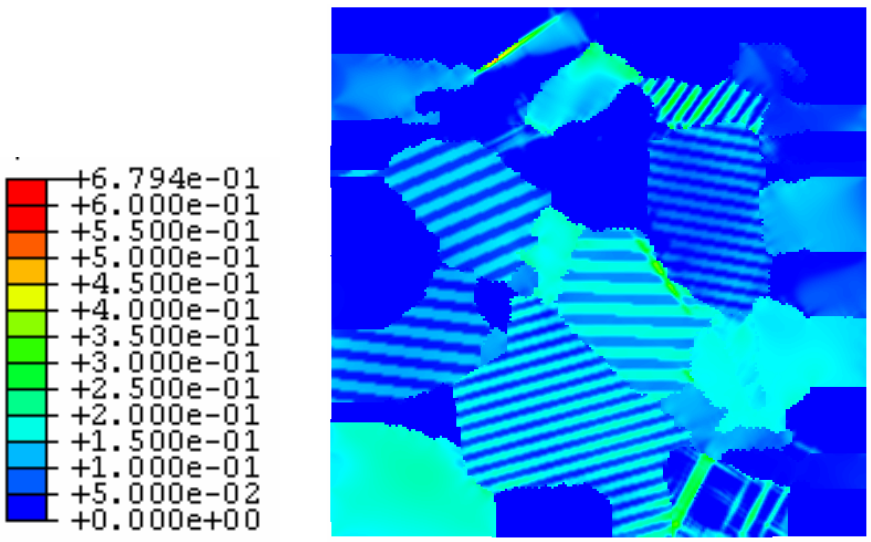

(a) Microstructure I

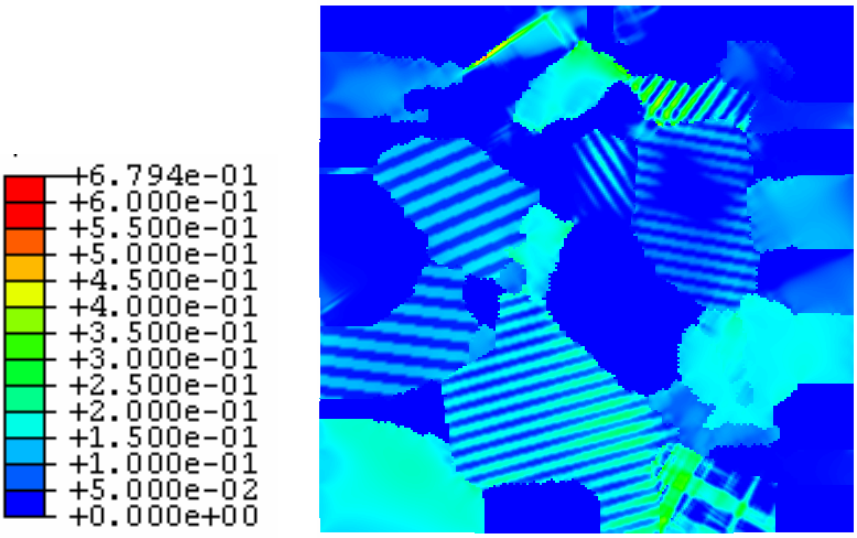

(b) Microstructure II

Figure 8.9 Contours of the cumulative plastic strain at time t_1.

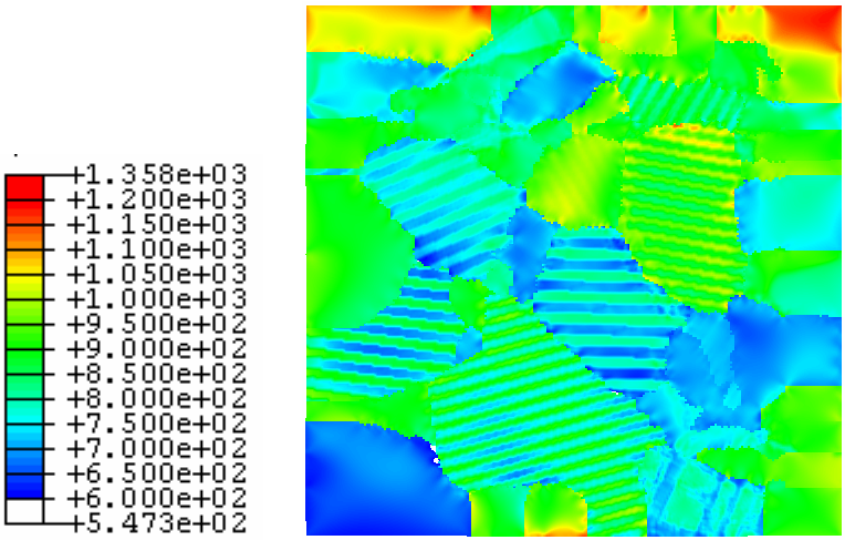

(a) Microstructure I

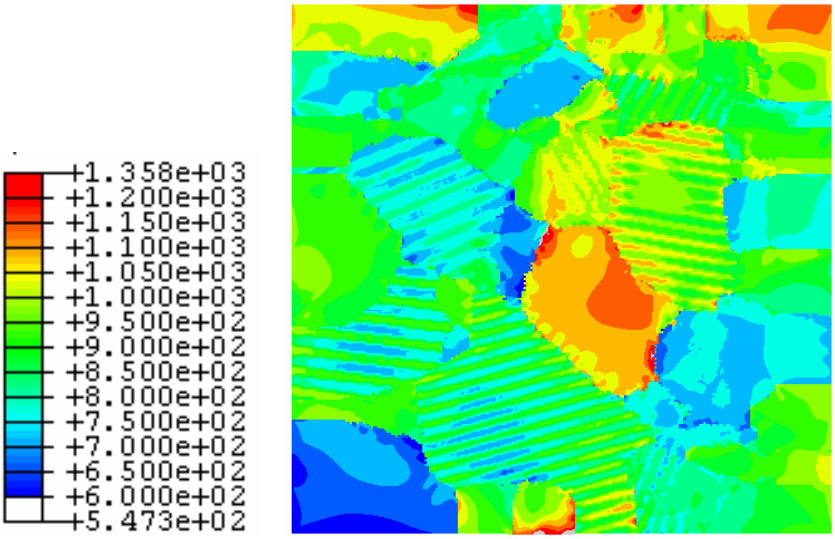

(b) Microstructure II

Figure 8.10 Contours of von Mises stress of two microstructures at time t_1.

Strain behavior can be characterized as belonging to one of five regimes: elastic, elastic shakedown, reversed cyclic plasticity, combined cyclic plasticity and ratcheting, and plastic ratcheting. The detailed definitions of these regimes have been given in Chapter 2. In this study, the characteristic regime of plastic strain behavior is determined over the 10^{th} loading cycle.

Table 8.2. Plastic strain behavior for two microstructures.

	Microstructure I	Microstructure II
$\overline{\varepsilon}^{p}_{\max}$	0.032	0.034
N_p (% of elements)	35008 (86.8%)	32378 (80.2%)
Elastic shakedown (% of N_p)	17.8	20.8
Reversed cyclic plasticity (% of N_p)	79.4	75.9
Combined cyclic and ratcheting (% of N_p)	2.8	3.3
Ratcheting (% of N_p)	0	0.1

Table 8.2 summarizes the plastic strain behavior for two microstructures. In Table 8.2, N_p denotes the number of elements that plastically deform and $\overline{\varepsilon}^{p}_{\max}$ is the maximum effective plastic strain over the microstructure at $t = t_1$. It is shown that Microstructure I has a larger number of plastically deformed elements due to the favored orientation of grain 2. Application of hard orientation to grain 2 in Microstructure II results in an increment of $\overline{\varepsilon}^{p}_{\max}$ due to stress intensification. The overall plastic strain behavior of Microstructures I and II is close. The dominant plastic strain behavior for Microstructures I and II is the reversed cyclic plasticity. Only a few percent of plastically deformed elements undergo combined cyclic and ratcheting plasticity.

All FIPs are calculated over the 10th cycle for the EBSD region of Microstructures I and II. FIPs in the expanded region are not used to evaluate the fatigue behaviors of two microstructures. The contours of P_{FS}, P_{BAND}, $P_{LAMELLAR}$, and P_{IMP} are given in Figs. 8.11, 8.12, 8.13 and 8.14, respectively. Both the maximum values and the frequency distributions of FIPs are potentially important for fatigue analysis. The maximum FIPs are listed in Table 8.3. In Table 8.3, the maximum P_{FS} at the grain boundary is given and compared with P_{IMP}. Variations of maximum FIPs for two microstructures are also listed in Table 8.3. The variation is given by

$$Variation = \frac{P\big|_{Microstructure2} - P\big|_{Microstructure1}}{P\big|_{Microstructure1}} \tag{8.6}$$

Figures 8.15, 8.16, 8.17 and 8.18 show the frequency distributions of P_{FS}, P_{BAND}, $P_{LAMELLAR}$, and P_{IMP} of two microstructures, respectively. The frequency distribution of P_{FS} at the grain boundary is given in Fig. 8.19.

The overall distributions of P_{FS} for two microstructures are close to the distribution of the cumulative plastic strain as shown in Fig. 8.9. In Fig. 8.11, P_{FS} of the primary α grains that plastically deformed is distributed in the band structure. The Fatemi-Socie parameter of Grain 2 of Microstructure II is close to zero since grain 2 mainly undergoes elastic deformation. Compared with Microstructure I, P_{FS} in the primary α grains 1, 3 and 4 of Microstructure II increases. The introduction of a hard grain in Microstructure II does not affect P_{FS} in grains 6 and 7. The maximum P_{FS} of two microstructures is found in lamellar colonies. In Table 8.3, introduction of hard grain in Microstructure II results in an 8.9% increment of maximum P_{FS}. The frequency distribution of P_{FS} displays a similar tendency as shown in Fig. 8.15. A larger number of elements in Microstructure II has higher P_{FS}. For example, Microstructure II has about

0.087% of elements with P_{FS} ranging between 0.021 and 0.03, while Microstructure I has only 0.03% of elements with P_{FS} in the same range. These observations show that compared with Microstructure I, Microstructure II has larger driving force for crack formation in both primary α phase and lamellar colonies due to introduction of hard grain. Therefore, the expected fatigue life of Microstructure II is shorter than that of Microstructure I based on P_{FS}. The reduction of fatigue life of Microstructure II is relatively modest since the maximum P_{FS} increases only a few percent.

The fatigue indicator parameter P_{BAND} is not calculated for lamellar colonies and grain boundaries. The other two FIPs, P_{IMP} and $P_{LAMELLAR}$, are used for these two regions. As shown in Fig. 8.12, the distribution of P_{BAND} is close to that of P_{FS} in primary α phase. Such a phenomenon can be attributed to the single slip behavior of primary α grains of Microstructures I and II under the currently considered loading history. The maximum plastic shear plane is the same as the slip plane of the active slip system. The slip plane is assumed to be the critical plane in P_{BAND}. Therefore, for primary α grains undergoing single slip, P_{BAND} and P_{FS} share the same critical plane and thus have same value. An increment of P_{BAND} in grains 1, 3 and 4 of Microstructure II is shown in Fig. 8.12. Grain 2 has P_{BAND} close to zero. In Fig. 8.16, the frequency distribution of P_{BAND} shows that the driving force for crack formation along the slip band increases. The maximum P_{BAND} increases moderately 22.6% for Microstructure II. It is shown that for the microstructure considered in this study, introduction of hard grain in Microstructure II results in a higher driving force for crack formation in neighboring primary α grains. It should be noted that this conclusion is only valid for the loading history used in this study.

Figure 8.13 shows that the overall distributions of $P_{LAMELLAR}$ are unchanged for Microstructures I and II. At the same time, the value of $P_{LAMELLAR}$ of Microstructure II is higher than that of microstructure I for almost all lamellar colonies. For the same strain-controlled loading, introduction of hard grain 2 results in a slight increment of stress in

Microstructure II and causes larger cyclic plastic deformation of lamellar colonies. Therefore, the driving force for decohision of lamellar interfaces increases. The same tendency is shown in the frequency distribution of $P_{LAMELLAR}$ in Fig. 8.17. The increment of the maximum $P_{LAMELLAR}$ (4.9%) of Microstructure II is about the same as that of maximum P_{BAND} (8.9%) but much smaller than P_{FS} (22.6%), as shown in Table 8.3.

It is generally believed that introduction of hard particles in the polycrystal would significantly decrease the fatigue crack formation life. Results show that fatigue indicator parameters P_{FS}, $P_{LAMELLAR}$ and P_{BAND} of Microstructure II increase from only a few percent to about 20%. Figure 8.14 shows that Microstructure II has much higher P_{IMP} than Microstructure I. In Microstructure I, a larger value of P_{IMP} is found at the boundary of grain 1, 4 and 7. Grain 4 has the largest P_{IMP}. A significant increase of P_{IMP} is found at the boundary between grain 1 and 2 of Microstructure II. An increase of P_{IMP} can be attributed to the increase of plastic strain in grain 1 and stress in grain 2 due to application of hard orientation to grain 2, as shown in Figs. 8.9 and 8.10. Therefore, the driving force for crack formation at the boundary between grain 1 and 2 greatly increases. This result is consistent with the simulation results obtained by Dunne et al. (2007). The frequency distribution of P_{IMP} (Fig. 8.18) also shows significant increase of the driving force for crack formation at the grain boundary of Microstructure II. Figure 8.19 shows the frequency distribution of P_{FS} at grain boundary. A moderate increase of P_{FS} in Microstructure II is shown. Thus, P_{FS} is insufficient to quantify the driving force of crack formation due to grain boundary impingement. The same tendency can be seen in Table 8.3. The maximum P_{IMP} increases over 46% while the maximum P_{FS} at the grain boundary increase about 23%.

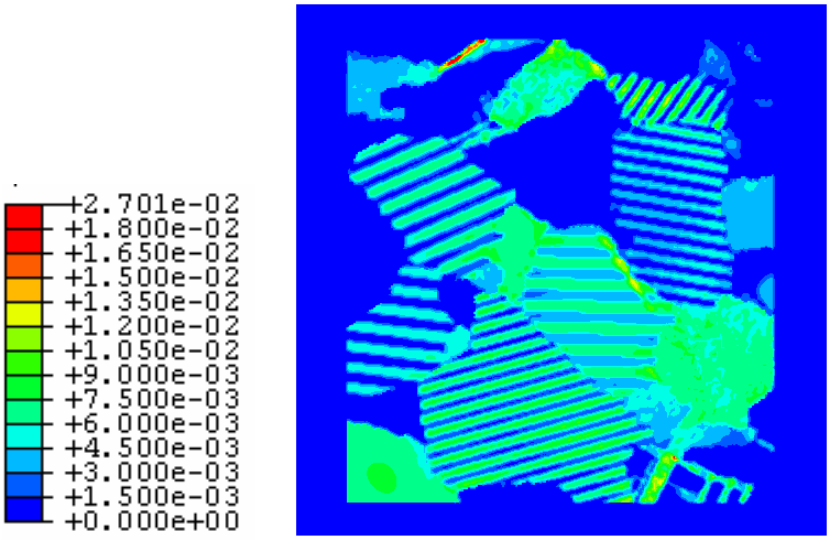

(a) Microstructure I

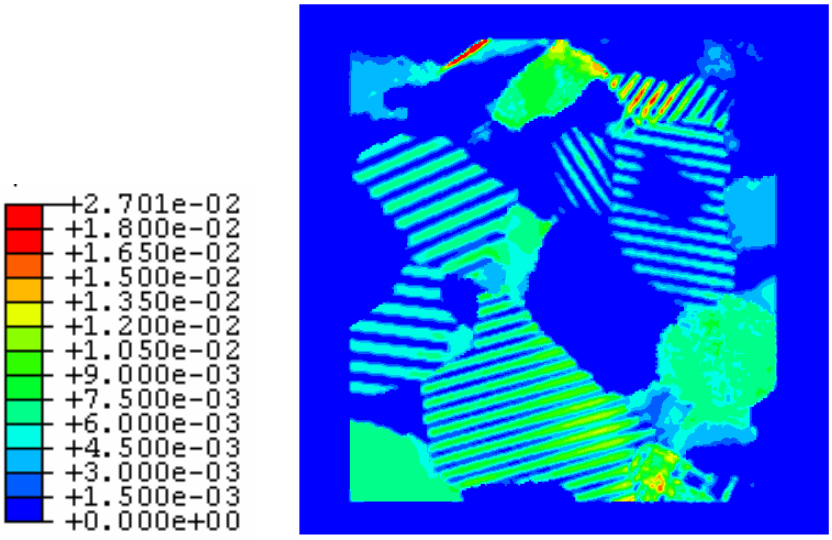

(b) Microstructure II

Figure 8.11 Distribution of P_{FS} for two microstructures.

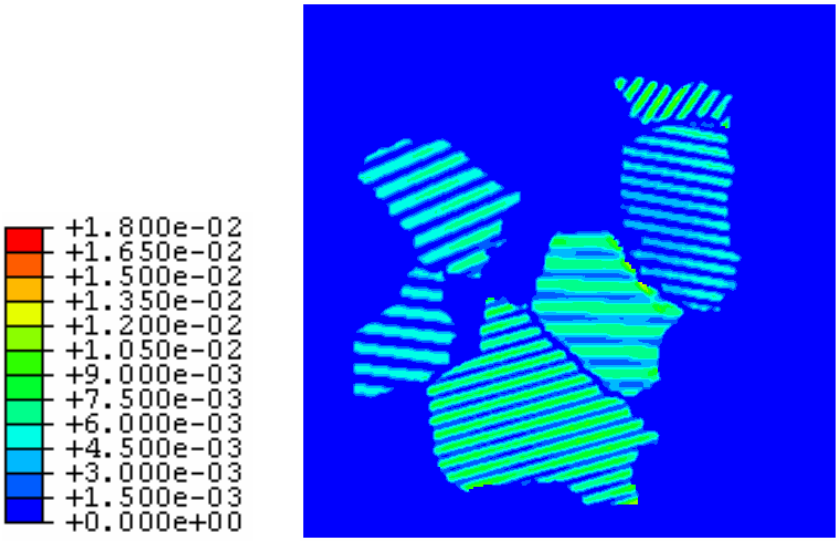

(a) Microstructure I

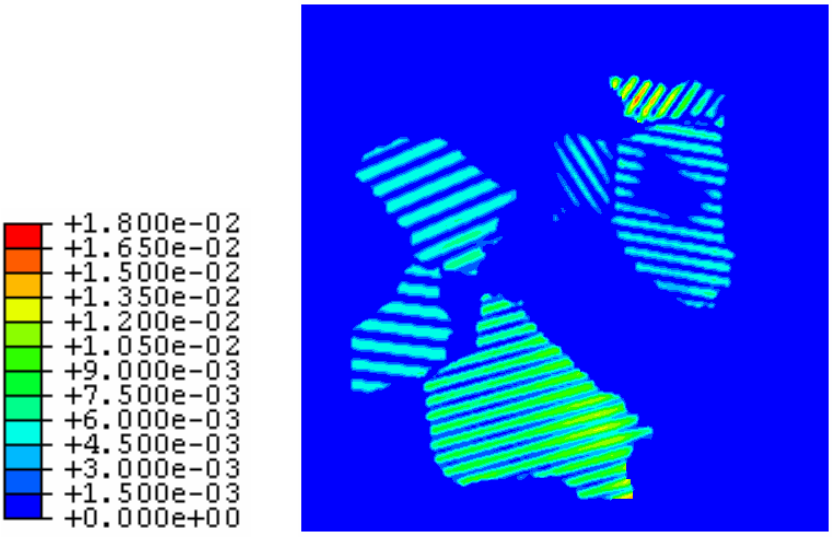

(b) Microstructure II

Figure 8.12 Distribution of P_{BAND} for two microstructures.

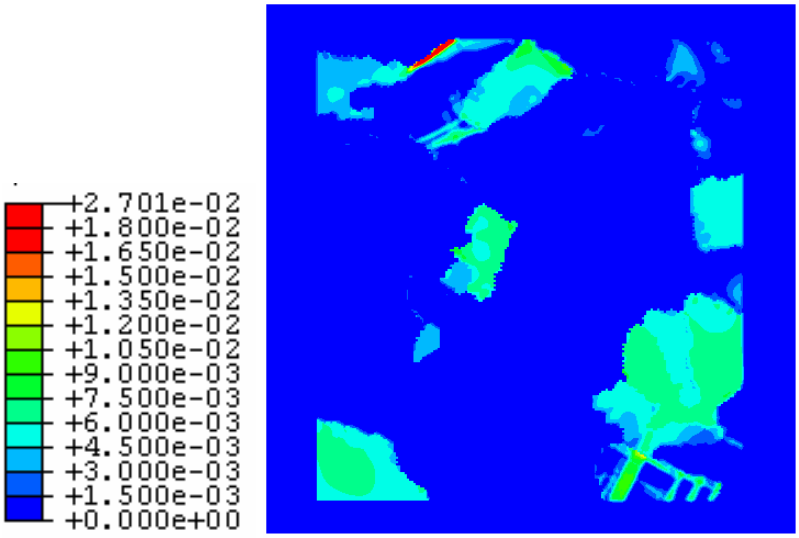

(a) Microstructure I

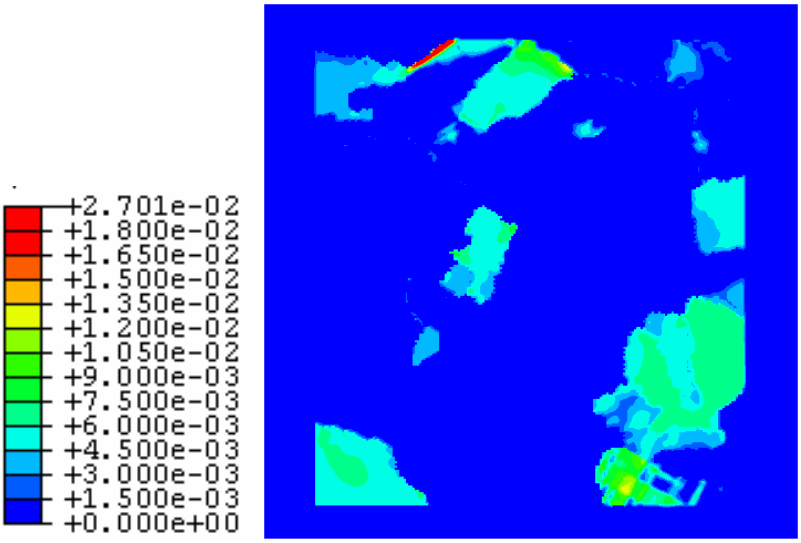

(b) Microstructure II

Figure 8.13 Distribution of $P_{LAMELLAR}$ for two microstructures.

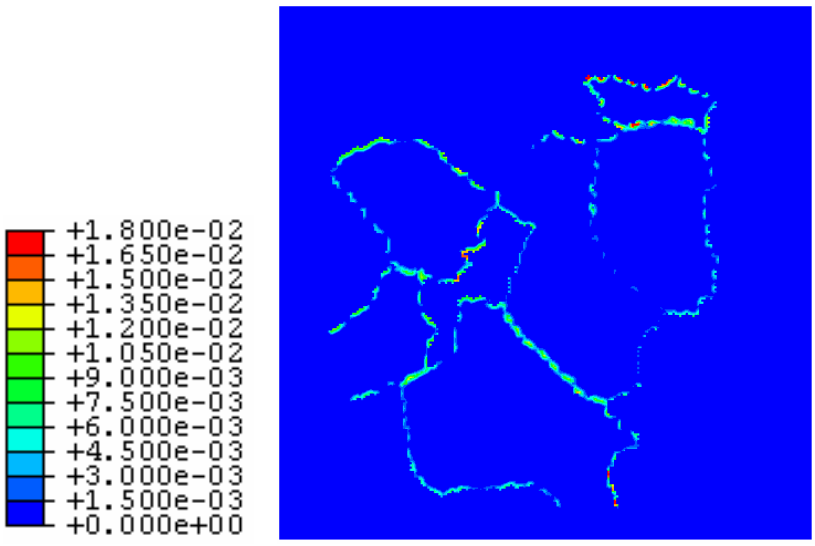

(b) Microstructure I

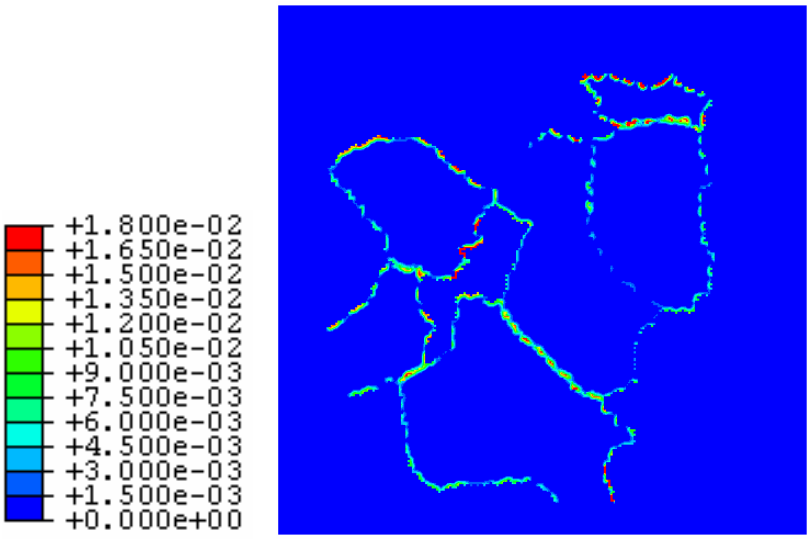

(b) Microstructure II

Figure 8.14 Distribution of P_{IMP} for two microstructures.

Table 8.3 Maximum FIPs for two microstructures.

	Microstructure I	Microstructure II	Variation, defined in Eq. (8.6)
Maximum P_{FS}	0.0269	0.0293	8.9%
Maximum P_{BAND}	0.0128	0.0157	22.6%
Maximum P_{IMP}	0.0124	0.0182	46.7%
Maximum $P_{LAMELLAR}$	0.0282	0.0293	4.9%
Maximum P_{FS} at Grain Boundary	0.0138	0.0171	23.2%

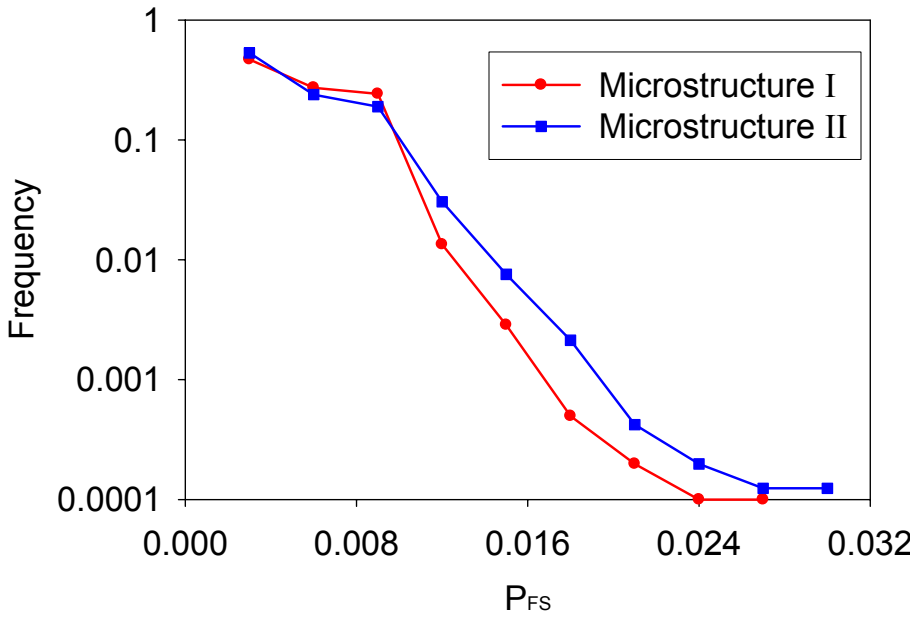

Figure 8.15 Frequency distribution of P_{FS} for two microstructures.

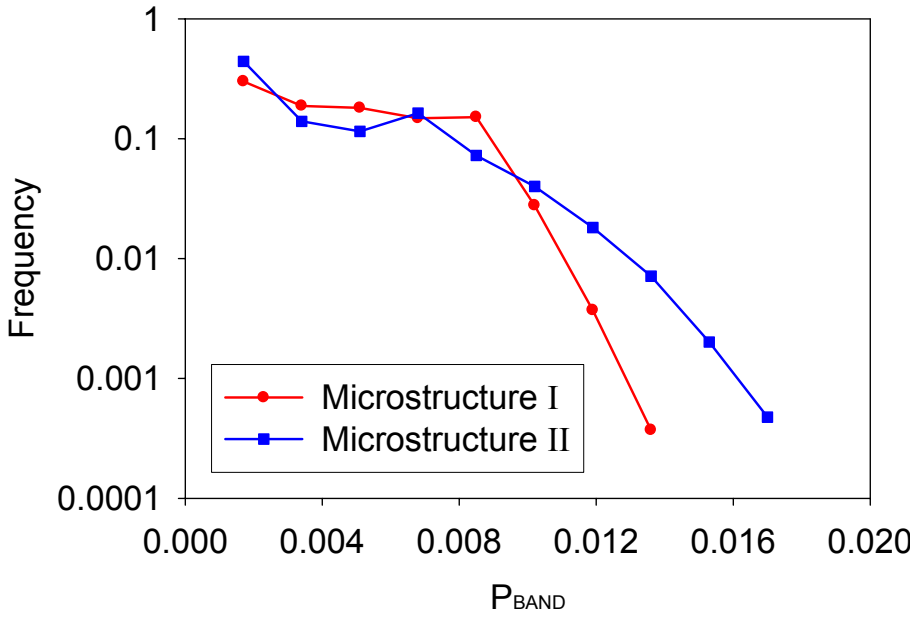

Figure 8.16 Frequency distribution of P_{BAND} for two microstructures.

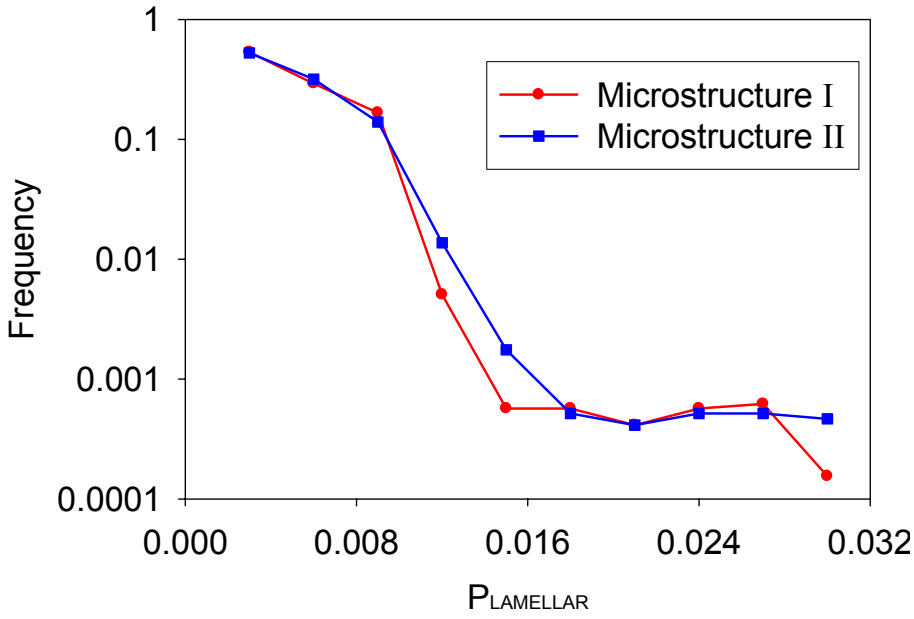

Figure 8.17 Frequency distribution of $P_{LAMELLAR}$ for two microstructures.

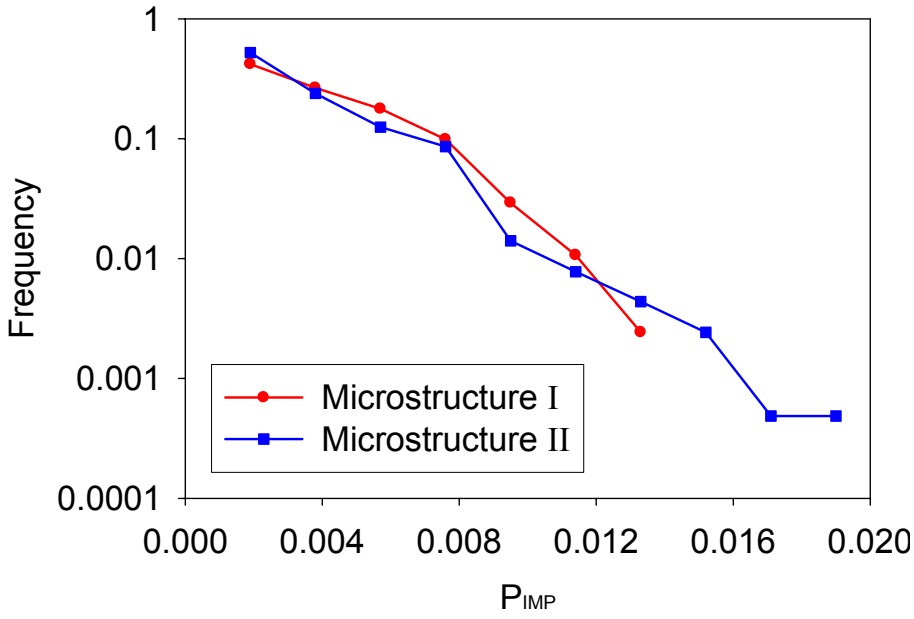

Figure 8.18 Frequency distribution of P_{IMP} for two microstructures.

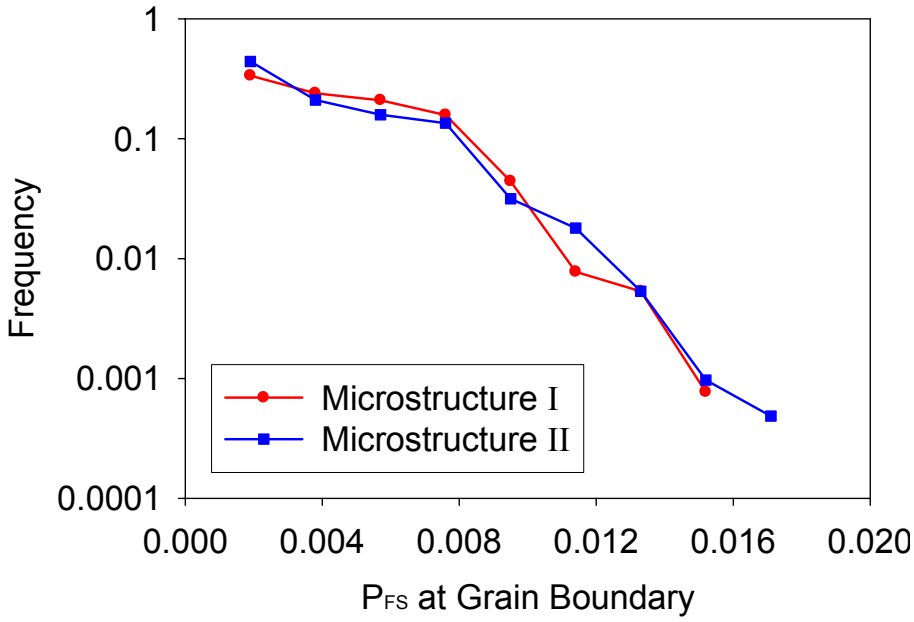

Figure 8.19 Frequency distribution of P_{FS} at grain boundary for two microstructures.

8.5 Summary

In the last Chapter, the proposed approach containing shear enhanced crystal plasticity constitutive relations and a softening strategy is used to simulate the formation of slip bands in primary α grains of Ti-6Al-4V. In this Chapter, fatigue analysis of Ti-6Al-4V is performed by combining this new approach with additional FIPs. These new FIPs account for various mechanisms of fatigue crack formation in Ti-6Al-4V. The aim of this study is to provide a new computational approach that can quantify the various driving forces for crack formation in primary α grains, grain boundaries and lamellar colonies.

In this Chapter, finite element simulations are carried out on two microstructures. The first microstructure is same as the one used in Chapter 7. A "rogue" grain combination is introduced in the second microstructure by changing the orientation of a grain in such way that its c-axis is parallel to the loading direction. Monotonic tension and cyclic deformation behaviors of two microstructures are examined. It is shown that the second microstructure has higher yield strength than the first one. Introduction of hard grain in Microstructure II affects the deformation behavior of the neighboring grains. At the same time, variation of deformation behavior of remote grains is negligible.

FIPs are calculated for the two microstructures at the 10^{th} cycle. It is shown that the driving forces for all three crack formation mechanisms increase for Microstructure II relative to Microstructure I. The increase of the grain boundary impingement parameter is much higher than that of P_{BAND} and $P_{LAMELLAR}$. Therefore, introducing the hard grain will greatly increase the possibility of crack formation at a grain boundary and the crack will likely propagate along the basal plane of the hard grain since the normal stress on the basal plane is high. It is shown that this effect cannot be captured by the Fatemi-Socie parameter.

The demonstration simulation shows that the new microstructure-scale fatigue analysis approach can effectively capture the effect of microstructure on the various fatigue crack formation mechanisms. This approach can therefore be used in other applications such as fretting fatigue.

CHAPTER 9

CONCLUSIONS AND RECOMENDATIONS

9.1 Overview

This thesis has addressed microstructure-sensitive crystal plasticity constitutive relations and algorithms for assessing fatigue crack formation probability of Ti-6Al-4V subjected to cyclic and fretting loadings. The physics-based model incorporates multiscale microstructure-dependent hardening and softening mechanisms of α/β TiAl alloys. Fatigue indicator parameters (FIPs) are used to represent the driving force for crack formation at the microstructure level. The aim of this study is to develop a computational approach that can capture the sensitivity of deformation and fatigue behaviors to microstructure of Ti-6Al-4V.

The approach presented here is generic and should translate to other alloy systems.

9.2 Microstructure-sensitive Crystal Plasticity Modeling

In Chapter 2, three-dimensional finite element simulations are conducted to study the effects of microstructure attributes on the cyclic deformation behavior of the duplex Ti-6Al-4V alloys. The deformation behaviors of primary α and α/β lamellar phases of Ti-6Al-4V at room temperature are described by a fully three-dimensional crystal plasticity constitutive relation developed by Mayeur and McDowell (2006). Microstructure attributes considered in this sensitivity study include crystallographic

texture, grain size, and grain size distribution. Voronoi tessellation is used to construct the three-dimensional finite element models with various grain size distributions.

In monotonic tension simulations at room temperature, a slight influence of texture on elasticity of polycrystalline Ti-6Al-4V is observed. Grain size and grain size distribution show no influence on the elastic stiffness. Strong dependence of material strength on grain size and texture is shown. Influence of grain size distribution on yield strength is minimal.

A completely reversed, strain-controlled loading history is applied in cyclic loading simulations at room temperature. The plastic strain behaviors and the distribution of the average maximum plastic shear strain among grains are analyzed and contrasted. The relative susceptibility for crack formation, including effects of various microstructure features, is assessed using the nonlocal Fatemi-Socie FIP. The results suggest that both average grain size and especially crystallographic texture have more influence on the plastic deformation and indicated fatigue behavior than the grain size distribution.

The fatigue crack formation lives of considered microstructures are calculated according to a Coffin-Manson relation. It is shown that the predicted fatigue crack formation lives is close to the experimental data. The microstructure has significant effect on the scatter of fatigue crack formation life of Ti-6Al-4V.

9.3 Microstructure-sensitive Fretting Fatigue Simulations

In Chapter 3, a methodology for using crystal plasticity to explore the sensitivity of fretting fatigue to microstructure and loading parameters was presented and demonstrated for duplex Ti-6Al-4V at room temperature. The crystal plasticity material model captures the crystallographic orientation dependence of the deformation behavior

for both primary α phase and the lamellar colonies. A three-dimensional finite element model is constructed to simulate the fretting contact in the partial slip regime between the two bodies. A Voronoi tessellation procedure is used to render grain size distributions in the contact region.

Three microstructure attributes are considered in this sensitivity study: crystallographic texture, average grain size, and grain size distribution. The distribution and maximum value of the effective plastic strain and related fatigue indicator parameters are all shown to depend on the microstructure. Moreover, the sensitivity of several other microstructure attributes can potentially be considered using this methodology. These include volume fraction of phases, differences in the distribution of primary α and lamellar colony sizes, thicknesses of the α and β lathes, as different spatial distributions of microstructural features.

To study the effects of normal and tangential forces on the fretting fatigue behavior of Ti-6Al-4V, various combinations of normal and tangential forces are applied to each microstructure. The influence of tangential force on the fretting behavior is examined at both low and high normal force.

Based on the relatively limited range of conditions considered in this demonstration study, the effect of microstructure attributes and loading parameters on the resistance to fretting fatigue can be summarized as:

1. Smaller average grain size results in increased fretting fatigue resistance.
2. In this study, the polycrystal Ti-6Al-4V is oriented in the way that the rolling and transverse directions are parallel to the y- and x-axes, respectively, corresponding to the considered textures shown in Fig. 2.2. The normal and tangential forces are respectively applied in the y- and x- directions. For this loading condition, transverse and basal/transverse textured material exhibit greater fretting fatigue

resistance, and the effect of texture on subsurface plasticity and FIP was more pronounced than that of the other two microstructure attributes.

3. The effect of grain size distribution is minimal.
4. Normal force has significant influence on the fretting fatigue of Ti-6Al-4V. The driving force for crack formation increases with increasing normal force. When the normal force is substantially lower than P_y, cracks are most likely formed at the edge of contact. With increasing normal force, the possibility of crack formation at subsurface region increase.
5. The driving force for crack formation increases with increasing tangential force at both low and high normal force. The tangential force has a larger influence on the driving force for crack formation at low normal force and dominates the fretting fatigue behavior of Ti-6Al-4V.
6. A Coffin-Manson relation is used to correlate the FS FIP with the fatigue crack formation life for various combinations of normal and tangential forces. It is shown that the general tendency of predicted crack formation lives is same as that of the experimental data.

9.4 Crystal Plasticity Modeling of Cyclic Deformation of Ti-6Al-4V

In Chapter 4, a three-dimensional scale-dependent model of the duplex Ti-6Al-4V is proposed. The model includes length scale effects associated with dislocation interactions with different microstructure features, and is calibrated using polycrystalline finite element simulations to fit the measured macroscopic responses (overall stress-strain behavior) of a duplex heat treated Ti-6Al-4V alloy subjected to a complex cyclic loading history. The finite element models are established to adequately represent the

microstructures of the tested material. Equivalent orientations with similar probability density distributions of the crystallographic orientations are assigned to the finite element mesh. The simulated annealing method is used to fit the disorientation distributions of the sample. For a given Ti-6Al-4V alloy, it is shown that its mechanical deformation behavior can be correctly predicted by conducting the simulations on the finite element model using the proposed material modeling. Effects of microstructural features are examined and compared with the experimental data in terms of their influence on the material yield strength. The results are shown to agree with the experimental observations. The microstructure sensitivity of the model enables its application to microstructure-sensitive fatigue analysis of duplex Ti-6Al-4V.

9.5 Effect of Grain Size Distribution on Monotonic Tension Behavior of Ti-6Al-4V

In Chapter 5, a computational approach is employed to study the effect of the grain size distribution on uniaxial tension deformation behavior of Ti-6Al-4V. The elastic-viscoplastic deformation behavior of Ti-6Al-4V is described by a fully three-dimensional, scale-dependent crystal plasticity constitutive relation described in Chapter 4. Microstructures with various grain size distributions are realized in FE meshes, using a sequence of error minimization operations (simulated annealing) performed on random Voronoi tessellations to fit microstructure attributes such as grain size distribution and orientation and disorientation distributions. A study of grain size distribution on tensile behavior of Ti-6Al-4V is carried out.

The results show that with increasing variance of grain sizes, the yield strength decreases slightly while the elastic modulus is unchanged. The grain size distribution has the most significant influence on tensile strain hardening behavior past initial yield.

9.6 Simulations of Single Crystal α Ti5Al Subjected to Cyclic Loading

In Chapter 6, a shear-enhanced crystal plasticity model is used to model the deformation behavior of the single crystal α Ti-5Al oriented for single and double prismatic slip. Softening of the threshold stress is introduced to incorporate the cyclic strain softening observed in the experiments. The cyclic strain softening is associated with highly planar slip of α–Ti5Al at room temperature. Finite element models are established to simulate the deformation and fatigue behaviors of the α Ti-5Al. In order to model the slip band effect, the element size and the distribution of the defects within the model are determined by the experimentally observed slip band structure. The simulated stress-strain responses are shown to be in good agreement with the experimental results at different orientations and various amplitudes of completely reversed cyclic strain at room temperature.

A new FIP, P_{band}, is proposed to correlate fatigue crack formation along the slip band. An averaging procedure for the FIP over integration points is employed to incorporate the crack formation mechanism over a physically representative scale on the order of slip band width. The nonlocal Coffin-Manson law is used to correlate the fatigue life and the FIP and is calibrated by fitting the fatigue lives of single crystal α Ti5Al oriented for double prismatic slip. Predicted fatigue lives are shown to be in good agreement with the experimental data of single crystal α Ti5Al oriented for single prismatic slip.

Two modeling parameters, mesh density and spacing of defects, are investigated in terms of their effects on the deformation and fatigue behavior of α Ti-5Al. It is found that these two parameters have minor effect on the macroscopic stress-strain response. However, the distribution of the effective plastic strain and FIP vary substantially with variation of these two parameters. The mesh size should be assigned to less than the slip

band width. Parameter l_d is an important material length scale that must be determined before conducting simulations.

9.7 Simulation of Slip Band Based on Shear Enhanced Crystal Plasticity Model

In Chapter 7, shear enhanced crystal plasticity constitutive relations are proposed to account for the slip softening due to breakdown of the short range order between titanium and aluminum atoms. In the primary α phase, the threshold stress evolves according to softening restricted to slip band only. Thus, slip concentrates in the slip bands due to their relatively low slip resistance. In this softening strategy, uniform thickness and wavelength of slip bands are assumed for all grains during deformation since the theoretical calculations of these two parameters are unavailable. This study employs a combination of typical values of thickness and wavelength obtained from experimental observations. The proposed model is calibrated by performing finite element simulations on a polycrystalline Ti-6Al-4V (PW1215). The 3D finite element model is constructed to precisely represent the microstructure of the polycrystalline Ti-6Al-4V as described in Chapter 4. The simulated stress-strain response is shown to be in good agreement with the experimental data provided by Pratt & Whitney up to 2.5% strain.

The slip behavior of a Ti-6Al-4V subjected to monotonic tension history is investigated. The two-dimensional finite element mesh is obtained from the EBSD observation (Bridier et al., 2005). The finite element simulation is performed with the proposed shear enhanced model and softening strategy. The contours of effective plastic strain are compared with the SEM images at various stain levels. It is shown that the proposed approach for slip band simulation can qualitatively capture the slip behavior measured in experiments. The slip bands often form on the basal or prismatic slip system

with the highest Schmid factor. The thickness and wavelength of the simulated slip bands are close but are often not same as the SEM observations. Such a discrepancy can be attributed in part to the constant thickness and wavelength of slip bands assumed in this approach.

This approach provides a useful computational tool to study the effect of slip bands on the deformation behavior of Ti-6Al-4V, particularly grain scale shear localization and stresses related to fatigue crack formation. It is also noted that slip bands play an important role in fatigue crack initiation in Ti-6Al-4V. Therefore, the approach can add value to the study of the microstructure-scale fatigue behavior of Ti-6Al-4V.

9.8 Microstructure-scale Fatigue Analysis of Ti-6Al-4V Based on Shear Enhanced Crystal Plasticity Model

In the Chapter 7, the proposed approach containing shear enhanced crystal plasticity constitutive relations and a softening strategy is used to simulate the formation of slip bands in primary α grains of Ti-6Al-4V. In Chapter 8, fatigue analysis of Ti-6Al-4V is performed by combining this new approach with additional FIPs. These new FIPs account for various mechanisms of fatigue crack formation in Ti-6Al-4V. The aim of this study is to provide a new computational approach that can quantify the various driving forces for crack formation in primary α grains, grain boundaries and lamellar colonies.

In Chapter 8, finite element simulations are carried out on two microstructures. The first microstructure is same as the one used in Chapter 7. A "rogue" grain combination is introduced in the second microstructure by changing the orientation of a grain in such way that its c-axis is parallel to the loading direction. Monotonic tension and cyclic deformation behaviors of two microstructures are examined. It is shown that

the second microstructure has higher yield strength than the first one. Introduction of hard grain in Microstructure II affects the deformation behavior of the neighboring grains. At the same time, variation of deformation behavior of remote grains is negligible.

FIPs are calculated for the two microstructures at the 10^{th} cycle. It is shown that the driving forces for all three crack formation mechanisms increase for Microstructure II relative to Microstructure I. The increase of the grain boundary impingement parameter is much higher than that of P_{BAND} and $P_{LAMELLAR}$. Therefore, introducing the hard grain will greatly increase the possibility of crack formation at a grain boundary and the crack will likely propagate along the basal plane of the hard grain since the normal stress on the basal plane is high. It is shown that this effect cannot be captured by the Fatemi-Socie parameter.

The demonstration simulation shows that the new microstructure-scale fatigue analysis approach can effectively capture the effect of microstructure on the various fatigue crack formation mechanisms. This approach can therefore be used in other applications such as fretting fatigue.

9.9 Recommendations for Future Work

Extensive computational studies relating to Ti-6Al-4V have been performed in this thesis. There are many areas for future work.

1. *Experiments*

   - *Tests for a wide range of microstructures*.

     In this thesis, a systematic study on effect of microstructure on deformation and fatigue behaviors is performed. The simulation results are compared with experimental data to calibrate and validate the

computational approach employed here. Due to very limited test data, the validation is preliminary. Therefore, cyclic and fretting fatigue tests should be conducted on a wider range of microstructures to validate the algorithm for using FIPs to rank order microstructures. The stress-strain data obtained from these tests can be used to validate the crystal plastic constitutive model and modeling algorithm.

- *Observations of slip banding*.

  Slip localization in primary α phase significantly affects the deformation and fatigue behavior of Ti-6Al-4V. A comprehensive experimental study on slip band has been conducted on single crystal α Ti5Al. SEM and EBSD study on the evolution of dislocation structures in polycrystalline Ti-6Al-4V should be conducted to gain better understanding of the deformation mechanisms. The observation results can be served as input into the constitutive model and can be used to validate the model.

- *Observations of fatigue crack formation*

  In this thesis, three mechanisms have been proposed to account for fatigue crack formation in Ti-6Al-4V. Cracks could be classified into three groups corresponding to three mechanisms. Thus, experimental observations on different types of crack shall be obtained to validate the proposed mechanisms and crack formation life prediction models.

2. *Improvement of shear enhanced crystal plasticity model*

   In this thesis, it is shown that the shear enhanced crystal plasticity model can capture the slip localization in primary α phase of Ti-6Al-4V. The softening strategy employed in this model assumes uniform slip band width and spacing which are obtained from experimental observations. This assumption is useful

for slip band modeling. However, a uniform distribution of slip bands is rarely found in polycrystalline Ti-6Al-4V deformed at room temperature. The dislocation structure varies with respect to microstructure, loading history. Thus, a predictive strategy (perhaps based on discrete dislocation theory) for slip band width and spacing is needed to improve the softening strategy and the shear enhanced crystal plasticity model.

3. *Actual microstructures.*

   Most simulations in this thesis are performed on the finite element model simulating the statistical microstructure attributes of Ti-6Al-4V. It would be interesting to establish three-dimensional FE models representing more measured microstructures. Simulations can be performed on Ti-6Al-4V subjected to cyclic and fretting loadings and will help us to validate and improve the microstructure-scale material model and assessment of relevant fatigue resistance of microstructure.

4. *More realistic and comprehensive loading conditional environments*

   Relatively simple cyclic and fretting loadings are used in this thesis to investigate the deformation and fatigue behavior of Ti-6Al-4V. These simulations can be improved by introducing actual loading conditions. For example, it is well known that turbine components made by TiAl alloys are subjected to harsh environments which induce material degradation. Therefore, the effect of environment could be introduced into the model. In this thesis, most fretting fatigue simulations are conducted at relative high normal force which is generally not used in real application. Additional simulations can focus on the low normal force regime which is closer to the loading conditions in the real applications. A finer mesh will be used in the trailing edges where the fatigue cracks are generally found. Wear of surface due to fretting should also be considered in future work.

5. *Hierarchical modeling of Ti-6Al-4V*

   Microstructure-scale models are of great important in reducing the costly experiments. Considerable work has been done to develop macroscopic viscoelastoplastic constitutive relations to model the multiaxial cyclic stress-strain response of engineering materials. These models are widely used in industry but do not contain an explicit dependence of microstructure features. Shenoy and coworkers (2006) developed a hierarchical methodology for Ni-based superalloy to embed the microstructure dependence in the macroscale model. This methodology can be applied to Ti-6Al-4V to develop a microstructure dependent macroscopic model. Key microstructure attributes such as average grain size, volume fraction of lamellar colony, lath thicknesses of secondary α and β phase, and texture should be considered.

REFERENCES

ABAQUS, Version 6.5, 2005. ABAQUS, Inc., Providence, RI.

Aifantis, J. (1984) "On the microstructural origin of certain inelastic models," *J. Eng. Mater. Tech*. Vol. 106, pp. 326-330.

Ambard, A., Guetaz, L., Louchet, F., Guichard, D. (2001) "Role of interphases in the deformation mechanisms of an α/β titanium alloy at 20 K," *Mat. Sci. and Eng A*, Vol. A319-321, pp. 404-8.

Ambrico, J.M., Begley, M.R. (2000) "Plasticity in fretting contact," *J. Mech. Phys. of Solids*, Vol. 48, pp. 2391-4217.

Amstrong, P.J., Frederick, C.O. (1966) "A mathematical representation of the multiaxial Bauschinger effect," *G.E.G.B Report RD/B/N*, pp.731

Ankem, S., Margolin, H. (1980) "The role of elastic interaction stresses on the onset of plastic flow for oriented two ductile phase structures," *Met. Trans. A*, Vol. 11A, pp. 963-972.

Antoniou, R.A., Radtke, T.C. (1997) "Mechanism of fretting-fatigue of titanium alloys," *Mat. Sci. Eng*., Vol. A237, pp. 229-240

Antonopoulos, J.G., Winter, A.T. (1976) "Weak-beam study of dislocation structures in fatigued copper," *Phil. Mag*. Vol. 33, pp. 87-95.

Araujo, J.A. and Nowell, D. (2002) "The effect of rapidly varying contact stress fields on fretting fatigue," *Int. J. Fatigue*, Vol. 24, pp. 763-775.

Argon, A.S. (1973) "The inhomogeneity of plastic deformation," ASM seminar, ASM, Metals Park, Ohio, Oct 16, 1971, pp. 161.

Asaro, R.J., Rice, J.R. (1977) "Strain localization in ductile single crystals," *J. Mech. Phys. Solids*, Vol. 25, pp. 309-338.

Asaro, R.J. (1983) "Micromechanics of Crystals and Polycrystals," *Advances in Applied Mechanics*, Vol. 23, pp. 1-115.

Asaro, R.J., Needleman, A. (1985) "Texture development and strain hardening in rate dependent polycrystals," *Acta Metallurgica*, Vol. 33, pp. 923-953.

Bache, M.R. Evans, W.J., Davies, H.M. (1997) "Electron back scattered diffraction (EBSD) analysis of quasi-cleavage and hydrogen induced fractures under cyclic and dwell loading in titanium alloys," *J. of Mat. Sci.*, Vol. 32, pp. 3435-3442.

Bache, M.R. Evans, W.J. (2003) "Dwell sensitive fatigue response of titanium alloys for power plant applications," *J. of Eng. for Gas Turbines and Power*, Vol. 125, pp. 241-245

Balint, D.S., V S Deshpande, V.S., Needleman, A., Van der Giessen, E. (2006) "Size effects in uniaxial deformation of single and polycrystals: a discrete dislocation plasticity analysis," *Modeling Simu. Mat. Sci. Eng*. Vol. 14, pp. 409-422.

Bammann, D.J., Mosher, D., Hughes, D.A., Moddy, N. R., Dawson, P. R. (1999) "Using spatial gradients to model localization phenomena," Sandia Report, SAND99-8588.

Barboza, M.J.R., Neto, C.M., Silva, C.R.M. (2004) "Creep mechanisms and physical modeling for Ti-6Al-4V," *Mat. Sci. and Eng*., Vol. A369, pp. 201-209.

Barbe, F., Decber, L., Jeulin, D., Cailletaud, G., 2001, "Intergranular and intragranular behavior of polycrystalline aggregates, Part I: FE Model," *Int. J. Plasticity*, Vol. 17, pp. 513-516.

Barton, N.R., Dawson, P.R. (2001) "On the spatial arrangement of lattice orientations in hot-rolled multiphase titantium," *Modeling Simul. Mater. Sci. Eng*., Vol. 9, pp. 433-463.

Bassani, J.L., Ito, K. and Vitek, V. (2001) "Complex macroscopic plastic flow arising from non-planar dislocation core structures," *Mat. Sci. Eng. A*, Vol. 319-321, pp. 97-101.

Batra, R.C., Wei, Z.G. (2006) "Shear bands due to heat flux prescribed at boundaries," *Int. J. of Plasticity*, Vol. 22, pp. 1-15.

Bennett, V. (1999). "A study of microscale phenomena in small crack propgation under multiaxial fatigue," Ph.D. Thesis, Georgia Institute of Technology.

Bennett, V. and McDowell, D.L. (2003) "Crack Tip Displacements of Microstructurally Small Surface Cracks in Single Phase Ductile Polycrystals," *Eng. Frac. Mechanics*, Vol. 70, pp. 185-207.

Berard, J.Y. and McDowell, D.L. (1992) "ΔJ based approach to biaxial fatigue", *Fatigue and Fract. of Eng. Mat. & Structures*, Vol. 15, pp. 719-741.

Berbenni, S., Favier, V., Berveiller, M., (2007) " Micro–macro modelling of the effects of the grain size distribution on the plastic flow stress of heterogeneous materials," *Comp. Mat. Sci*., Vol. 39, pp. 96-105

Bieler, T.R., Semiatin, S.L. (2001) "The effect of crystal orientation and boundary misorientation on tensile boundary cavitation during hot tensile deformation of Ti–6Al–4V," In: Jata, K. (Ed.), Lightweight Alloys for Aerospace Applications VI (PDF-only edition). TMS, Warrendale, PA, 161–170.

Blackbrun, M.J., Williams, J.C. (1969) "Strength, deformation modes and fracture in titanium-aluminum alloys," *ASM-Trans*, Vol. 62, pp. 398-409.

Brandes, M., Mills, M.J., (2004) "Static recovery in titanium alloys at lower temperatures," *Mat. Sci. and Eng*., Vol. 387, pp. 570-575.

Bridier, F., Villechaise, P., Mendez, J. (2005) "Analysis of the different slip systems activated by tension in a α/β titanium alloy in relation with local crystallographic orientation," *Acta Mat*., Vol. 53, pp. 555-567.

Bridier, F., Villechaise, P., Mendez, J. (2007) "Analysis of slip and crack initiation processes activated by fatigue in a α/β titanium alloy in relation with local crystallographic orientation," Fatigue 2006, May 2006, Atlanta, GA.

Charach, Ch., Chen, C.K., Fife, P.C. (1999) "Developments in phase-field modeling of thermoelastic and two-component materials," *J of Statistical Phy*., Vol. 95, pp. 1141-1164.

Cizelj L, Riesch-Oppermann H. (2002) "Modelling the early development of secondary side stress corrosion cracks in steam generator tubes using incomplete random tessellation," *Nucl. Eng. Design*, Vol. 212, pp. 21–29.

Clayton, J.D., Schroeter, B.M., McDowell, D.L. (2002) "Distributions of stretch and rotation in polycrystalline OFHC Cu," *Trans. of ASME*, Vol. 124, pp. 302-312.

Cortez, R., Mall, S. and Calcaterra, J.R. (1999) "Investigation of variable amplitude loading on fretting fatigue behavior of Ti-6Al-V," *Int. J. Fatigue*, Vol. 21, pp. 709-717

Dao, M., Asaro, R.J., (1993) "Non-Schmid effects and localized plastic flow in intermetallic alloys," *Mat. Sci. and Eng*., Vol. A170, pp. 143-160

Dao, M., Asaro, R.J., (1996) "Localized deformation modes and non-Schmid effects in crystalline solids. Part I. Critical conditions of localization," *Mech. of Mat*. Vol. 23, pp. 71-102

Dao, M., Asaro, R.J., (1996) "Localized deformation modes and non-Schmid effects in crystalline solids. Part II. Deformation patterns," *Mech. of Mat*. Vol. 23, pp. 103-132.

Dawson, P.R., Boyce, D.E., Hale, R., Durkot, J.P. (2005) "An isoparameteric piecewise representation of the anisotropic strength of polycrystalline solid," *Int. J. of Plas*., Vol. 21, pp. 251-283.

Dick, T., Cailletaud, G. (2006) "Fretting modeling with a crystal plasticity model of Ti-6Al-4V," *Compu. Mater. Sci*., Vol. 38, pp. 113-125.

Differt, K., Essmann, U. (1993) "Dynamical model of the wall structure in persistent slip bands of fatigued metals I. dynamical model of edge dislocation walls," *Mater. Sci. and Eng. A*, Vol. 164, pp. 295-299.

Dunst, D., Mecking, H. (1993) "Analysis of Experimental and Theoretical Rolling Textures of Two-Phase Titanium Alloys," *Z. Metallkd.*, Vol. 33, pp. 498-507.

Dunne, F.P.E., Rugg, D., Walker, A. (2007) "Lengthscale-dependent, elastically anisotropic, physically-based hcp crystal plasticity: Application to cold-dwell fatigue in Ti alloys," *Int. J. Plas*., Vol. 23, pp.1061-1083.

Essmann, U., Differt, K. (1996) “Dynamical model of the wall structure in persistent slip bands of fatigued metals I. the wall spacing and the temperature dependence of the yield stress in saturation,” *Mater. Sci. and Eng. A*, Vol. 208, pp. 56-68.

Evans, W.J., Bache, M.R. (1994) “Dwell-sensitive fatigue under biaxial loads in the near-alpha titanium ally IMI685,” *Fatigue*, Vol. 16, pp. 443-452.

Fager, D.N., Spurr, W.F. (1968) “Some characteristics of aqueous stress-corrosion in titanium alloys,” *ASM Transactions*, Vol. 61, pp. 283-292.

Fatemi, A. and Socie, D. (1988) “A critical plane approach to multiaxial fatigue damage including out of phase loading,” *Fat. Frac. Eng. Mat. Struc*., Vol. 11, pp. 145-165.

Findley, W.N., (1959) "A Theory for the Effect of Mean Stress on Fatigue of Metals Under Combined Torsion and Axial Loading or Bending," *J. of Eng. for Industry*, Vol. 21, pp. 301-306.

Fleck, N.A., Muller, G.M., Ashby, M.F., Hutchinson, J.W. “Strain gradient plasticity: theory and experiment,” *Acta Meta*., Vol. 42, pp. 475-487.

Flourist, S., Forest, S., Rémy, L. (2003) “Strain localization phenomena under cyclic loading: application to fatigue of single crystals,” *Comp. Mat. Sci*., Vol. 26, pp. 61-70.

Fridrici, V., Fouvry, S., Kapsa, P., Perruchaut, P. (2005) “Prediction of cracking in Ti–6Al–4V alloy under fretting-wear: use of the SWT criterion,” *Wear*, Vol. 259, pp. 300-308.

Fried, E, Gurtin, M.E. “Continuum theory of thermally induced phase transitions based on an order parameter”, *Physics D*, Vol. 68, pp. 326-343.

Fu, H., Benson, D.J., Meyers, M.A., 2004, “computational description of nanocrystalline deformation based on crystal plasticity”, *Acta Materialia*, Vol. 52, pp. 4413-4425

Fundenberger, J.J., Philippe, M.J., Wagner, F., Esling, C. (1997) “Modeling and prediction of mechanical properties for materials with hexagonal symmetry (zinc, titanium and zirconium alloys),” *Acta Mater.*, Vol. 45, pp. 4041-55.

Gall, K., Horstemeyer, M.F., Degner, B.W., McDowell, D.L., Fan, J., (2001) "On the driving force for fatigue crack formation from inclusions and voids in a case A356 aluminum alloy," *Int. J. of Fatigue*, Vol. 108, pp. 207-233.

Gallagher, J., vanStone, R.H., deLaneuville, R.E., Gravett, P., Bellows, R.S., Slavik, D.C., Hudak, S.J., Dunyak, T.J., Berens, A.P., Farris, T.N., Chan, K.S., McClung, R.E., Annis, C.G., Corbly, D.M., Grandt, A.F., Anton, D.L., Kurath, P., Sheldon, J.W., Weeks, Y.N., Lenets, C.A., Lawless, B.H., Ruschau, J.J. (2001) "Improved high-cycle fatigue (HCF) life prediction," Final report for AFRL-ML-WP-TR-2001-4159.

Gallagher, J., Nicholas, T., Gunderson, A., Ruschau, J., Miedlar, P., Hutson, A., Hardy, G., Walls, D., Annis, C., deLaneuville, R., Gravett, P., Hindle, E., Szolwinski, M., Naik, R., Cowles, B., Adamson, J., Pettit, R., Kersey, K., Marotta, M., Corbly, D., VanStone, R., Slavik, D., Hartle, M., McClain, R., Wright, K., Merrick, H., Cameron, D., Lenets, Y., Hartman, J., Cornet, K., Wildman, D., Weeks, C., Bastnagel, P., Cook, T., Chaterjee, A., Hudak, S., Chan, K., McClung, C., Davidson, D., Chell, G., Der Lee, Y., Farris, T., Grandt, A., Golden, P., Murthy, H., Bartha, B., Matlik, J., Garcia, D., Perez-Ruberté, E., Rajeev, P., Kallmeyer, A., Kurath, P., Glinka, G., Lawless B., (2005) "Advanced high cycle fatigue (HCF) life assurance methodologies", Final report for AFRL-ML-WP-TR-2005-4102.

Goh, C.-H. (2002) "Crystallographic plasticity in fretting of titanium alloy", PhD Thesis, GWW School of Mechanical Engineering, Georgia Institute of Technology.

Goh, C.-H., Wallace, J.M., Neu, R.W. and McDowell, D.L. (2001) "Crystal Plasticity Simulations of Fretting Fatigue," *Int. J. of Fatigue*, Vol. 23, 2001, pp. S423-S435.

Goh, C.-H. (2002) "Crystallographic Plasticity in Fretting of Ti-6Al-4V," Ph.D. Thesis, Georgia Institute of Technology.

Ghosh, A.K., Raj, R., (1981) "Grain size distribution effects in superplasticity," *Acta Metallurgica*, Vol. 29, pp. 607-616

Granasy, L., Pusztai, T., Borzsonyi, T., Toth, G., Tegze, G., Warren, J.A., Douglas, J.F., (2006) "Phase field theory of crystal nucleation and polycrystalline growth: a review," *J. of Mat. Research*, Vol. 21, pp. 309-319.

Gregor, H., Kratochvil, J. (1998) "Internal stress, width, and density of persistent slip bands," *Scripta Mate*., Vol. 40, pp. 491-496.

Gregor, H., Kratochvil, J., Saxlova, M. (1998) "Width and density of persistent slip bands as a consequence of deformation mesostructure," *J. Phys. IV France*, Vol. 8, pp. 181-188.

Gross, D., Li, M., 2002, "Constructing microstructures of poly- and nanocrystalline materials for numerical modeling and simulation," *App. Phy. Letters*, Vol. 80, pp. 746-748.

Guo, Y.B., Wen, Q., Horstemeyer, M.F. (2005) "An internal state variable plasticity-based approach to determine dynamic loading history effects on material property in manufacturing processed," *Int. J. of Mech. Sci*., Vol. 47, pp. 1423-1441.

Horalek V. (1990), "ASTM grain-size model and related random tessellation models," *Materials Characterization*. Vol. 25, pp. 263-284.

Hasija, V., Ghosh, S., Mills, M.J., Joseph, D.S. (2003) "Deformation and creep modeling in polycrystalline Ti-6Al alloys," *Acta Mat*., Vol. 51, pp. 4533-4549.

Hecker, M. (1998), "Elastic Energy of a Periodic Wall-Channel Structure with Heterogeneous Plastic Shear Strain," *Phys. Stat. Sol. (B)*, Vol. 205, pp. R17-R18.

Hill, R., Rice, J.R. (1972) "Constitutive analysis of elastic-plastic crystals at arbitrary strain", *J. Mech. Phys. Solids*, Vol. 20, pp. 401.

Hill, R. (1962) "Acceleration waves in solids," *J. of the Mech. and Phy. of Solids*, Vol. 10, pp. 1-16.

Hollomon, J.H., Zener, C. (1946) "Problems in fracture of metals," *J of App. Phy*., Vol. 17, pp. 82-90.

Kalidindi, S.R., Salem, A.A., Doherty, R.D. (2003) "Role of deformation twinning on strain hardening in cubic and hexagonal polycrystalline metals," *Adv. Eng. Mat.*, Vol. 5, pp. 229-232.

Kar, S. (2005) "Modeling of mechanical properties in alpha/beta-titanium alloys." MS Thesis, Department of Materials Science and Engineering, The Ohio State University.

Kar, S., Searles, T., Lee, E., Viswanathan, G.B., Tiley, J., Banerjee, R., Fraser, H.L. (2006) "Modeling the tensile properties in β-processed α/β Ti alloys," *Metal. And Mat. Trans*., Vol. 37A, pp. 559-566.

Kassner, M.E. (1997) "In-situ cyclic deformation of Al single crystals in the HVEM and the concept of internal backstresses," Meter. Sci. and Eng. A, Vol. 234, pp. 110-114.

Kassner, M.E., Perez-Prado, M.T., Vecchio. K.S., Wall, M.A. (2000) "Determination of internal stresses in cyclically deformed copper single crystals using convergent-beam electron diffraction and dislocation dipole separation measurements," *Acta. Mater.*, Vol. 48, pp. 4247-4254.

Kassner, M.E., Wall, M.A., Delos-Reyes, M.A. (2001) "Primary and secondary dislocation dipole heights in cyclically deformed copper single crystals," *Mater. Sci. and Eng. A*, Vol. 317, pp. 28-31.

Kratochvil, J. (2001) "Self-organization model of localization of cyclic strain into PSBs and formation of dislocation wall structure," *Mater. Sci. and Eng. A*, Vol. 310, pp. 331-335.

Kruzic, J. J., Campbell J. P., Ritchie, R. O. (1998) "Fatigue-crack propagation in gamma-based titanium aluminide alloys at large and small crack sizes," MRS Fall Meeting--Boston, 1998

Kumar S., Kurtz S.K., (1994) "Simulation of material microstructure using a 3D Voronoi tessellation: calculation of effective thermal expansion coefficient of polycrystalline materials," *Acta Metal. Mater*., Vol. 42, pp. 3917-3927.

Kumar, R.S., Wang, A.-J., and McDowell, D.L. (2006) "Effects of microstructure variability on intrinsic fatigue resistance of nickel-base superalloys – a computational micromechanics approach," *Int. J. Fract*. Vol. 137, pp. 173 - 210.

Kurzydlowski, K.J., (1990) "Investigations of three-dimensional geometry of annealing twins in FCC metals," *Scripta Metall. Mater*. Vol. 24, pp. 879-885.

Landau, L.D., Khalatnikov, I.M. (1965) "On the theory of superconductivity," Collected Papers of L.D. Landau (ed. TerHaar, D.) Pergamon, Oxford.

Lankford, J. and Kusenberger, F.N. (1979) "Initiation of fatigue crack in 4340 steel," *Mett. Trans*. Vol. 4, pp. 553-559.

Lebensohn, R.A., Canova, G.R. (1997) "A Self-Consistent Approach for Modeling Texture Development of Two-Phase Polycrystals: Application to Titanium Alloys," *Acta Mater.*, Vol. 45, pp. 3687-3694.

Le Biavant, K., Pommier, S., Prioul, C. (2002) "Local texture and fatigue initiation in a Ti-6Al-4V titanium alloy," *Fatigue Frac. Eng. Mat. Structure*, Vol. 25, pp. 527-545.

Lee, D., Backofen, W.A. (1966) "The effect of microstructure on the deformation modes and mechanical properties of Ti-6Al-2Nb-1Ta-0.8Mo. I. Widmanstatten structures," *AIME Transactions* Vol. 236, pp. 1696-1704

Lemonds, J., Asaro, R.J., Needleman, A. (1985) "A numerical study of localized deformation in Bi-crystals," *Mech. of Mat*., Vol. 4, pp. 417-435.

Lin, F.S., Starke, E.A., Chakrabortty, S.B., Gysler, A. (1984) "The effect of microstructure on the deformation modes and mechanical properties of Ti-6Al-2Nb-1Ta-0.8Mo. I. Widmanstatten structures," *Metallurgical Transactions A (Physical Metallurgy and Materials Science)*, Vol. 15A, pp. 1229-46.

Lovrich, N.R. (2004) "Fretting Fatigue of Ti-6Al-4V: Experimental Characterization and Simple Design Parameter", Master Thesis, GWW School of Mechanical Engineering, Georgia Institute of Technology.

Lütjering, G.,Gysler, A. (1992) Titanium '92, Science and Technology, TMS, pp. 1635-1646.

Lütjering, G., Ivasishini, O.M. (1995) "Influence of Cooling Rate and Beta Grain Size on the Tensile Properties of (alpha + beta) Ti-Alloys," Titanium '95, Science and Technology, TMS, pp. 1163-1170.

Lütjering, G., (1998) "Property Optimization Through Microstructural Control in Titanium and Aluminum Alloys", Proceedings-9th World Ti conference, 1998.

Lütjering, G. (1998) "Influence of processing on microstructure and mechanical properties of (alpha + beta) titanium alloys," *Materials Science and Engineering A*, Vol. 243, pp. 32-45.

Lütjering, G, Williams, J.C. (2003) *Titanium*. Springer, Berlin, New York.

Ma, B.T., Laird, C. (1989) "Overview of fatigue behavior in copper single crystals - II. population, size distribution and growth kinetics of stage I cracks for tests at constant strain amplitude," *Acta Metallurgica*, Vol. 37, pp. 337–348.

Majorell, A., Srivatsa, S., Picu, R.C. (2002) "Mechanical behavior of Ti-6Al-4V at high and moderate temperatures-Part I: Experimental results," *Mat. Sci. Eng. A*, Vol. 326, pp. 297-305.

Marin, E.B., Dawson, P.R. (1998) "On the modeling the elasto-viscoplastic response of metals using polycrystal plasticity," *Comput. Methods Appl. Mech. Engrg*., Vol. 165, pp. 1-21.

Mayeur, J.R. (2004). "Three Dimensional Modeling of Ti-Al Alloys with Application to Attachment Fatigue", Master Thesis, GWW School of Mechanical Engineering, Georgia Institute of Technology.

Mayeur, J.R., McDowell, D.L., and Neu, R.W. (2006) "Role of Texture and Microstructure in Fretting Fatigue of Ti-6Al-4V," 9th International Fatigue Congress (Fatigue 2006), Atlanta, GA, 14-19 May 2006.

Mayeur, J.R., McDowell, D.L. (2007) "A three-dimensional crystal plasticity model for duplex Ti-6Al-4V", *Int. J. Plas*., in press.

McDowell, D.L. (1994) "Multiaxial effects in metallic materials," Symposium on Durability and Damage Tolerance, ASME AD-Vol. 43, ASME Winter Annual Meeting, Chicago, IL, Nov. 6-11, pp. 213-267.

McDowell, D.L. (1996a) Multiaxial fatigue strength. *ASM Handbook*, Vol. 19 on Fatigue and Fracture, ASM International, pp. 263-273.

McDowell, D.L. (1996b) "Basic issues in the mechanics of high cycle metal fatigue," *Int. J. Fracture*, Vol. 80, pp. 103-145.

McDowell, D.L. (2005) "Microstructure-sensitive computational fatigue analysis," Handbook of Materials Modeling, Part A: Methods, eds. Sidney Yip and M.F. Horstemeyer, Springer, the Netherlands, pp.1193-1214.

McDowell, D.L. (2007) "Simulation-based strategies for microstructure-sensitive fatigue modeling," *Mat. Sci. Eng. A*, doi:10.1016/j.msea.2006.08.129.

McGinty R.D., Ph.D Thesis. The GWW School of Mechanical Engineering, Georgia Institute of Technology, Atlanta, GA, USA, 2001.

McGinty, R. and McDowell, D. (1999). "Variable Resolution Polycrystal Plasticity: Assignment of Shearing Rates. Constitutive and Damage Modeling of Inelastic Deformation and Phase Transformation," A.S. Khan, ed.: pp.823-826.

Medina Perilla, J.A., Gil Sevillano, J. (1995) "Two-dimensional sections of the yield locus of a Ti-6%AL-4%V alloy with a strong trasverse-type crystallographic α-texture," *Mat. Sci. Eng. A*, Vol. 201, 103-110.

Miodownik, M. Godfrey, A. W., Holm, E. A., Hughes, D. A. (1999) "On boundary misorientation distribution functions and how to incorporate them into three-dimensional models of microstructural evolution," *Acta Mater*. Vol. 47, pp. 2661-2668.

Morrissey, R., Goh, C.-H. and McDowell, D.L. (2003) "Microstructure-scale modeling of HCF deformation," *Mat. Sci. Eng*., Vol. 35, pp. 295-311.

Morrison, D.J., Moosbrugger, J.C. (1997) "Effects of grain size on cyclic plasticity and fatigue crack initiation in nickel," *Int. J. of Fatigue*, Vol. 19, pp. S51-S59.

Mughrabi, H. (2001) "The effect of geometrically necessary dislocations on the flow stress of deformed crystals containing a heterogenerous dislocation distribution," *Mat. Sci. and Eng. A*, Vol. 319, pp. 139-143.

Mughrabi, H. (2004) "On the current understanding of strain gradient plasticity," *Mat. Sci. and Eng. A*, Vol. 387, pp. 209-213.

Naka, S., Lasalmonie, A. (1982) "Prismatic glide in the plastic deformation of alpha-Ti single crystals below 700K," *Mat. Sci. Eng. A*, Vol. 56, pp. 19-24.

Naka, S., Lasalmonie, A., Costa, P., Kubin, L.P. (1988) "The low-temperature plastic deforation of α-titanium and the core structure of a-type screw dislocations," *Phil. Mag. A*, Vol. 57, pp. 717-740.

Neal, D.F., Blenkinsop, P.A. (1976) "Internal fatigue origins in a-b titanium alloys," *Acta Meta.,* Vol. 24, pp. 59-63.

Nealea, K.W., Inala, K., Wub, P.D. (2003) "Effects of texture gradients and strain paths on localization phenomena in polycrystals", *Int. J. of Mech. Sci*., Vol. 45, pp. 1671–1686.

Neeraj, T., Mills, M.J., (2001) "Short-range order (SRO) and its effect on the primary creep behavior of a Ti-6wt.%Al alloy," *Mat. Sci. Eng. A*, Vol. 319-321, pp. 415-419.

Neeraj, T., Hou, D.-H., Daehn, G.S., Mills, M.J. (2000) "Phenomenological and microstructural analysis of room temperature creep in titanium alloys," *Acta mater.*, Vol. 48, pp. 1225-1238.

Neeraj, T., Mills, M.J., (2002) "Observation and analysis of weak-fringing faults in Ti-6 wt%Al," *Phil. Mag*. *A*, Vol. 82, pp. 779-802.

Neeraj, T., Savage, M.F., Totalovich, J., Kovarik, L., Hayes, R.W., Mills, M.J. (2005) "Observation of tension-compression asymmetry in α and α/β titanium alloys," *Phil. Mag*., Vol. 85, pp. 279-295.

Nygards M. (2003), "Number of grains necessary to homogenize elastic materials with cubic symmetry," *Mech. Mat.* Vol. 35, pp. 1049–1059.

Olmstead, W.E., Nemat-Nasser, S., Ni, L. (1993) "Shear bands as surfaces of discontinuity," *J. Mech. Phys. Solids*, Vol. 42, pp. 697-709. **O**

Onuki, A. (2003) "Plastic flow in two-dimensional solids," *Physical Review E*, Vol. 68, pp. 1-17.

Ortiz, M., Repetto, E.A. (1999) "Nonconvex energy minimization and dislocation structures in ductile single crystals," *J. Mech. Phys. Solids*, Vol. 47, pp. 397-462.

Ortiz, M., Repetto, E.A., Stainier, L. (2000) "A theory of subgrain dislocation structures," *J. Mech. Phys. Solids*, Vol. 48, pp. 2077-2114.

Ostoja-Starzewski, M., Sheng, P.Y., and Jasiuk, I. (1994) "Influence of random geometry on effective properties and damage formation in composite materials," *ASME J. Engng. Mater. Techn.*, Vol. 116(3), pp. 384-391.

Paidar, V., Pope, D.P., Vitek, V., (1984) "A theory of the anomalous yield behaviour in $L1_2$ ordered alloys," *Acta Metallurgica*, Vol. 32, pp. 435-48.

Paton, N.E., Backofen, W.A., (1970) "Plastic deformation of titanium at elevated temperatures," *Met. Trans.*, Vol. 1, pp. 2839-2847.

Paton, N.E., Williams, J.C., Rauscher, G.P. (1973) "The deformation of α -phase titanium," *Titanium Science and Technology*, Oxford: Plenum, pp. 1049-1069.

Picu, R.C., Majorell, A. (2002) "Mechanical behavior of Ti-6Al-4V at high and moderate temperatures-Part II: Constitutive modelling," *Mat. Sci. Eng. A*, Vol. 326, pp. 306-316.

Randel V. and Engler, O. (2000) *Introduction to Texture Analysis, Macrotexture, Microtexture and Orientation Mapping*, Gordon and Breach Science Publishers, Amsterdam, the Netherlands.

Savage, M.F., Tatalovich, J., Zupan, M., Hemker, K.J., Mills, M.J. (2001) "Deformation mechanisms and microtensile behavior of single colony Ti-6242Si," *Mat. Sci. Eng. A*, Vol. 319-321, pp. 398-403.

Savage, M.F., Totalovich, J., Mills, M.J. (2004) "Anisotropy in the room-temperature deformation of α–β colonies in titanium alloys: role of the α–β interface," *Phil. Mag*. Vol. 84, pp. 1127-1154.

Saylor D. M., Fridy, J., El-Dasher, B. S., Jung, K. Y., and Rollett, A. D. (2004) "Statistically Representative Three-Dimensional Microstructures Based on Orthogonal Observation Sections," *Metallurgical and Mat. Trans*., Vol. 35A, pp. 1969-1979.

Schoenfeld, S.E., Kad, B. (2002) "Texture effects on shear response on Ti-6Al-4V plates," *Int. J. of Plas*., Vol. 18, pp. 461-486.

Shenoy, M., (2006), "Constitutive Modeling and Life Prediction in Ni-Base Superalloys" PhD thesis, Georgian Institute of Technology.

Simmons, G. and Wang, H. (1971) *Single Crystal Elastic Constants and Calculated Aggregate Properties: A Handbook*, The MIT Press, Cambridge, MA

Singh, N., Gouthama, Singh, V. (2002) "Low cycle fatigue behavior of Ti alloy IMI 834 at room temperature," *Mat. Sci. and Eng*., Vol. 325, pp. 324-332.

Smit, R.J.M., Brekelmans, W.A.M., and Meijer, H.E.H. (1998) "Prediction of the mechanical behavior of nonlinear heterogeneous systems by multi-level finite element modeling," *Comp. Meth. Appl. Mech. Eng.* Vol. 155, 181-192.

Smith, R., Watson, P. and Topper, T. (1970) "A stress strain parameter for the fatigue of materials," *J. of Fatigue*, Vol. 5, pp. 767-778.

Sluys, L.J., Estrin, Y. (2000) "The analysis of shear banding with a dislocation based gradient plasticity model," *Int. J. of Solids and Structures*, Vol. 37, pp. 7127-7142.

Steinbach, I., Pezzolla, F., Nestler, B., Sedklberg, M., Ptieler, R., Schmitz, G.J., Rezende, J.L.L. (1996) "A phase field concept for multiphase systems," *Physica D*, Vol. 94, pp. 135-147.

Steninger, J., Melander, A. (1982) "The relation between bendability, tensile properties and particle structure of low carbon steel," *Scand. J. Metall*., Vol. 11, pp. 55–71.

Stroh, A.N. (1957) "A theory of the fracture of metals," *Advances in Physics*, Vol. 6, pp. 418-465.

Suri, S., Viswanathan, G.B., Neeraj, T., Hou, D.H., Mills, M.J. (1999) "Room temperature deformation and mechanisms of slip transmission in oriented single-colony crystals of an α/β titanium alloy," *Acta Materialia*, Vol. 47, pp. 1019-1034.

Sukmar, N., Chopp, D.L., Moes, N., Belytschko, T. (2001) "modeling holes and includsions by level sets in the extended finite element method," *Compu. Meth. Appl. Mech. Engrg*., Vol. 190, pp. 6183-6200.

Szolwinski, M. P., Matlik, J. F., and Farris, T. N. (1999). "Effects of HCF loading on fretting fatigue crack nucleation." *Int. J. of Fatigue*, Vol. 21, pp. 671-677

Sztwiertnia, K., Pospiech, J., Haessner, F. (1999) "Reduction of misorientations between two cubic crystals into the base domain of axis-angle space," *Texture and Microstructures*, Vol. 12, pp. 233-242.

Van der Sluis, O., Schreurs, P.J.G., Brekelmans, W.A.M., and Meijer, H.E.H. (2000) "Overall behaviour of heterogeneous elastoviscoplastic materials: effect of microstructural modeling," *Mech. Mater.* Vol. 32, pp. 449-462.

Venkataraman, G., Chung, Y.W., Mura, T. (1991) "Application of minimum energy formalism in a multiple slip band model for fatigue - I. calculation of slip band spacings," *Acta Metall. Mater*. Vol. 39, pp. 2621-2629.

Venkataraman, G., Chung, Y.W., Mura, T. (1991) "Application of minimum energy formalism in a multiple slip band model for fatigue - II. Crack nucleation and derivation of a generalized Coffin-Manson law," *Acta Metall. Mater*. Vol. 39, pp. 2631-2638.

Viswanathan, G.B., Lee, E., Maher, D.M., Banerjee, S., Fraser, H.L. (2005) "Direct observations and analyses of dislocation substructures in the a phase of an a/b Ti-alloy formed by nanoindentation," *Acta Mat*., Vol. 53, pp. 5101-5115.

Wang, Y.Y., Yao, W.X. (2004) "Evaluation and comparison of several multiaxial fatigue criteria*," Int. J. of Fatigue*, Vol. 26, pp. 17-25.

Wang, Y.U., Jin, Y.M., Cuitin, A.M., Khachaturyan, A.G. (2001) "Phase field microelasticity theory and modeling of multiple dislocation," App. Phy. Letter, Vol. 78, pp. 2324-2326.

Williams, J.C., Baggerly, R.G., Paton, N.E. (2002) "Deformation behavior of HCP Ti-Al alloy single crystals," *Met. Mat. Trans.*, Vol. 33, pp. 837-850.

Winter, A.T. (1974) "A model for the fatigue of copper at low plastic strain amplitudes," *Philos. Mag.* Vol. 30, pp. 719–738.

Winterfeld PH, Scriven LE, Davis HT, (1981) "Percolation and conductivity of random two-dimensional composites," *J. Phys. C: Solid State Phys*., Vol. 14, pp. 2361-2376.

Xue, Q., Meyers, M.A., Nesterenko, V.F. (2002), "Self-organization of shear bands in titanium and Ti–6Al–4V alloy", *Acta Materialia*, Vol. 50, pp. 575–596.

Xiao, L., Umakoshi, Y. (2002) "Cyclic deformation behavior and dislocation structure of Ti-5at.% Al single crystals oriented for double prism slip," *Phil. Mag. A*, Vol. 82, pp. 2379-2396.

Xiao, L., Umakoshi, Y. (2003) "Cyclic deformation behavior and saturation bundle structure in Ti-5at.% Al single crystals deforming by single prism slip," *Phil. Mag. A*, Vol. 83, pp. 3407-3426.

Xiao, L., Umakoshi, Y. (2003) "Orientation dependence of cyclic deformation behavior and dislocation structure in Ti-5at.% Al single crystals," *Mat. Sci. Eng. A*, Vol. 339, pp. 63-72.

Yang, Q., Mota, A., Ortiz, M. (2006) "A finite-deformation constitutive model of bulk metallic glass plasticity", *Compu. Mech*., Vol. 37, pp. 194-204.

Zaiser, M., Avlonitis, M., Aifantis, E.C. (1998) "Stochastic and deterministic aspects of strain localization during cyclic plastic deformation," *Acta Mater*. Vol. 46, pp.4143-4151.

Zhang, M., Mayeur, J., McDowell, D.L., Neu, R.W. (2005) " Three Dimensional Crystal Plasticity Simulation on Fretting Fatigue of Ti-6Al-4V", 2005 ASME International Mechanical Engineering Congress and Exposition (IMECE 2005), Orlando, FL, November 13 - 18, 2005.

Zhang, M., Zhang, J., McDowell, D.L., Neu, R.W., (2006a) "Investigation of complex polycrystalline grain structures on fretting of duplex Ti-64 using 3D Voronoi tessellation," Fatigue 2006, May 2006, Atlanta, GA.

Zhang, M., Zhang, J., McDowell, D.L., (2006b) "Microstructure-scale Modeling of Mechanical Deformation of Ti-6Al-4V Based on Computational Crystal Plasticity", 43rd Annual Technical Meeting of the Society of Engineering Science (SES2006), State College, PA, Aug. 13-16, 2006.

Zhang, M., Zhang, J., McDowell, D.L. (2007) "Microstructure-Based Crystal Plasticity Modeling of Cyclic Deformation of Ti-6Al-4V," *Int. J. of Plas.,* Vol. 23, pp. 1328-1348.

Zhang, M., McDowell, D.L., Neu, R.W., (2007) "Microstructure sensitivity of fretting fatigue based on computational crystal plasticity," submitted to *Tribology International*.

Zhou, D., Moosbrugger, Y., Morrison, D.J. (2006) "Finite element simulation of PSB macroband nucleation and propagation in single crystal nickel cycled at low plastic strain amplitude," *Int. J. of Plas*., Vol. 22, pp. 1336-1366.

Zhou, D., Moosbrugger, Jia, Y., Y., Morrison, D.J. (2005) "A substructure mixture model for the cyclic plasticity of single slip oriented nickel single crystal at low plastic strain amplitudes," *Int. J. of Plas*., Vol. 21, pp. 2344-2368.

Zikry, M.A., Pothier, M.R., Baucom, J.N. (2000) "high strain-rate shear-strain localization in fcc crystalline materials: a perturbation analysis," *Int. J. of solids and structures*, Vol. 37, pp. 6177-6202.